Aeroelastic Analysis and Optimizations for Composite Blades on Floating Offshore Wind Turbine

ZhongSheng Deng

A thesis submitted in fulfilment of the requirements for the degree of

Doctor of Philosophy

Department of Naval Architecture, Ocean and Marine Engineering

University of Strathclyde

Glasgow

Supervised by: Professor Qing Xiao, Dr Liu Yang

September 2025

Declaration

This thesis is the result of the author's original research. It has been composed by the author and has not been previously submitted for examination which has led to the award of a degree.

The copyright of this thesis belongs to the author under the terms of the United Kingdom Copyright Acts as qualified by University of Strathclyde Regulation 3.50. Due acknowledgement must always be made of the use of any material contained in, or derived from, this thesis.

ZhongSheng Deng

Signature: ZHONGSHENG DENG Date: NOV 5 2025

Acknowledgements

First and foremost, I would like to express my most sincere gratitude to my supervisors Professor Qing Xiao and Dr Liu Yang for their continuous supports and inspiring mentorship throughout my PhD journey. No matter where I am going and what career I will be taking, their rigorous attitudes in research, open mindsets and the sense of responsibility have greatly shaped my academic development. My deepest hope is to always keep the long-term relations with them as they are not only my mentor in research, but also a model in my future work and life-long self-improvements.

I am sincerely thankful to Dr Yang Huang, Professor Yuanchuan Liu and Professor Enhao Wang, for their insightful discussions, experience and generous support to my research. Their extensive knowledge and encouragements have always been great treasure that helped me get on the right track during my studies.

I gratefully acknowledge the supports from Professor Xiu T Yan, Dr Saishuai Dai, Dr Yang Luo, Dr Yang Zhou and Dr Marvin Wright for their generous help and encouragements during my PhD study. Their expertise from different research backgrounds have inspired me a lot during my interdisciplinary research topic.

I also would like to thank my colleagues and friends in the Strathclyde community and the Department of Naval Architecture, Ocean and Marine Engineering for their supports.

Special thanks to my comrade, my brother-in-arms, Dr Yunxin Xu. I feel very lucky meeting and knowing him. Our PhD journey has been challenging but we made it. We share a memory that never dies which will always encourage us to overcome any difficulties.

Finally, to my beloved family, my parents, I own my deepest thanks to them for their unconditional support and love. Their emotional support has been the foundation of my perseverance throughout the ups and downs of this long journey.

Abstract

Modern wind energy industry has embraced larger turbine solutions with ultra-long blades that has reached a 100-150 meter scale for maximising the amount of power extraction and increasing the levelized cost of energy (LCOE) of the wind turbines. One key driving factor of this technological advancement is the necessity for in-depth understandings of the blade aeroelastic behaviour and its structural responses of the composite blades, particularly under complex operational conditions such as those experienced by floating offshore wind turbines (FOWTs). However, analysing the aeroelastic responses of such composite structures can encounter significant computational challenges, such as the difficulties in capturing global-local coupled behaviours and anisotropic material effects due to the excessive computational expenses.

This thesis is structured in two main parts: (1) the development of a high-fidelity aeroelastic analysis framework for composite FOWT blades via fluid–structure interaction (FSI); and (2) multi-objective structural optimization of composite blades using surrogate-assisted algorithms.

In the first part, an FSI framework aiming for the structural response investigations of composite wind turbine blade on FOWT is developed. This work is a further development based on previous developed FSI framework established by Yuanchuan Liu (2018) who integrated the open-source computational fluid dynamics (CFD) code OpenFOAM and the multibody dynamics (MBD) method MBDyn for the flexible structure aeroelastic predictions. In parallel, the fully-resolved finite element analysis (FEA) for the composite blade is conducted using the commercial package Abaqus CAE, where the blade aeroelastics being resolved in FSI can be applied explicitly for the field recovery for stress inspections on the blade.

This FSI framework is used for FOWT blade aeroelastic investigations with consideration of anisotropic composite material properties. To reasonably account for the influence of platform motions, a prescribed sinusoidal motion function resembling the FOWT platform motions under a regular wave condition is applied, allowing a realistic reproduction of the dynamics on the FOWT blades. The present FSI

framework performs more computationally efficient than existing FSI strategies by reducing nearly 25% of core-hours of computing resources while offering detailed multi-hierarchy composite structural insights into the non-uniform stress behaviour across the blade under dynamic loading conditions.

In the second part of this work, we presented a further extension based on the established FSI framework for blade structural optimizations, aiming to achieve higher strength-weight ratio blade designs to support the upscaling trend of the future wind turbine blades. A nondominated sorting genetic algorithm II (NSGA-II), is integrated with a machine learning (ML) based artificial neural network (ANN) surrogate model for approximating the objective outputs (i.e. blade weight and max. Von Mises stress). This approach streamlined the conventional FEA approach so that a significant reduction in computational expenses is achieved. A notable challenge of the distribution drifting issue of the surrogate model is identified and addressed, improving the generalisability and predictive accuracy of the ANN during iterative optimization. The framework demonstrates its robustness and effectiveness in high-dimensional design spaces, achieving substantial blade weight reduction without compromising structural integrity.

This work systematically introduced a numerical FSI analysing and optimization workflow by taking the advantages of CFD, MBD and FEA, for the FSI investigations for the flexible composite structures. The novelty of this work is that we provide a general-purpose FSI-driven surrogate-assist structural optimization framework for designing flexible composite structures with higher strength-to-weight performance. The proposed framework in this work is also capable of handling applications beyond wind turbines to other complex systems that are prone to interactive environments between the fluid and structure physical fields accompany with different forms of dynamic motions, offering detailed insights in aero- or hydroelastics terms and has a great potential in the light-weight designs for composite structures.

Publications

Journal Papers

Deng, Z., Xiao, Q., Yang, L., Liu, Y., & Wang, E. (Pending). Active Sampling Surrogate with NSGA-II for Effective Multi-objective Optimisation: Structural Improvement of Composite Blade. (Under preparation).

Deng, Z., Xiao, Q., Yang, L., Liu, Y., & Wang, E. (2025). Aeroelastic investigations of composite blade on floating offshore wind Turbine: Insights into stress responses on multi-hierarchy blade structures. *Ocean Engineering, 330*, 121305. https://doi.org/10.1016/j.oceaneng.2025.121305

Deng, Z., Xiao, Q., Huang, Y., Yang, L., & Liu, Y. (2024). A general FSI framework for an effective stress analysis on composite wind turbine blades. *Ocean Engineering, 291*, 116412. https://doi.org/10.1016/j.oceaneng.2023.116412

Collaborate Journal Paper

Bergua, R., Robertson, A., Jonkman, J., Branlard, E., Fontanella, A., Belloli, M., Schito, P., Zasso, A., Persico, G., & Deng, Z., Xiao, Qing. (2022). OC6 project phase III: validation of the aerodynamic loading on a wind turbine rotor undergoing large motion caused by a floating support structure. *Wind Energy Science Discussions*, 1-33. https://doi.org/10.5194/wes-8-465-2023

Conference Papers

Deng, Z., Xiao, Q., & Yang, L. (2023). Decomposed FSI Analysis for Fast Stress Reconstruction on Composite Wind Turbine Blades. *Wind Energy Science Conference*. Glasgow, UK.

Deng, Z., Xiao, Q., Yang, L., & Liu, Y. (2022). FSI Investigation of Composite Material Blade Aero-elastic Performance on Wind Turbines. *International Offshore Wind Technical Conference*. Boston, Massachusetts, USA.

Deng, Z., Xiao, Q., & Yang, L. (2020). Investigating structural behaviour of wind turbine composite blade using FSI method. *In 7th PRIMaRE Conference*. Plymouth, UK.

Posters and Presentations

Deng, Z., Xiao, Q., & Yang, L. (2024). Aeroelastic Validated Lightweight Blade Design for FOWT. *CENSIS Technology Summit.* Glasgow, UK.

Deng, Z., Xiao, Q., & Yang, L. (2023). Decomposed FSI Analysis for Fast Stress Reconstruction on Composite Wind Turbine Blades. *Wind Energy Science Conference*. Glasgow, UK.

Table of Contents

List of Figures

List of Tables

Nomenclature

Roman Symbols

A	Surface area
A_S	Platform surge amplitude
C_p	Pressure coefficient
EA	Axial extensional stiffness
EJ_y	Edgewise bending stiffness
EJ_z	Flapwise bending stiffness
GA_y	Local in-plane (rotor) shear stiffness
GA_z	Local out-of-plane (rotor) shear stiffness
GJ	Torsional stiffness
GCI_{fine}	Grid convergence index between the fine and medium grid solutions
P	Power output
p	Pressure
R^2	Coefficient of determination
Re	Reynolds number
r/R	Spanwise distance on the blade
T_S	Platform surge period
U	Velocity of fluid flow
U_0	Freestream speed

UX	Velocity of fluid flow on X direction

Greek Symbols

σ	Stress
θ	Fibre orientation
λ	Tip speed ratio
ρ	Density of the fluid
ν	Kinematic viscosity of fluid
ω	Specific dissipation rate
γ	Diffusivity coefficient for dynamic mesh
Ω_0	Rotation speed of rotor
ϕ_x^T	Jacobian transpose of the constraint equations

Abbreviations

ALM	Actuator Line Model
AMI	Arbitrary Mesh Interface
ANN	Artificial Neural Network
AOA	Angle-of-Attack
BEM	Blade Element Momentum Theory
CFD	Computational Fluid Dynamics
DAE	Differential-Algebraic Equation
DLC	Design Load Case
DOE	Design of Experiment

ESM	Effective Stiffness Matrix
FAST	Fatigue, Aerodynamics, Structures, and Turbulence analysis code
FEA	Finite Element Analysis
FOWT	Floating Offshore Wind Turbine
FSI	Fluid Structure Interaction
FVW	Free Vortex Wake Method
GA	Genetic Algorithms
GDW	Generalized Dynamic Wake
GELU	Gaussian Error Linear Unit activation function
IEA	International Energy Agency
IEC	International Electrotechnical Commission
LCOE	Levelized Cost of Energy
LES	Large Eddy Simulation
LHS	Latin Hypercube Sampling
LLFVW	Lifting Line FVW Method
MAE	Maximum Average Error
MBD	Multibody Dynamics
MC	Monte Carlo
ML	Machine Learning
NREL	National Renewable Energy Laboratory

NSGA-II	Non-dominated Sorting Genetic Algorithm II
NWS	Normal Windmill State
OC4	Offshore Code Comparison Collaboration, Continuation
OML	Outer Mold Layer
PS	Propeller State
RANS	Reynolds-Averaged Navier–Stokes Equations
RMSE	Root Mean Square Error
ROM	Reduced-Order Model
RVE	Representative Volume Element Model
SW	Shear Web
TO	Topology Optimization
TSR	Tip-Speed Ratio
TWS	Turbulent Wake State
UD	Uni-Directional
VABS	Variational Asymptotic Beam Sectional Analysis code

Chapter 1 Introduction

1.1. Background and Motivation

1.1.1 Upscaling Floating Wind Turbines

Over the past decades of rapid expansions of wind power, the wind industry has reached a mutual agreement to push the upscale limit of the wind turbines and develop floating offshore wind turbine technologies.

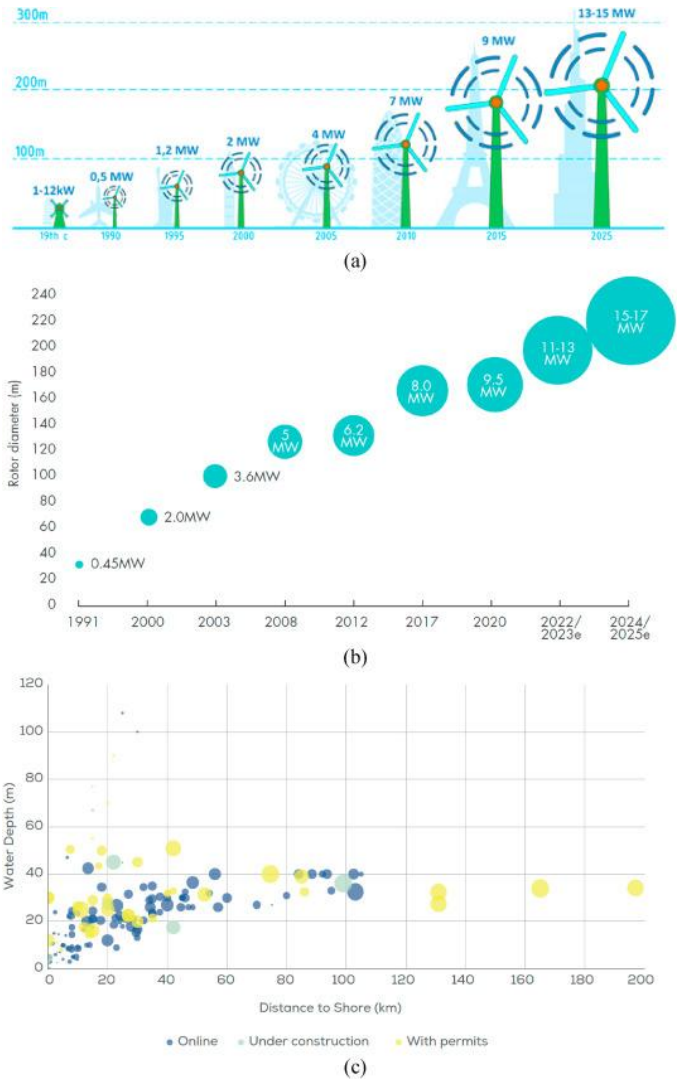

Figure 1-1. Progression of (a). Turbine and rotor size, (b). Turbine capacity, and (c) Average water depth and distance to shore for offshore wind farms in Europe (Kusuma et al., 2024).

The offshore wind outperforms the conventional onshore wind counterpart due to two reasons: i). it receives more consistent and uniform wind resources with higher speed U for power productions, and ii). it has access to much more free offshore areas and deeper waters for massive installation (Esteban et al., 2011) of offshore bottom-fixed or floating wind turbines. Such trend perfectly follows the guidance of the fundamental theoretical equation of wind power generation (Kalmikov, 2017), where ρ is the air density, A is the swept area of the wind turbine and U is the velocity of the incoming freestream.

$$P = \frac{1}{2} \cdot \rho \cdot A \cdot U^3 \tag{1.1}$$

Reported by the Global Wind Energy Council (GWEC), the total global offshore wind power capacity has reached to 64.3 GW by 2022, with a new installed capacity of approximately 8771 MW being added in the same year (Figure 1-2).

The development mainly took place in the Asia-Pacific (APAC) and European region due to the massive energy demands, supportive policies and advanced technologies as the foundations of such developments.

It is anticipated that the APAC and European region will continue contribute to 49% and 41%, respectively, aiming for reaching a 380 GW of new global offshore wind capacity from 2023 to 2032 (Williams & Zhao, 2023).

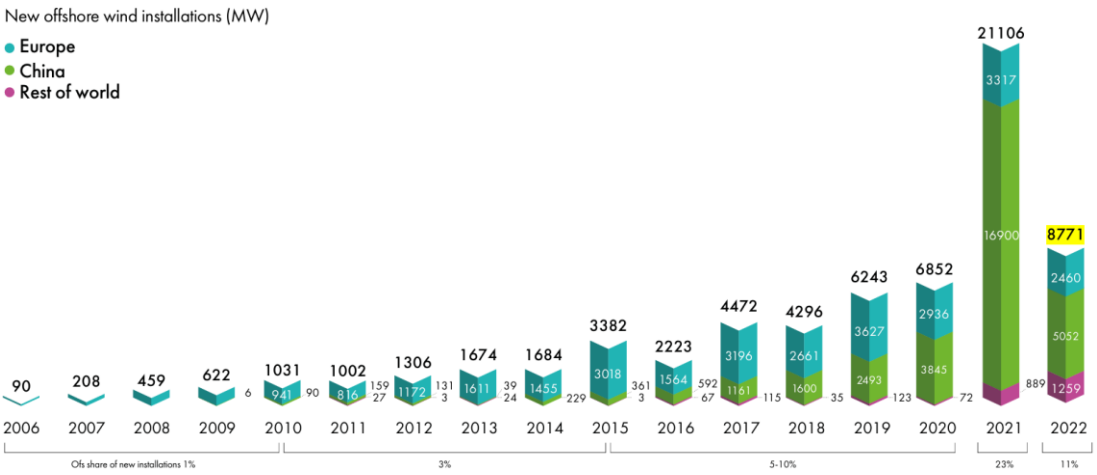

Figure 1-2. Global new installations of offshore wind capacity.

Such fast expansion in offshore wind relies on the continuous advancements and developments of larger-scale wind turbines, especially to accelerate the transitions of floating wind turbines from demonstration to pre-commercial phases. With such upscaling trend of modern wind turbines, there has been a growing need to enhance the structural strength of composite blades (Mark & Feng, 2023). Typical FOWT platform concepts are demonstrated in Figure 1-3.

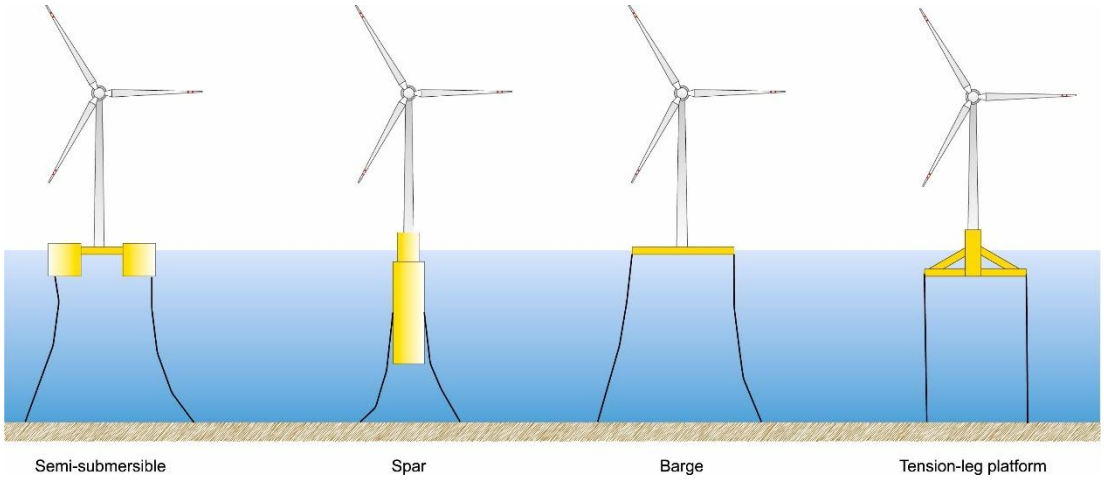

Figure 1-3. Common platform concepts of FOWTs (Micallef & Rezaeiha, 2021).

Unlike conventional bottom-fixed offshore wind turbines grounded to the seabed, as illustrated in Figure 1-4, the loading characteristics of FOWT are considerably more complex due to the additional six-degree-of-freedom (6-DoF) platform motions.

In practice, larger FOWTs necessitate advanced design methodologies to ensure robust structural integrity under severe dynamic loads, including extreme and fatigue loading. The blades must be designed to survive a service life of approximately 20–25 years.

As turbine capacities approach and exceed 10–15 MW, the corresponding blade lengths have surpassed 100 m, which further exacerbates the vulnerability of the structures under such highly coupled aero-hydro-elastic conditions.

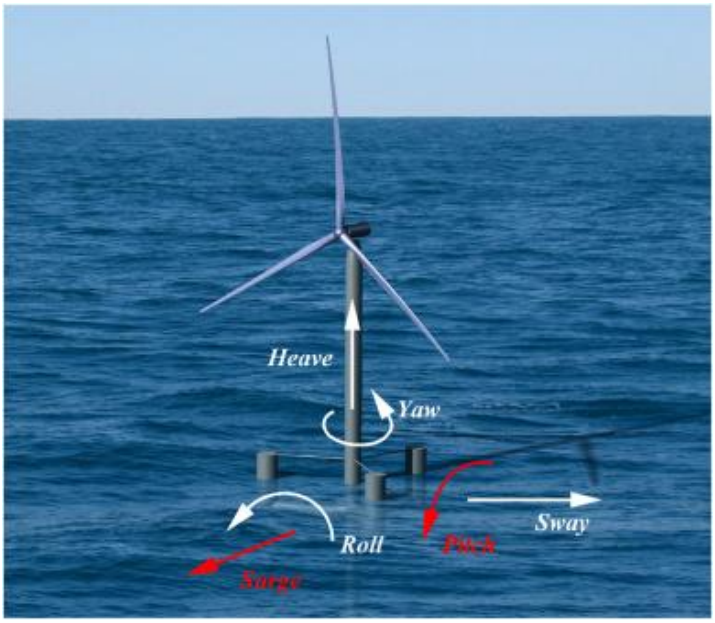

Figure 1-4. Diagram of 6-DoF motions of an FOWT.

Beyond these engineering and structural challenges, floating offshore wind systems also introduce broader environmental, operational, and sustainability considerations throughout their life cycle. Compared with fixed-bottom wind farms, FOWTs are deployed in deeper waters, where installation, towing, and maintenance operations are exposed to harsher metocean conditions, resulting in higher cost, risk, and logistical complexity (Jiang, 2021; Chitteth Ramachandran et al., 2022).

Recent studies have further highlighted that the life-cycle environmental impact of floating wind farms, covering materials production, platform and mooring manufacturing, transportation, and decommissioning. These can significantly influence the total carbon footprint and sustainability performance (Danovaro et al., 2024).

Moreover, the interaction between FOWTs and the marine ecosystem has raised increasing concern, as underwater noise, electromagnetic fields, and seabed disturbance may affect local habitats and marine species (Rezaei et al., 2023).

These multidisciplinary challenges emphasize that the design and optimisation of floating wind turbine blades should not only target structural efficiency but also

integrate life-cycle and environmental perspectives to ensure long-term sustainability and minimal ecological footprint.

In this context, the present research aims to contribute to these goals by developing advanced aeroelastic modelling and optimisation methodologies for large composite blades, enabling improved structural reliability and material efficiency within the broader sustainability framework of floating offshore wind energy.

1.1.2 Composite Materials in Upscaling FOWT Blades

The composite material refers to the constituents consisting of two or more types of materials with distinct properties, which usually performs a heterogeneous characteristic in structural terms, and anisotropic stiffnesses in terms of loading performance (Gunwant & Bisht, 2024).

Given that the blade mass generally exhibits a cubic relationship with the rotor diameter, the modern wind turbine blades are constructed using high performance fibre-reinforced composite materials as they possess higher specific modulus and strength comparing with the conventional isotropic metallic materials (Xu et al., 2024), meaning that the composite blades can achieve a higher cost-effectiveness using the stronger materials with significant weight reductions and less material demands.

Due to the large length-to-thickness ratio characteristic, the composite blade is typically considered as a thin-walled (shell) structure (Zheng et al., 2023). Multiple composite laminates are stacked layer-by-layer with specific configurations and plans, forming the shell structure with non-uniform thickness distributions along the blade. There are several reasons for such design. First, the shell structure can effectively distribute the primary bending and torsion loads of the operating blade across the structure. Second, the utilizations of composite material are primarily deployed in the limited thickness of shell structures, so that the materials are preforming effectively. Third, to feasibility implement precise shape and quality control of the blade during the manufacture process, the shell structure is an easier configuration to construct, which is important for achieving a desired aerodynamic performance.

Geometrically, as depicted in Figure 1-5, a blade generally consists of the upper, lower shells and shear web structures with continuous shape variations. Besides, the blade cross-sections along the blade span are arranged with varying twist angles with respect to the blade pitch axis.

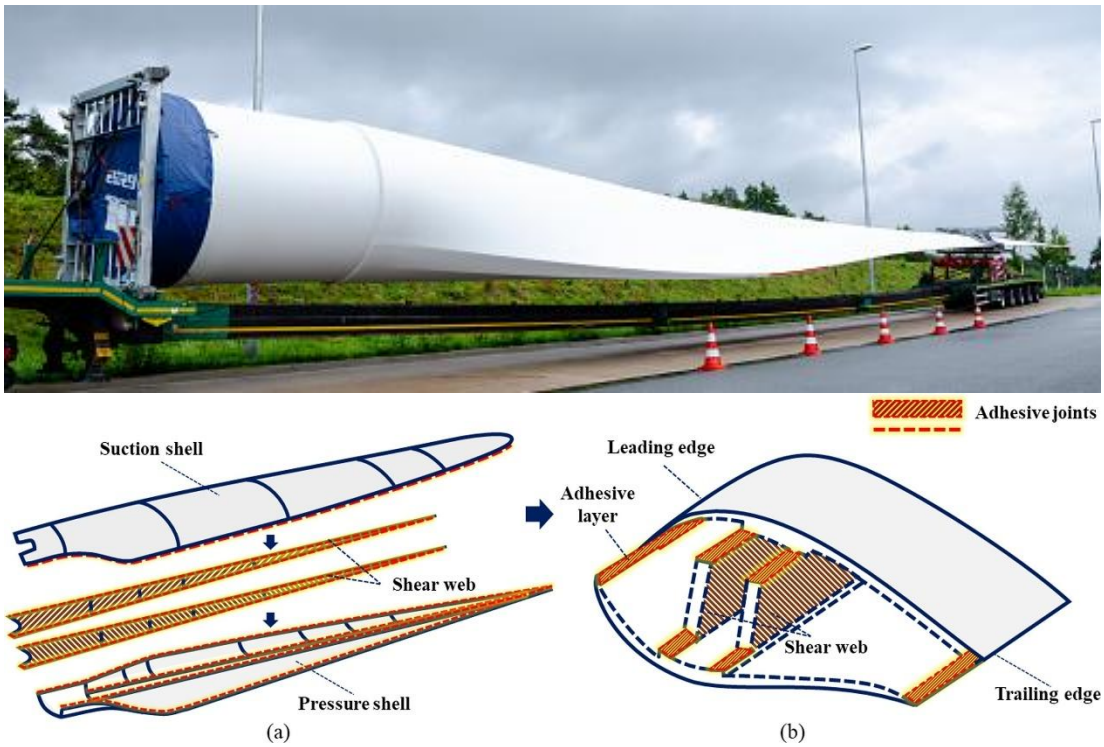

Figure 1-5. Top: Real blade, Bottom: Internal structure of the blade (Liu et al., 2024).

Due to the unsteady, non-uniform aerodynamic loading characteristics on the blade, the localised structural reinforcements are implemented, which are reflected by the non-uniform thickness changes of the composite layups across the blade shell structures, with deployments of different materials. An example of composite blade illustrating such non-uniform characteristics is depicted in Figure 1-6.

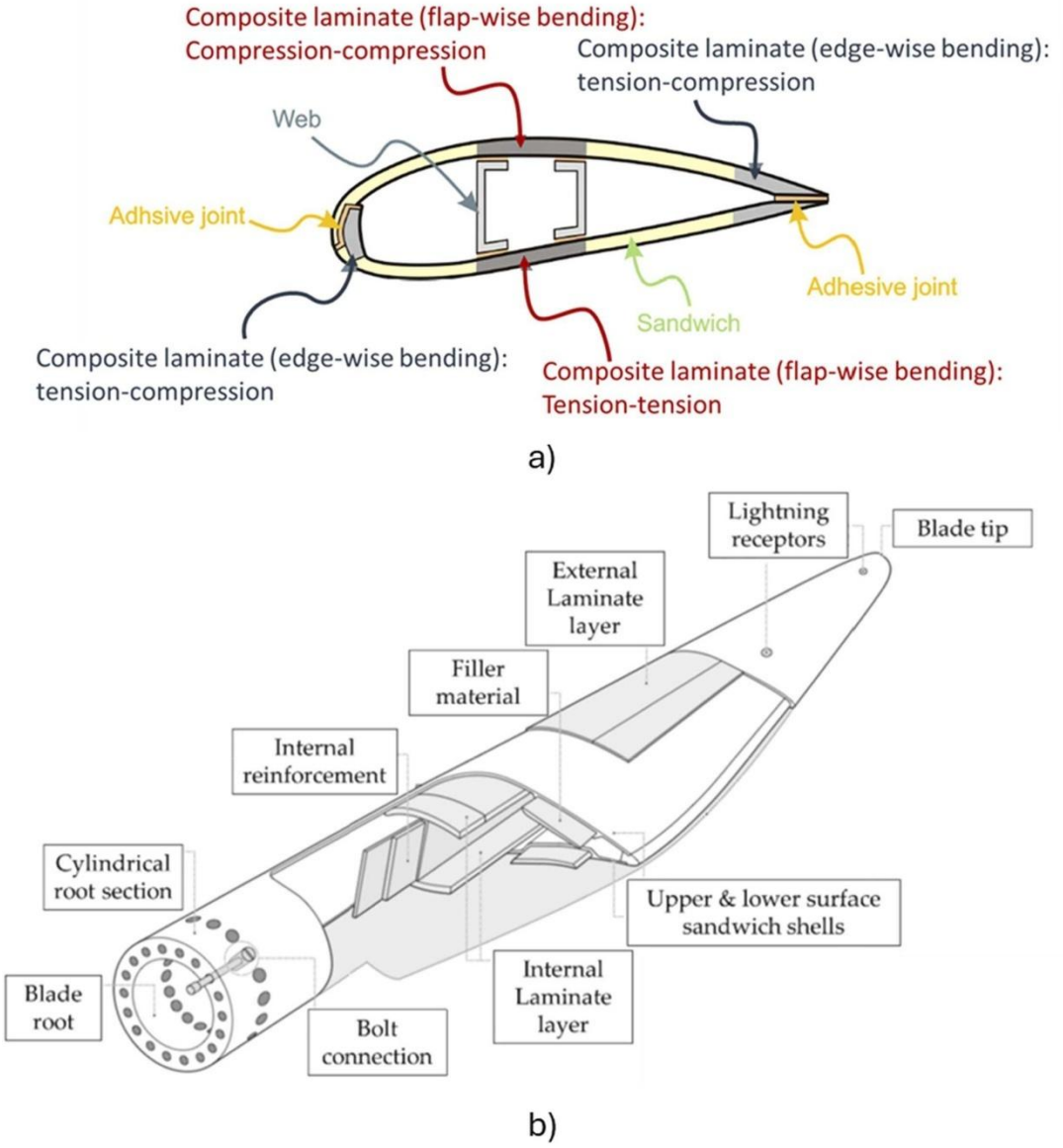

Figure 1-6. Schematic diagrams of (a). cross-sectional composite specifications and typical load types, and (b). overall layout of composites on a single wind turbine blade (Martulli et al., 2025).

It is reasonably expected that the composite structural performances in response to the FOWT loads can be highly nonlinear due to the interactions between the dynamic loads and the geometric nonlinearity, where the mechanical properties in the composite constituents are non-consecutively distributed.

Furthermore, several other crucial factors such as the deployment locations, stacking sequence, the numbers of laminate layers, the laminate thickness, and the in-ply fibre

angles orientations, etc. (Resor, 2013), can also significantly affect the aeroelastic performances of the composite blade. The actual designs of composite structures are oriented by the blade's aeroelastic characteristics and mechanical requirements of the materials under specific operation conditions. Figure 1-7 shows a numerical modelling of the NREL 5MW wind turbine blade, which reflects the complexities in modelling a composite blade.

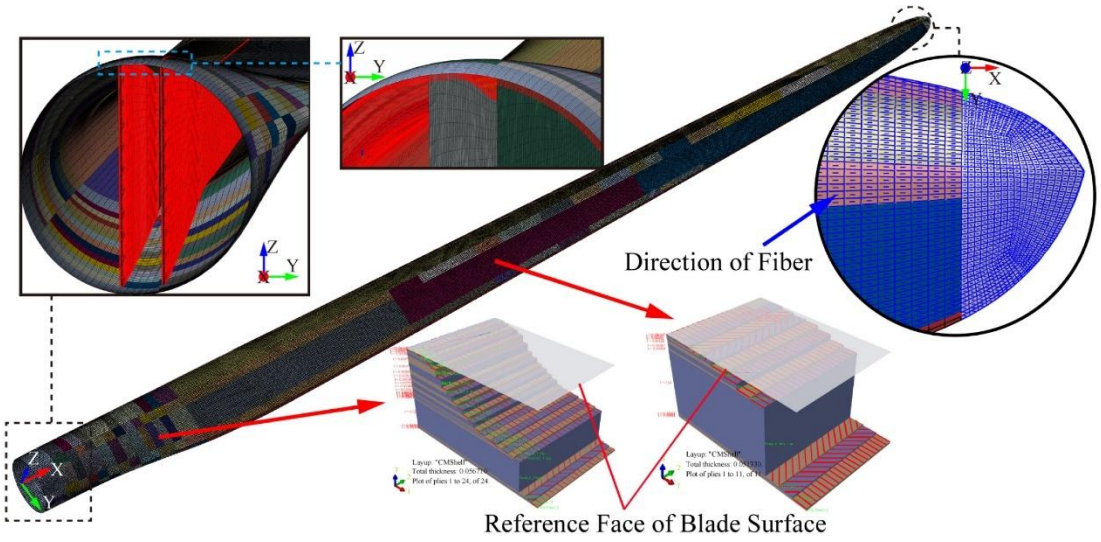

Figure 1-7. Example of a composite blade model, resolving for the non-uniform thicknesses, deployments and orientation of composite materials (Miao et al., 2019).

Such intricacies need to be comprehensively investigated by focusing on the composite structure response under the realistic loading conditions. To do this numerically, the individual composite laminates and core materials must be well organised to meet stress, stiffness, and fatigue requirements under certain loading conditions.

For the upscaling wind turbine, on the one hand, it needs to withstand the significant static loads due to the centrifugal and gravity effects, and the ultimate load under the severe load conditions, for instance, the extreme condition defined by the IEC design load case (DLC) 6.1 (IEC, 2005; Resor, 2013). On the other hand, during the operations, the couplings among the blade bending, torsion and shear loads can induce cyclic local stress concentrations, which appears to be more influential to the blade fatigue strength over its operational lifespan. For instance, the cycling of flapwise and edgewise deflections may lead to repeated out-of-plane and in-plane bending motions,

thus causes dynamic stress fluctuations along the blade shell composite structures. This can subsequently cause failures such as composite delamination or debonding, and ultimately, accelerates the degradation of the blade structural strength and integrity.

With a successful implementation of quantitative analysis of the composite blade, then, the optimization of the blade can be conducted to further improve its performances. This is usually a multi-disciplinary work which involves comprehensive considerations of numerical analysis, physical requirements and feasibility assessment of the optimization designs.

Considering these ultra-long blades are usually operated in highly nonlinear aeroelastic regimes, the neglection of coupling effects between aerodynamic loads and structural deformations can lead to suboptimal designs. For composite blade designs, the array of objectives such as the stiffness, mass, cost, durability, aerodynamic performance, etc., must be well balanced while navigating constraints related to manufacturability and safety margins.

1.1.3 Numerical Approaches for Blade Aeroelastics

The FOWT blades are operated under a highly interactive condition, where the local deflections, global rotation, platform motions and the incoming flows, are coupled together. This can lead to continuous aeroelastic unsteadiness, for instance, the variations in angle-of-attack on blades, where the apparent flow on blades changes significantly that causes surging in thrust and power (Li et al., 2025), and under some extreme situation, the destructive flutter can occur that severely jeopardize the safe operation of the wind turbine.

Such unsteadiness on the blade can potentially cause severe flow separations, so that the FOWT power outputs may exhibit large fluctuations. In structural terms, the blade may withstand large loads that exceed the allowable strength of the blade structures.

Therefore, it is essential to investigate the interactive mechanism and analyse the potential consequences for such coupled, nonlinear system. The revealing of blade aeroelastics underlying physics is very much depending on advanced numerical techniques, to provide quantitative inspections of the blade's aeroelastic behaviours

under interested load conditions. To properly capture the intense interactive behaviours in the blade's aeroelastics, the fluid structure interaction (FSI) approaches are developed, which have extensively adopted in the past research.

The roadmap of existing numerical approaches for FOWT blade aeroelastic FSI studies is illustrated in Figure 1-8. A well practice of such numerical study can accelerate the development of FOWT designs and assist the blade optimizations.

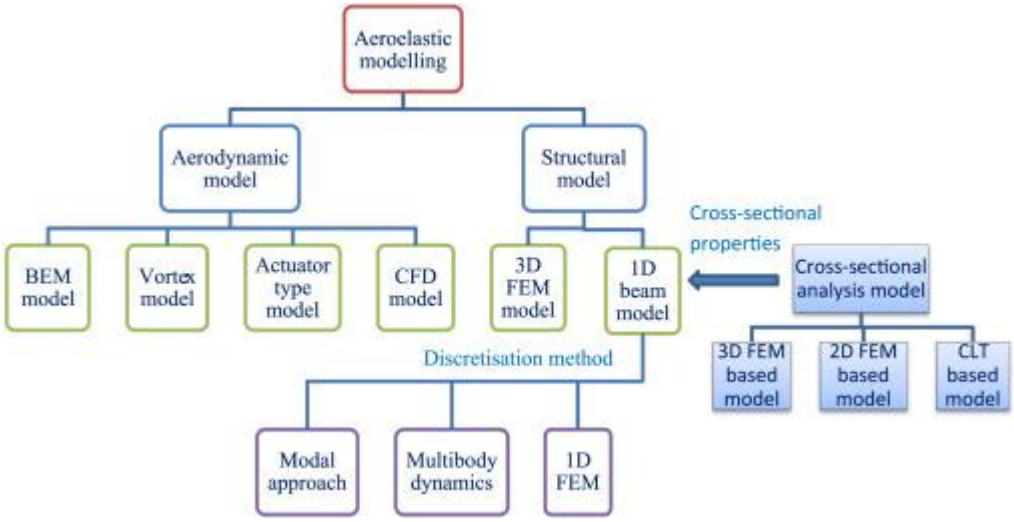

Figure 1-8. Optional technical routes for wind turbine blade aeroelastic investigations. (Wang, Liu, et al., 2016).

Conventional blade design frequently relies on simplified structural representations, but the significant improvements in composite layup configurations has led to a more complex structure, so that the purely empirical or simplified methods are inadequate in accurately capturing dynamic behaviours of the blade.

Consequently, recent research has moved toward more comprehensive approaches, including multi-scale analyses and detailed finite element modelling (Zhu et al., 2025), to capture the composite anisotropic material behaviours.

This suggests that the accurate predictions of aeroelastic performance of the FOWT blade is of great importance to a successful FOWT design, relying on adoptions of suitable numerical methods, although it is rather challenging.

On the one hand, from the aspect of maintaining the numerical fidelity and accuracy, numerical methods typically revolve around fully resolved Computational Fluid Dynamics (CFD), which provides detailed insight into flow structures, boundary layer development, and potential flow separation. CFD codes based on Reynolds-averaged Navier-Stocks equations (RANS) can capture mean flow features at a relatively computational affordability, whereas more accurate models like Large-Eddy Simulation (LES) or hybrid RANS-LES methods may further capture unsteady, turbulent eddies with greater details.

These advanced CFD tools can handle complex blade geometries, account for transient flowing conditions, and reliably predict flow states in both attached and post-stall regimes. In combination of CFD method with finite element analysis (FEA) in two-way FSI analysis, they also enable researchers to resolve local strain gradients, interlaminar stresses, and anisotropic behaviour in laminated composite structures.

On the other hand, however, such high-fidelity two-way FSI simulations can be computationally demanding (Wang, Liu, et al., 2016). Meeting the numerical requirements for mesh resolution (particularly near the boundary layers, blade tips, or flow separation regions) and solver stability often necessitates large computational grids and iterative solution procedures. This challenge gets intensified when investigating the transient phenomena, which usually demand strict control and well tune of numerical specifications for prediction accuracy in both fluid and structural solvers.

Considering the prohibitively high computational expenses, engineering practice often adopts one-way coupling for FOWTs, provided that the blade deformation is not significant enough to drastically alter the flow field. Nonetheless, as turbines grow in size and rotor flexibility increases, ignoring fluid-structure feedback may jeopardize the accuracy of predicted loads and lifetime estimations, making more advanced coupling strategies a core focus of ongoing research.

One trade-off strategy for addressing the expensive computational issue is to partially or completely use the reduced-order or surrogate models for specific subsystems during the FSI simulations. For instance, the Blade Element Momentum (BEM) or

Free Vortex Wake (FVW) methods may be employed for aerodynamic load assessments. While for the structural dynamic predictions, the beam-element models have been extensively justified and used by many studies as they perform rather robustly and accurately.

It is realised that the inspections to local stress states in composite plies is particularly important for next-generation FOWT blades, where the optimizations and designs for the composite blade often require well configurations of lamination thickness, fibre orientation, or new material combinations in order to achieve higher stiffness-to-weight ratios.

If the aerodynamic loads are not properly predicted, the blade designs may suffer from insufficient or excessive redundancy of meeting the specific designing requirements, and lead to unexpected failures under severe operational or environmental conditions. Therefore, the further development of a general-purpose FSI analysis framework is needed, which is capable of accurate aeroelastic predictions for FOWT applications, with considerations of anisotropic composite properties.

1.1.4 Structural Optimization of Composite Blade

Historically, the optimizations for composite blade structures are often conducted using decoupled sequential optimizations, where the intense interactive nature of the blade aeroelastics were omitted (Scott et al., 2020; Lee & Shin, 2022), or used the reduced-order models (ROMs) (Tarfaoui et al., 2019; Wang et al., 2020; Couto et al., 2023).

However, we argue that a successful composite blade optimization strongly relies on the accuracy and fidelity of the numerical predictions, where the aeroelastic nonlinearity should be carefully considered. This is important as either over or underestimations of the blade aeroelastic characteristics would lead to excessive design redundancy or inadequacy of the composite blade structural performances on FOWTs, then ultimately, influence the long-term levelized cost of energy (LCOE) performance of FOWTs.

Past structural optimization studies typically focused on, not limited to, minimizing blade mass (Barnes & Morozov, 2016), maximizing structural stiffness (Roth-Johnson et al., 2014) and enhancing fatigue strength (Lobitz et al., 2001), where the optimizations usually involve multiple times of iterative processes (hundreds to thousands) over a high-dimensional design space, i.e. a large number of input variables (Kassapoglou, 2013).

This means the actual responses of the blade behaviour can perform nonlinearly with discontinuous or multimodal characteristics, thus characterized as a high-dimensional, non-convex, multi-objective optimization problem. Such characteristic makes it a computationally intensive problem for searching the global optimal solution (Ghiasi et al., 2009; Albazzan et al., 2019).

Moreover, when integrating the FEA code for calculating composite structural responses directly in-the-loop during optimization process, the computational cost would become even higher, also it may requires additional specific communication protocols for parametrical designs (Bhosekar & Ierapetritou, 2018).

To alleviate these issues, there are two strategies that have been adopted by many studies: (1). to effectively explore the design space using the Metaheuristic algorithms such as Genetic Algorithms (GA), Particle Swarm Optimization (PSO), Imperialistic Competitive Algorithm (ICA) and Firefly Algorithm (FA), and (2). to streamline the time-consuming FEA by the surrogate models with, e.g. the Response Surface model (RSM), Kriging method, Support Vector Regression (SVR) and Radial Basis Function (RBF) models and the data-driven models based on Machine Learning (ML) techniques.

On the one hand, the metaheuristic algorithms are a class of biological or physical-processes inspired methods, which are naturally suitable for addressing nonlinear, multimodal, multi-objective, combinatorial, or constrained optimization problems. These algorithms do not rely on gradient information of the objective functions. Instead of finding the exact global optimal solution, they tend to identify sufficiently good approximate solutions toward the global optimum within a reasonable computational cost.

On the other hand, the implementation of surrogate models in the metaheuristic algorithms can massively empower the efficiency of the optimization process. The training of a well-fitting surrogated model often requires for a proper preparation of the training samples to fit the actual solution space of the targeting input-output system.

Specifically, these training samples should be good representatives of the actual solution space, which are usually calculated beforehand using analytical or numerical methods, e.g. the FEA method. Besides, the number of sampling points need to be sufficient enough with a uniform distribution across the solution space (Kapusuzoglu et al., 2022; Guo et al., 2023).

To prepare such sampling points, the Design of Experiment (DOE) techniques including the pseudo-random sampling (RS), Monte Carlo Sampling (MCS), quasi-random sampling (QRS) and Latin Hypercube Sampling (LHS) (Cruz et al., 2024), are often common approaches, while the selection of these methods is depending on the objectives of the surrogate model, as well as the dimensional and temporal/spatial characteristics of the input parameters.

Given the above considerations, in this work, the realistic loading characteristics of the blade will be considered during the optimization process. The careful selections of the optimization algorithm and applicable surrogate model are depending on the characteristics of the presented problem, including the complexity of the design variables and objective functions of the composite blade system.

1.2. Research Objectives

The first objective of this research is to establish a general-purpose, high-fidelity two-way FSI analysis framework for composite wind turbine blade aeroelastic analysis. This part of work is based on the previous research outcomes established by Liu (2018) and we further developed the FSI features by considering anisotropic composite properties and actual non-uniform composite layups of the structures.

Then, the second objective is to propose an effective multi-objective structural optimization workflow, specifically aiming to handle the high-dimensional optimization problems.

When designing the workflows, the principle is that a well balance between the numerical accuracy and computational efficiency should be maintained. To achieve the research objectives, the key milestones are marked as follows:

1. **Analysing the nonlinear aeroelastic responses of composite blades on FOWTs.** Using the CFD-MBD FSI framework, the unsteady aerodynamic loadings and structural deformations can be fully captured. The stress distributions of the blades are subsequently resolved using the FEA. The effective stiffness matrices are calculated and used in MBD model to correctly reflect the stiffness properties of an actual composite blade in three-dimensional space. This serves as the analysing foundation for further optimization work of the ultra-long (61.5 meters and more) composite blade structures.

2. **FEA modelling of the anisotropic composite blades on FOWT**. A detailed finite element modelling methodology is to be established, resolving non-uniform material distributions, laminate stacking sequences, thickness variations, and fibre orientation effects. The effects of geometric nonlinearities and material heterogeneities on structural performance should be considered during modelling process.

3. **Establishing the surrogate-assist structural optimization workflow for the composite blade design.** Advanced metaheuristic algorithms (e.g., GA, PSO) are to be implemented for high-dimensional, multimodal, multi-objective optimization. Surrogate models (e.g., RSM, Machine Learning-based models) are to be integrated to accelerate the optimization while maintaining high prediction fidelity. Specifically, the high-dimensional variable feature of such structural optimization problem for composite blade is considered.

4. **Generating optimised composite blade designs with numerical verifications and comparisons.** The design objectives are to minimize blade mass while maximizing structural strength, stiffness, and fatigue resistance. The optimized blade designs are to satisfy extreme load survivability

requirements (e.g., severe surge load case or standard IEC DLC 6.1) and long-term operational durability.

5. **Proposing design guidelines for next-generation composite blades for FOWTs.** This may include material deployment strategies, laminate layup designs, and aeroelastic tailoring concepts for ultra-long, highly flexible blades. The aim is to enhance structural robustness and reduce the Levelized Cost of Energy (LCOE) for floating wind energy systems.

1.3. Thesis Outline

The thesis structure is outlined as follows:

Chapter 1 introduces the background and motivations of this research. We firstly highlighted the turbine upscaling trend and the impacts of such trend to the FOWTs. Then, the numerical challenges in aerodynamics, structural and coupling schemes are discussed, especially for a numerical system considering the composite properties and configurations. It is concluded that the industrial trend has suggested that the developments of numerical analysis tools for ultra-long composite blade aeroelastics are crucial for supporting the technological advancement for the future blade designs.

Chapter 2 reviews the previous findings in the physics of blade aeroelastics, as well as the recent numerical approach developments for aeroelastic investigations and multi-objective optimizations of wind turbine blades. This Chapter guides the selection of research methodology in the present work.

Chapter 3 explains the adopted numerical methodologies in detail and pictures a detailed roadmap of the framework for conducting this research.

Chapter 4 demonstrates a series of preliminary study outcomes that validate the numerical methods. This is where the author gained plenty of experience and built the confidence.

Chapter 5 marks the first milestone where the CFD-MBD FSI analysis framework with consideration of composites using FEA is established. Here, we firstly validated

the framework with the composite blade on a bottom-fixed NREL 5MW wind turbine, with quantitative comparisons against the results from other literatures.

Chapter 6 extends the framework's capability in considering the composite blade aeroelastics under a FOWT loading condition, where a prescribed sinusoidal function is used for resembling the platform surge motion under a regular wave condition. The relationships between the platform surge motion parameters (inc. amplitude and period) and the peak stress magnitude on the composite blade are quantitatively investigated. This part of work also provides datasets of blade loading characteristic under FOWT surge motion, which will be subsequently used for the following optimization studies.

Chapter 7 establishes an effective structural optimization workflow for composite blade design and optimization, which combines the advantages of metaheuristic algorithms (i.e. NSGA-II) and ML-based surrogate models (i.e. ANN). To properly handle the high-dimensional characteristic of the present optimization problem, an active-sampling with semi-in-the-loop FEA validation optimization scheme is proposed, showing a significant accuracy improvement of such surrogate-assist optimization process.

To conclude the work, in **Chapter 8** we summarise the main findings, research outcomes, and the contributions of each part of work. We will discuss and comment on the generality and applicability of the proposed numerical workflow. Some limitations are pointed out which requires further improvements. Suggestions are also given in terms of conducting the optimization work for the composite blade structures. We also suggest the future works that can be further conducted based on the present studies.

Chapter 2 Literature Review

Numerous studies have provided aerodynamic and structural insights of FOWT and composite blade performances. In this Chapter, critical problems and technical limitations in the existing research in composite blade aeroelastics on FOWTs are reviewed.

For aerodynamic and structural modelling, the numerical features of various reduced-order methods and high-fidelity methods will be discussed, including the insights provided by these methods.

The review will discuss the principles of method selections and introduce the advantages of available numerical approaches for successful numerical investigations of FOWT composite blade aeroelastics, where the code's capabilities, accuracy, fidelity and computational efficiency are the metrics under considerations.

2.1 FOWT Blade Aerodynamics

Aerodynamically, many studies (Tran & Kim, 2016b; Liu et al., 2017; Tran & Kim, 2018; Liu et al., 2019; Lienard et al., 2020; Ortolani et al., 2020; Micallef & Rezaeiha, 2021) have pointed out that the FOWTs inherently perform more unsteady comparing to the bottom-fixed counterparts.

The reduced-order numerical methods have been extensively developed and used for blade aerodynamic investigations as they perform rather efficiently in computational terms. For instance, the Blade element momentum (BEM) theory method (Ledoux et al., 2021) is one of the industry-standard methods for blade aerodynamic predictions (Papi et al., 2023).

The BEM ideally assumes the rotor to be composed of a series of independent annular elements, where each element experiences axisymmetric, steady, and uniform flow, thus the computational efficiency can be very high. However, due to the actual radial flow and unsteady aerodynamic phenomena in three-dimensional space are neglected, the model usually requires for additional corrections (Moriarty & Hansen, 2005;

Sebastian et al., 2019) to accurately predict for the complex flows, e.g. the Generalized Dynamic Wake (GDW) (Ferreira et al., 2022).

Sebastian et al. (2019) conducted a code-to-code comparison using both BEM and Lifting Line FVW methods (LLFVW) for the DTU 10MW reference wind turbine aerodynamics prediction (Figure 2-1). The results shown that both models performed similar under the constant uniform inflow conditions. However, the instantaneous thrust and power predicted by the BEM performed a higher variation under the turbulent flow conditions (IEC 61400-1 ed. 3, DLC 1.1 and 1.2), which may cause an over-predicted bending momentum at the blade root, thus can lead to unnecessary design redundancy and cost increase.

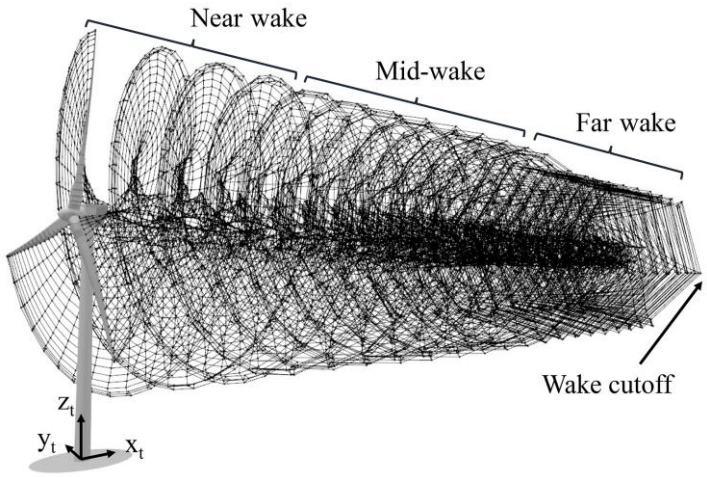

Figure 2-1. The wake structure modelled using LLFVW method (Sebastian et al., 2019).

Cheng et al. (2019) discussed on the influences of platform motion frequency and amplitudes to the aerodynamic loads on the NREL 5MW FOWT. They found that the platform surge and pitch motions have significant influences on the relative velocity between the rotor and incoming flows, thus caused unsteadiness to the blade aerodynamics.

The blade's aerodynamic forces were calculated using the Actuator Line Model (ALM) as it outperforms than the BEM by considering the blade-wake interactions, which is anticipated to happen when the platform motion becomes significant.

However, these simplified methods may fail in in some cases when predicting the nonlinear blade aerodynamics, for instance, under dynamic inflow conditions of a FOWT, or investigating for the flow separation phenomenon, as they are developed based on linear assumptions (Lago et al., 2013; Yu & Kwon, 2014; Yu et al., 2020).

A more comprehensive way of predicting blade's aerodynamics is to conduct the Computational Fluid Dynamics (CFD) analysis, as not only it can provide the time-varying aerodynamic forces history, but also to resolve the detailed flowing phenomenon such as the flow separation and re-circulation.

Tran and Kim (2016b) investigated the NREL 5MW OC4 DeepCWind FOWT blade unsteady aerodynamics using CFD, pointing out that the interactions between the turbulent wake, tip and shedding vortices can significantly influence the blade aerodynamic performance. They also emphasised the importance of considering the wind-wave-structure interactions in accurate predictions of FOWT blade aerodynamics.

A fully-coupled wind-wave-structural interaction system using CFD was developed by Liu et al. (2017) for investigating the aerodynamics of NREL 5MW OC4 DeepCWind FOWT under different FOWT operation situations where the uniform incoming flow was considered for the rigid blade aerodynamic predictions under the regular wave conditions.

Further in 2019, (Liu et al.) extended the code by coupling CFD with MBD for a two-way FSI investigations for the NREL 5MW FOWT blade aeroelastics under a prescribed platform surge motion. A postpone of aerodynamic loads with respect to the surge motion is observed. It was revealed that the instantaneous apparent flow significantly varies during the surge motions, so that the angle-of-attack (AOA) changes consistently, causing noticeable variations of pressure distributions during the surge motions. This also caused the fluctuations in thrust and power of FOWT. A 'time-lag' misalignment between the prescribed motion and the resultant aerodynamic loads was observed, which is due to the dynamic coupling of the blade structural flexibility and the imposed non-uniformly distributed aerodynamic loads.

Similarly, Lee and Lee (2019) observed significant oscillation in the NREL 5MW FOWT blade's aerodynamics due to the periodic variations of AOA on the blade. They pointed out such unsteady inflow condition induced by the platform surge motion can deteriorate the blade's aerodynamic efficiency due to the excessive flow separations.

Ortolani et al. (2020) used CFD to illustrate the significant variations of pressure coefficient distributions at different span locations on the blade, when experiencing platform pitch motion. The results indicated that the unsteady aerodynamic loads are directly affected by the AOA between the local blade profile and the imposed apparent flow velocity.

Li et al. (2025) quantified the rotor's thrust and torque variations under three different states of operations as the FOWT operates under a prescribed surge motion – (1). the Normal Windmill State (NWS); (2). the Turbulent Wake State (TWS); and (3). the Propeller State (PS). The altering of operation states will occur continuously due to the periodic change of the platform motions, suggesting large oscillatory aerodynamic variations that a FOWT would experience.

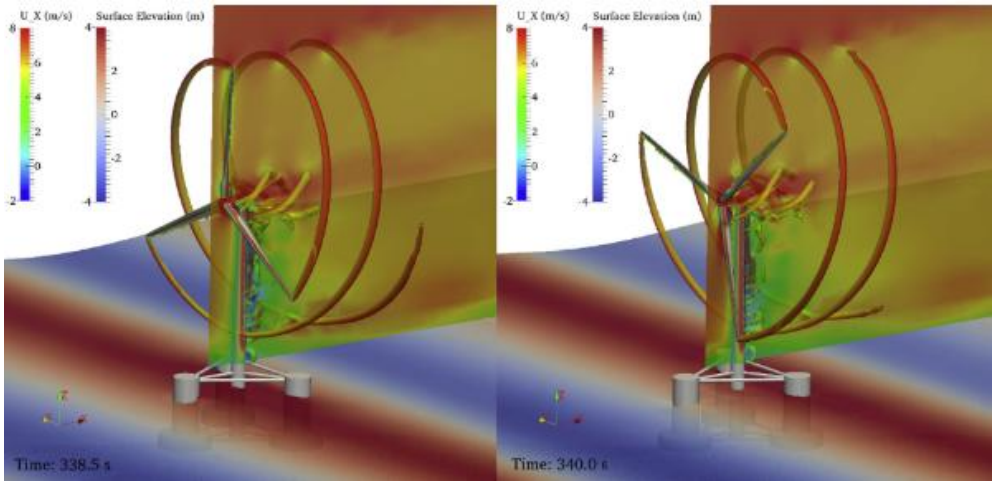

Figure 2-2. Flow field calculated by CFD with visualizations of flow interactions and wake structures (Liu et al., 2017).

Suggested by these previous studies, the aerodynamics on the FOWT blade may suffer from several sources of nonlinearities, such as flows interactions in three-dimensional space, the blade tip losses and the flow separations as the AOA adversely changes, etc.

Therefore, the CFD approach is a more general way for accurate predictions of aerodynamic loads due to its applicability in considering various boundary conditions and ability in capturing sophisticated flowing phenomenon.

2.2 Motions of FOWT Platform

The wave-induced platform motions can bring in additional momentum to the blade aeroelastic performance on an FOWT, significantly amplifying the load oscillations and causing unstable power performance (Li & Bachynski, 2021; Deng et al., 2025). A proper reflection of the FOWT platform motions in the numerical studies is vital for the reasonable predictions to the blade aeroelastic responses, so that making it sensible for the further improvements of blade structural designs.

The strategies of defining the platform motions can be roughly classified in two categories: 1). resolving the 6-DoF platform motions by coupling the platform hydrodynamics, and 2). prescribing the platform motion (specific DoFs of interests).

The first approach is possible to fully resolve for the actual wave-induced platform motions under given wind-wave conditions.

Liu et al. (2017) conducted an aerodynamic investigation for the NREL 5MW FOWT with a fully-coupled aero-hydrodynamic framework. A regular wave on the incoming flow direction is defined. The interactions between the aerodynamic (blades) and hydrodynamic (platform) loads were studied, illustrating that the rotor aerodynamic loads impose substantial pitching moments to the platform, where the quasi-static mean pitch motion shifts from its original state, then reversely affecting the aerodynamic loading characteristics on the blades.

Y. Zhou et al. (2022) further explained the wind shear can lead to unsteady aerodynamics loads, thus exert additional pitch moment to the floating platform. The resultant moment of the combined aerodynamic loads and platform hydrodynamic forces causes the rotor and blade inclination backward against the incoming flow, reducing the rotor effective swept area. This leads to a decrease in both the rotor thrust and power output. Additionally, it was found that the difference in incoming flow characteristics (e.g. turbulent or uniform flows) have limited influences on the

platform hydrodynamic response amplitude (RAOs), while it can be influential to the instantaneous blade aerodynamics with a more fluctuated loading performance being observed.

The second approach, which is more numerically feasible, is to prescribe the platform motion on the interested DoFs, which commonly can be achieved by a sinusoidal function, assuming a regular wave condition.

Wen et al. (2017) analysed the NREL 5MW rotor power and thrust performances at different tip-speed ratio (TSR) under prescribed surge motions. Three surge amplitudes of 0.5, 1.5 and 2.5 meters combining three surge frequencies of 0.03, 0.1, and 0.2 Hz were studied. A nondimensional parameter of reduced frequency, k, is used for considering the total influence of amplitude and frequency to the aerodynamic thrust and power. It was observed that the mean power and thrust at low and high TSRs are nonlinearly corelated with k. For instance, for the mean power at low TSRs, it decreases along with the reduced frequency k. While for high TSRs, such trend reverses. Then, for the mean thrust at all TSRs, it decreases as the reduced frequency k increases, except for one TSR = 12. All superimposed surge motion conditions have been witnessed adversely influencing the instantaneous power performance of the rotor.

Zhang et al. (2023) investigated the IEA 15MW FOWT aeroelastics by prescribing the surge and pitch motions to the platform. Quantifications to the rotor instantaneous power and thrust were finalised, illustrating severe loading amplifications can happen that severely impacting the safe operations of the FOWT.

The prescribed motion approach is a trade-off that only exploring the rotor aerodynamics under the interested DoFs of the FOWT platform motions, for example, the platform motions under the regular wave condition can be reasonably approximated by a sinusoidal function. Although it may impair the correctness and accuracy of the predicted aerodynamic performance to some extent, the prescribe function is an efficient way for preliminary studies and design validations at early-stages of design.

A brief summary of several existing parametrical studies for the prescribed platform surge motion load cases are given, as listed in Table 2-1. All of the listed studies were focusing on the aerodynamics of the rigid blade on the NREL 5MW reference wind turbine, where the blade flexibility was not considered.

Table 2-1. Selection of prescribed platform motions specifications conducted for the rigid full-scale NREL 5MW FOWT aerodynamics studies.

Studies	Numerical methods	Prescribed motions A_S (m), T_S (s)	Wind speed, U_0 (m/s)	Rotation speed, Ω_0 (rpm)
Sun et al. (2023)	CFD	A_S = 0.916, 1.348, 2.56 T_S = 12.67, 13.33, 15.38	11.4	12.1
Yang et al. (2023)	CFD	A_S = 2, 4, 6 T_S = 10.00, 15.00, 20.00	11.4; 18	12.1
Lienard et al. (2020)	CFD	A_S = 8, 16 T_S = 9.92	11.4	12.1
Wen et al. (2017)	CFD	A_S = 1.5 T_S = 5.00, 10.00, 33.33	11.4	13.8
Tran and Kim (2016a)	CFD	A_S = 8 T_S = 8.16, 12.56, 25.64, 50.00	11.2	12.1
Micallef and Sant (2015)	BEM	A_S = 2.125, 2.15, 2.2 T_S = 9.00	11.4	7.08; 12.39; 19.47
De Vaal et al. (2014)	BEM	A_S = 4, 8, 16 T_S = 8.16, 12.56, 25.51, 49.50	11.2	12.1

2.3 Structural Models in Fluid Structure Interaction

From structural point of view, wind-turbine blades can undergo large, unsteady deflections under time-varying aerodynamic loads. Therefore, structural solvers must be able to capture such behaviour. The blade structural behaviour has conventionally been modelled using equivalent beam models and their variants (Riziotis et al., 2008; Lago et al., 2013; Yu & Kwon, 2014), geometrically exact beam models (Wang et al.,

2014; Wu et al., 2022; L. Zhou et al., 2022; Wu et al., 2024), the multibody dynamics method (Riziotis et al., 2008; Liu et al., 2019), the isotropic structure with homogeneous assumption (Bazilevs et al., 2011) and the fully-resolved finite element analysis (FEA) approach (Wang, Quant, et al., 2016; Miao et al., 2019; Zhang et al., 2023).

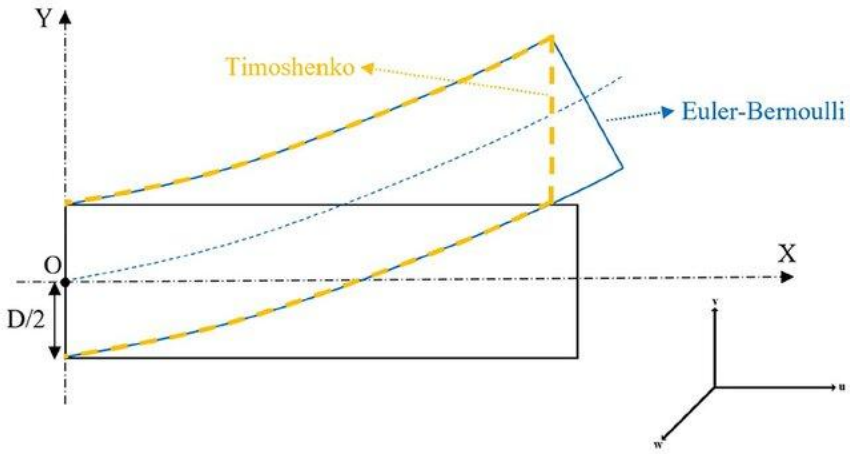

Figure 2-3. Example of classical equivalent beam models. Diagram shows the differences of deforming behaviour between the Euler-Bernoulli and Timoshenko beam models (Rostami et al., 2021).

The choice of structural modelling strategy within FSI strongly affects both the predicted aeroelastic responses and the computational cost. Most importantly, it also determines the analysis scale for structural behaviour, ranging from system-level response at macroscale to local/ply-level stress assessment, and whether the one-way or two-way FSI should be implemented.

Riziotis et al. (2008) presented that the second-order beam (Hodges & Dowell, 1974) and the multibody model based on Timoshenko beam performed similar in capturing the nonlinear structural behaviours, while the first-order beam suffers from a suppression issue that can fail in the highly nonlinear structural predictions. The importance of considering the blade bending-torsion moment coupling effects was emphasised, especially for large flexible blades.

Yu and Kwon (2014) considered the full representation of the NREL 5MW blade's with the Euler-Bernoulli model, where the flap-lag-torsion coupling dynamics were

accounted by the dimensional reduction theory developed by Hodges and Dowell (1974); (Yu, Hodges, et al., 2002). It was suggested that the flexibility of the blade must be considered to accurately resolve the blade structural responses under the unsteady aerodynamic loads.

Liu et al. (2019) used the viscoelastic beam model in multibody dynamics code, MBDyn, for the investigations of FOWT aeroelastics. A regular wave condition is analysed by prescribing a sinusoidal function to the platform. By conducting a two-way FSI analysis, it is observed that the blade deformations in bending and twisting directions dominate the change in instantaneous angle of attack (AoA). Additionally, the imposed platform motion intensifies the nonlinear fluid-structure coupling and magnifying the resulting unsteady pressure gradients and intermittent flow separation.

Tang et al. (2021) captured the blade's nonlinear geometrical foreshortening using the geometrically-exact beam model, observing a decreased projected effective area of the rotor normal to the incoming flow velocity. This is due to the structural stiffening due to the mutual effects of extensional and centrifugal forces, causing the inward blade deflection under the aerodynamic loads. The foreshortening of the blade can lead to reduction in aerodynamic loads and complicated structural behaviours, which requires more in-depth investigations to the structural performances.

Incorporating high-fidelity FEA into FSI further enriches the description of component interactions and resolution of local stress/strain fields (Wang, Quant, et al., 2016; Miao et al., 2019), while the adoptions of one-way or two-way FSI is case dependent.

The one-way FSI method only considers the aerodynamic loads transfer from the fluid to structural domain, while the displacement from the structure to fluid is omitted. This simplification reduces computational cost and facilitates the use of high-fidelity solvers. For instance, Wang, Quant, et al. (2016) adopted an one-way FSI by coupling CFD-FEA for the preliminary aeroelastic investigations of the full-scale WindPACT 1.5 MW wind turbine blade. The aerodynamic pressure and stress distributions on the composite blade were resolved, showed a safe stress and deflection level under various wind conditions. It was observed that the max. relative tip flapwise deflection is only 5.23% with-respect-to the rotor radius.

Zhang et al. (2023) proposed a one-way CFD–FEA model for the IEA 15 MW FOWT and reported more pronounced aerodynamic fluctuations in flexible blades. The platform-induced translational velocity amplified the peak thrust and power, producing substantial periodic load variations, large deflections, and local peak stresses in blade critical regions, such Spar caps and near-the-root locations. This emphasises the needs of detailed inspections in localized stress concentrations on critical blade regions.

Notably, the applicability of one-way coupling is conditional. This approach is only appropriate when the structural deformation is insignificant (Greco et al., 2023), or to be adopted for preliminary aeroelastic assessments.

By contrast, two-way FSI exchanges the force and displacement data streams by establishing the bidirectional communications between the fluid and structural fields. When the CFD is coupled with FEA in a two-way FSI scheme, the computational demand is usually massive, primarily due to the frequent data exchanges among a large number of nodes at the coupling interfaces between the solvers. Such expense would be higher when the fluid and structural meshes are refined for capturing higher resolution of the field quantities, where the second-order discretization the temporal and spatial terms are usually needed in CFD solvers, especially for high Reynolds number problems.

For ultra-long blades on the upscaled FOWT applications, larger structural deformations with strong interaction between the fluid and structure could be anticipated. The FSI has to consider the synchronizations across the coupling interfaces to properly reflect the physical reality, i.e. the two-way coupling. Another consideration is that the predicting accuracy and confidence of nonlinear unsteady flow using reduced-order aerodynamic codes, such as the severe tip losses and the flow separations on the blade. Thus, the CFD approach can serve as a more general solution for numerical predictions under arbitrary conditions, especially for FOWTs.

To summarise, the selection of FSI coupling strategy and participating solvers should be guided by the specific load case, expected aeroelastic behaviour, and the available computational resources. For non-severe load conditions or early-stage investigations, the one-way FSI is more applicable approach as it balances between accuracy and

computational efficiency, whereas the complete two-way FSI is typically required for critical load cases or final validations.

The observations of intensified interactions in unsteady blade aeroelastics underscore the necessity of resolving the nonlinearities, especially to consider the composite properties of the blade and to identify the critical stress regions under the platform-induced motions.

2.4 Composite Blade FEA Modelling

The selections of the modelling technique for the composite structure are oriented by the types of structural analysis, which can be roughly categorised as: (1). the overall structural behaviour under multiaxial load conditions (Tavares et al., 2022; Keprate et al., 2023); (2). the localised component structural interactions; and (3). the composite internal stress and strain conditions on ply-to-ply structures. The first and second are essentially macroscale structural analysis, while the third steps into a more detailed domain where mesoscale inspections can be carried out for more comprehensive investigations of composite behaviours.

A typical composite blade layout is depicted below in Figure 2-4, showing the localised material assignments and internal subcomponents deployments in different regions of the blade.

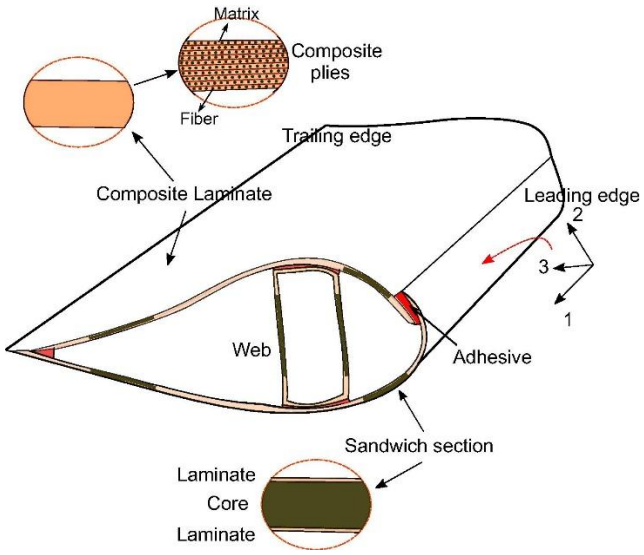

Figure 2-4. Typical composite blade layout (Verma et al., 2019).

To conduct structural analysis for each scale of composite blade behaviour, the FEA method is capable of handling accurate modelling at an arbitrary fidelity. This has been adopted in many studies (Yang et al., 2013; Kim et al., 2014; Muyan & Coker, 2020) and industrial design projects (Ashwill, 2010). An example of routine modelling procedure for the composite blade structure in FEA is depicted in Figure 2-5.

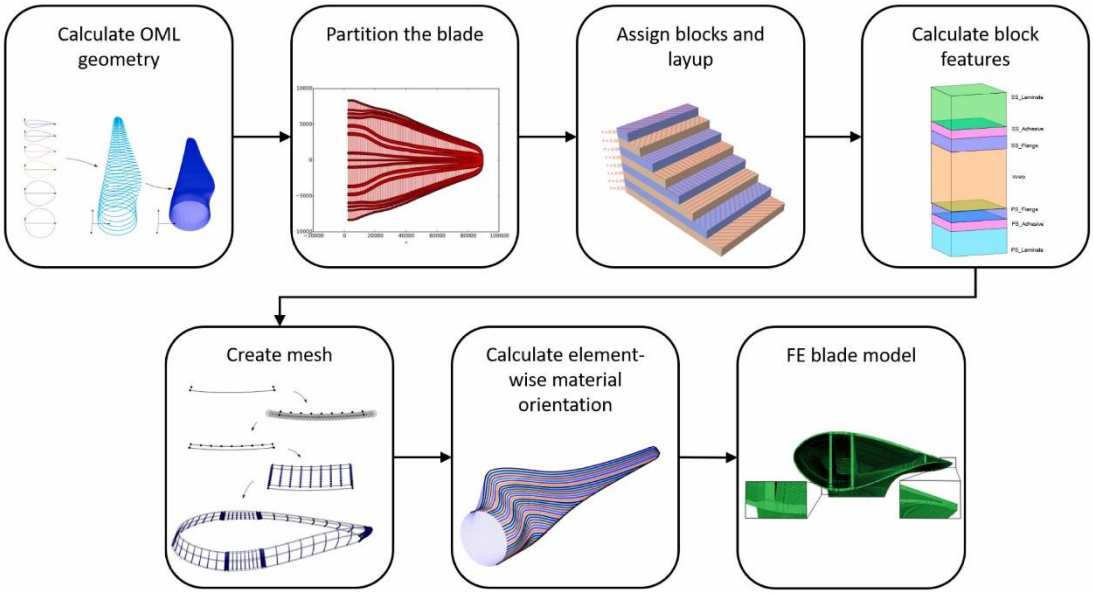

Figure 2-5. Examples of composite blade modelling procedure in FEA (Tavares et al., 2022).

To start with, the blade can usually be discretized using the shell element or solid element in a FEA code, some studies also demonstrated the possibility of adopting a hybrid solution such as the shell-solid modelling (Verma et al., 2019).

Numerous FEA studies for the composite wind turbine blade have adopted the shell elements, where in the context of Abaqus CAE (a commercial FEA code), the common shell element of S3 / S4R / S8R (Yang et al., 2013; Kim et al., 2014; Fagan et al., 2018; Navadeh et al., 2021; Luo et al., 2024; de Almeida et al., 2025), or in ANSYS Mechanical context, the SHELL181 / SHELL281 elements (Herrema et al., 2019; Camarena et al., 2021; Finnegan et al., 2021; Wiegard et al., 2021; Scott et al., 2022).

These studies have demonstrated good performance of the shell element models in capturing the structural mass, overall deflections, and in-plane longitudinal and

transverse strains, however, few studies discussed their discrepancies relative to three-dimensional (3D) solid element models, particularly for through-thickness stresses and torsion-dominated responses.

Reported by Ashwill (2010), the layered shell elements are usually more efficient and generally accurate for thin skin-type structures and global torsional/bending response, whereas the 3D solid elements are preferred when through-thickness stresses are of interested, so that the normal stress σ_3, and two shear stresses τ_{13}, τ_{23}, in the blade shell thickness direction can be resolved.

A numerical study conducted by Peeters et al. (2018a) compared the S8R shell element and C3D20R solid element for a 43-m long composite blade. Comparing with the experiments, both models can properly predict the in-plane longitudinal and transverse strains in the spar cap regions, also for the bending moments at the blade root. However, due to the Brazier effect, a non-negligible strain difference between the inner and outer surface was observed.

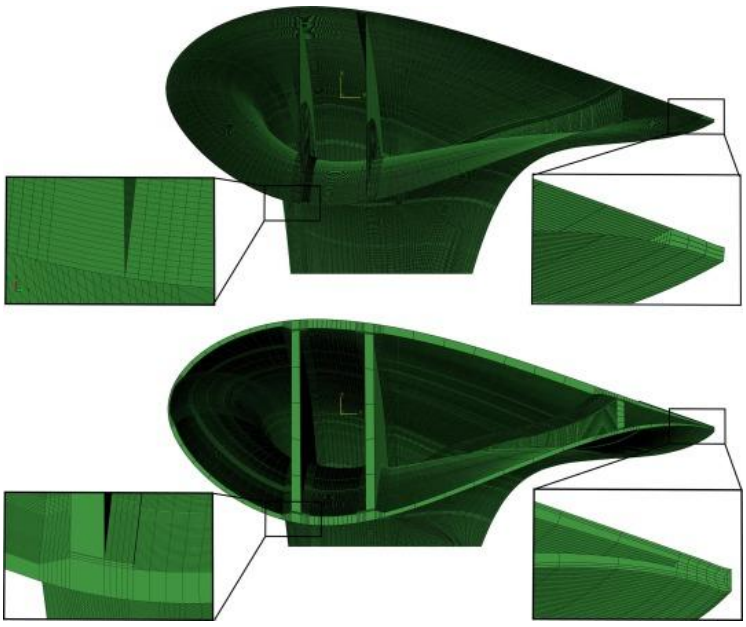

Figure 2-6. Example of FEA models using shell and solid elements (Peeters et al., 2018b).

Tavares et al. (2022) further assessed and explained the differences of FEA modelling using shell and solid elements via static structural studies. Observed that under the

torsion-dominated loadings, due to the interplay between the reference-surface offset, reduced integration of shell element formulation, and the rotation about the shell normal (named 'drilling DoF'), the shell element may underestimate the local stress/strain fields since the torsional stiffness is underpredicted. When the through-thickness normal stress σ_3 is of interest, the 3D solid element should be used, since the shell elements enforce a plane-stress assumption and cannot directly resolve σ_3 (Laird et al., 2005).

Another important aspect in composite modelling is to acquire material properties for defining the stiffnesses. The EU UPWIND program subtask – Rotor Structures and Materials (Mishnaevsky Jr et al., 2012) highlighted that material nonlinearity and multiaxial behaviour should not be neglected. It validated the impact of modelling fidelity on macroscopic prediction accuracy, demonstrating that the accurate predictions of structural responses at the macroscale strongly depends on the precision of the input material parameters.

For the composite modelling specifications, an example is the Sandia National Laboratory released the open-access reference model of the NREL 5MW baseline wind turbine (Resor, 2013), including detailed geometrical specifications, material definitions, composite configurations. The results for validations such as the mass distributions and modal frequencies are provided. It has been widely utilised as a guidance for modelling the composite blade structures in many existing research (Miao et al., 2019; Meng et al., 2022).

If the material properties are not accessible, it is still possible to estimate the properties analytically or numerically. For instance, in the case of a composite laminate composed by multiple isotropic constituents, the effective stiffness of a laminate composite can be calculated using analytical method (Zuo & Xie, 2014). Additionally, a study conducted by Camarena et al. (2021) demonstrated a way to fully characterise the fibre-reinforce laminate mechanical properties by using the Representative Volume Element (RVE) model, as depicted in Figure 2-7, in a homogenization analysis.

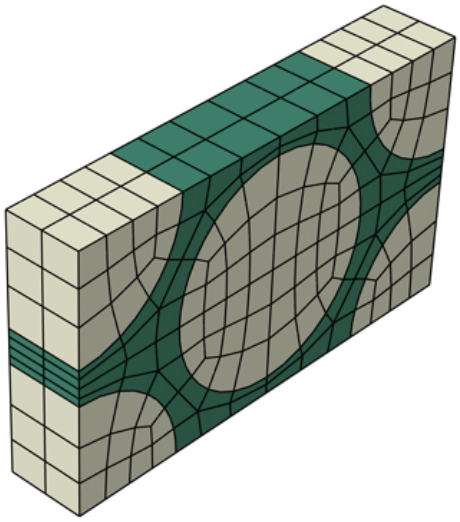

Figure 2-7. RVE model for numerically estimating the effective stiffnesses of the fibre-reinforced composites (Camarena et al., 2022).

The macroscale structural analysis is essential for understanding the global deformation behaviour, load distribution mechanisms, and stress distribution patterns across the composite structures. It serves as a basis for further detailed meso- or microscale analyses, assisting the localized stress inspections, fatigue evaluations, and material optimizations in critical regions.

In the context of a two-way FSI, a limited number of studies were found adopting the fully-resolved FEA for the composite blade modelling due to the high computational costs. For instance, Miao et al. (2019) established a fully-resolved FEA model for 61.5m long composite blade of the NREL 5MW baseline wind turbine. The blade maximum tip deflections and the stress distributions under the IEC DLC 6.1 extreme load condition is investigated, observed that the local stress concentration occurred in the Spar cap region which is close to the blade transitional and blade root regions.

To mitigate the cost of computations of a two-way FSI, in modelling practice, proper simplifications to the blade structure need to be made (Peeters et al., 2018a). Some prior principles for simplifications are suggested in several studies.

For instance, the accurate composite blade modelling firstly relies on proper geometrical representations of the Outer Mold Layer (OML) (Tavares et al., 2022). The OML is the aerodynamic surface that reflects the transitions of the cross-section

shape and the localised twist of the blade. In FEA modelling, the OML severs as the base surfaces for the normal offsets of the material, thus determines the accuracy of the composite stackings.

2.5 Multi-objective Optimization of Composite Structures

Fundamentally, numerous studies have conducted optimizations for improving the composite laminate stiffnesses, strengths and weight performances (Zuo & Xie, 2014; Allaire & Delgado, 2016; Serhat & Basdogan, 2019; Serhat, 2021) by optimizing the fibre orientations, stacking sequence and material selections. It has noticed the optimizations for such localised, sub-system level structure performed a well computational efficiency due to simplicity of design variables and geometrical specifications in their optimization problems.

However, for high-dimensional composite blade structure optimization problems, the nonlinear objective performances are usually interested, such as stress and stiffness, on the blade nonuniform, nonlinear configured composite structures. The term "high-dimensional problem" refers to an optimization considering a large number of design variables as inputs, whereas it seems no mutual understanding of the exact threshold for distinguishing a high- to a low-dimensional optimization problem. Yet, suggested by Lee et al. (2022), a high-dimensional problem can have up to 20 design variables as inputs.

To effectively handle the high-dimensional blade structural optimization problems, there are generally three precautions: (1). The effective Metaheuristic algorithms should be used to accelerate the searching process for the groups of 'good' solutions near the optimum point. (2). Instead of directly couple FEA codes in the optimization, a surrogate model that can properly fit the input-output relationship shall be used to massively accelerate the optimization process. (3). The load condition must be a well representative that realistically reflects the blade's unsteady loading characteristics under the interactions of fluid and structure.

Many studies have demonstrated the effectiveness of Metaheuristic algorithms in their studies. Chen et al. (2013) conducted a single objective optimization for the weight

reduction of a 2MW, 31 meter long blade using particle swarm optimization (PSO). The continuous thickness variations of 7 laminates and different location of 1 shear web deployment were defined as design variables, while the other shear web is fixed. The blade tip clearance and Tasi–Wu failure criterion were applied as the constraint for the termination of the optimization process. Wang, Kolios, et al. (2016) optimised the ELECTRA 30 kW vertical-axis wind turbine by considering the number of laminates deployments on a partitioned wind turbine blade, as shown in Figure 2-8. Multiple constrains including allowable stresses, buckling, blade tip clearance, natural frequencies, manufacturing manoeuvrability and the laminate layup continuity are applied for the feasibility and practicality of the optimised designs.

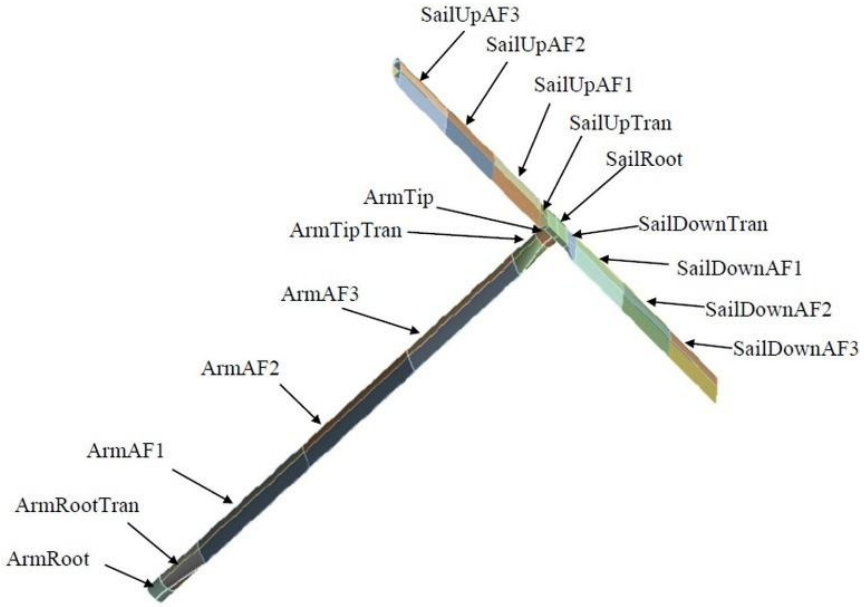

Figure 2-8. Deployment of laminates with different number of layers from Wang, Kolios, et al. (2016).

Fagan et al. (2018) employed the Non-dominated Sorting Genetic Algorithm II (NSGA-II) to optimize a 15 kW blade by minimizing both total mass and tip deflection as the objective functions. The study also revealed the significant impact of shear web configurations on blade stiffness as it is relatively thicker compared to the aerodynamic shells of the blade surfaces.

Albanesi et al. (2020) combined the genetic algorithms (GA) with continuous Topology Optimization (TO) methods to achieve notable reductions in blade mass and improvements in tower clearance for a 1.5 MW turbine.

In recent years of studies, it has witnessed that many successful attempts of implementing the surrogated models, especially those based on Machine Learning techniques, in multi-objective optimizations using the Metaheuristic algorithm approaches for small-scale low-dimension problems.

Liu et al. (2023) proposed a minimum weight designing approach by incorporating the Artificial Neural Network (ANN) and Genetic Algorithm (GA) for optimizing the localised laminate structure configurations. The inputs in their problem are limited to the laminate thicknesses, stiffener dimensions and lamination parameters (defining bending stiffnesses, $\boldsymbol{D}$).

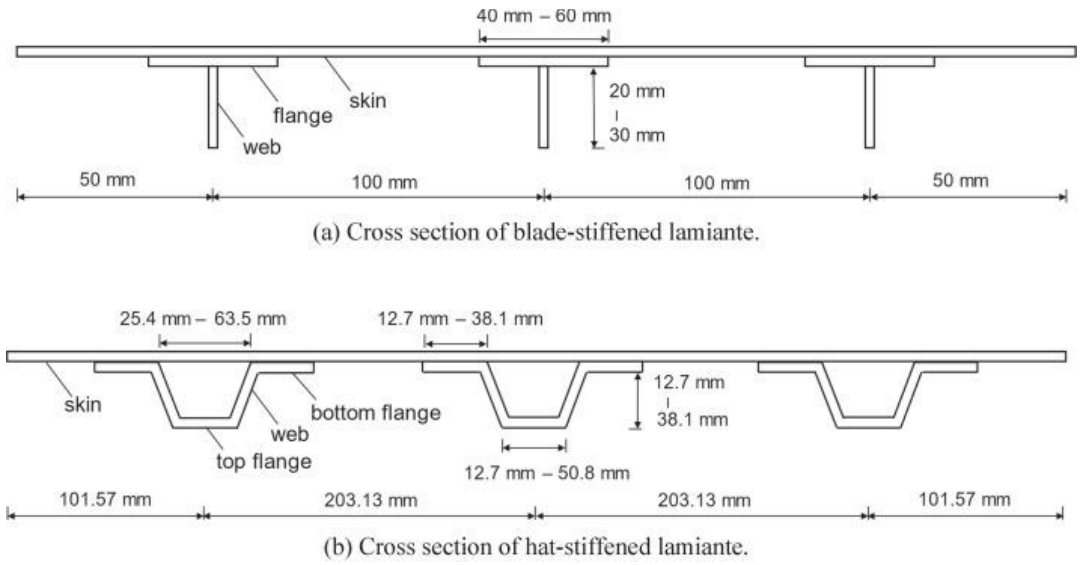

Figure 2-9. Laminate configuration optimizations by Liu et al. (2023).

Cao et al. (2025) enhanced the stiffness and resonance margin of a composite fan blade by coupling the Generalised Regression Neural Network (GRNN) in the NSGA-II optimization process. Two input variables of fibre angles were considered with four fixed lamination combinations, thus the order of dimension was significantly reduced.

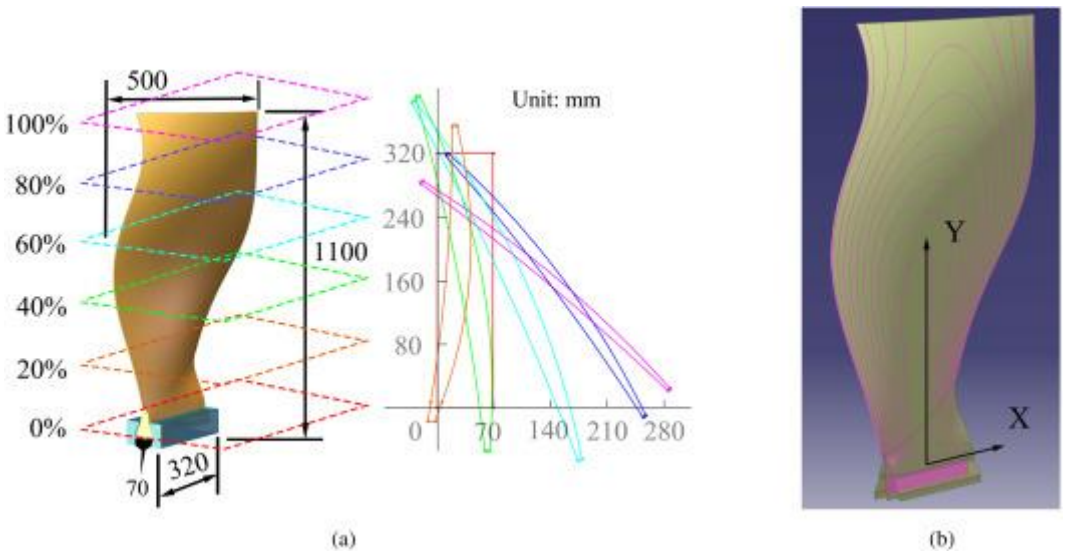

Figure 2-10. Composite fan blade structural layout Cao et al. (2025).

From above studies, we further noticed some potential issues that need to be properly handled. Normally, these studies used up to dozens of design variables (less than 20) for their works, which makes the optimizations can be effectively conducted with a well performance being demonstrated in terms of prediction accuracy.

However, in the scope of large composite blade structural optimizations, the low-dimensional assumption may fail as it neglects the nonlinear input-output response and the synergistic interactions among distributed variables, especially when the blade is exposed under the severe nonlinear load conditions. There are limited numbers of research discussed how a low-dimensional optimization would affect the accuracy of the predicted optimal composite blade designs.

This actually opens another page of the story to discuss on the nonlinear approximation performance of the surrogate model and the intrinsic challenges when using surrogate models in a high-dimensional optimization problem.

2.6 Surrogate Models in Optimization Process

In the scope of this work, the surrogate models are used for replacing high-fidelity codes in predicting the outputs of the nonlinear objectives, which can massively accelerate the navigations of solutions during the optimization process (Thapa & Missoum, 2022; Haddad et al., 2023). To train a surrogate model that can accurately

predict the system input-output responses, especially for the nonlinear objectives (e.g. peak stress on composite blade), requires a sufficiently large number of training sample points, on which the surrogate model can learn the input-output relationship (mapping pattern) for objective predictions.

Previous studies have demonstrated the advantages of surrogate models. For instance, Albanesi et al. (2018) incorporated the ANN surrogate model with genetic algorithm (GA) for single objective (mass) optimization of a 40 kW wind turbine blade. The blade is simplified with 10 partitions along the spanwise direction. The design variables are the number of laminate and the ply-drops in 10 regions of E-glass fibre laminates. The total number of design variables is 22. Same as the previous study, the ANN is also trained one-time-off on a static set of 2500 sampling points (static surrogate). The result of blade mass prediction is regulated by the constraints of, i.e. the max. tip deflection, max. stress and natural frequencies. Under such simplifying treatment, it was presented that the Maximum Average Error (MAE) and Root Mean Square Error (RMSE) for constraining functions were very low.

Luo et al. (2021) adopted an Artificial Neural Network (ANN) for approximating the FEA responses for an asymmetrical composite laminate structure. The ANN is trained on 3400 training samples calculated by FEA. It was used for predicting the process-induced distortions objective considering 6 design variables, where the ANN predictions and the FEA validated objectives shown a small difference of 3.84% based on the averaged RMSE criteria. It was noticed that the optimization was not included in his study, where the ANN is trained one-time-off on a static training sample set.

This actually triggers two questions that is the static training dataset a problem that may affect the approximation accuracy of surrogate model in an optimization process? Would such static surrogate model still perform accurate if the system (e.g. a composite blade) was not simplified but kept as realistic as possible?

Golzari et al. have expressed their concerns early in (2015), pointed out that in a multiple iterations optimization process, such static surrogate model will suffer from accuracy issues. To explain, due to the fact that the optimization process tends to push the objectives to a sparse space when minimising the objectives, the surrogate model

may not ‘recognise’ the data in these regions as they are trained based on a static set of training datasets.

This is essentially an extrapolation problem due to the out-of-distribution issue during the surrogate training process, which can cause unacceptable deviations between the optimization predictions and the actual objective results. Unfortunately, it has not seen relevant studies of composite blade optimization talking on this potential issue.

2.7 Concluding Remarks

In this chapter, a comprehensive review of the existing literatures on the aeroelastic behaviours and composite structural modelling of FOWT blades is given. Advancements and challenges in structural optimizations were discussed, especially on the aspect of high-dimensional optimization that featuring the composite blade problems. Several challenges and research gaps from the previous literatures have been extracted and will be resolved in this work, detailed as follows:

1. Although the reduced-order methods are commonly used for aerodynamic predictions due to their efficiency, as pointed in many studies, these methods have shown limitations in handling severe, complicated load cases, and may oversimplify the actual aerodynamic responses on the blade.

2. Existing FSI studies tend to pay insufficient attention to the complexities of composite material behaviour, while structural analysts often overlook the nuances of real-world aerodynamic loading. As a result, the system’s overall responses are not fully captured, and predictions of the actual loads experienced by the blades can deviate significantly from reality.

3. For ultra-long blades, the optimization should consider the interactive nature of the blade aeroelastics. Therefore, the two-way FSI coupling scheme should be implemented to properly track the moving interface. While the one-way coupling scheme may lead to inaccuracy of load predictions.

4. Many existing optimization studies focused on simplified problems with limited number of design variables, while the high-dimensional

characteristics of the large-scale composite blade optimization have not been extensively discussed.

5. To purely rely on the data-driven surrogate model for approximating a nonlinear physical system can cause few issues, including poor extrapolation and limited generalizability. The quality of the sampling points and so as the approximating performance of the surrogate model needs to be evaluated and improved during the iterative optimization process.

To fill the gap and overcome the difficulties as mentioned above, a three-steps task need to be completed to ultimately develop a general-purpose FSI analysis and optimization framework for the composite wind turbine blade.

1. Rather than sacrificing the fidelity in aerodynamic analysis, the reduced-order structural code MBD model is employed to compensate for the high computational costs in a two-way FSI. With the structural response being solved via the two-way FSI, comprehensive FEA analyses can be conducted using the accurately predicted kinematics as boundary conditions, so that the detailed stress, strain conditions under arbitrary state can be restored, which is much more efficient comparing to the direct coupling of CFD and FEA.

2. To fully consider the composite structures of the blade, the laminate anisotropic behaviours and geometric nonlinearities are resolved in FEA. This part of work is essential for accurately predicting the quasi-static or dynamic responses and stress conditions and providing reliable training sampling points for the subsequent optimizations.

3. Different from prescribing the periodic or static ultimate loads, the actual loading characteristics on the composite blade can be considered during the structural optimizations. Also, an improved surrogate-assist optimization workflow is proposed as we noticed a distribution drifting issue during the optimization process, which can typically occur in the surrogate-assist optimizations for high-dimensional systems. Detailed introduction of this

workflow in given in the Methodology. Briefly, we leverage the rapid predicting capability of the surrogate model to find the design candidates that exhibit with the highest uncertainties when they are predicted by the surrogate model. These candidates will be progressively corrected using FEA to acquire the accurate objective responses, then, the dataset for training the surrogate model can be updated with corrected data of objective responses. By doing so, a significant improvement in surrogate approximation accuracy is achieved via a limited number of FEA corrections. This avoids frequent pulls of expensive finite-element analyses throughout the whole optimization process and ensures the robust convergence of optimization when handling a high-dimensional system.

Chapter 3 Methodology

3.1 Computational Fluid Dynamics Method

3.1.1 Overview

In this work, the aerodynamics predictions for the FOWT blades are conducted using the open-source C++ code OpenFOAM (Jasak et al., 2007) using the pimpleDyMFoam solver. This code is based on the finite volume method, where many well-verified turbulence models and discretization methods are implemented that allows the user to freely configure for their simulations.

3.1.2 Governing equations

The incompressible, viscous unsteady flow is governed by the Unsteady Reynolds-Averaged Navier-Stokes equations (URANS). The governing equations for the incompressible flow are expressed using the Einstein summation convention as follows:

$$\frac{\partial U_i}{\partial x_i} = 0 \tag{3.1}$$

$$\frac{\partial U_i}{\partial t} + \frac{\partial \left[\left(U_j - U_{g,j} \right) U_i \right]}{\partial x_j} = -\frac{1}{\rho}\frac{\partial p}{\partial x_i} + \frac{\partial}{\partial x_j}\left[\nu_{eff} \left(\frac{\partial U_i}{\partial x_j} + \frac{\partial U_j}{\partial x_i} \right) \right] \tag{3.2}$$

where U_i is the flow velocity components in controlled volume, $U_{g,j}$ is the velocity components of moving grid nodes. p is the pressure of the fluid, ρ and stands for the fluid density. Due to the mesh dynamic motions, in the diffusion term, a treatment to account for the viscous stress tensor is made, using effective kinematic viscosity ν_{eff} which is the sum of kinematic (ν) and eddy viscosity (ν_t), respectively.

3.1.3 Turbulence modelling

Typically, the Reynolds number of FOWT aerodynamic problems can reach up to 10^6 – 10^7. To effectively estimate the eddy viscosity of the turbulent flow, in this work, the

k-ω Shear Stress Transport (SST) turbulence model (Menter et al., 2003; Menter, 2009) is used, thus the Reynold stress term in the equation is enclosed.

This is a well-known turbulence model in capturing complex flow behaviours during the transitioning of the flow shedding from the blade surface to the wake region. Due to its flexibility in switching between the $k-\omega$ and $k-\epsilon$ formulations for capturing the flowing in the near-wall viscous sub-layer, and far field regions, the $k-\omega\ SST$ model has been extensively used and well justified as a reliable model for capturing the flow separation properly and predicting aerodynamic performance accurately in a various of applications that cope with high Renolds Number problems.

For incompressible viscous fluid, two additional scalar transport equations accounting for the turbulent kinetic energy k and the specific dissipation rate ω are formulated as follows, using the Einstein notation:

$$\frac{\partial \rho k}{\partial t} + U_i \frac{\partial \rho k}{\partial x_i} = \frac{\partial}{\partial x_i}\left[(\mu + \sigma_k \mu_t)\frac{\partial k}{\partial x_i}\right] + \tilde{P}_k - \beta^* \rho k \omega \tag{3.3}$$

$$\frac{\partial \rho \omega}{\partial t} + U_i \frac{\partial \rho \omega}{\partial x_i} = \frac{\partial}{\partial x_i}\left[(\mu + \sigma_\omega \mu_t)\frac{\partial \omega}{\partial x_i}\right] + P_\omega - \beta \rho \omega^2 + 2(1 - F_1)\frac{\rho \sigma_{\omega 2}}{\omega}\frac{\partial k}{\partial x_i}\frac{\partial \omega}{\partial x_i} \tag{3.4}$$

On the left side of the first transport equation are the convective terms describing the rate of transportation due to the temporal and advection. The first term on the right-hand side of the equation is the diffusion term that controlling the 'mixing' of the viscous fluid, where the term $\mu + \sigma_k \mu_t$ is the effective viscosity accounting for the molecular (dynamic) viscosity and turbulence eddy viscosity. The dissipation terms for both scalars are denoted as $-\beta^* \rho k \omega$ and $-\beta \rho \omega^2$.

$\tilde{P}_k$ and P_ω quantifies the rates of production of turbulent kinetic energy and dissipation rate, respectively, due to the average flow shear stress in turbulent flows:

$$\tilde{P}_k = min(P_k, c_1 \beta^* \rho k \omega) \tag{3.5}$$

$$P_k = \mu_t \frac{\partial U_i}{\partial x_j}\left(\frac{\partial U_i}{\partial x_j} + \frac{\partial U_j}{\partial x_i}\right) \tag{3.6}$$

$$P_\omega = \alpha \frac{\tilde{P}_k}{\nu_t} \tag{3.7}$$

To numerically avoid the singularity of the ν_t, where ω could be excessively over-predicted at the wall boundaries, a bounded ν_t is used here given as follows. The term S is the strain-rate (scaler) invariant measuring the shear/extension rate of the mean flow:

$$\nu_t = \frac{a_1 k}{\max(a_1\omega, b_1 S F_2)} \tag{3.8}$$

$$S = \sqrt{2S_{ij}S_{ij}} \tag{3.9}$$

Till this point, two blending functions (F_1 and F_2) in SST model show up. F_1 is introduced in the last cross-diffusion term in the second transport equation for smoothly switching between the $k-\omega$ model when $F_1 = 1$ (near the wall), and $k-\epsilon$ model when $F_1 = 0$ (away from the wall), based on the nearest distance of the local cells to the wall y. F_2 operates in same way while it governs the turbulent viscosity in near-wall flows and free flows in far-field regions. The formulations for both blending functions are given below.

For F_1:

$$F_1 = tanh(arg_1^4) \tag{3.10}$$

$$arg_1 = min\left[max\left(\frac{\sqrt{k}}{\beta^*\omega y}, \frac{500\nu}{y^2\omega}\right), \frac{4\rho\sigma_{\omega 2}k}{CD_{k\omega}y^2}\right] \tag{3.11}$$

$$CD_{k\omega} = max\left(2\rho\sigma_{\omega 2}\frac{1}{\omega}\frac{\partial k}{\partial x_i}\frac{\partial \omega}{\partial x_i}, 10^{-10}\right) \tag{3.12}$$

For F_2:

$$F_2 = tanh(arg_2^2) \tag{3.13}$$

$$arg_2 = max\left(\frac{2\sqrt{k}}{\beta^*\omega y}, \frac{500\nu}{y^2\omega}\right) \tag{3.14}$$

In addition, the F_1 also blends four constants (ϕ) in the SST model for adapting the flows in different regions, i.e. the turbulent Prandtl numbers in two transport equations σ_k and σ_ω, production coefficient α and dissipation coefficient β. Described as:

$$\phi = F_1\phi_1 + (1 - F_1)\phi_2 \tag{3.15}$$

The constants in the equations are empirically determined, as listed in Table 3-1:

Table 3-1. k- ω SST model coefficient constants.

σ_{k1}	σ_{k2}	$\sigma_{\omega1}$	$\sigma_{\omega2}$	α_1	α_2	β_1	β_2	β^*	a_1	b_1	c_1
0.85	1.0	0.5	0.856	0.556	0.44	0.075	0.0828	0.09	0.31	1.0	10.0

The implementation of the isotropic k- ω SST model has been justified in both academic and industrial wind turbine CFD analyses as an optimal practice due to its numerical accuracy and computational efficiency (Guo et al., 2020; Chemengich et al., 2022; Dewan et al., 2023). For more sophisticated anisotropic models such as the Reynolds Stress Models (RSM), it is expected that they would perform more computationally expensive and numerically unstable in highly three-dimensional transient FSI simulations, which often requires additional stricter numerical configurations.

3.1.4 Dynamic mesh

The Arbitrary Mesh Interface (AMI) technique (Chandar & Gopalan, 2016) is implemented to enable the relative sliding motions (rotations) of the wind turbine blades. The wind turbine rotor is included in a partitioned slave cell zone, where the designated angular speed of the wind turbine rotor can be assigned. The field quantities are transferred via a patch face-weighted interpolation between the master and slave interfaces on the AMI patches. To maintain the robust field quantity interpolations across the AMI patches throughout the simulation, the in-house code library (Liu et al., 2019) is developed that prevents the deterioration of the mesh quality due to any undesired mesh penetration across the sliding interfaces.

During the FSI process, the flexible blade structure experiences the transient aerodynamic loads, resulting dynamic response usually with nonlinear displacement distributions on the structure. To capture the deformations of the blade, the mesh nodes on the blade surfaces need to be updated via a diffusive model by solving the inverse distance Laplace equation in each coupling iteration (Jasak & Tukovic, 2006):

$$\nabla \cdot (\gamma \nabla \boldsymbol{u}) = 0 \, , \gamma = \frac{1}{r^2} \tag{3.16}$$

where $\boldsymbol{u}$ denotes the displacement vector of the mesh node on target wall surface, γ stands for the diffusivity coefficient which is calculated as the quadratic inverse of the node offset distance r from its original cell centroid to the deformed location. The mesh topology remains unchanged throughout the FSI process, which ensures the consistency of the mesh sequencing and avoid extensive data interpolations in mesh.

Worth noting that although techniques such as re-meshing and over-set meshing are more flexible for large-deformation problems, they typically require excessive interpolations among the mesh nodes, thus introduce additional computational overheads and iterative numerical errors.

3.2 Multibody Dynamics Method

The beam-element multibody dynamics (MBD) method has been extensively adopted in many studies with proven capability in predicting the structural dynamics accurately (Simeon, 2006; Bauchau & Nemani, 2021). In FSI process of this work, the MBDyn code is coupled with the CFD solver for calculating the dynamic responses of the structure composed by the three-node beam element model (Ghiringhelli et al., 2000). A linear viscoelasticity constitutional law is applied, where the 6×6 symmetrical stiffness matrices with proportional damping, accounting for the equivalent stiffness properties of a 3D composite blade structure, are assigned to the beam cross-section. To estimate such stiffness matrix, a more detailed introduction is given in the Section 3.4. The resultant internal stress $\boldsymbol{\sigma}(t)$ with given strains $\boldsymbol{\varepsilon}(t)$ is formulated in a simplified variant of Rayleigh damping form:

$$\boldsymbol{\sigma}(t) = \boldsymbol{D}\boldsymbol{\varepsilon}(t) + \boldsymbol{\eta}\dot{\boldsymbol{\varepsilon}}(t) \tag{3.17}$$

$$\boldsymbol{\eta} = k\boldsymbol{D} \tag{3.18}$$

$\boldsymbol{D}$ is the generic form of cross-sectional stiffness matrix and $\boldsymbol{\eta}$ is the viscosity matrix. k is the proportional factor of 0.01 which is applied to all beam elements for preventing numerical instability, as suggested by Resor (2013). An example $\boldsymbol{D}$ in diagonal form is written as follows:

$$\boldsymbol{D}_{ii} = \{GA_y, GA_z, EA, EJ_y, EJ_z, GJ\} \tag{3.19}$$

From left to right the diagonal elements are the shear stiffnesses on the local in and out-of-plane directions GA_y and GA_z; axial extensional stiffness, EA; edgewise and flapwise bending stiffnesses, EJ_y and EJ_z; and torsional stiffness, GJ.

Under the holonomic kinematic constrains, a Newton-Euler motion equation in an implicit differential-algebraic equation (DAE) form is used to provide a generically expression as (Masarati et al., 2014):

$$\boldsymbol{M}(\boldsymbol{x})\dot{\boldsymbol{x}} = \boldsymbol{p} \tag{3.20}$$

$$\dot{\boldsymbol{p}} + \phi_x^T \boldsymbol{\lambda} = \boldsymbol{f}(\boldsymbol{x}, \dot{\boldsymbol{x}}, t) \tag{3.21}$$

$$\phi(\boldsymbol{x}, t) = 0 \tag{3.22}$$

where $\boldsymbol{M}$ is the mass matrix dependant on the nodal system $\boldsymbol{x}$ in 3D Cartesian coordinates; $\boldsymbol{p}$ is the nodal momentum; $\boldsymbol{f}$ accounts for the force and moment vectors; the term ϕ_x^T denotes the Jacobian transpose of the constraint equations with respect to the corresponding nodes in $\boldsymbol{x}$**,** solving for the forces and moments; $\boldsymbol{\lambda}$ is the Lagrange multiplier indicating the determinations of the nodal kinematics under given constraints. The boundary conditions are formulated in Eq. 3.22, defining the regulated nodal kinematics by the holonomic constraints.

3.3 Finite Element Method

In Abaqus CAE, the fully resolved finite element model of the composite blade is established. To resolve the plane normal and curvature variations along the blade geometry surface, a linear-interpolated four-node shell element with reduced-integration S4R element is used for structure discretization in the FEA code. The S4R

element is suitable for modelling composite structures for wind turbine blades and effectively avoiding transverse shear locking, and no need to concern about the potential hour-glassing phenomenon (SIMULIA, 2014). The shape function in the S4R shell element extrapolates of nodal displacements, and subsequently obtains the strain tensor fields of the discretized model.

Given that the composite laminate exhibits orthotropic macroscopic mechanical properties, there is no coupling between the components of stresses and strains on the principal axial and transverse shear directions, besides, the in-plane shear stresses have no effects to the strains in other orthogonal planes. The linear elastic constitutive of the materials defined in Abaqus CAE is formulated as the following assembled compliance matrix with 6 independent variables:

$$\begin{Bmatrix} \varepsilon_1 \\ \varepsilon_2 \\ \gamma_{12} \end{Bmatrix} = \begin{bmatrix} \frac{1}{E_1} & \frac{-\nu_{12}}{E_1} & 0 \\ -\frac{\nu_{12}}{E_1} & \frac{1}{E_2} & 0 \\ 0 & 0 & \frac{1}{G_{12}} \end{bmatrix} \begin{Bmatrix} \sigma_{11} \\ \sigma_{22} \\ \tau_{12} \end{Bmatrix} \tag{3.23}$$

Or, in a simple form to describe the strain – stress relation:

$$\varepsilon_i = C_{ij}\sigma_j \tag{3.24}$$

where the matrix includes two in-plane Young's modulus in 2 orthogonal directions E_1, E_2; Poisson's ratio ν_{12} (ν_{21} is implicitly defined as $\nu_{21} = (E_2/E_1)\nu_{12}$); and Shear modulus G_{12}, in addition, two other shear modulus G_{13}, G_{23} are required when the transverse shear needs to be calculated in shell models.

The preparation of the blade FEA model mainly consists of 4 stages:

Stage 1. Partitioning the blade. The blade three-dimensional shell geometry is divided into multiple sections based on the composite material configurations and the smoothness control of the thickness transitions on blade shells.

Stage 2. Defining coupling constraints. In Abaqus FEA model, the coupling constraint is used to assign the motions to the structures by a series of reference points, enabling

the definition of distributed motions to the structures as boundary conditions. Specifically, before applying loads to the composite structure in FEA, the coordinate conversion for the loads need to be done, ensuring the correct load mapping from the global to local coordinate systems.

Stage 3. Configure for the static analysis step with stress and strain field outputs defined explicitly for the composite blade at multi-hierarchy levels. The term "multi-hierarchy" refers to the multiple structural levels that exist in the composite structure, ranging from the microscale fibre–matrix constituents to the mesoscale lamina and the macroscale laminate or blade assembly.

Stage 4. Conduct mesh convergence analysis. An absolute element size of 0.1 m is used in space discretization to accurately predict the asymmetrical in-plane, out-of-plane deflections and the non-uniform stress distributions on the composite blade.

3.4 Effective Stiffness Matrix for Beam Element Structural Analysis

The effective stiffness matrices (ESMs) specifically refer to a type of matrix that enabling the 1D beam-element model to equivalently reflect the actual composite structural behaviour in 3D space. With this tool, the macroscale structural behaviours can be properly predicted in the FSI process with reduced-order beam-element structure models, thus saves significant amount of computational resources.

Historically, the ESMs can be processed with the Variational Asymptotic Beam Sectional Analysis code (VABS) developed by the Purdue University (Cesnik & Hodges, 1997; Yu, Volovoi, et al., 2002; Chen et al., 2010), BECAS developed by the DTU (Blasques, 2011), and PreComp code developed by the NREL (Bir, 2001; Bir & Migliore, 2004).

The accuracy of the equivalized ESMs is essential for MBDyn to predict structure response of the blade under the same load, which simplifies the 3D stiffness properties into 1D form, allowing a much more efficient numerical structural predictions by only considering a 6×6 diagonal stiffness matrix $\boldsymbol{D}$ on each cross-section between every adjacent partitioned blade sections, where the definition of $\boldsymbol{D}$ has been previously given in Eq. 3.19.

The ESMs distribution calculated in the present work are compared against the results from Resor et al. (2014) and Jonkman et al. (2009), as shown in Figure 3-1. The blade EJ_z, EJ_y and GJ of the present study agreed well with the corresponding counterpart results. The EA in the present study well approximates the Resor et al. (2014) results, as indicated by red curve.

Observed a significant variation in EA between the Resor et al. (2014) and present results against Jonkman et al. (2009). The reason of such variance is not clear, however, it is considered that the EA is a relatively insignificant parameter influencing the blade aeroelastic performances due to the relatively low rotation speed of the blade, as commented in (Jonkman et al., 2009). Thus, the influence of EA will not be discussed in the aeroelastic analysis while focusing the influences of prominent factors of EJ_z, EJ_y and GJ with quantitative evidence.

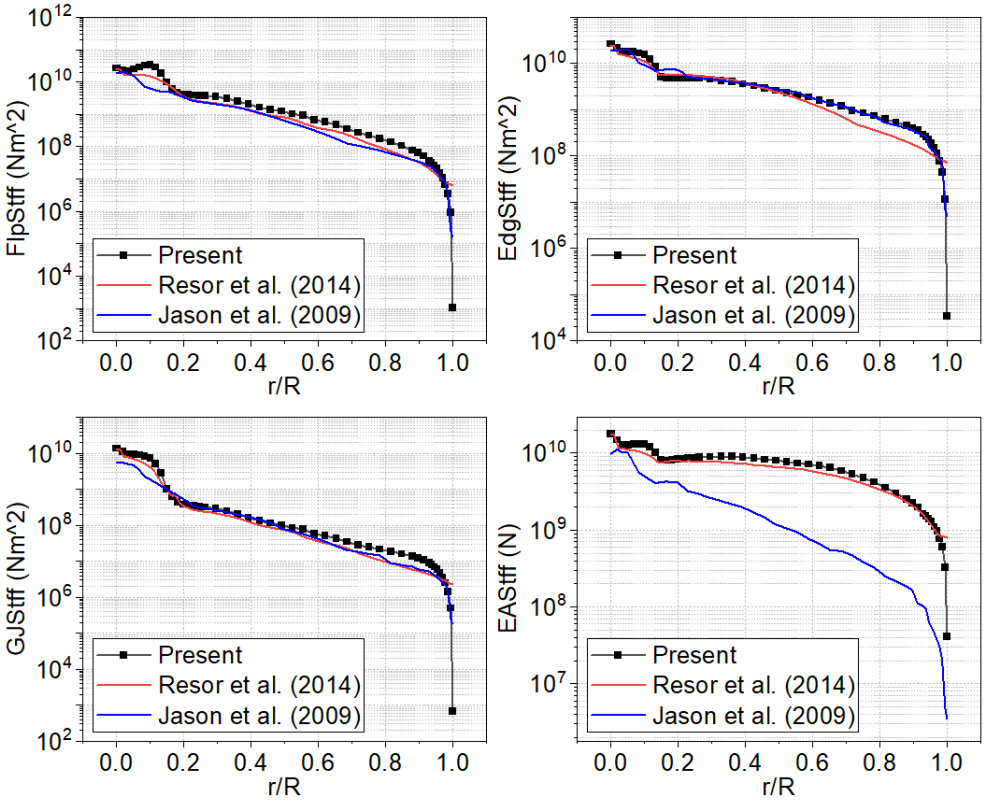

Figure 3-1. Blade stiffness properties comparisons. Present study uses NuMAD (Berg & Resor, 2012) for stiffness calculations.

3.5 FSI analysis framework

The architecture of the proposed FSI framework is presented in Figure 3-2. Briefly, the data streams being transferred during the two-way FSI are the distributed force integration (from OpenFOAM to MBDyn) and the node displacement (from MBDyn to OpenFOAM), whilst the FEA model in Abaqus can receive the instantaneous nodal displacement (or force) data at arbitrary moment of simulation time for static load analysis. Detailed introduction for the proposed FSI analysis framework procedure is given in the following.

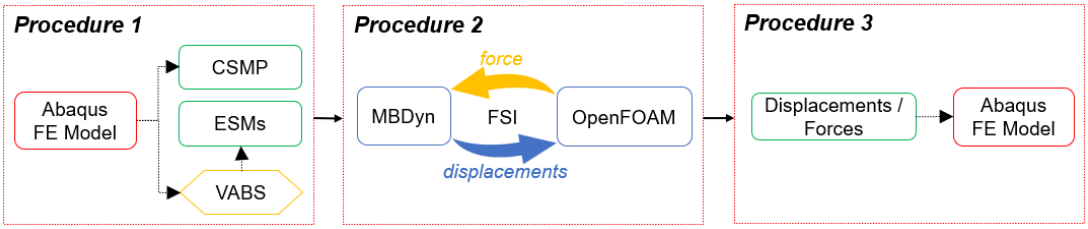

Figure 3-2. Diagram of the proposed FSI framework of stress analysis.

At the beginning of the analysis, the fully resolved FE model is firstly established in Abaqus CAE. Following with 3 main procedures, ending with the stress field establishing procedure in Abaqus CAE, which completes the analysing procedures.

In Procedure 1, the structural properties of the FE model are extracted and preserved as the intermediate datasets of the composite structural mass properties (CSMP) and the effective stiffness matrices (ESMs) of each partitioned section of the FE model in Abaqus. The mechanical properties of the composite structure FE model in 3D space can be accounted by the ESMs in the beam model, which is required by the multibody dynamics method of MBDyn (Masarati et al., 2014) in Procedure 2.

Then, in Procedure 2, the strong-coupling two-way FSI analysis is conducted, where the transient aerodynamic loads with turbulent effects can be considered by high-fidelity CFD, and the structural dynamic performance under aerodynamic conditions are solved in MBDyn. The structure inertial, centrifugal, deformational response can be well captured during the FSI coupling.

With Procedure 1 and 2, the actual macroscopic structural response can be accounted by the beam model in MBDyn in a strong-coupling two-way FSI. Unlike the direct CFD-FEA FSI coupling, the proposed procedures would perform more efficient, since the outstanding computational costs and strict controlling of coupling interface are avoided.

Finally, in Procedure 3, the blade kinematics preserving macroscopic structure responses solved by MBDyn will be explicitly interpolated onto the blade FE model as the boundary condition (BC) in the Abaqus static structure analysis, to establish the Von Mises stress field in the composite blade FE model.

The Von Mises stress is an equivalent stress which combines the influence of both normal principal stresses and shear stresses on the material. By comparing the Von Mises stress on the simulated material against the experimental results, it evaluates the material stress condition under the specified loads, so that the potential vulnerable locations of material and structure can be identified.

In this procedure, the displacement fields solved by MBDyn during the strong-coupling FSI process can accurately reflect the blade nonlinear structure responses at arbitrary moments, under any operation conditions with or without complex motion couplings. Factors such as the moment of inertia, the centrifugal and gravitational effects, and the additional excitations due to the active rotor rotation, can be well preserved and reflected in the structural displacement data. In the scope of present FSI framework for stress analysis, the adoption of displacement is faster in terms of operations. A precise control and calibration of the displacement distribution on the structures is easier to be realised comparing with that using the force field. Therefore, it shows a better applicability and precision for establishing the stress fields using the displacement fields in the scope of our proposed framework.

3.5.1 Coupling scheme

As depicted in Figure 3-3, the staggered coupling strategy allows the fluid and structure fields to interact in a decomposed manner. The convergence of the coupling is separately governed and tighten in each solver, thus, the accuracy of the coupling

can be well guaranteed. Multiple iterations are defined during every timestep intervals which further improve the accuracy of the data transfer, i.e. passing the forces and displacements between the fluid and structure domains, thus reached a strong-coupling process.

Briefly, the FSI coupling between the CFD and MBDyn with the presence of non-matching gird is achieved by aligning the locations of aerodynamic centres of each CFD grid patch to their corresponding structural nodes in MBDyn. Therefore, for the force mapping, the integrated force on each grid patch (in CFD) is directly mapped to the corresponding structural node (in MBDyn), whereas the displacement mapping from the structural node to the CFD patch is conducted via a bi-linear distance-weighted interpolation (Liu et al., 2019). The detailed elaborations of the FSI approach are given in the following.

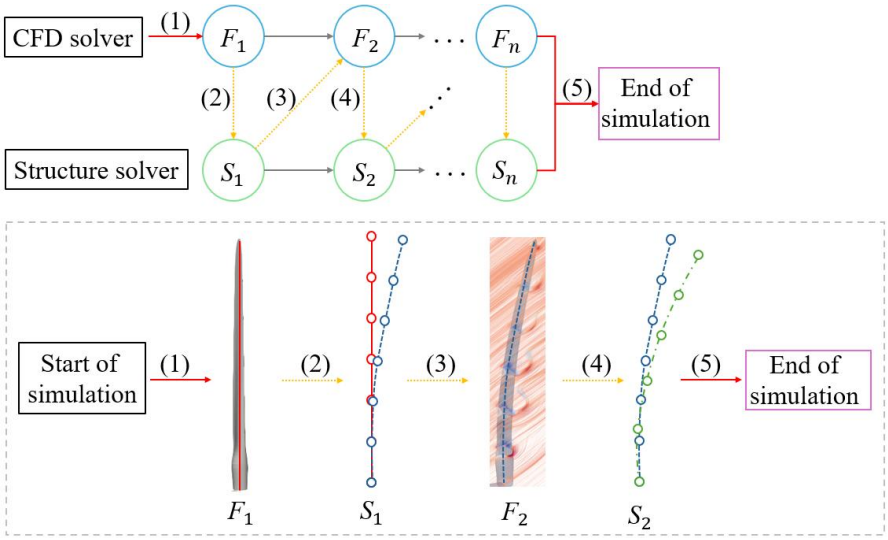

Figure 3-3. Flowchart of the two-way strong-coupling FSI process.

Actions during the FSI process are explained in a sequential order. To begin, the coupling initiates from F_1 at the 1st timestep, t_1, where the aerodynamic forces exert on the blade surfaces are calculated in the fluid domain $\boldsymbol{\Psi}_{\boldsymbol{f},t_1}$. Once the flow converges, the integration of forces is computed and transferred to the corresponding structure nodes $\boldsymbol{\Psi}_{\boldsymbol{s},t_1}$, updating the structural dynamics for all nodes, as indicated by S_1, where the new locations of each structure node can be obtained, i.e. the displacements of the nodes. The force mapping is generalised as:

$$\boldsymbol{\Psi}_{\boldsymbol{f},t_1} \rightarrow \boldsymbol{\Psi}_{\boldsymbol{s},t_1} \tag{3.25}$$

The timestep size Δt is a constant for both solvers participating the FSI to maintain the synchronization of the coupling process. The vector $\boldsymbol{\Psi}$ denotes the blade is partitioned into N multiple sections in order to capture distributed loads along the blade, so that the dynamics of the blade can be solved as the structure node receives the aerodynamic force accordingly. The number of sections N used in this study is 49, which has been extensively validated as a suitable choice in balancing the numerical accuracy and coupling efficiency (Liu et al., 2019; Deng et al., 2024). At an arbitrary time t_j, the aerodynamic force and blade structural kinematics in the fluid domain and multibody system are expressed in a partitioned form for each blade section:

$$\boldsymbol{\Psi}_{\boldsymbol{F},t_j} = \left[\boldsymbol{\Psi}_{f1,t_j}, \boldsymbol{\Psi}_{f2,t_j}, \dots, \boldsymbol{\Psi}_{fi,t_j}\right], i = N \tag{3.26}$$

$$\boldsymbol{\Psi}_{\boldsymbol{S},t_j} = \left[\boldsymbol{\Psi}_{s1,t_j}, \boldsymbol{\Psi}_{s2,t_j}, \dots, \boldsymbol{\Psi}_{si,t_j}\right], i = N \tag{3.27}$$

Considering the Reynold stress in the turbulent viscous flow, the discretised forces in the control volume consists of the fluid pressure forces $\boldsymbol{F}_p$ and the Reynold shear stresses $\boldsymbol{F}_\tau$, the sectional force integration on the i-th section of the blade at t_j, $\boldsymbol{\Psi}_{fi,t_j}$, is calculated by summing the discretized force vector on the surrounding finite volume of the particular blade section in a surface area of A_i, i.e.

$$\boldsymbol{\Psi}_{fi,t_j} = \int_{A_i} \left(\boldsymbol{F}_{i,p} + \boldsymbol{F}_{i,\tau}\right) dA \tag{3.28}$$

$$\boldsymbol{F}_{i,p} = -p\boldsymbol{n} \tag{3.29}$$

$$\boldsymbol{F}_{i,\tau} = [\mu(\nabla \boldsymbol{u} + (\nabla \boldsymbol{u})^T) - \rho\overline{u'u'}] \cdot \boldsymbol{n} \tag{3.30}$$

$\boldsymbol{n}$ denotes the global coordinate direction vector locates at each surface grid on the blade wall boundaries, pointing outwards into the fluid interior.

Next, the updated displacements of each structure node $\boldsymbol{\Psi}'_{\boldsymbol{S},t_j}$ in the lumped mass system $\boldsymbol{M}$ are calculated as:

$$\boldsymbol{\Psi}'_{\boldsymbol{S},t_j} = \boldsymbol{\Psi}_{\boldsymbol{S},t_j} + \frac{\boldsymbol{\Psi}_{\boldsymbol{F},t_j}}{\boldsymbol{M}}\Delta t \tag{3.31}$$

The local deformation $\boldsymbol{k}$ of the i-th structure node at t_j timestep is thus calculated as:

$$\boldsymbol{k}_{i,t_j} = \frac{\boldsymbol{\Psi}_{fi,t_j}}{\boldsymbol{M}}\Delta t$$

The new nodal locations are fed back to the fluid domain for mesh updates at the timestep of t_2, as depicted by F_2. A bi-linear distance-weighted interpolation approach is used for a robust control for the mesh-update mapping process, formulated as:

$$\boldsymbol{\Omega}_{t_{j+1}} = \alpha_{i-1}\left(\boldsymbol{k}_{i-1,t_j} + \boldsymbol{R}_{i-1,t_j}\boldsymbol{d}_{i-1}\right) + (1-\alpha_{i-1})\left(\boldsymbol{k}_{i,t_j} + \boldsymbol{R}_{i,t_j}\boldsymbol{d}_i\right), i = N \tag{3.32}$$

$$\alpha = \frac{\boldsymbol{l}\cdot\boldsymbol{d}}{|\boldsymbol{l}|^2} \tag{3.33}$$

$\boldsymbol{\Omega}_{t_{j+1}}$ denotes the updated blade surface grid point locations in the 3D fluid domain at t_{j+1} timestep. $\boldsymbol{d}$ is the distance vector pointing from the structure node to the blade surface grid vertices, and $\boldsymbol{l}$ is the vector connecting the adjacent structure nodes. α is the distancing weight calculated by the vector projection from $\boldsymbol{d}$ to $\boldsymbol{l}$, evaluating the contributions of the adjacent structure node motions to the in-between fluid surface grids. $\boldsymbol{R}$ represent the quaternion matrix accounting for the rotations of the structure node. Due to the coordinates of the fluid and structure models are aligned at the initiation of the FSI, there is no need for additional transformations of the rotation matrix.

As the coupling loop into subsequent timestep t_{j+1}, the aerodynamic forces are calculated with the updated surface mesh $\boldsymbol{\Omega}_{t_{j+1}}$, and then the process repeats transferring force to the structure solver, forming a meta-loop of a complete FSI process. Upon the stopping condition is satisfied, usually defined as the final timestep is completed in both solvers, the FSI coupling terminates.

3.5.2 Advantages of the FSI framework

In this FSI framework, the fluid and structure coupling participants are based on high-fidelity CFD and robust Multibody dynamics method, respectively. The considerations for composite materials and the detailed structural stress and strain performance are conducted in finite element based Abaqus CAE code.

The CFD solver performs much more generally in terms of capturing the evolution and interactions of the flow in three-dimensional space, with considerations of turbulent effects. The governing equations in CFD strictly obeys the laws of conservations for mass and energy, thus it can deal with any types of flowing problems and not requiring additional corrections during the CFD numerical computations.

Other available order-reduced fluid solvers such as the BEM and FVW are not used in this work, though they perform rather computationally efficient, the precision of the flow predictions using these codes cannot be well guaranteed, especially for FOWT problems where the geometry or the fluid flowing conditions are complicated, the accuracy of the order-reduced codes is hard to maintained and requires correction models by conducting comprehensive experimental investigations (Lanzafame & Messina, 2012; Sharifi & Nobari, 2013; Sayed et al., 2019).

For the structure solver, the governing equation for the multibody dynamic code follows the basic idea of Newton's second law of motion. Additionally, the integration of Abaqus CAE enables a thorough investigation of the composite structure at all structure hierarchy, depending on the fidelity of the constructed finite element model.

3.6 Active Sampling coupled NSGA-II Optimization

In this section, the active sampling coupled non-dominated sorting genetic algorithm (NSGA-II) optimization (Deb et al., 2002) is proposed and explained. This method is developed for effectively handle the surrogate model approximation failure due to the out-of-distribution issue during the surrogate training.

Such issue is commonly encountered when a surrogate model is adopted for the multi-input-multi-output (MIMO) system optimization, where the common practice is to use regression models (e.g. neural network models) to replace the conventional numerical codes for feasibly predict the responses of objectives due to the consideration of computational efficiency.

The complete workflow of active sampling coupled NSGA-II optimization is depicted in Figure 3-4. The realistic aeroelastic loading characteristics of the blade structure are firstly calculated by the high-fidelity two-way FSI analysing framework. The structural responses are subsequently resolved using FEA. Then, in the active sampling optimization workflow, the ANN surrogate model and the NSGA-II optimization process are dynamically interplaying with each other for maintaining the accuracy of the predicted Pareto front solutions.

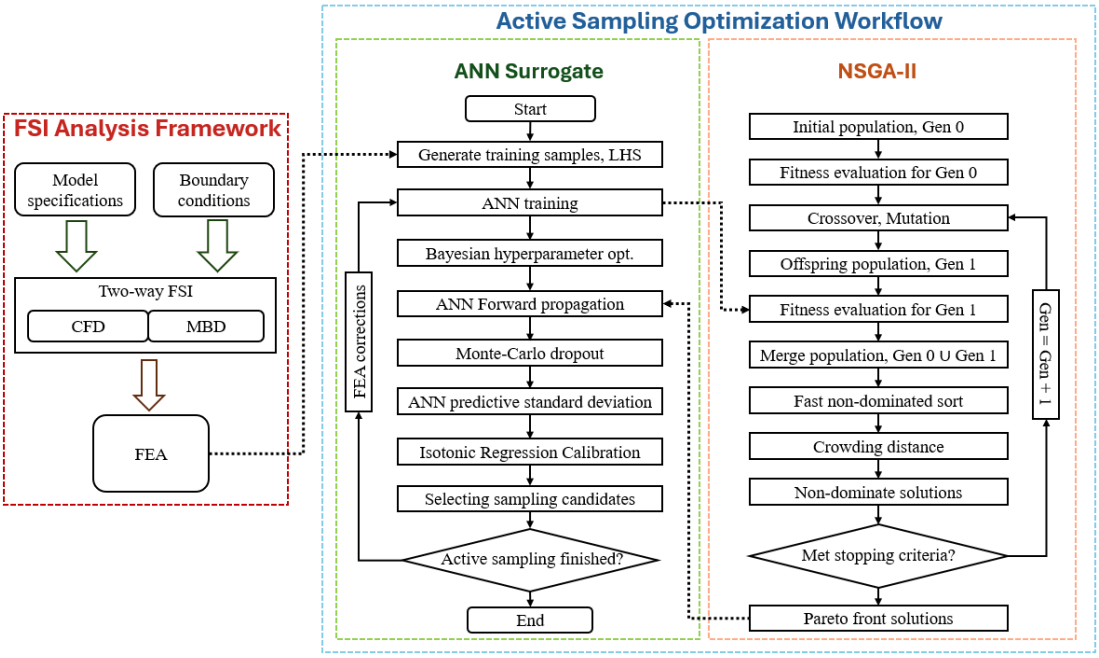

Figure 3-4. Complete FSI-driven analysis and optimization workflow for wind turbine blade.

Detailed explanations to the specifications of the NSGA-II optimization and Artificial neural network surrogate model are given in the following sections.

3.6.1 NSGA-II optimization

The NSGA-II (Deb et al., 2002) is realised in distributed evolutionary algorithms in python (DEAP framework). It starts by firstly generating an initial population P_t of size N, where N defines the number of individuals (vector of design variables, $\boldsymbol{x}$) that will be carried to the next generation. Then, the crossover and mutation are performed on the selected individuals from P_t to generate new offspring population Q_t of size M that introduces diversity and expand the search space of the possible solutions.

The crossover and mutation probability are the individual probabilities that invoke the crossover and mutation operators in each generation. The crossover in DEAP is implemented using a crossover operator to blend the design variables (genes) of two randomly selected parents, $\boldsymbol{x}_p^{(1)}$ and $\boldsymbol{x}_p^{(2)}$, then generate two offspring, $\boldsymbol{x}_o^{(1)}$ and $\boldsymbol{x}_o^{(2)}$ using a random blending factor γ_i that satisfies a uniform distribution $\mathcal{U}$, defined by a ranging modifier α, i.e.

$$\gamma_i \sim \mathcal{U}[-\alpha, 1+\alpha], \alpha = 0.5 \tag{3.34}$$

$$\boldsymbol{x}_o^{(1)} = (1-\gamma_i)\boldsymbol{x}_p^{(1)} + \gamma_i \boldsymbol{x}_p^{(2)} \tag{3.35}$$

$$\boldsymbol{x}_o^{(2)} = (1-\gamma_i)\boldsymbol{x}_p^{(2)} + \gamma_i \boldsymbol{x}_p^{(1)} \tag{3.36}$$

The mutation uses a Gaussian operator (mutGaussian function) which applies a local perturbation (stochastic noise) to each gene. The noise satisfies the Gaussian distribution, which is characterised by the mean value, *mu*, with a standard deviation, *sigma*. A mutation threshold is defined by the independent probability, *indpb*, meaning that if the functioning random number for each gene is lower than *indpb*, the noise will be applied so that the corresponding gene will be mutated. This generates the merged population defined as $R_t = P_t \cup Q_t$.

Next, the individuals in R_t are fed in the FEA code or surrogate model to compute the objective solutions. The non-dominated sorting procedure ranks solutions based on Pareto dominance, followed by crowding distance sorting to maintain solution diversity. The elitism mechanism in NSGA-II ensures that high-quality solutions are retained across generations through a combination of non-dominant sorting and crowding distance preservation. The algorithm terminates when the predefined stopping criteria are met, which typically defined as reaching the maximum number of generations, or the solutions of generation is no longer improved. The NSGA-II specifications are listed below in Table 3-2.

Table 3-2. NSGA-II specifications for initializing the optimization.

Items	**Values**
Initialization	Uniform, random sampling
Size of population	750
Number of generations	50
Crossover probability	0.7
Mutation probability	0.3
Crossover operator	0.5
Mutation operator	mutGaussian (mu=0, sigma=0.1, indpb=0.2)
Early Stopping	Yes (if no improvements for 10 generations)

3.6.2 Artificial neural network training

To accelerate NSGA-II process for a high-dimensional non-convex optimization problem, an ANN is trained serving as a surrogate model that approximates the nonlinear solution space of the composite blade FEA model. In this study, given the high-dimensional input-output characteristic of the optimization problem, the Latin hypercube (LHS) sampling approach was chosen, as it ensures uniform coverage of the solution space while reducing the cost of sampling point seedings. A physical inductive biased network is established where two types of variables (thickness and fibre orientation) are considered in two branches of hidden layers. This enables the network to focus on the weight distributions for each variable separately, improving the control and the interpretability to the network. The ANN is trained on an 8-core Intel i7 11800H (base frequency 2.3 GHz) and Nvidia RTX 3070 GPU (8GB memory) machine.

To train the ANN, a Bayesian hyperparameters optimization of 100 iterations is conducted based on the Optuna framework (Akiba et al., 2019) in Python, tunning the number of neurons in each layer, number of hidden layers, dropout rate, mini-batch size, initial learning rate and weight decay of the AdamW optimizer (Loshchilov & Hutter, 2017) for ANN training.

We firstly calculate 10000 sets of high-fidelity results of structural responses using FEA. A data filtering process is conducted to remove the apparent outliers and non-physical entries, resulting 9896 valid datasets for ANN training, where the proportions of training, validation and testing datasets are randomly partitioned in a ratio of 60% / 20% / 20% to ensure the well capture of the nonlinear relationships between the design variables and objective responses.

A 100-iteration Bayesian hyperparameter optimization has been conducted to explore a hyperparameter combination that minimises the predictive error of ANN for the nonlinear system. To quantify the training error of ANN, the Huber loss function L_H is adopted due to its piecewise behaviour that blends the quadratic penalty for small residuals as mean-squared error (MSE), whereas the larger residuals are linearly penalised as mean-absolute error (MAE). This hybrid form preserves the high sensitivity of MSE to small residuals, r, yet reduces the influence of large residuals, achieving the balance between the accuracy and robustness of the hyperparameter optimization for ANN. Standardizations of training datasets are implemented. The Huber loss function L_H is formulated as follows where $\boldsymbol{\delta}$ is the threshold distinguishing the between the quadratic and linear regions of the Huber loss:

$$r = |\hat{y} - y| \tag{3.37}$$

$$L_H(r) = \begin{cases} \frac{1}{2}r^2 & , \quad |r| \leq \boldsymbol{\delta} \\ \boldsymbol{\delta}|r| - \frac{1}{2}\boldsymbol{\delta}^2, & \quad |r| > \boldsymbol{\delta} \end{cases} \tag{3.38}$$

Worth noting that the determinations of hyperparameter ranges and intervals are dependent on the training sample size, the empirical adjustments for model fitting (avoid over or underfitting) and the balance between model approximating accuracy

and cost of training. The specifications of the Bayesian hyperparameter optimization are given in Table 3-3.

Table 3-3. Bayesian hyperparameter optimization specifications.

Hyperparameters	Object of action	Values
Number of hidden neurons	Branch 1	64, 128, 192, 256
Number of hidden neurons	Branch 2	32, 64, 96, 128
Number of hidden neurons	FC layer	128, 256, 384, 512
Number of hidden layers	Branch 1, Branch 2, Head layer, MLP	1, 2, 3, 4
Dropout rate	All hidden layers	0.00, 0.05, 0.10, 0.15, 0.20
Mini-batch size	Sample division	64, 128, 256, 512
Learning rate	AdamW optimizer	[1e-05, 3e-04]
Weight decay	AdamW optimizer	[1e-06, 1e-04]

The maximum number of neurons are defined for each hidden layer, avoiding the excessive number of parameters while maintaining the ANN capability of capturing the highly nonlinear responses.

The number of hidden layers is kept below 4 since a deeper layer did not yield improvements in approximation accuracy during the test runs, while it significantly increases the training time.

To prevent the overfitting and increase the generalizability of the ANN model, a maximum dropout rate is regulated to 0.2. To feasibly train the model on this GPU, the mini-batch size that controls the throughput of data is restricted to the range 64–512, preventing the out-of-memory issues of GPU.

The AdamW optimiser (Loshchilov & Hutter, 2017) is used for updating the weights and bias of the network during backpropagation due to its proven converging stability and better generalisation performance comparing with the Adam optimizer.

The search for the initial learning rate and weight decay span ranges from conservative fine-tuning values to moderately aggressive settings. An overly large value can cause highly oscillatory weight updates and potentially lead to the overfitting of the ANN model. The resultant structure of ANN is depicted in Figure 3-5.

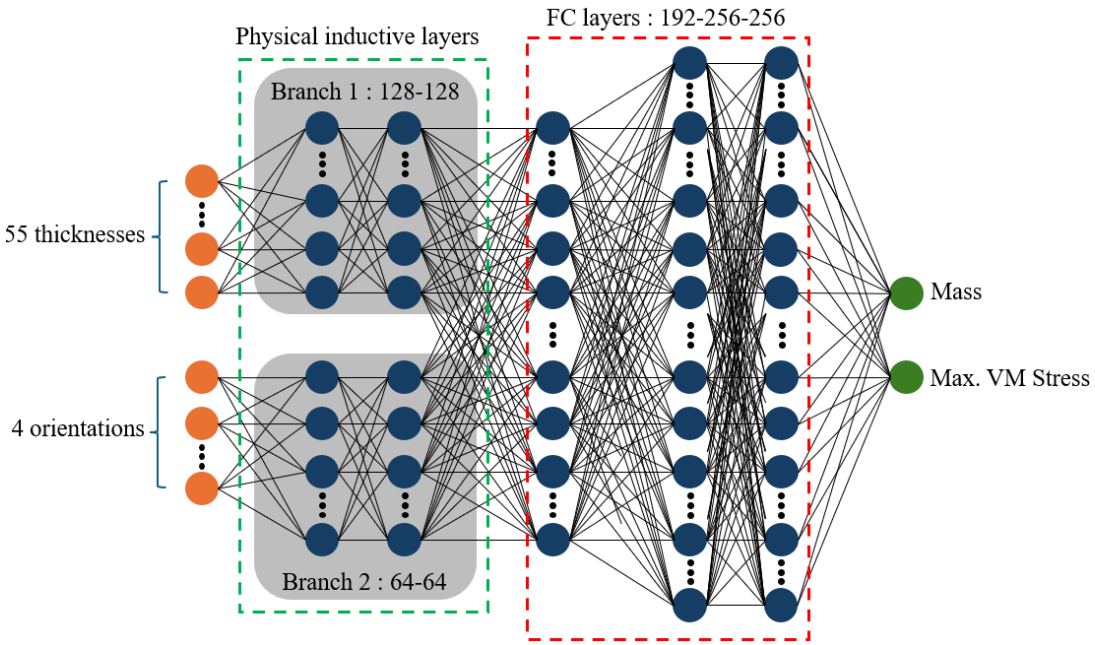

Figure 3-5. Physical inductive biased ANN structure for nonlinear objective approximations, with indication of inputs (thicknesses and fibre orientations) and outputs (blade mass and Max. Von Mises stress).

The Gaussian Error Linear Unit (GELU) activation function (Hendrycks & Gimpel, 2016) helps mitigating the vanishing gradient problem, also improves the nonlinear approximating capability and the training effectiveness. The formulation of GELU is given as follows, with its range of response showing in Figure 3-6:

$$GELU(x) = x \cdot \frac{1}{2}\left[1 + erf\left(\frac{x}{\sqrt{2}}\right)\right] \tag{3.39}$$

$$erf(x) = \frac{2}{\sqrt{\pi}}\int_0^x e^{-t^2}dt \tag{3.40}$$

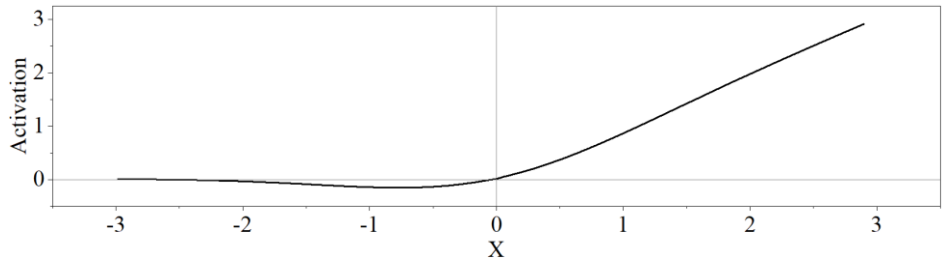

Figure 3-6. GELU activation function.

3.6.3 Active sampling workflow

During the optimization, the NSGA-II continually pushes the candidate solutions to corners of the design space, where the ANN can fail in interpolating and is forced to extrapolate, which causes a severe drop in predictive accuracy. To resolve this issue, the active sampling technique is proposed for dynamically improving the training set integrity of ANN during the active sampling coupled optimization, helping the ANN to adapt the evolving solution space explored by the NSGA-II.

The schematic workflow of active sampling is generalized in Figure 3-7. A single iteration of active sampling (displayed in row) consists of five subtasks, including: 1). the Pareto front predictions by ANN-assist NSGA-II, 2). the feedforward propagations through ANN of all Pareto front candidates, 3). identification of mis-predicted Pareto candidates, 4). FEA corrections for the mis-predicted Pareto candidates, and 5). the re-training of ANN with corrected candidates being added to the training datasets.

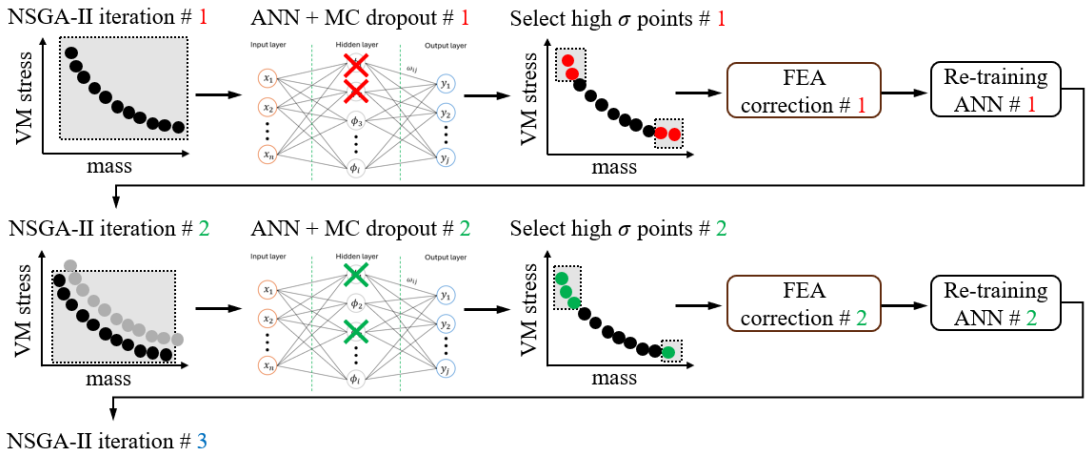

Figure 3-7. Schematic workflow of active sampling.

Worth noting that the ANN training during the active sampling coupled optimization will adopt the optimal hyperparameter specification that is previously given in Section 3.6.2. During the active-sampling optimization process, the proportion of training and validation datasets for the ANN surrogate model is 80% / 20%. The testing set is not required since the ANN in active sampling is predicting the objective response instead of evaluating the ANN performance. A 20% of validation set is needed for evaluating the validation loss for the implementation of early stopping of the ANN training.

One of the important subtasks is the feedforward propagations with the Monte-Carlo (MC) dropout for the stochastic neuron deactivation. Specifically, for each set of design variable, we perform multiple feedforward propagations that pass the variables through the ANN again with MC dropout, yielding a collection of spread predicted objectives. Such spread of new predictions reflects the uncertainty of ANN surrogate model, which is the source of predictions inaccuracy during the optimization process. To quantify such uncertainty, the standard deviation σ of the predicted objectives can be calculated as follows:

$$y^{(i)} = f_{\phi}^{dropout}(\boldsymbol{x}) \tag{3.41}$$

$$\mu = \frac{1}{N}\sum_{i=1}^{1} y^{(i)}, \ \ i = 1,2,\dots,N \tag{3.42}$$

$$\sigma = \sqrt{\frac{1}{N-1}\sum_{i=1}^{N}(y^{(i)} - \mu)^2} \tag{3.43}$$

where $y^{(i)}$ stands for the predicted objective values after i-th times of the ANN MC dropout process (Total number of N times). μ is the average of the objective value. σ is the standard deviation of the objective.

Noted that the ANN predictive uncertainty only quantifies the confidence of the objective predictions for each Pareto candidate, however, it is not necessarily reflecting the true errors between the predicted and real objective responses. Therefore, to establish the relationship between the ANN prediction uncertainty σ and the ANN prediction error to the objectives err, an isotonic regression calibration is attempted to quantify the monotonic mapping relationship between the σ and the err:

$$err = f(\sigma) \tag{3.44}$$

i.e. for each point of (σ_j, err_j) in a set of (σ, err), we can find a monotonic non-decreasing function f that best fits the data:

$$min \sum_{j} \left(f(\sigma_j) - err_j\right)^2$$

$$s.t.\ f(\sigma_j) < f(\sigma_{j+1})\ whenever\ \sigma_j < \sigma_{j+1}$$

Such isotonic regression calibration ensures that the ANN uncertainties are equivalently reflecting the true errors of the ANN predictions.

To do so, the σ of all Pareto candidates are firstly ranked in a descending order, where the first *k_sample* of candidates with the highest uncertainty of stress prediction σ are selected for FEA cross-validation. Then, the err_j for each candidate is calculated as:

$$err_j = \frac{\left|y_j^{ANN} - y_j^{FEA}\right|}{y_j^{FEA}} \times 100\% \tag{3.45}$$

Then, in each active sampling loop, the isotonic regression is conducted to fit the monotonic non-decreasing function f on all pairs of (σ_j, err_j) for all Pareto candidates, finding the candidates that are most inaccurately predicted by the ANN for FEA correction, for instance, the top M candidates, where M can be adjusted depending on whether the number of selected candidates for correction is enough for the improvements of surrogate model approximation accuracy. Subsequently, the true objective responses of these candidates can be added to the training samples for re-training of the ANN model in the next loop of NSGA-II optimization with active-sampling.

By conducting *max_iter* times of active-sampling iterations, the Pareto candidates that exhibit a relatively larger error can be identified constantly throughout the active-sampling optimization. Then, these large-error Pareto candidates in each active-sampling iteration can be dynamically picked for FEA corrections, so that the accurate objective responses can be acquired for improving dataset distribution of ANN surrogate training, thus improving the approximation accuracy of the ANN.

The training sample dataset expands with each iteration, and for each round the iteration the ANN is trained from scratch on the latest dataset, where the weights and

biases of the ANN are updated for adapting the dynamic solution space during the NSGA-II optimization.

The advantage of using such hybrid approach is obvious, where the ANN approximating accuracy can be rapidly improved with the focus on underperformed candidates, while avoiding the waste of computational resources on full simulations across the entire design space using conventional FEA.

The specifications for the execution of active sampling process are listed below in Table 3-4, noting that the determination of the active sampling specifications is problem-dependent. The calculation specifications may require adjustments for achieving a well balance in terms of numerical accuracy and efficiency depend on the complexity of the analysed problem.

Table 3-4. Specifications of active sampling in optimization.

Items	Values	Notes
max_iter	50	Total number of active sampling iteration
k_sample	150	Number of designs for FEA corrections in each active sampling iteration
i	50	Number of feedforward with MC-dropout for each to-be-corrected design

The active sampling acts as a data selector, which measures the uncertainties for each Pareto candidates where the predicting accuracy of the ANN is low and dynamically picking these candidates for FEA corrections. The corrected datasets will be added back to the training set for ANN re-training.

This features as a hybrid method which combines the advantages of both rapid-response neural network model and the accurate FEA approach, i.e. improving the ANN approximating performance effectively with a limited number of key datasets, also, avoiding the waste of computational resources on massive sampling across the entire design space using conventional FEA.

Chapter 4 Validation Studies

4.1 NREL 5MW Composite Blade Specifications

Before the discussions on numerical validations, a detailed introduction of the NREL 5MW wind turbine blade is given for a clear understanding of the problem.

The cross sectional profiles on a NREL 5MW wind turbine blade are shown in Figure 4-1 (a), including DU and NACA series airfoils as detailed in Table 4-1.

Figure 4-1 (b) shows fifty partitioning surfaces for intercepting the intermediate blade cross sections for a smoother transitional shape and thickness variations along the blade. From the cross-sectional view (A-A') in Figure 4-1 (c), the chordwise stacking partitioning areas are displayed, including: the leading edge (LE), leading edge panel (LE_Panel), Spar Cap (Cap), trailing edge panel (TE_Panel), trailing edge reinforcement (TE_Reinf) and trailing edge (TE).

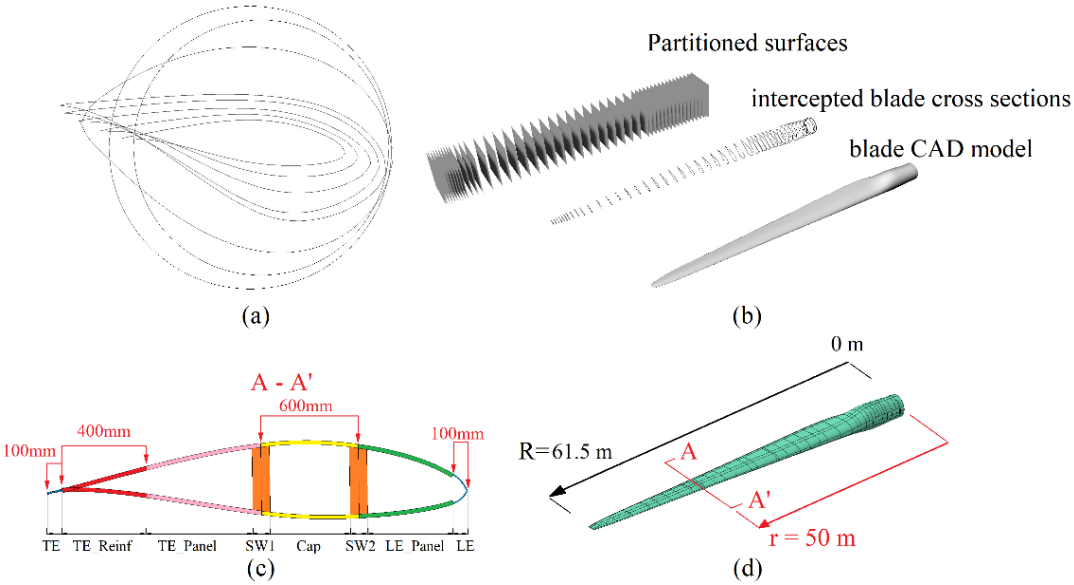

Figure 4-1. The designated airfoils on the blade, (b) CAD model of the blade geometry, (c) Local partitioning on a blade cross section, NACA 64-618 airfoil, and (d) Blade FE model with A-A' plane depicted on blade spanwise r/R = 81.3%.

Additionally, the Shear webs (SW1, SW2) which are the main supporting component to endure the shear stress under the aerodynamic loads. Figure 4-1 (d) demonstrated

the completed blade model, applied with composite stacks and non-uniform distributed sectional dimensions.

Table 4-1. Airfoil allocations along the blade.

Airfoil Shapes	Begin cross-sectional locations (m)
Cylinder1	1.8
Cylinder2	5.98
DU W-405	10.15
DU W-350	15.00
DU 97-W-300	20.49
DU 91-W2-250	26.79
DU 91-W-210	34.22
NACA 64-618	42.47

As shown below, the number of composite laminate layers (Figure 4-2) and the layer stacking sequence along the blade are configurated non-uniformly along the blade. This suggests that in the FEA model, the blade geometry needs to be divided into multiple regions in both spanwise and edgewise for the localised definition of materials.

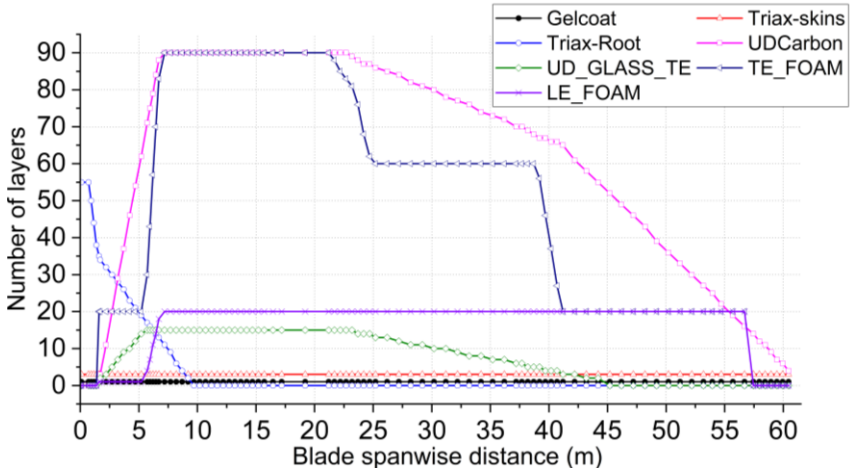

Figure 4-2. Number of layers distribution along the blade spanwise for composite laminates.

The definition of composite materials used for the NREL 5MW wind turbine blade is given in Table 4-2. The stack names are defined that clarifies the locations of material assignments to the corresponding blade regions.

Table 4-3 defines the stacking sequence of the composite materials. Following this table, the blade needs to be firstly divided piecewise on both spanwise and edgewise (i.e. chordwise, see Figure 4-1 (c)) directions.

For example, for the blade shell structures, the numbering from left to right, e.g. '1,2,3,2', means that the order of composite material stacking should be organised as 'Gelcoat, Triax Skins, Triax Root, Triax Skins', with corresponding number of stack layers being used as given in Figure 4-2. The first layer of stack is defined as the reference surface, so that the stacking sequence of local composite material is unified.

Table 4-2. Definition of stack and material names.

Locations	Stack ID	Stack name	Materials
Blade shells	1	Gelcoat	Gelcoat
	2	Triax Skins	SNL(Triax)
	3	Triax Root	SNL(Triax)
	4	UD Carbon	Carbon(UD)
	5	UD Glass TE	E-LT-5500(UD)
	6	TE Foam	Foam
	7	LE Foam	Foam
Blade Shear webs (SW)	8	Saertex(DB)	Saertex(DB)
	9	SW Foam	Foam

Table 4-3. Stacking sequence and starting locations in each blade region spanwise direction.

Blade span (m)	TE	TE_REINF	TE_PANEL	CAP	LE_PANEL	LE
0	1,2,3,2	1,2,3,2	1,2,3,2	1,2,3,2	1,2,3,2	1,2,3,2
1.3667	1,2,3,2	1,2,3,2	1,2,3,2	1,2,3,2	1,2,3,2	1,2,3,2
1.5	1,2,3,2	1,2,3,5,6,2	1,2,3,6,2	1,2,3,4,2	1,2,3,7,2	1,2,3,2
6.8333	1,2,3,2	1,2,3,5,6,2	1,2,3,6,2	1,2,3,4,2	1,2,3,7,2	1,2,3,2
9	1,2,2	1,2,5,6,2	1,2,6,2	1,2,4,2	1,2,7,2	1,2,2
43.05	1,2,2	1,2,5,6,2	1,2,6,2	1,2,4,2	1,2,7,2	1,2,2
45	1,2,2		1,2,6,2	1,2,4,2	1,2,7,2	1,2,2
61.5	1,2,2		1,2,2	1,2,2	1,2,2	1,2,2
Blade span (m)	**Shear webs (SW)**					
1.3667	8*,9**,8*					
61.5	8*,9**,8*					

Notes: * Each stack of #8 consists of 2 glass-fibre reinforced layers, forming the Saertex(DB); ** For stack #9, the Foam thickness is 50 mm, according to SNL report.

A proper arrangement of the composite stacking sequence and the number of layers variations on both spanwise and chordwise for each partitioned area is crucial. Any

misalignment in material stacking orders can result in inaccurate blade mass and stiffness properties.

The geometrical definitions for the NREL 5MW wind turbine are given in Table 4-4. The blade precone, shaft-tilt angles and the overhang were set to zero, since the impacts of these configurations to the blade structural response is found to be insignificant (Dose et al., 2018), especially for a FOWT scenario, the most significant source of aeroelastic instability is the platform motions. In the scope of this study, we have reasonably neglected the precone, shaft-tilt angles and overhang to accelerate the preparations of the blade geometry and dynamic mesh configuration in the FSI simulations.

Table 4-4. Blade geometrical definition between the reference and present values.

Definitions	Reference values	Present values
Rotor orientation, # of blades	Upwind, 3 blades	Upwind, 3 blades
Rotor, Hub diameter (m)	126, 3	126, 3
Blade length (m)	61.5	61.5
Overhang (m)	5	0
Shaft-tilt (degree)	5	0
Pre-cone angle (degree)	2.5	0

4.2 Aerodynamic Validation of the NREL 5 MW FOWT

Before conducting numerical investigations for the blade aeroelastic responses under different FOWT surge motion conditions, a numerical validation has been conducted for the NREL 5MW FOWT blade aeroelastic with a code-to-code comparison against the results from Liu et al. (2019). This part of CFD validation is corresponding to the studies as subsequently introduced in Chapter 6 and Chapter 7.

To properly capture the aerodynamic loads on the blade, we modified and generated a mesh as shown in Figure 4-3. The computational domain is divided into 2 regions, the rotor and stator cell zones. The blades (rotor) are placed at the origin of the global coordinate system.

To mitigate boundary effects and potential flowing disturbance, a large computational domain is given, measures as 15D × 10D × 10D in X, Y and Z directions in space, respectively. The radius of the internal rotor cell region Rc = 150 meters, and it spans L = 200 meters in X direction.

This offers a sufficient space for the flexible blades to deform during the FSI process, preventing the blade wall boundaries from colliding with the interfaces of the sliding mesh. This may also avoid mesh quality deterioration due to the undesired collapse of the cells, especially in the blade tip regions.

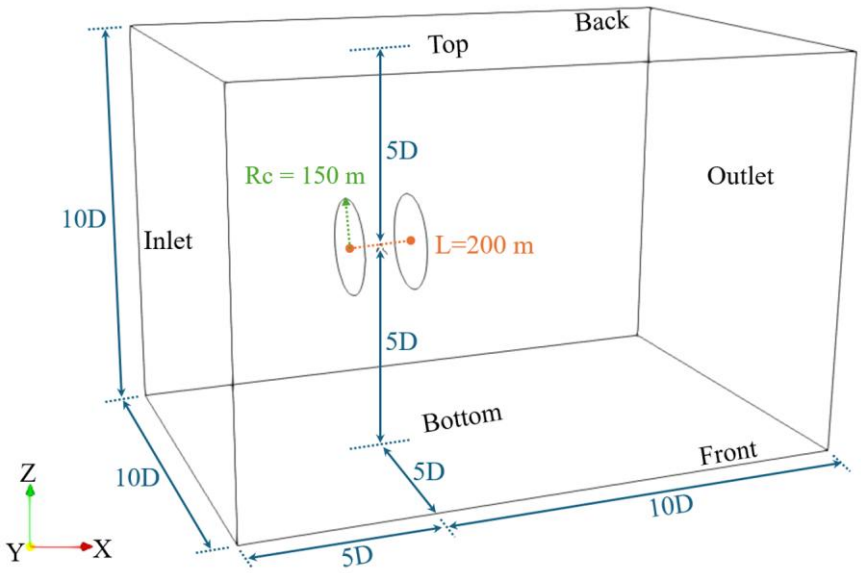

Figure 4-3. Mesh for FOWT blade aeroelastic investigations. With dimensions indicated in the domain.

The aerodynamic shape of the NREL 5MW wind turbine blade is well resolved in the CFD mesh, as shown in Figure 4-4, a tight spacing at the leading edge is applied to capture the curvature of the blade. Given that the local near wall velocity around the blades is varying during the dynamic simulation, especially when the blade flexible deformation is coupling the platform surge motions, a good quality inflation layer mesh is needed.

A well-tuned boundary layer mesh with prism layer cells is applied to the blade surface (Figure 4-5), where the first cell height on the blade surfaces is 0.002 m with an expansion ratio of 1.25. The blade wall y+ is checked and constrained within the range

of 30 to 300 to assure a reliable performance of the wall functions, so that the near wall flows and resultant forces can be properly predicted across all possible velocity profiles in our present load cases.

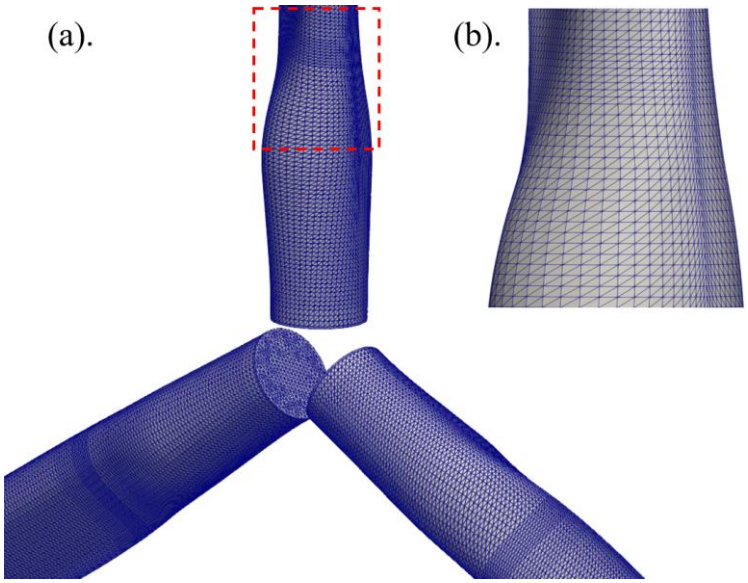

Figure 4-4. Leading edge spacing for curvature capturing. (a). the isometric view at the rotor centre; (b). the zoom-in view of the blade.

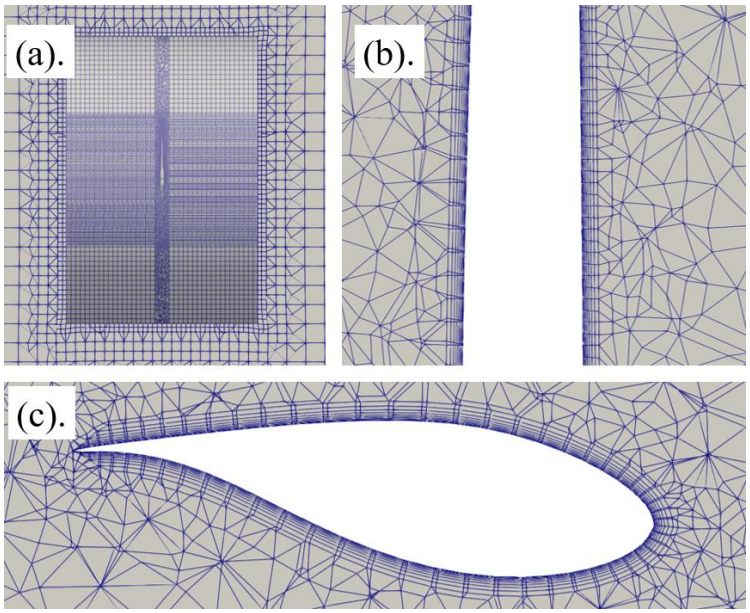

Figure 4-5. (a). Overall mesh from the side view; (b). the boundary layer mesh on blade spanwise direction; (c). the boundary layer mesh around the blade cross section.

An identical load case of surge amplitude As = 2 m and surge period Ts = 12 s with same initial flowing conditions is applied. For better clarity, the results in one complete normalised surge period are compared, reflecting the thrust and power history in time domain. As depicted in Figure 4-6 (a) and (b), the thrust and power in this study agrees well with literatures' on FSI and the FAST simulation results, where FAST (Fatigue, Aerodynamics, Structures, and Turbulence) is an open-sourced wind turbine system simulation tool developed by the NREL (Bonnie & Jason, 2016). The variations of the max. thrust between the present and two counterpart studies are 3.75% and 6.96%, respectively.

Additionally, in Figure 4-6 (c), the flapwise deflection at the blade tip within one surge motion period is also well agreed with the literature result, with a small difference between the max. deflection of approximately 4.41%.

The results shows that when exposed under the prescribed surge motion, the aerodynamic and structural responses of the blade can be well captured with satisfying accuracies.

The small discrepancies in max. quantities comparing to the FSI counterpart's results can be explained. First, the mesh configurations such as total cell number, wall y-plus distributions and transitions in cell size are different. Second, in the counterpart FSI study using CFD (Liu et al., 2019), the convective terms for the turbulence quantities k and ω were discretized using bounded schemes (flux-limited treatments), which can introduce additional numerical bounding to suppress unphysical overshoots but may slightly smooth out local peaks.

In the present study, the Gauss upwind scheme is employed instead, which has been verified in many existing literature and preliminary tests (Lee, 2018; Omidi & Baumann, 2025; Reid et al., 2025) to balance between numerical accuracy and efficiency. The implementation and theory of discretization and interpolation with different numerical schemes are comprehensively discussed and can be found in the work of (Jasak, 1996; Moukalled et al., 2015).

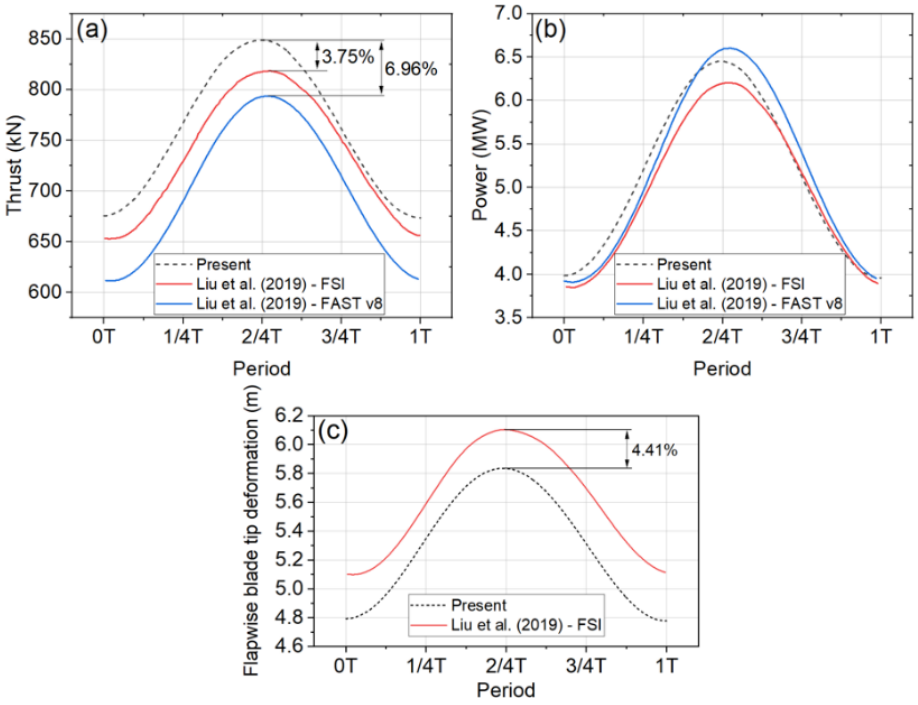

Figure 4-6. Validation of (a) thrust, (b) power and (c) flapwise blade tip deflection within one surge period for load case of As = 2 m, T = 12 s

4.3 Composite blade and FEA validation

Validations of the composite blade model and the modelling details are given in this section. The composite blade modelling process follows the detailed material definitions, layup distributions and composite stacking specifications as provided by Resor (2013) for the NREL 5MW reference wind turbine blade.

Based on the composite stacking configurations provided above, the blade FEA model is established in Abaqus CAE using the S4R element.

A mesh convergence study is firstly conducted by quantifying the influence of mesh to the resultant maximum Von Mises stresses magnitude under a uniform pressure load of 100 kN on the pressure surface of the blade as boundary condition.

Following the detailed instructions for the mesh convergence validation (Celik et al., 2008), three different mesh element sizes, namely the coarse, medium and fine meshes are tested for the blade FE model, with the stress results being shown in Table 4-5.

The grid refinement factor r is 1.95. The basis mesh size for the mesh convergence study is 0.1 m as this value is conventionally adopted in the literatures for blade FEA studies.

The numerical uncertainty for the predicted maximum Von Mises stresses on the medium mesh is $GCI_{fine} = 0.54\%$, indicated a small sensitivity of the resultant max. Von Mises stress to the change of number of elements in the mesh, therefore, the element size of 0.10 m is used in order to enable a balance of accuracy and computational efficiency.

Table 4-5. Mesh convergence study for blade FE model under a constant flapwise tip displacement load of 5 m.

	Element size (m)	**Number of elements**	**Max. Von Mises stress (Pa)**	**Diff (%)**	**GCI (%)**
Fine	0.0512	245019	1.1022E+09	/	/
Medium	0.10	63895	1.0970E+09	-0.47	GCI_{fine}=0.54
Coarse	0.195	17129	1.0870E+09	-1.38	GCI_{medium}=1.11

Then, the validated blade FEA model is established as depicted in Figure 4-7.

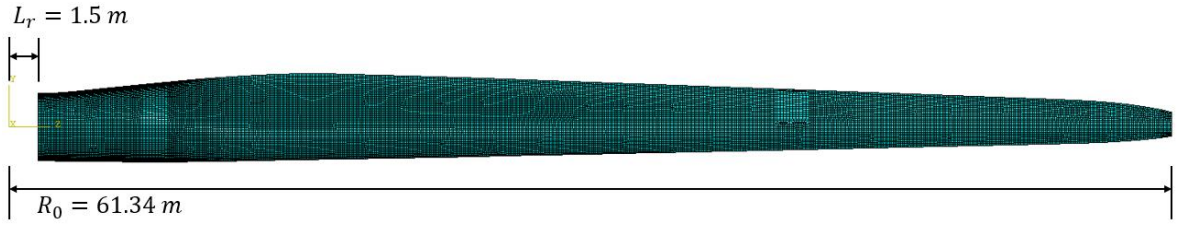

Figure 4-7. Blade finite element model established in Abaqus CAE.

Subsequently, the blade mass and mode of frequencies are validated as listed in Table 4-6 and Table 4-7, by comparing against the benchmark blade properties given by SNL.

This ensures the composite blade can provide reliable structural responses. The displacement response of the blade under the first to the sixth vibration modes are also depicted in Figure 4-8.

Table 4-6. Blade mass properties comparisons.

Descriptions	Desired	**Resor (2013)**	Present Model	Diff to desired values
Mass (kg)	17740	17700	17435.87	-1.71%
Mass centre* (m)	20.475	19.102	19.79	-3.35%
1st mass moment of inertia** (kg m)	3.63E+05	3.38E+05	3.45E+05	-5.00%
2nd mass moment of inertia** (kg m^2)	1.18E+07	1.10E+07	1.11E+07	-5.74%

Note: *. Locate on blade spanwise direction; **. With respect to the rotation centre of the blade

Table 4-7. Modal frequency comparisons.

Mode #	Frequency (Hz)		Diff	Description
	Ansys (Resor, 2013)	Present		
1	0.87	0.86	-0.77%	1st flapwise bending
2	1.06	1.10	+3.79%	1st edgewise bending
3	2.68	2.72	+1.38%	2nd flapwise bending
4	3.91	3.94	+0.75%	2nd edgewise bending
5	5.57	5.51	-1.00%	3rd flapwise bending
6	6.45	6.36	-1.40%	1st torsion

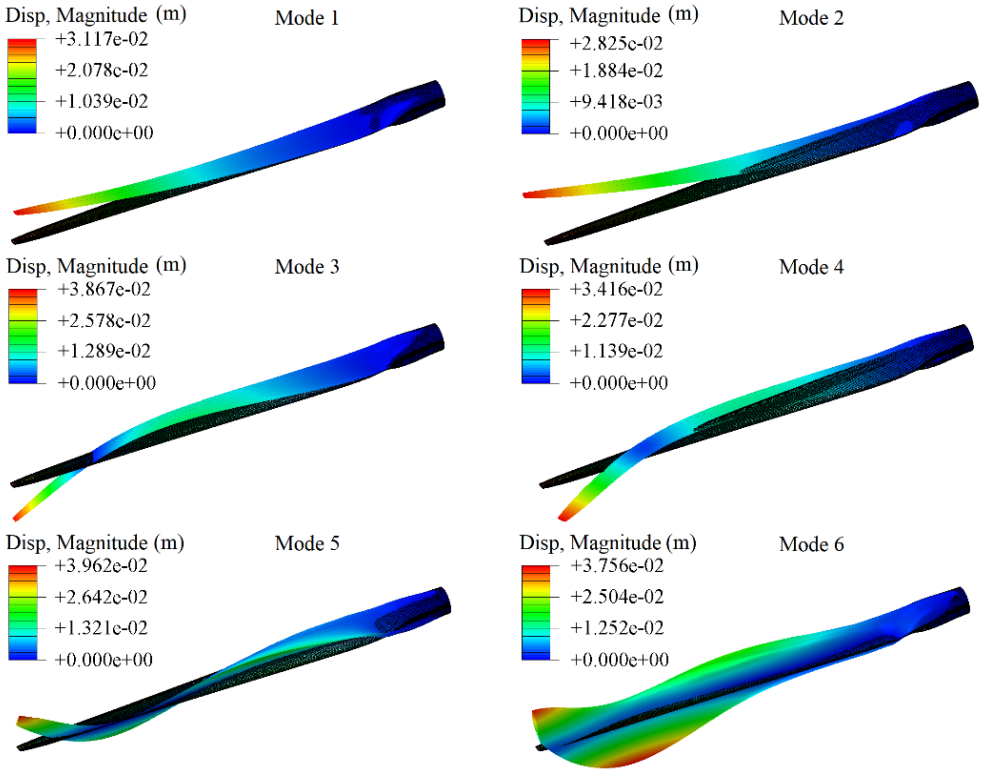

Figure 4-8. Modal shapes (1-6th modes) of the composite blade FE model, with displacement magnitude contours.

In addition, to evaluate the mesh sensitivity to the potential singularity issue, the second mesh convergence study is also conducted when the explicit direct displacement boundary condition is applied to the model. This sub-task is relevant with the case study that has been presented in Section 5.3.2.

The designated displacement boundary condition can be retrieved from the Section 5.3.2, where we applied the identical displacement responses (solved under the aerodynamic condition IEC DLC 6.1) to the blade FEA models with an increasing number of elements. The resultant maximum Von Mises stress being depicted in Figure 4-9.

A clear convergence of the responding maximum Von Mises stress is observed, which is also justified by the converging stress deviation as the number of elements increases. This confirms that the mesh resolution employed in the subsequent simulations is sufficient to capture the stress distribution accurately and is free from the numerical singularity effects.

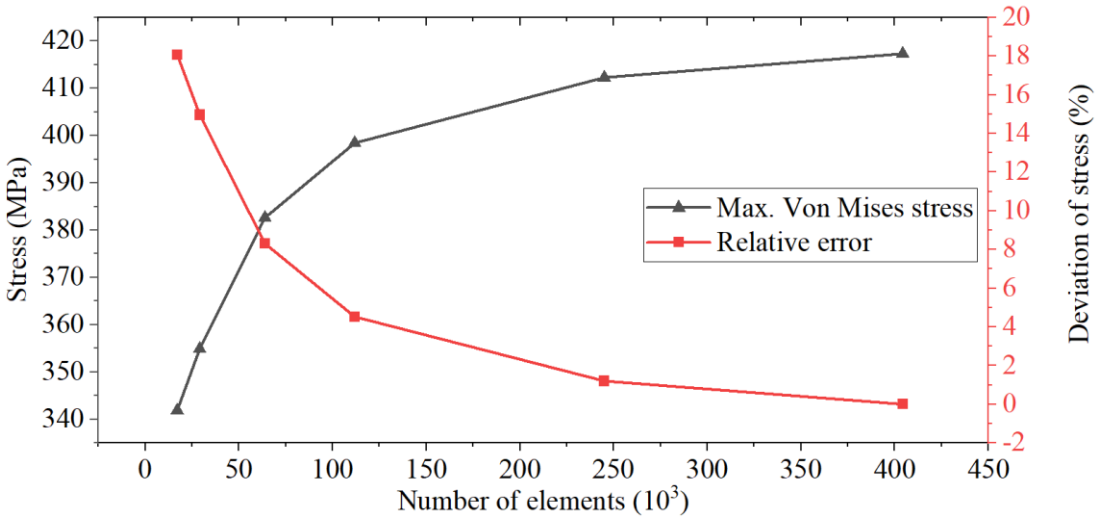

Figure 4-9. Max. Von Mises stress responses on the meshes with different number of elements. Explicit displacement loads are applied.

4.4 Validations of the stress field recovery procedure – a case on a composite tube

As the key step for resolving the stress fields on general composite structures in FEA, it is necessary to justify the validity and applicability of the proposed field recovery procedure.

In this section, a validation study using a simple cylindrical tube geometry is conducted, comparing the static structural response and the stress fields between a FEA shell model and a MBDyn beam element model, demonstrating the consistency of two codes in predicting structural responses.

As depicted in Figure 4-10, the length of the tube $L = 61.5\ m$, with a diameter of $d = 5\ m$ are assigned which resembles a similar scale of the wind turbine blade. The tube is partitioned into 25 sections in both MBDyn and Abaqus FE models for the convenience of the boundary conditions assignments. The exact locations of the partitions are given in Table 4-8.

Note that the number of partitioned sections can be further increased if the load condition or the geometry is expected to be complicated.

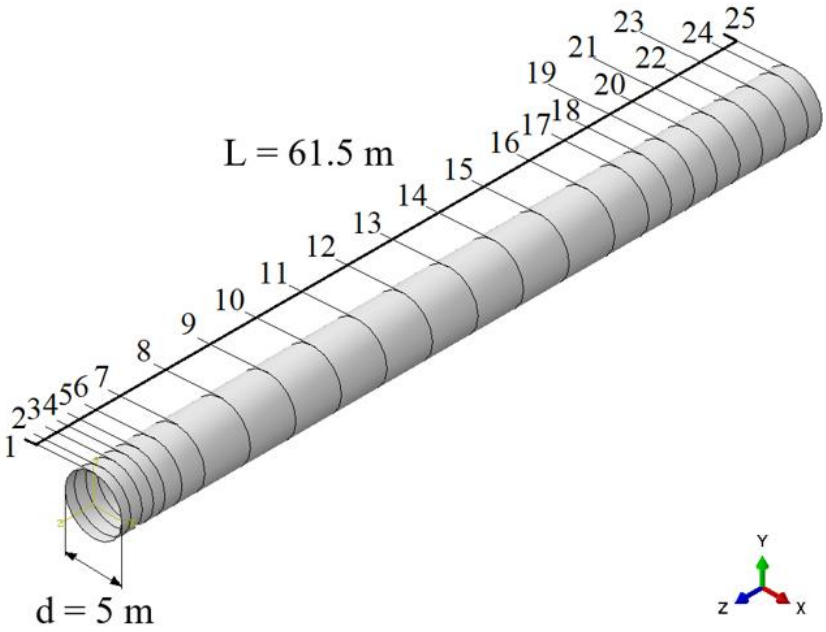

Figure 4-10. Tube dimensions and partitions.

Table 4-8. Locations of partitioning nodes for both tube FEA and MBDyn models.

Partitioning Nodes ID	Location on Z-direction (m)	Partitioning Nodes ID	Location on Z-direction (m)
1	61.5	14	26.2
2	60.7	15	22.2
3	59.7	16	18.2
4	58.7	17	15.2
5	57.7	18	13.2
6	56.2	19	11.2
7	54.2	20	9.2
8	50.2	21	7.2
9	46.2	22	5.2
10	42.2	23	3.2
11	38.2	24	1.2
12	34.2	25	0.2
13	30.2		

The schematic diagrams of the FEA and MBDyn tube models are given in Figure 4-11 for better understanding of the problem. First, the tube FE model is established in Abaqus.

The glass and carbon fibre laminates configured in a ± 45 degrees orientation are applied on the tube, where the laminate stiffness properties are specified in Table 4-9. An even thickness of t = 0.047 m is assigned for each laminate, uniformly distributed along the tube model.

Subsequently, the tube model is established in MBDyn, where the sectional effective stiffness matrices (ESMs) are calculated using VABS for defining the stiffnesses on the MBDyn beam model, which is given in Table 4-10.

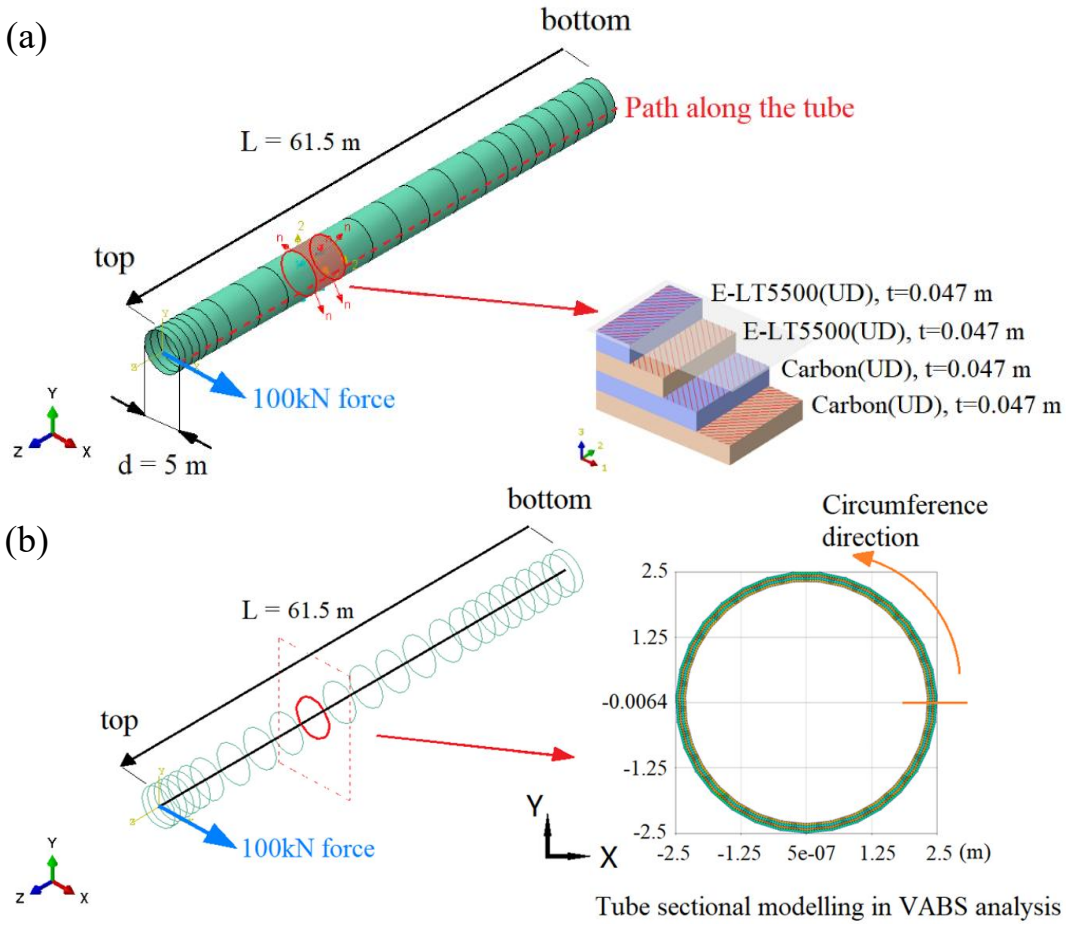

Figure 4-11. Diagrams of (a) tube model in FEA showing the composite layups and (b) tube model in MBDyn, equipped with ESMs from VABS analysis.

Table 4-9. Composite laminate stiffnesses defined in FEA model.

Properties	**Lamina**	
	E-LT5500(UD)	Carbon(UD)
E1	4.1800E+10	1.1450E+11
E2	1.40E+10	8.39E+09
Nu12	0.28	0.27
G12	2.63E+09	5.99E+09
G13	2.63E+09	5.99E+09
G23	5.4688E+09	3.3032E+09

Table 4-10. ESM of the composite tube in diagonal form for MBDyn model.

Extension Stiffness-EA (Pa)	torsional stiffness-GJ (Pa)	Principal bending stiffness-EI22 (Pa)	Principal bending stiffness-EI33 (Pa)	Principal shear stiffness-GA22 (Pa)	Principal shear stiffness-GA33 (Pa)
4.1813E+10	2.9959E+10	2.9959E+10	3.5083E+11	1.2211E+11	1.2211E+11

The boundary conditions (BCs) are specified and depicted in Figure 4-11 (a) and (b). A concentrated constant force of 100 kN on X direction is applied at top node of the tube.

A fixed BC is applied locking all nodal DOFs on the bottom of the tube. A Path containing a series of nodes of interest is defined for plotting the flapwise displacement distributions along the tube, denoted in red dash line.

The flapwise displacements predicted by Abaqus and ESMs-equipped MBDyn are firstly compared. As shown in Figure 4-12, the flapwise displacement distributions predicted by both solvers agrees well with each other, this consistency indicates the 3D composite structural properties of the tube can be accurately preserved by the ESMs-equipped 1D beam model in MBDyn, providing close predictions of structural response as it would perform in a FEA model.

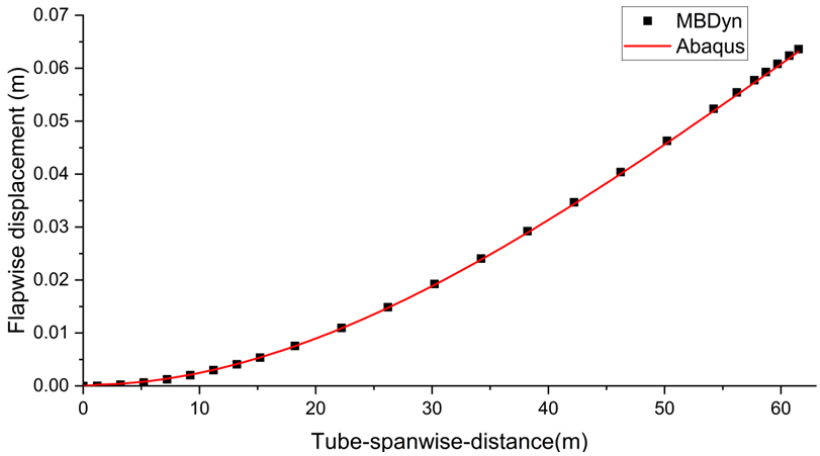

Figure 4-12. Comparisons of flapwise displacement distributions on the Path predicted by Abaqus FE model and MBDyn beam model.

Next, Figure 4-13 (a1) shows the stress field directly solved in FEA model with the defined top concentrated force and fixed bottom BC. Also, Figure 4-13 (a2) displays the recovered stress field solved by displacement BCs that are calculated by the MBDyn.

For better clarity, the stress fields on a cylindrical tube are unfolded and flattened for comparison. The horizontal axis denotes the percentage of the circumference of the unfolded tube, beginning at the middle left of the cross section, with an anti-clockwise precession to complete a full cycle of the circumference, as denoted in Figure 4-11 (b).

Indicated in Figure 4-13 (a1), the stress concentration locates at the bottom of the tube where the distance on Z direction is 1.282 m, at the circumferential locations of 0% and 50% that are symmetrically distributed.

A rapid stress gradient variation is found around the stress concentration location. In the stress field resolved by the displacements, as shown in Figure 4-13 (a2), the stress concentration is found to be located in the similar region at the bottom of the tube. The stress distribution in both stress fields performs similar in the region where the tube spanwise distance $l > 10\ m$.

An underestimation of Von Mises stress concentration is found, as shown in Figure 4-13 (b), where a deviation of predicted maximum stress of both stress fields is $\Delta\sigma_{max} = 14\ \%$.

Given that the stress fields are solved with different boundary conditions through different procedures, it is inevitable that certain discrepancies would arise in two stress distributions.

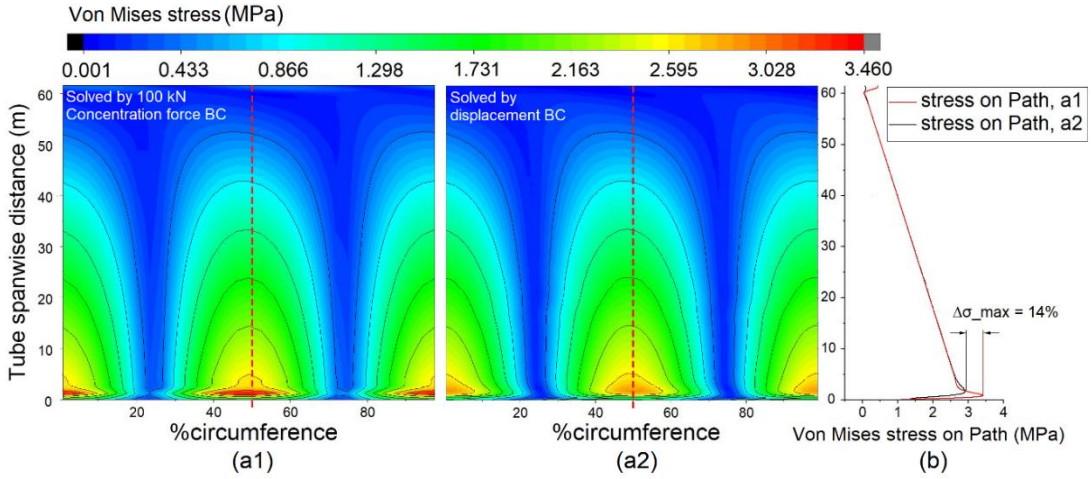

Figure 4-13. Von Mises stress contours on the unfolded cylinder surface, solved by (a1) Abaqus –stress field resolved under the 100 kN concentration force; (a2) Abaqus – stress field resolved under displacements acquired from the ESMs-equipped MBDyn; (b) Comparison of the Von Mises stress distributions along the Path.

From the comparisons, it is validated that the stress field can be accurately recovered using the proposed mapping approach. The disparity of the maximum Von Mises stresses magnitudes between two stress fields remains in an acceptable range, with a reasonable agreement in stress distributions on the Path along the tube.

This justifies that the proposed FSI framework is feasible to obtain the stress distributions on a composite structure as demonstrated on a tube model.

It is anticipated that, by increasing the number of partitioned sections at the location of stress concentration, the maximum stress deviation could be further mitigated and perform better in capturing the rapid stress gradient around the stress concentration location.

Chapter 5 A General FSI Framework for Effective Composite Blade Aeroelastic Analysis

5.1 Overview

In this chapter, the aero-elastic behaviours of the composite blade on the bottom-fixed NREL 5MW wind turbine are firstly analysed. Two case studies of different load cases are conducted for the composite blade on the NREL 5MW wind turbine, where in Case 1, the IEC extreme design load case (DLC) 6.1 condition is examined, then, in Case 2, a rated operation condition is analysed.

The outcomes of this work provided quantified evidence of the accuracy and effectiveness of the proposed FSI analysis framework, which will serve as the basis for future composite blade aeroelastic investigations under the FOWT conditions.

5.2 Model Description

The full-scale NREL 5MW wind turbine blade mesh in CFD model is generated using the snappyHexMesh meshing utility. The tower and nacelle are not included in the model to minimise the complexity of the mesh. In the blade CFD mesh, the blade precone and pitch angle, and the rotor axial tilt angle are set to zero degree.

The centre of the rotor is placed at the coordinate origin (0, 0, 0) in the global system as shown in Figure 5-1. The domain dimensions on X, Y, and Z directions are ranged from -1.5D to 1.5D, where D=126 m is the diameter of the rotor.

The blockage effect is neglected as the inlet and all the side boundaries are treated as the uniform velocity inlet condition, enclosed by the outlet where a zero-gradient pressure condition is applied.

Worth mentioning that in this study, the CFD mesh is different from the one used in Chapter 6 and 7. In this study, a regional refinement is implemented in the rotating cell zone to assure a proper capture of the flowing behaviours. In the near wall region, a boundary layers y^+ in a range between 30 and 300 is assigned, so that the wall

functions are applied to account for the viscous flow in the boundary layer. The characteristic cell size is Δd = 0.0625 m to properly resolve the curvature on the blade surface, as illustrated in a blade cross section view in Figure 5-1 (b). The resultant total number of cells is 13.1 million.

The specifications of boundary conditions applied in both cases are illustrated in Figure 5-1 (d). To balance between the numerical accuracy and efficiency, considering a rated operation conditions (rotor speed is 12.1 RPM), the time step size for both cases was defined to 0.36 degree of rotation per time step, i.e. approximately 0.005 s. It has been tested that a larger time step would lead to numerical instability at the beginning of the simulation, or cause divergence issues.

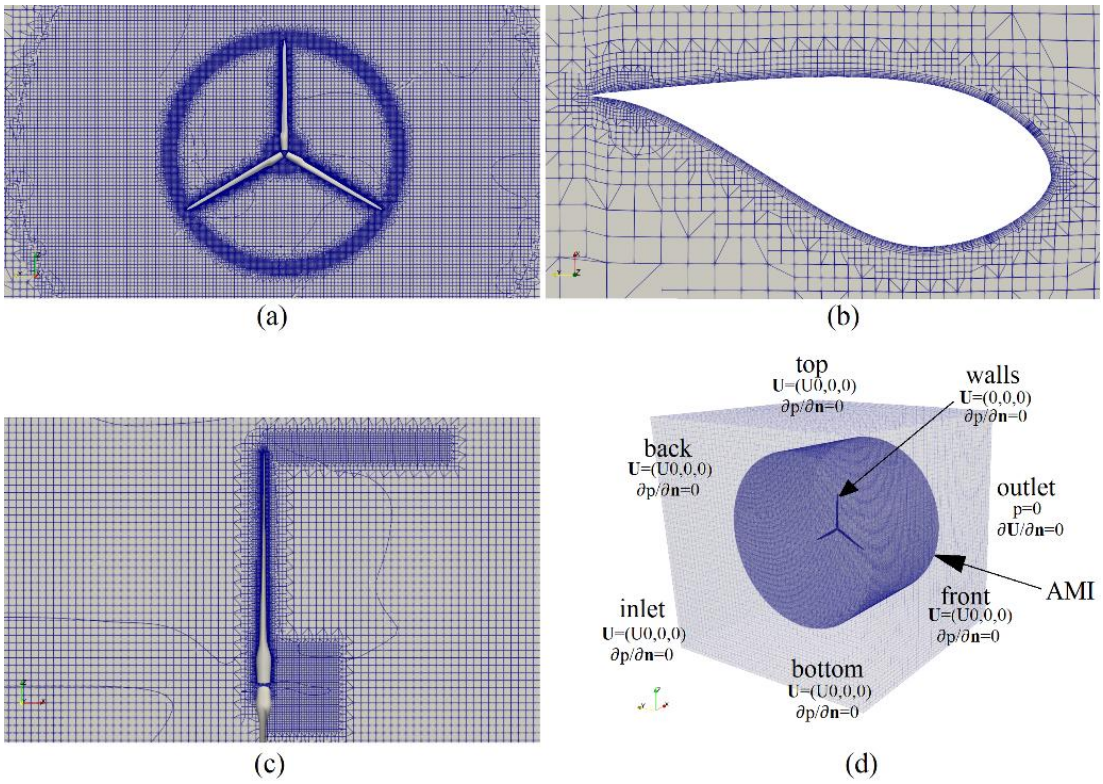

Figure 5-1. CFD domain. From (a) X; (b) Z; (c) Y view and (d) the overall mesh.

For the structure participant, as previously mentioned, the multibody dynamics code MBDyn serves as the structural participant in the FSI process, where 24 interconnected 3-node beam elements are used accounting for the elasticity for each blade, i.e. 49 nodes are used for each blade. Additionally, 2 nodes situated at the rotor centre and the fixed ground. This gives a total number of structure nodes of 149 for the rotor.

5.3 Simulation Results – Case 1

The IEC DLC 6.1 accounting for a 50-year wind state extreme condition (DLC 6.1) is firstly analysed (Resor, 2013; Miao et al., 2019). The free-stream velocity of air $U0 = 50\ m/s$, which leads to a blade characteristic Reynolds number of Re = 2.1e+08.

Under the cut-out condition of the wind turbine, the rotor angular speed is zero. In Case 1, the instantaneous fluid and structural results focusing at the moment when the blade reaches to its maximum flapwise displacement are analysed in the following sections.

5.3.1 Fluid field results

The detailed CFD results of kinematic pressure and velocity fields on global X direction are shown in Figure 5-2 and Figure 5-3, respectively. The kinematic pressure field p of an incompressible fluid problem is defined as follows, where p_s is the static pressure, and ρ is the fluid density:

$$p = \frac{p_s}{\rho} \tag{5.1}$$

Due to the flow stagnations, a higher pressure occurs on the upstream as the flow approaches to the blade surface, then, a low-pressure region forms on the downstream of the blade, spans from the blade tip to the blade transitional area, where the blade cross section shape is transitioning from circular shape to DU-series airfoils (Resor, 2013), as illustrated in Figure 5-2 (b).

The local maximum pressure gradient occurs at the blade transitional area. This is likely due to the local rapid change of the blade geometrical shape, a significant flow separation is easier to occur in this area. The streamline plot of the velocity field on X direction justifies the existence of this flow separation phenomenon as illustrated in the streamline plot in Figure 5-3 (b).

In fact, a low pressure region distribution is observed along the blade, where a swirl structure is formed on the blade downward side and gradually becoming more prominent as it reaches to the blade transitional area of position B.

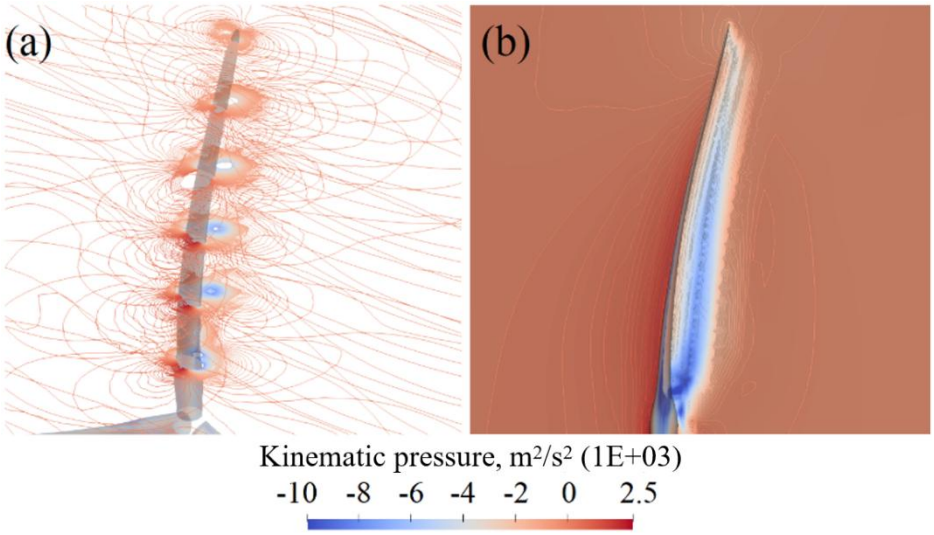

Figure 5-2 Kinematic pressure contours (a) around the blade, and (b) side-view using a slice plane.

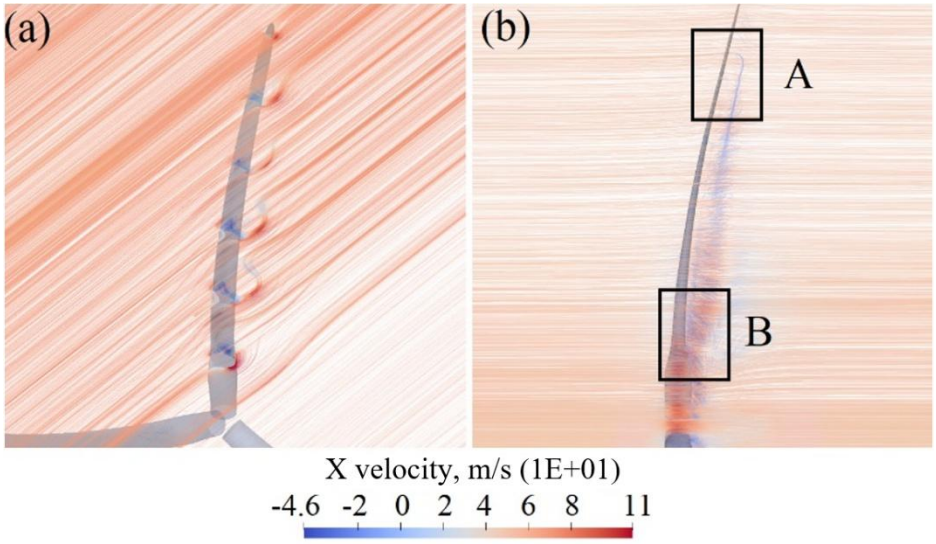

Figure 5-3 X velocity field (a) around the blade, and (b) side-view with streamlines

The distribution of aerodynamic thrust (black curve) and the blade flapwise aerodynamic moment are shown in Figure 5-4. Due to the non-uniform shape and dimension variations of the blade profiles, the thrust is not prominent at first due to the cylindrical profile in this blade region, while it becomes larger till the blade transitional sections and reaches to the max. thrust per unit length due to the blade's local widest projection area with respect to the incoming freestream. Then, as the blade span increases till the tip, the thrust gradually reduces.

At the blade spanwise distance of $r/R = 0.17$, a global maximum aerodynamic thrust of approximately 42000 N/m is observed, which is related to a larger cross section chordwise dimension in this blade region. Then, as it further spans to the blade tip, the thrust magnitude decreases.

The flapwise moment on the blade is calculated by firstly multiplying the thrust with the blade sectional spanwise distance r, and then compute the integral of moments from the blade tip to the root.

It can be seen that the maximum flapwise aerodynamic moments locates at the root of the blade of approximately 15400 $kN \cdot m$, indicating that the fluid imposes a significant bending moment onto the blade structures.

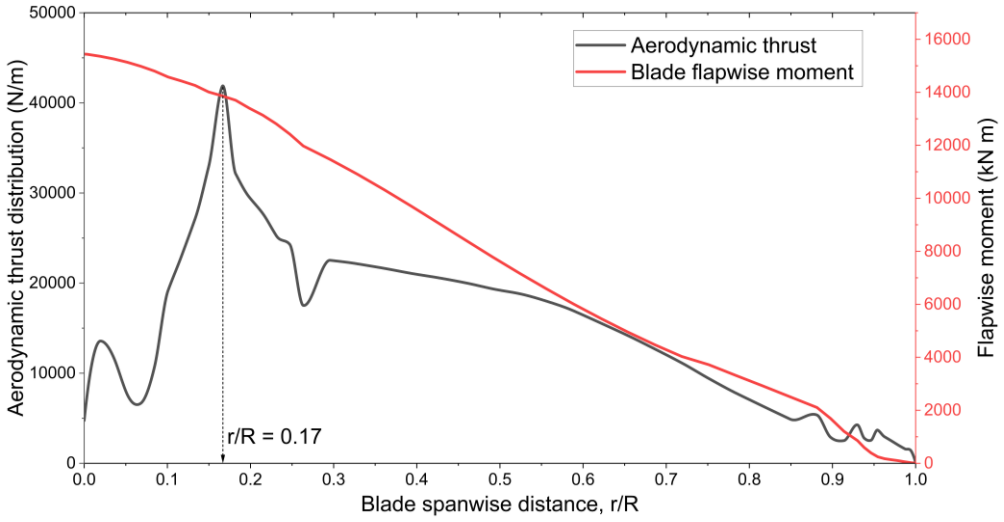

Figure 5-4 Blade aerodynamic thrust distribution and the blade flapwise moment, under DLC 6.1 condition

5.3.2 Stress analysis and comparison

The stress field on the composite blade FE model is established and compared with the results from Miao et al. (2019), where the blade structural dynamics responses from a direct CFD-FEA two-way FSI process are provided.

Worth being noted that the present blade dynamic responses are solved with stiffness properties given by NREL official document (Jonkman et al., 2009), which differs

from the stiffness properties performed in Miao's study. Due to the absence of available studies that performs FSI analysis with a fully resolved composite material blade, our comparison is a promising attempt that quantifies the difference of aeroelastic predictions using the present approach of FSI analysis and other methods from the open literatures.

The blade dynamics are firstly analysed to assure the accuracy of the stress field. In Figure 5-5 (a), the blade maximum tip flapwise displacement is 9.25 m, with a deviation of -9.4% comparing with the results from Miao et al. (2019) of 10.21 m. The present edgewise and spanwise tip displacements are -3.35 m and -1.08 m, respectively.

As shown in Figure 5-5 (b), the maximum rotational displacement (Euler orientation angle) about the X, Y and Z axis are 0.094, 0.257 and -0.115 radians, respectively. A prominent deviation is observed for the twist angle predictions between the present and Miao et al. (2019), where the maximum twist angle about Z axis is -0.201 radians in Miao's result.

A reasonable agreement is achieved for the comparisons of blade displacement along X direction. This is because the blade shear webs layup are the same in both studies, so that the bending stiffness properties perform similar in terms of enduring the flapwise aerodynamic bending moments.

However, the stiffnesses of the blade surfaces composite structures in two studies are not entirely identical due to the nuance in blade FEA modelling, therefore, it is reasonable to observe discrepancies for the blade twisting behaviour as the torsion stiffnesses are primarily affected by the composite structures on the blade surfaces.

Besides, different numerical processes of FSI procedures are adopted for solving the complex blade structural dynamics, which may also explain such disparities.

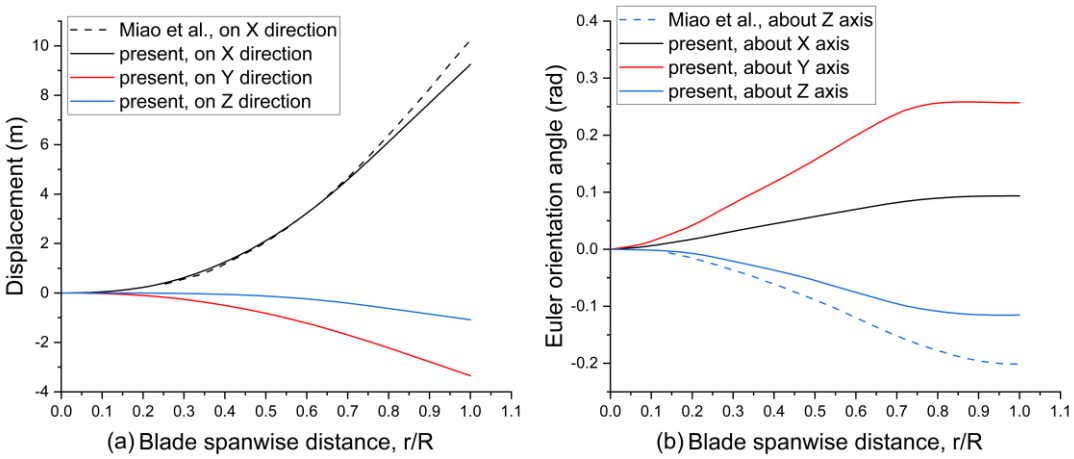

Figure 5-5 Blade (a) displacements and (b) Euler orientation angles on the blade section aerodynamic centre, under global coordinate system

The contours of displacement fields are displayed in Figure 5-6. From sub-figure (a) and (b), the flapwise and edgewise maximum displacement are +8.830 m and -3.198 m, respectively, occurring at the tip of the blade.

A blade in-plane bending response is observed from Figure 5-6 (c), which indicates an occurrence of the strain imbalance where the blade surface in the trailing edge is under tensile loading condition, while the leading edge is experiencing compression loads on spanwise direction.

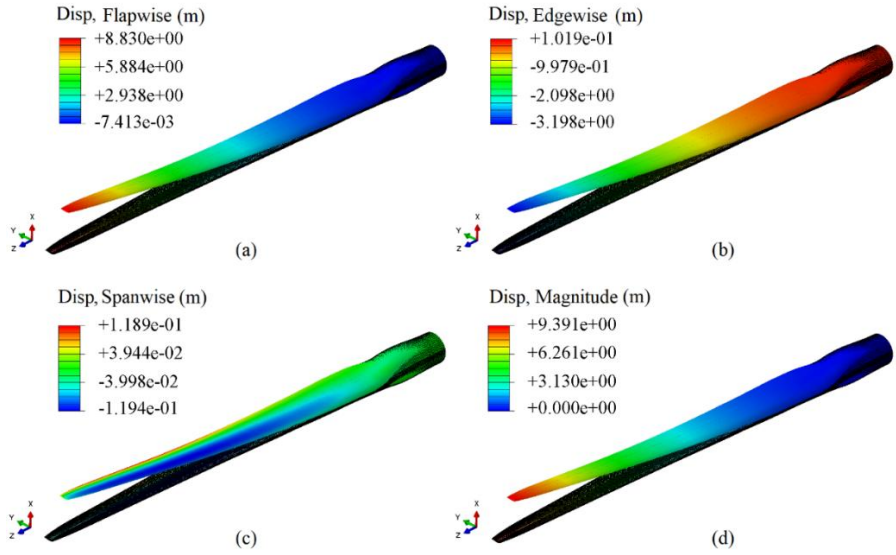

Figure 5-6 Translational displacement contours of (a) flapwise, (b) edgewise, (c) spanwise, and (d) displacement magnitude on the composite blade FE model.

As analysed previously, the blade transitional region is exposed under a severe aerodynamic drag, causing an accumulated aerodynamic moment especially in the blade transitional areas.

Figure 5-7 (a) shows the resolved stress field on the composite blade. The stress concentration with a maximum Von Mises stress of 3.832E+08 Pa occurs in the blade root LE_Panel region on the blade suction side, at the spanwise distance of $r/R = 0.189$ from the centre of the rotor.

The concentrated stress comparisons with the literature are listed in Table 5-1, the maximum Von Mises stress concentration from the literature is 3.964E+08 Pa, occurs at the spanwise distance of $r/R = 0.172$.

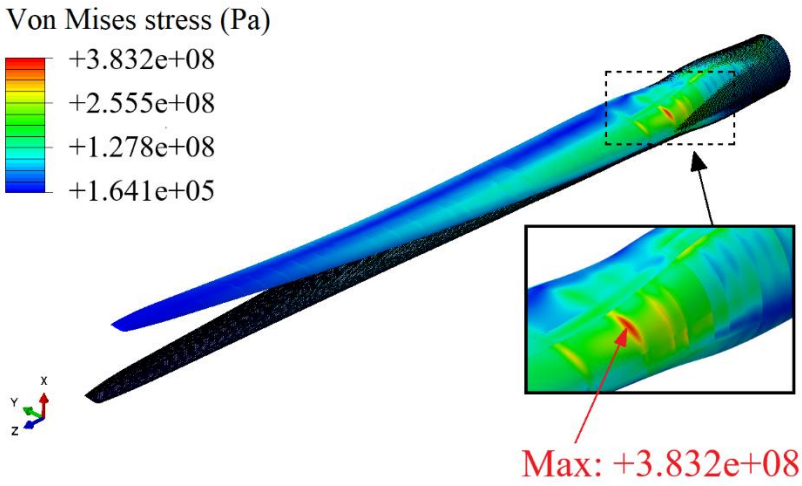

Figure 5-7. Von Mises stress field contour on the composite blade surface in Case 1.

Table 5-1. Von Mises stress comparisons of the composite blade in Case 1.

	Max Von Mises stress (Pa)	**Location on blade spanwise, r/R**
Present study	3.832E+08	0.189
Miao et al. (2019)	3.964E+08	0.172
Diff	-3.33%	+10.33%

To examine the stress distribution more clearly, a Node Path is defined by the intersected edge of the shear web and the blade suction surface. The stress distribution

with a local concentration in the blade transitional area can also be observed from Figure 5-8.

An oscillating stress and thickness plots are observed. This reflects a highly nonlinear pattern due to the non-uniform distributions of composite layups and stacking thickness along the blade.

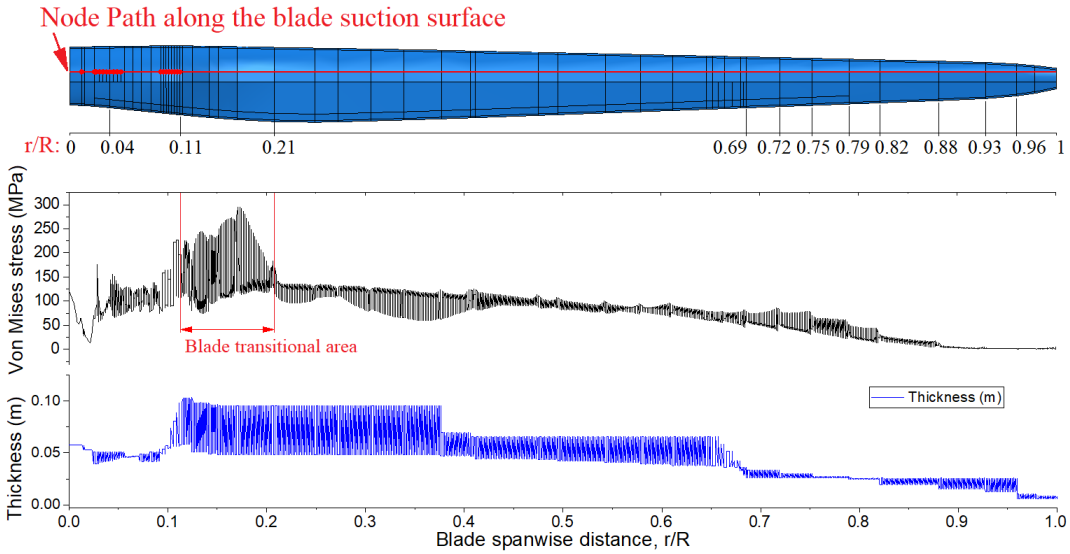

Figure 5-8. Von Mises stress and blade shell thickness distributions along the Node Path on the blade for Case 1.

Besides, the banded pattern of the plot is seen due to the sharing integration point located on the Node Path. For a better understanding to the cause of such banded plot, an example of the local inspection to the cross-section location (r/R = 0.2) on the Node Path is depicted in Figure 5-9. It can be seen that the measured local shell thicknesses on the Node Path are 0.04799 m and 0.09569 m for the Spar cap and TE_Panel region, respectively, where these are exactly reflected by the lower and upper bounds of the banded thickness plot.

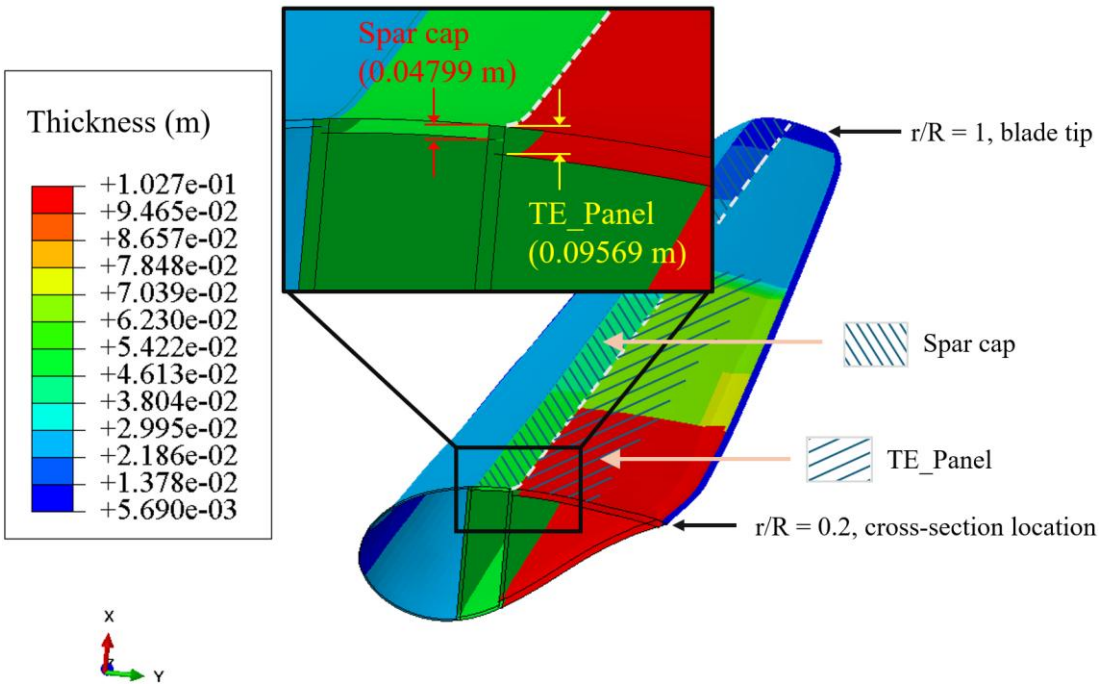

Figure 5-9. Illustration of thicknesses on the Node Path for both Spar cap and TE_Panel.

5.3.3 Computational cost allocations

The present study of Case 1 is conducted using the Cirrus HPE/SGI ICE XA Cluster standard computing service, equipped with the 18-core Intel Xeon E5-2695 (base frequency 2.1 GHz).

For parallel computing, the CFD simulation job in the FSI analysis uses 252 cores with 172 hours assigned to achieve the quasi-steady state (converge in field quantities) of the simulation.

Comparing with a conventional surface-to-node (between CFD and FEA) interpolation as conducted by Miao et al. (2019), the proposed FSI framework has shown a significant reduction in computational costs by 24.75% in terms of core-hours, as detailed in Table 5-2.

Through the comparison, it has demonstrated that the proposed FSI framework is much more efficient in computational terms comparing with the direct CFD-FEA FSI

coupling approach. Meanwhile, it is still capable of providing detailed structural insights into the composite blade structures at an equivalent level of fidelity.

Table 5-2. Comparisons of computational costs for FSI analysis between the present study and literature.

	No of CPU cores	**Physical time (h)**	**Total core-hour to reach convergence**
Present study	252	172	43344
Miao et al. (2019)	96	600	57600
% reduction	/	/	–24.75

5.4 Simulation Results – Case 2

In Case 2, a FSI analysis is conducted for the composite wind turbine blade with a bottom-fixed configuration, where the rated operation condition is replicated defining a constant rotating angular speed of ω=12.1 rpm for the blades (rotor), and the freestream velocity $U0$ =11.4 m/s for the incoming flow. This leads to a tip speed ratio (TSR) of λ=7 is being analysed in Case 2.

5.4.1 Fluid field analysis

Due to the coupling of blade local deformation and global rotation motions, a significant blade nonlinear aerodynamic performance is anticipated.

Taking the advantages of the high-fidelity CFD in the proposed framework, we will present the simulated wake vortex structure of the rotor in relation to the time-averaged rotor aerodynamic thrust and pressure coefficient distributions along the blade.

Table 5-3 compares the converged aerodynamic thrust predictions among the present study and other literatures that uses the same blade geometrical configurations and operation conditions, showing that the thrust is reasonably predicted in our simulations (Yu & Kwon, 2014; Dose et al., 2018; Liu et al., 2019).

Table 5-3. Thrust comparison for the NREL 5MW wind turbine under rated operation condition.

Flexible blade FSI studies	Thrust (kN)
Present study	682.5
Yu and Kwon (2014)	656.4
Liu et al. (2019)	733.0
Dose et al. (2018)	771.3

As illustrated in Figure 5-10, a formation of vortex on the blade is observed, suggesting an active flow separation with an intensive transient flowing interaction occurred, especially in the local blade root and tip regions. The contour of q-criterion = 0.05 shows the visual boundary of the vortex, mapped with flow velocity on X direction. The q-criterion describes the relationship between the local vorticity and fluid shear strain and determines the vortical regions in the flow field based on the second invariant of the rate of strain tensor Q.

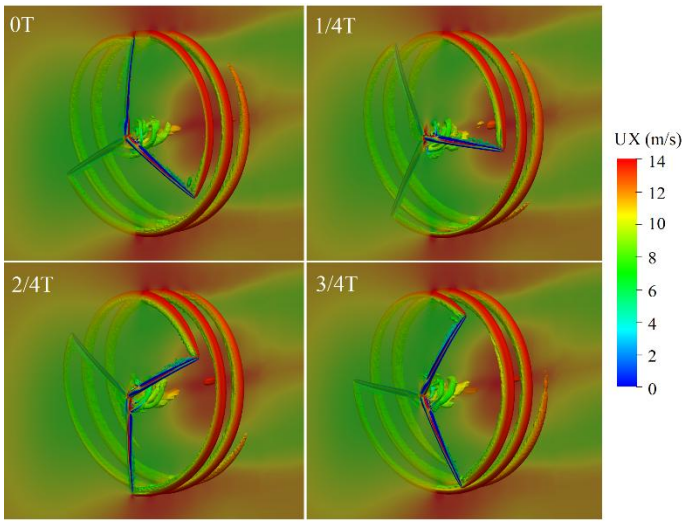

Figure 5-10 Instantaneous vortex structures, illustrated by the iso-surface of q-criterion = 0.05 in a complete rotation cycle, mapped with fluid velocity on X direction.

Figure 5-11 illustrates the aerodynamic thrust distributions on the blade 1 at four moments, where the results perform quite similar due to the fully developed flow around the blade during a stable rotation. Meanwhile, a rapid decrease of the local

thrust is also observed in the blade tip region where the spanwise distance ranges from $r/R \in (0.9, 1)$.

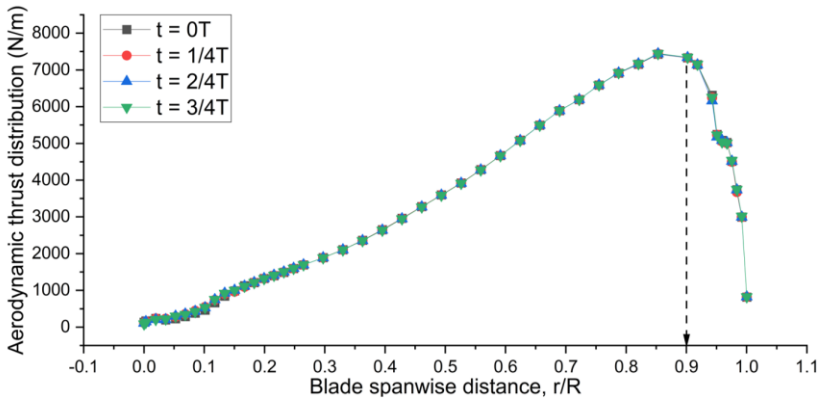

Figure 5-11 Blade spanwise aerodynamic pressure loads during the stable rotation cycle, under the rated operation condition.

The streamlines of the fluid X velocity distributed along the blade depict the evolution of such flowing degradation as it spans to the blade tip region. As shown in Figure 5-12, as approaching to the blade tip from the blade span of $r/R = 0.15$ to 0.9, a negative X velocity field gradually becomes significant on the blade suction side near the trailing edge of the blade cross section, indicating the occurrence of a significant flow detachment.

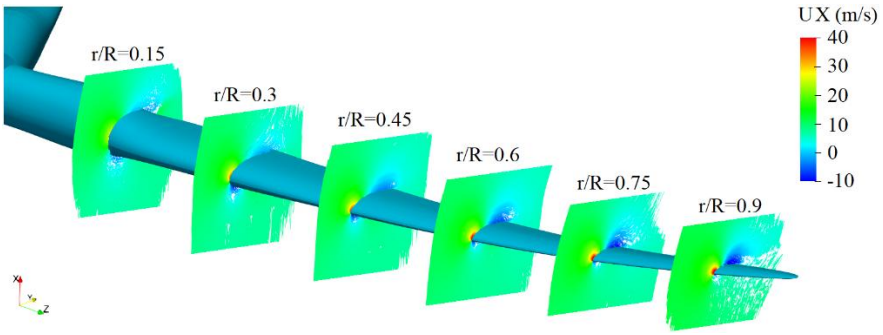

Figure 5-12 Streamlines of the instantaneous velocity fields on global X direction (UX) at $t = 0T$, evenly distributed along the blade spanwise of $r/R \in (0.15, 0.9)$

The pressure contours and coefficient distributions on three blade cross sections at r/R = 0.3, 0.6 and 0.9 are presented in Figure 5-13, which further evident the occurrence

of flow separations as is spans to the blade tip. The definition of pressure coefficient C_p is formulated as:

$$C_p = \frac{p_0 - p_\infty}{0.5\rho\left[{U_0}^2 + (\Omega_0 r)^2\right]} \tag{5.2}$$

where p_0 is the local static pressure at the blade cross section; p_∞ is the reference pressure which is zero pascal in the present study; ρ is the air density; U_0 is the free stream velocity; Ω_0 denotes the rotating angular speed; and r stands for the local spanwise distance of the cross-section airfoil along the blade.

It can be seen from the pressure contour at cross section $r/R = 0.9$, a negative pressure region with adverse pressure gradient is formed near the leading edge on the suction surface of the blade, while it becomes less prominent for the local pressure at $r/R = 0.6$ and 0.3 as the spanwise distance decreases, towards the root of the blade.

The non-dimensional pressure coefficient C_p distributions on three cross sections are displayed accordingly. Illustrated by comparing the C_p distributions of the blade cross sections at $r/R = 0.6$ and 0.3, that the local thickness and the shape of the blade cross section may significantly affect the magnitude of blade C_p distribution.

The changing pressure distributions at the leading and trailing edges on the blade cross section profile would result in different local aerodynamic moments, with respect to the local aerodynamic centre of the blade profiles.

Therefore, the twist moment of blade sections along the spanwise direction could perform unevenly, so that a persistent non-uniform twist moment is imposed to the blade, which may lead to further structural instabilities of the blade due to the dynamic load balancing between the structure and fluid fields.

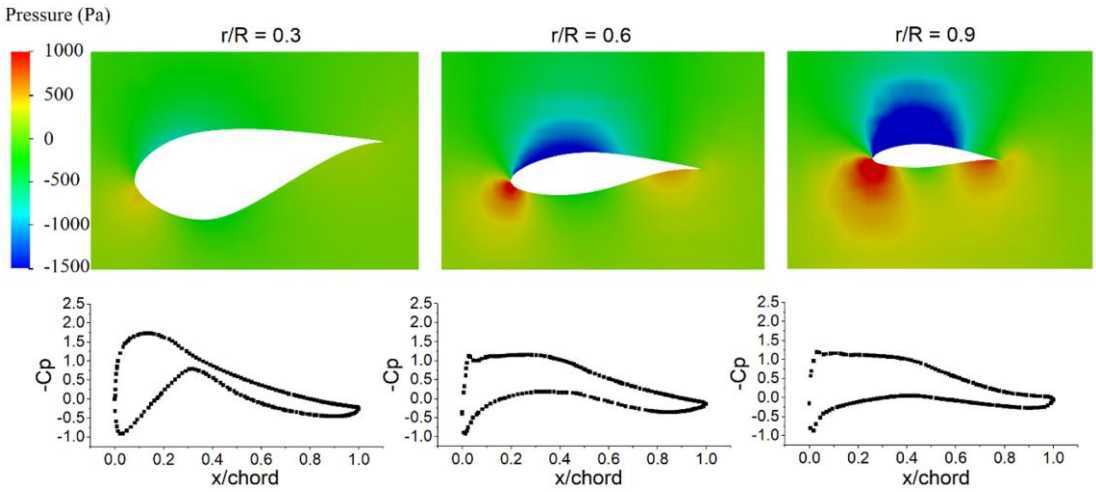

Figure 5-13 Pressure coefficient distributions on the spanwise distances cross section airfoils of *r/R* = 0.3, 0.6, and 0.9. At $t = 0T$ within a complete rotation cycle.

5.4.2 Blade dynamics and stress analysis

To analyse the stress field on the blade, as depicted in Figure 5-14, four blade azimuth positions of $\alpha = 0°$, $90°$, $180°$ and $270°$, during one stable rotation are identified, at corresponding moments of $t =$ 0T, 1/4T, 2/4T and 3/4T, respectively. For simplicity purpose, the dynamics response of blade 1 will be used as the representative to extract the translational and rotational displacements as the boundary condition for establishing the stress fields. Noted that three local coordinate systems following the right-hand rule are also depicted in Figure 5-14 for each blade in the global system.

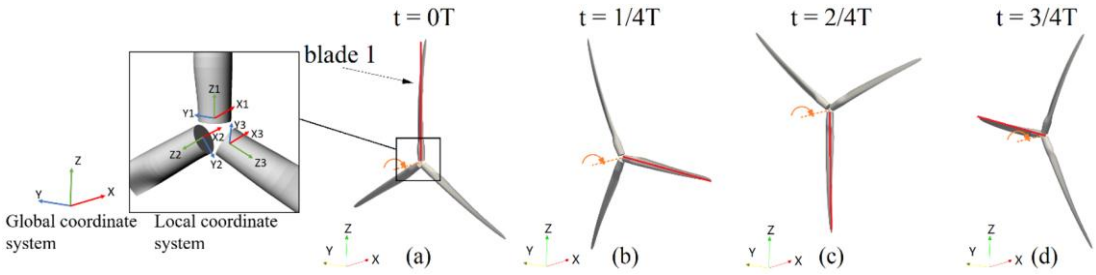

Figure 5-14 Four blade key positions (marked in red) for examination of stress fields, at (a) maximum tip displacement position; initial azimuth position of (b) $\alpha_1 = 0°$; (c) $\alpha_2 = 90°$; (d) $\alpha_3 = 180°$; and (e) $\alpha_4 = 270°$.

Due to the periodic aerodynamic loads and gravitational effects to a rotating blade structure, a symmetrical blade deforming distribution pattern is captured in the blade's

deformations on Y and Z direction, as presented in Figure 5-15 (a2) and (a3). The blade sectional twist about the local Z direction (blade spanwise direction) is shown in Figure 5-15 (b3). Starting from t = 0T indicated by the solid red line, the blade twist angle maintains at a low amplitude with small fluctuations among four moments during the stable rotation.

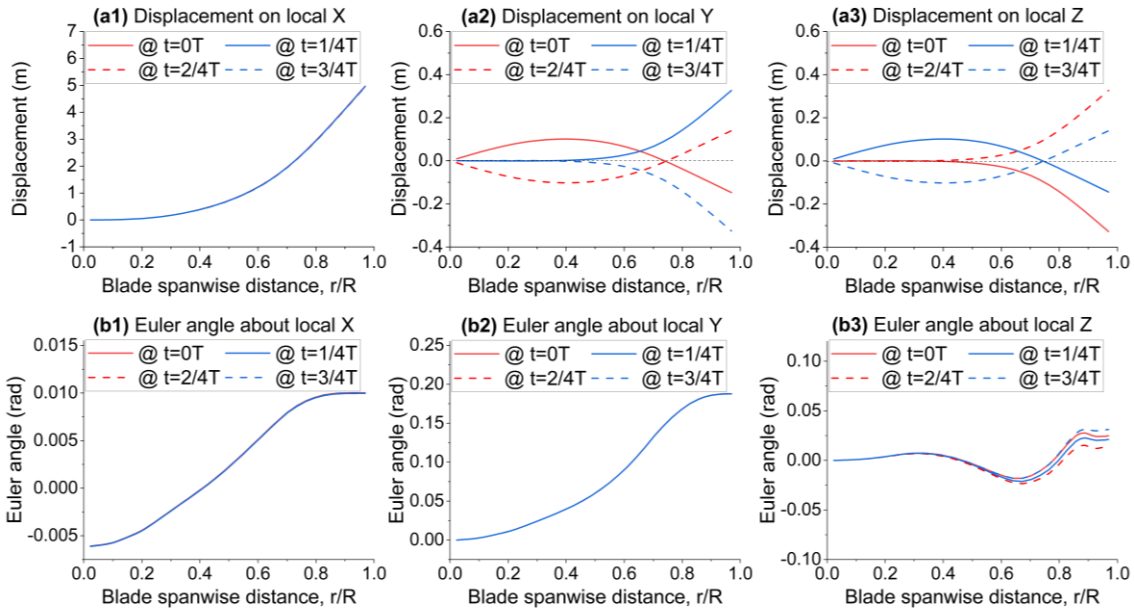

Figure 5-15 Blade (a1-a3) displacements and (b1-b3) Euler orientation angles on the blade section aerodynamic centre, under local coordinate systems at $t = 0T, 1/4T, 2/4T$ *and* $3/4\,T$ in a complete cycle

Figure 5-16 reveals the relationships among the principal strain and stress on X direction, flapwise displacement and non-uniform thickness distribution on the blade at $t = 0T$ moment. It can be seen from Figure 5-16 (a) that the principal strain on X direction on the blade surface with a relatively higher magnitude is mainly distributed within the blade spanwise where $r/R \in (0.121,\ 0.857)$, on the LE_Panel, Spar Cap and TE_Panel regions, as depicted in green and yellow.

This suggests a significant higher stress can occur in the corresponding region as can be seen from Figure 5-16 (b). While the principal strain on X direction in the blade trailing edge and the blade tip regions is lower, suggesting that a smaller principal stress on X direction will occur in the accordance blade regions.

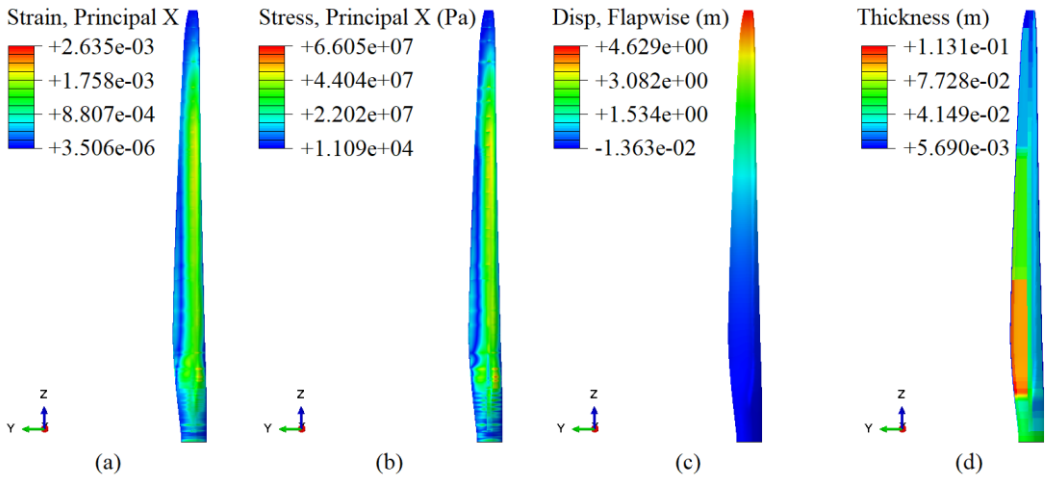

Figure 5-16 Contours of (a) principal strain on X direction; (b) principal stress on X direction; (c) flapwise displacement and (d) thickness distribution on the blade FE model, at $t = 0T$ during the blade stable rotation cycle

In Figure 5-17, the stress distributions on the blade pressure and suction surfaces are presented. To demonstrate the stress concentration more clearly, the stress distributions on the shear web components are excluded in this figure.

During the blade's stable rotation from $t = 0T$ to $t = 3/4T$, the Von Mises stress within the TE_Panel and TE_Reinf areas gradually increases and subsequently decreases. This can be also seen as denoted from 'a' to 'd', a periodic location shifting of the local stress along the blade spanwise in the TE_Panel, TE_Reinf and TE regions is observed on both the blade pressure and suction surfaces.

Such alternating distribution of stress situated in these regions reflects the structural response of the composite blade subjected to the periodic in-plane deformation. As evident from Figure 5-15 (a2), it reflects the blade is exposed under a periodic loading condition.

This emphases the necessities of partitioning a reinforcement region of TE_Reinf on the blade trailing edge, with reinforced glass fibre laminates employed as the principal load-resistance components within this region.

The stress concentrations of all four moments occur at nearly the same spanwise location within the blade transitional region of the LE_Panel area. During the blade's

stable rotation, due to the existence of the coupled effects of in-plane displacement and blade torsion, the maximum stress appears alternatively on both the pressure and suction surfaces during the moment between $t = 3/4T$ to $t = 1/4T$, where the maximum stress shifts to the blade suction surface at $t = 0T$.

Throughout the complete rotation cycle, the largest stress concentration magnitude of approximately 8E+07 Pa occurs at t=2/4T on the pressure surface. The order of predicted amplitude of the concentrated Von Mises stress ranges approximately from 70 to 80 MPa, which indicates a reasonable estimation of the stress on the blade.

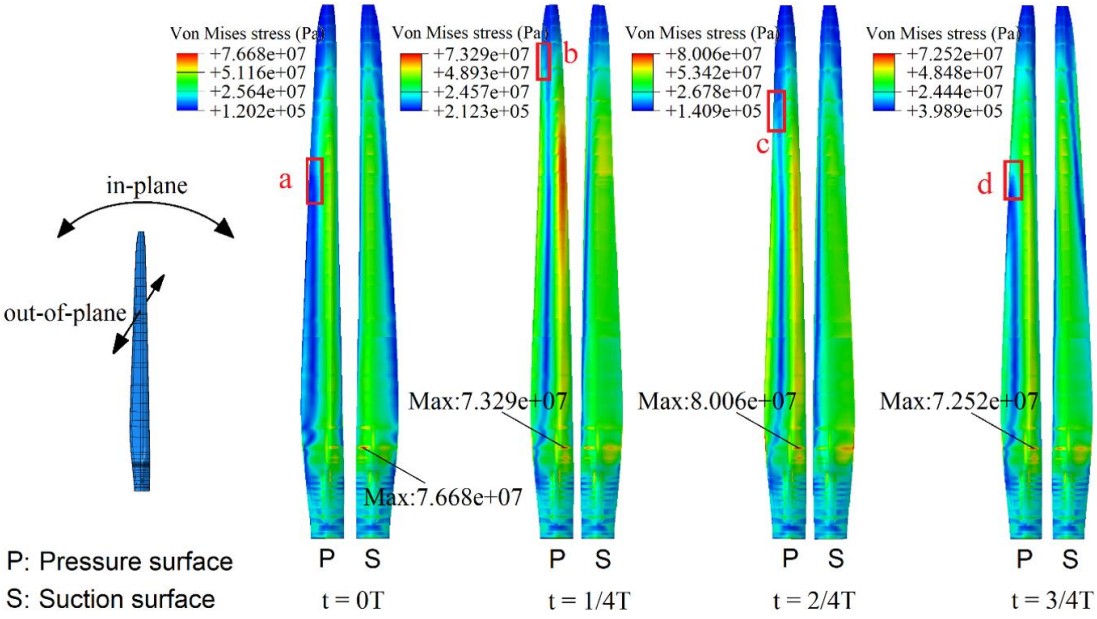

Figure 5-17 Von Mises stress distributions on the composite blade pressure and suction surfaces at four key moments during a rotation cycle

The stress concentration on the shear webs is also captured. As shown in Figure 5-18, for all four moments, the maximum stresses locate at the blade transitional region, offset to the suction side of the blade surface.

During a stable rotation, the maximum Von Mises stress of 1.035E+08 Pa occurs on the shear webs at $\mathrm{t} = 2/4\mathrm{T}$. Additionally, a local high stress region is also observed as approaching to the blade tip region, where the spanwise distance of $r/R \in (0.69, 0.86)$ with a lower stress magnitude.

Figure 5-19 presented an example of Von Mises stress distributions at four moments on the blade suction surface along the Node Path, as denoted in red line. Combining the stresses and the thickness plots, it is observed that the stress evolution performs highly nonlinear along the blade spanwise direction, which is relevant with the localised structural thickness with a non-uniform distribution.

During the blade stable rotation, the Von Mises stress distributions perform similar in the spanwise distance of $r/R \in (0, 0.11)$, in the blade near-root areas as denoted in region A.

In the blade transitional areas where spanwise distance of $r/R \in (0.11,0.21)$, the Von Mises stress fluctuates significantly, and the Von Mises stress at $t = 0T$ outperforms the stress magnitudes of other three moments, as denoted in region B and C. While in the spanwise distance of $r/R \in (0.69, 1)$, as denoted in region D, the Von Mises stress at t=3/4T outperforms the other three time moments in this area.

It is observed that the locations of the sudden increase of Von Mises stress occurs at the connecting edges of each adjacent blade sections, where the local thickness of the composite structure changes rapidly because of the ply-drops (Jin et al., 2023) of the stackings of composite laminates in the numerical FE model.

This may lead to a potential localised long-lasting strain imbalance between adjacent blade sections, causing abrupt variation in stress distribution.

To further investigate the nonlinear rapid variations of stress on the composite layups with ply-drops, a detailed localised modelling of the corresponding blade sections with solid elements might be necessary.

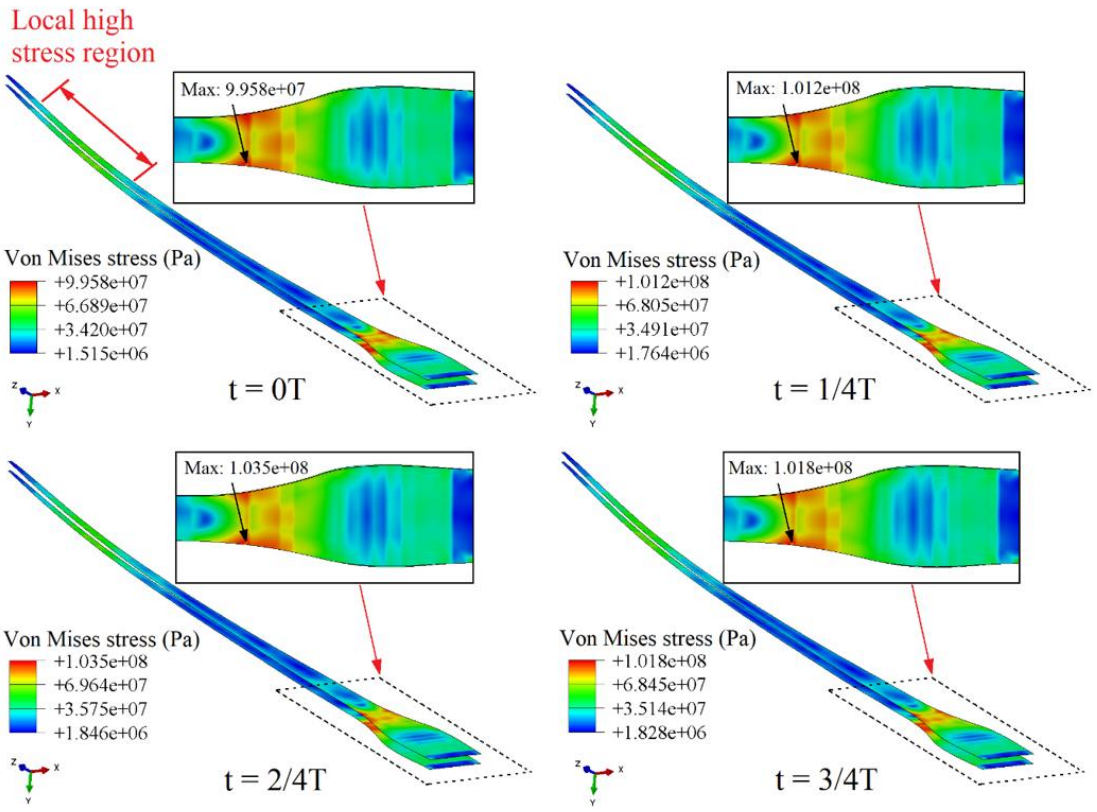

Figure 5-18 Von Mises stress distributions on the composite blade shear webs at four key moments during a rotation cycle

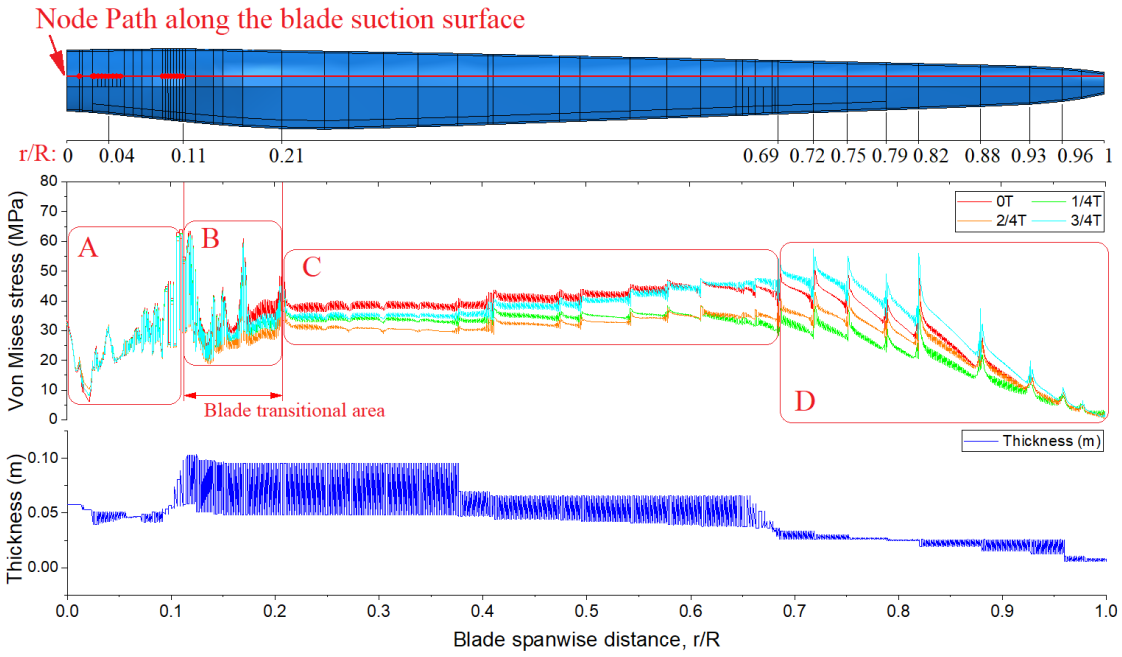

Figure 5-19 Von Mises stress distribution along the Node Path on the blade

5.5 Concluding Remarks

Two case studies have been tested to demonstrate the capability of the proposed framework by resolving the detailed blade aerodynamic behaviours under the operation condition and the stress field distributions on a full-scale NREL 5MW wind turbine composite blade.

In Case 1, the interacting mechanism of the instantaneous blade kinematics under the aerodynamic load is revealed. It is observed that the aerodynamic bending moment would accumulate in the blade root and transitional areas.

This results in a stress concentration in this local blade region. The location of the occurrence of the max. aerodynamic bending moment ($r/R = 0.17$) is close to the location of stress concentration ($r/R = 0.189$).

Meanwhile, a reasonable agreement of the Von Mises stress concentration is observed comparing to the literature results, due to a similar blade bending stiffnesses performance.

A promising computational cost reduction of 24.75% is realised using the proposed FSI framework for analysing the blade aeroelastic performance under the DLC 6.1 condition, comparing with the study conducted by Miao et al. (2019).

The proposed FSI framework avoided the direct surface-to-surface interpolations, which is conventionally being applied in a CFD-FEA FSI process, therefore, the deviation in computational efficiency is considered mainly originates from the HPC computing capacity comparing with other studies.

In Case 2, considering the rated operation conditions, a thorough blade aeroelastic analysis using the proposed FSI framework is given. The impacts of the blade aerodynamics to the composite structure are revealed. The composite blade Von Mises stress fields at four moments during a complete blade rotating cycle are analysed.

Under the realistic aerodynamic conditions, the identifications of the critical locations exposed to the relatively high stress, and intense localised stress fluctuation regions are achieved.

A high nonlinearity of stress distribution along the blade spanwise is captured. With our proposed FSI framework, it is found that the factors of the non-uniform thickness distribution, the orthotropic composite properties and the non-consecutive composite stacking configurations on the blade may influence the structural performance significantly and cause a highly nonlinear stress distribution in the composite layers on the blade.

Without modelling the composite blade structure with such fidelity, such as using a beam element model accounting for the blade aeroelastics as the works by Dose et al. (2018) and Liu et al. (2019), the stress status on the blade cannot be accessed and inspected. This part of work function as the basis of the future structural optimizations for light-weight blade designs.

Chapter 6 Investigations of FOWT Platform Motions Impacts to the Composite Blade Stress Behaviours

6.1 Overview

In this chapter, we investigated the blade aero-elastic behaviours on the NREL 5MW floating offshore wind turbine (FOWT) under different platform surge motion conditions, where the surge amplitude and period are defined based on the common range from other peer literatures.

The result shows that a shorter surge period and larger surge amplitude can lead to significant amplification in stress on the FOWT composite blade.

The stress concentrations are predominantly observed on the blade substructural shear webs, underscoring the need for local stress inspections. A linear relationship between surge amplitude and local max. Von Mises stress magnitude is identified, offering a valuable method for a quick preliminary blade design.

The study demonstrates the effectiveness of the FSI framework in capturing complex interactions and offers insights into enhancing the durability of FOWT blades.

6.2 Model Description

The geometrical model of the blade for this study is identical to the one used in last chapter, as previously listed in Section 4.1.

It is worth noting that the wake is not the focus of the present study, therefore, the wake region mesh is not being refined, thus it significantly saves the cells in the computational domain, resulting a total number of cells of 3.72 million. The detailed comparison that validates the current mesh accuracy has been given in Section 4.2, where the aerodynamic thrust, power and the flexible blade tip displacement are compared with several numerical studies from open literatures.

The selection of the time step size follows the definition as previously given in Section 5.2, where a time step size of 0.005 s (accounting for approximately 0.36 degree of

rotation per time step) is used to ensure the numerical stability and convergence of the simulations while improve the numerical efficiency as much as possible.

6.3 Composite blade and material specifications

The composite blade modelling process follows the detailed material definitions, layup distributions and composite stacking specifications as provided by Resor (2013) for the NREL 5MW reference wind turbine blade. The blade mass and mode of frequencies have been validated in detail as has been introduced in Section 4.3.

6.4 Definition of surge load cases

To replicate the impacts of the wave-induced platform motions to the blade aeroelastic performance on an FOWT, the surge motion is considered in this study as it is one of the dominating motions that can bring significant instability to the blade aeroelastic performances. A prescribed surge motion equation is applied to the rotor centre, imposing a periodic oscillation to the rotor centre, formulated as:

$$S(t) = ramp(t) \cdot A_S \cdot \sin\left(\frac{2\pi}{T_S} \cdot t\right) \tag{6.1}$$

$$ramp(t) = k \cdot \begin{cases} 0\,, & t = 0 \\ t - t_0\,, & (t_0 \le t \le t_{end}) \\ t_{end} - t_0, & (t_{end} \le t) \end{cases} \tag{6.2}$$

where, the A_S and T_S are the amplitude and the period of the prescribed surge motion, respectively. The $ramp(t)$ function guarantees a gradual exerting process of platform motion to the rotor, preventing numerical instability at the initial stage of the FSI simulation. k controls the slope of the $ramp(t)$ function. t_0 and t_{end} are the functional time of the $ramp(t)$ function and the end time of the FSI simulation, respectively.

As previously discussed in Section 2.2, the selections of surge motion parameters can vary widely due to different ocean conditions, leading to a broad parameter range. In general, a severer load case facilitates the occurrence of a more significant nonlinear blade aeroelastic performance, while it may cause numerical instability.

Therefore, to balance between the observation of dynamic effects and computational robustness, the specifications of the surge motions used in the present study are listed below in Table 6-1. For the convenience of the result discussions in Section 6.5, two groups of case studies accounting for the loads with different surge periods and amplitudes are divided into G1 and G2, respectively.

Table 6-1. Load case specifications of different surge motions.

Load Case type	**Bottom fixed**	**Platform surge motion**									
Load Case ID	LC0	LC1	LC2	LC3	LC4	LC5	LC2	LC6	LC7	LC8	LC9
Groups	/	G1					G2				
$\boldsymbol{A_S}$ (m)	/	2	2	2	2	2	2	3	4	5	6
$\boldsymbol{T_S}$ (s)	/	6	9	12	15	18	9	9	9	9	9
$\boldsymbol{U_0}$ (m/s)	11.4										
$\boldsymbol{\Omega_0}$ (rpm)	12.1										

6.5 Results and Analysis

6.5.1 Thrust and power

Figure *6-1* depicts the aerodynamic thrust and power of all load cases versus the normalised platform surge periods. In G1 plots, the varying magnitudes of thrust and power are inversely related to the surge period, indicating that a shorter surge period can result in greater flapwise load on the blade.

For comparisons in G2, the thrust and power variation increase as the surge amplitude becomes larger. Particularly, from the LC9 results, an instantaneous rotor aerodynamic fluctuation can be clearly observed, with an obvious forward shift from the 2/4T.

This reflects that the evolution of the aerodynamic thrust and power of an FOWT is asymmetrical. Such asymmetrical phenomenon is considered to be a physical behaviour due to the coupling between the given boundary conditions in aerodynamics (e.g. platform surge motion, the constant incoming flow) and the elastic blade structure mass system. During the forward platform surge motion (against the incoming flow), the blade experiences a higher relative flow velocity compared with that in the

backward motion phase. This can explain such asymmetrical performance in the aerodynamic thrust and power due to the presence of asymmetrical apparent flow velocity on the blade.

Additionally, the nonlinear flow separation can also exacerbate such asymmetrical aerodynamic performance. It should also be noted that the mesh metrics and overall quality can influence the capture of such asymmetrical performance since it strongly relies on the proper estimation and capture of turbulent flow effects.

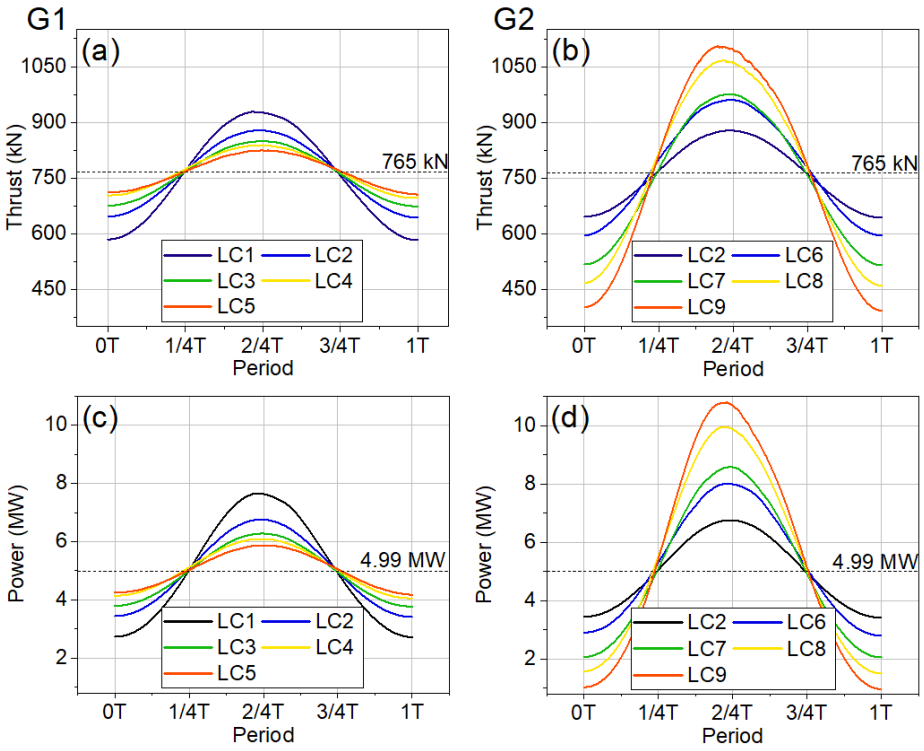

Figure 6-1. Time history of the thrust and power within one normalised surge period.

To better understand such aerodynamic evolution, an example of LC1 (As = 2m, T = 6s) is given in Figure 6-2. In the frontal half-period from 0T to roughly 2/4T, the rotor firstly travels to the maximum surge distance on the downstream (point a to b), then reverses its direction towards the upstream.

A relative velocity U_{rel} is defined by the subtraction of the free stream velocity U_0 from platform surge velocity U_{surge}.

The maximum U_{rel} reaches to V1 when the rotor arrives at the surge origin (point c), thus causing the highest relative velocity on the rotor. Then, the minimum of U_{rel} (V2) is achieved when the rotor returns to the surge origin at point e. The delays of Δ1 and Δ2 are both seen for the occurrence of the max. and min. thrusts, with respect to V1 and V2.

This reflects that the thrust evolution on the blade always lags behind the relative velocity, which leads to an unbalanced process in the thrust. Specifically, the duration for the thrust increase to its maximal is shorter to that to its minimal. Such asymmetrical behaviour can be especially significant for a more severe load case, where the thrust increases rapidly and decreases slowly in a surge period. This may bring in additional instabilities in both structural and aerodynamics to the blade, e.g. an increased fatigue stress and lower aerodynamic efficiency.

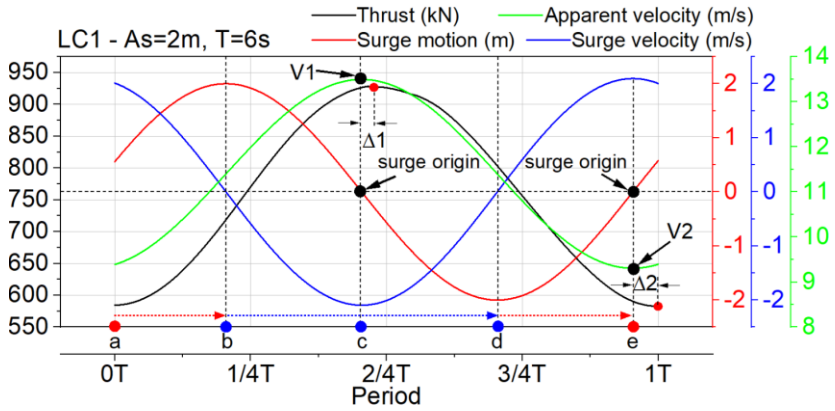

Figure 6-2. Example of LC1 – demonstration for the delay of the aerodynamic thrust.

Figure 6-3 display the maximum, minimum and averaged values of thrust and power among all load cases. To quantify the significance of the offsets between the extreme and averaged values, a modified standard deviation $\tilde{\sigma}$ is used, formulated as:

$$\tilde{\sigma} = \frac{\sigma}{Thrust_{avg}} \times 100\% \tag{6.3}$$

$$\sigma = \sqrt{\sum_{i=max,min} \frac{(Thrust_i - Thrust_{avg})^2}{2}} \tag{6.4}$$

An example is from Figure 6-3 (a), the $\tilde{\sigma}$ decreases from 22.76% to 7.73%, showing that the aerodynamic thrust converges to the averaged thrust value as the surge period increases from LC1 to LC5. The power plots depicted in Figure 6-3 (c) also shown a similar performance.

Comparatively, the thrust and power curves in G1 plots appears a more gradual and smoother evolution, while in G2 plots, the thrust and power curves under different surge amplitudes shown a less consistent evolution, where it is also reflected from the average curves from G1 and G2 plots (dash line in black). This means that the FOWT aerodynamic performance can be more prone and sensitive to the change surge amplitude rather than surge period.

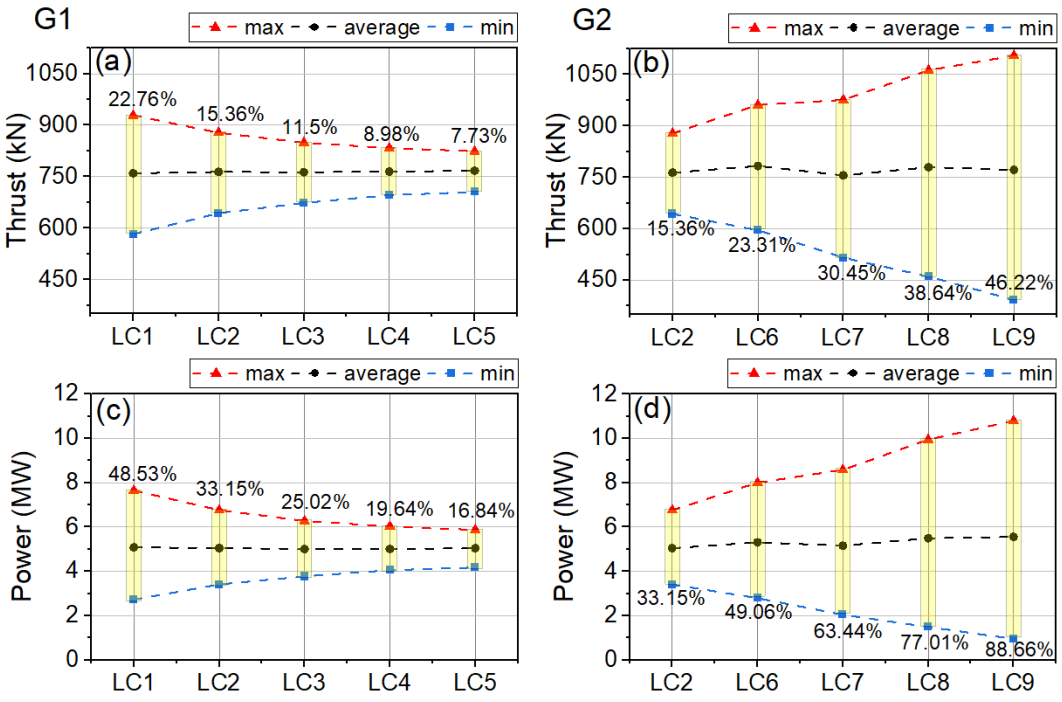

Figure 6-3. Thrust and power ranges for all load cases, grouped in G1 and G2.

Next, to give a more in-depth inspection to the aerodynamic performance of the blades, the instantaneous aerodynamic thrust distributions along a single blade are shown in Figure 6-4. The thrust distributions for each load case are acquired from the corresponding moments when the maximum flapwise deflections of the blade tip are reached.

In G1 plots, it can be seen that the curve of the thrust distribution shifts from high to low as the surge period increases. While in G2 plots, as the surge amplitude decreases, the thrust distributions curves shift downward, meaning that the thrusts become smaller. This also justifies the previously analyses as given for Figure 6-1.

Furthermore, the zoom-in plots in G1 and G2 of the instantaneous aerodynamic thrust distributions reveals that the thrust occurring at the blade root and transitional region (r/R = [0.04, 0.16]) undergoes significant disturbance, indicating a pronounced nonlinear aerodynamic behaviour. Such aerodynamic nonlinearity becomes particularly evident in the load cases presented in G2, which might explain the less consistent evolution of the thrust and power curves as previously depicted in Figure 6-3.

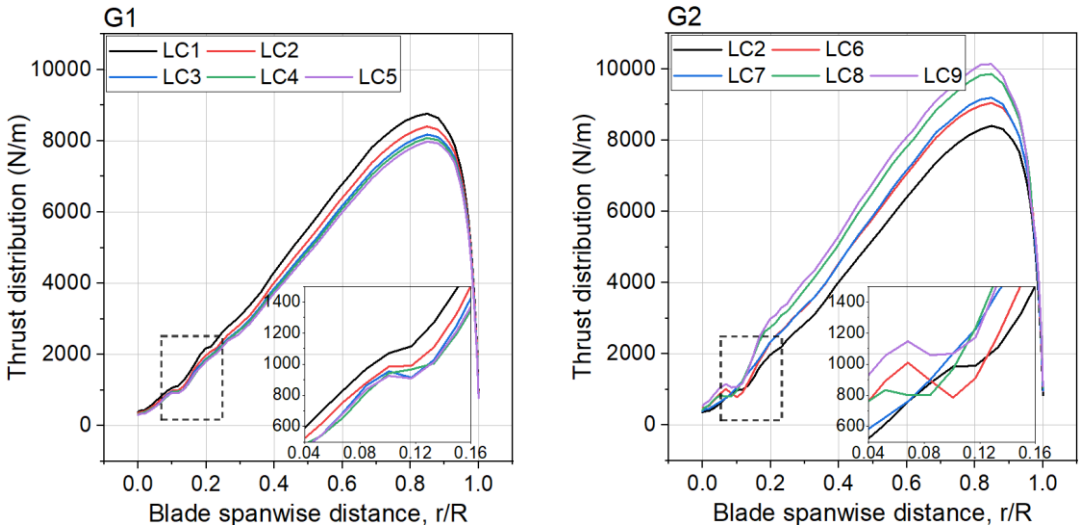

Figure 6-4. Aerodynamic thrust distribution along the blade, comparisons between the load cases of (a). different surge periods and (b) different surge amplitudes.

To illustrate the fluid dynamics around the blade under different platform motion load cases, the fluid field contours of LC1, LC2 and LC9 are extracted. Note that the extracted fluid field results are in correspondence to the moment when the max. blade deflection occurs for each load case. Firstly, the comparisons of the pressure coefficients C_p on three cross-section locations on the blade (r/R = 0.3, 0.6 and 0.9) are shown in Figure 6-5. The formulation of C_p is given as:

$$C_p = \frac{P_0 - P_\infty}{0.5\rho[U^2 + (\omega r)^2]} \tag{6.5}$$

where P_0 is the static pressure at the specified blade cross-section, P_∞ is defined as 0, representing the pressure at the infinite far field. The total flow speed relative to the blade includes both the freestream velocity and the rotational velocity, where r is the distance from the blade cross-section to the rotor centre, and ω is the angular velocity in rad/s.

In the C_p plots, LC9 shows the most significant variation compared to LC1 and LC2 across all cross-sections. At r/R = 0.3, the maximum absolute values of C_p are 3.86 for LC9, 2.81 for LC2, and 2.55 for LC1. As r/R increases from 0.3 to 0.9 along the blade span, the variations in C_p become less noticeable. At r/R = 0.9, the C_p values on the pressure and suction sides for LC1 and LC2 almost overlap. For LC9, a positive pressure is found on the blade suction surface of the cross-section leading edge at r/R = 0.9, exerting a downward moment on the corresponding blade cross-section locations.

The contours below depicted the C_p distributions around the blade spanwise cross-section locations under LC1, LC2 and LC9, the max. limit of the legend has been set to $-C_p$ = 2 for a clearer view of the nuance differences C_p distributions among three load cases.

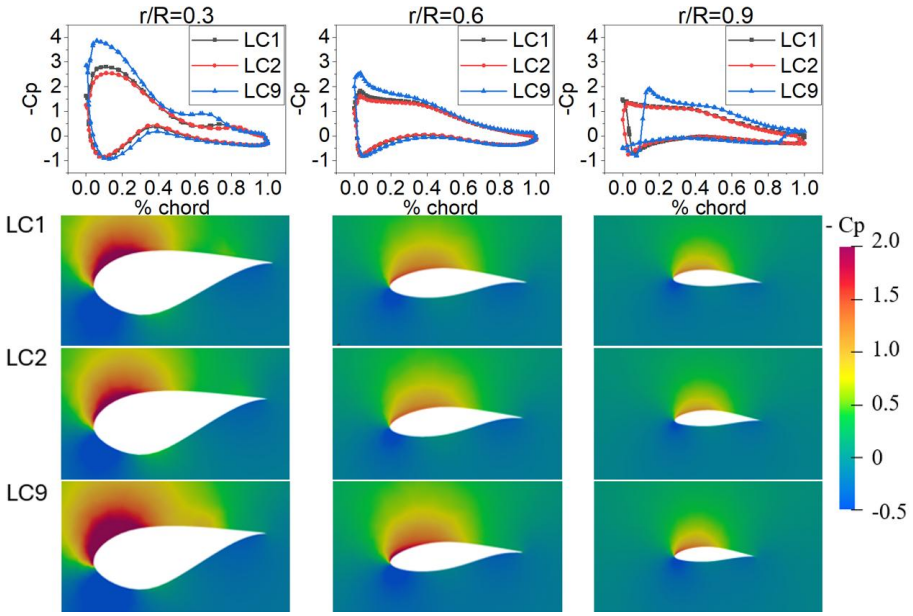

Figure 6-5. Pressure coefficient (C_p) plots and contours at blade span r/R = 0.3, 0.6 and 0.9 for LC1, LC2 and LC9.

The velocity field around the LC9 blade is shown in Figure 6-6, illustrating the instantaneous velocity in the global X direction at the occurrence of the max. blade tip displacement on different cross-sections along the blade span. The highest X velocity is seen at the leading edge of each blade section. Additionally, reverse flow occurs across all sections of the blade. From the root (r/R = 0.3) to the middle (r/R = 0.6), the reverse flow becomes more pronounced but then decreases in significance as it approaches the blade tip (r/R = 0.9).

This suggests the occurrence of the flow separation on the blade suction surface. The reasoning to this is that the blade is experiencing the largest aerodynamic thrust loads at this particular moment (when the max. blade deflection occurs), which is also when the relative flow velocity closes to the largest value within the platform surge period.

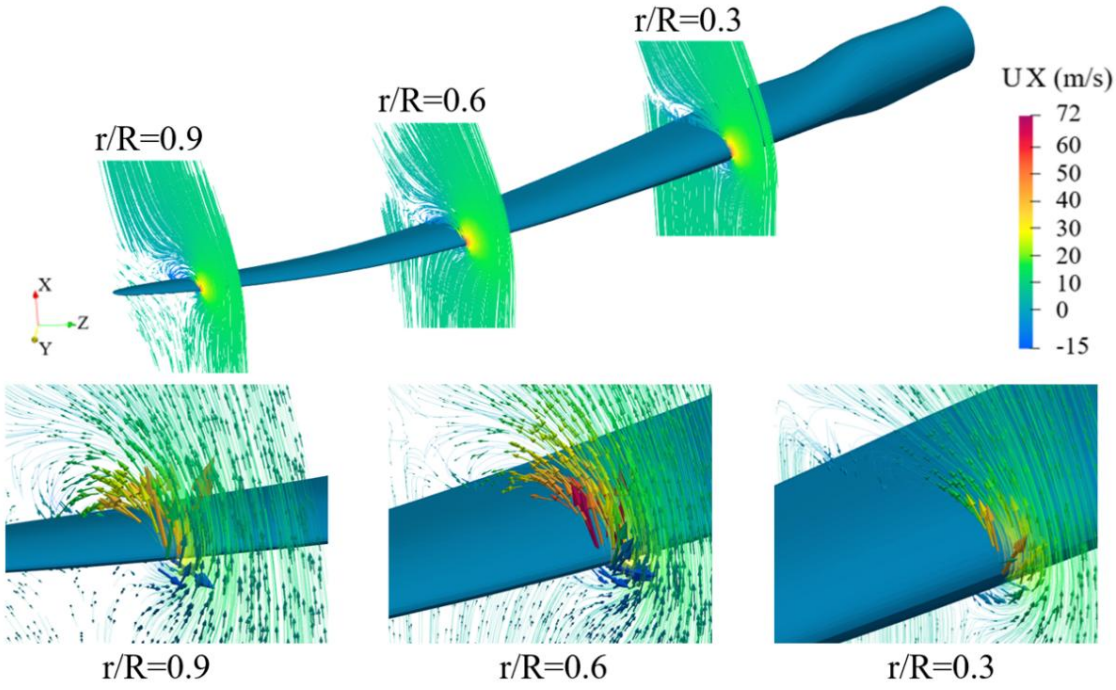

Figure 6-6. Instantaneous X velocity contours at the occurrence of max blade tip displacement on different blade spans for LC9, with streamline plotted for each blade span location.

6.5.2 Blade deflections

In this section, the blade aeroelastic characteristics are indicated by the local deflection Δx, and global displacement X of the blade tip, as shown in Figure 6-7. The relation between Δx and X is:

$$\Delta x = X - S(t) \tag{6.6}$$

where the definition of the surge displacement $S(t)$ was previously given in Eq. 6.1.

Notably, as depicted in LC9 deflection curve in Figure 6-7 (b), the increase of surge amplitude results in fluctuations in blade deflection, which brings additional higher-order frequencies to the blade dynamics.

This may have introduced extra instabilities to the blade aeroelastics. A Fast Fourier Transform (FFT) analysis will be given later on, as illustrated in Figure *6-8*, to explain the aeroelastic instability as reflected in LC9 in detail.

To quantify the local deflections in G1 and G2 plots, the differences (in percentage) between the maximum blade flapwise deflections Δx and the converged blade tip displacement of 5.4 m (marked in black dot line in Figure 6-7), acquired from LC0, is given as listed in Table 6-2.

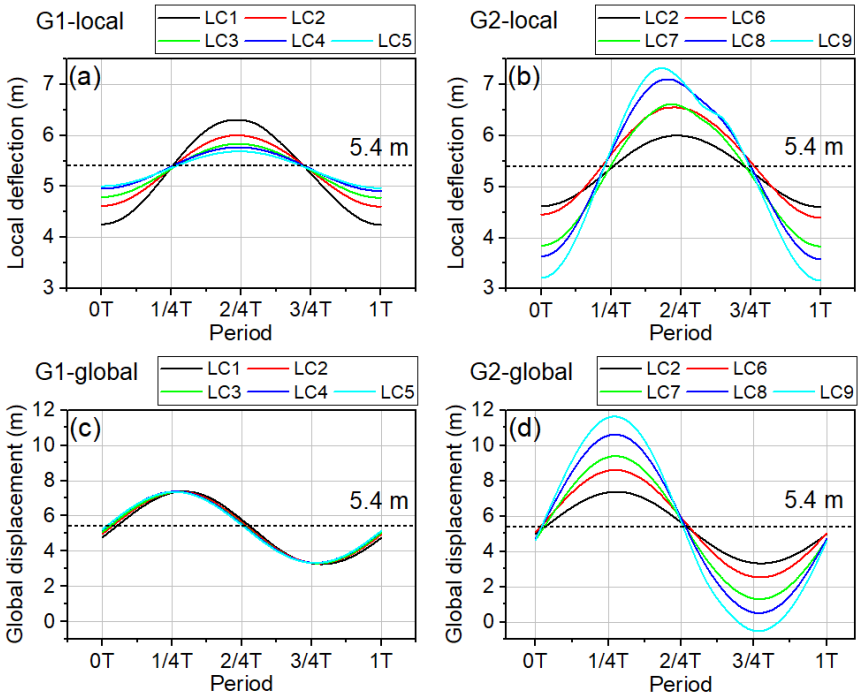

Figure 6-7. Time history of the blade tip deflections and global displacements on flapwise direction for all load case.

Table 6-2. Max. local flapwise deflections of the blade tip for all load cases.

G1			**G2**		
Load cases	Δx (m)	Diff	Load cases	Δx (m)	Diff
LC0	5.400	/	LC0	5.400	/
LC1	6.304	16.75%	LC2	6.003	11.16%
LC2	6.003	11.16%	LC6	6.554	21.38%
LC3	5.835	8.06%	LC7	6.618	22.55%
LC4	5.769	6.84%	LC8	7.105	31.58%
LC5	5.687	5.32%	LC9	7.327	35.69%

The above results quantitatively evaluate the maximum deflection of the blade under designated surge motions, which can be quite useful for determining the tower clearance of the blade during the designing process of the FOWT. Additionally, based on the time history of blade deflections, the FFT analysis are conducted as depicted in Figure 6-8 for load cases grouped in G1 and G2, respectively.

From Figure 6-8 (a), it is found the dominant response frequency of each load case increases as the surge period decreases from LC5 (18 s) to LC1 (6 s). This indicates that shorter surge periods can induce more pronounced nonlinear features in the blade dynamics, potentially leading to enhanced dynamic instabilities of the blade structure.

In Figure 6-8 (b), an additional frequency component at approximately 0.119 Hz is consistently observed across all load cases in Group G2 with the same surge period.

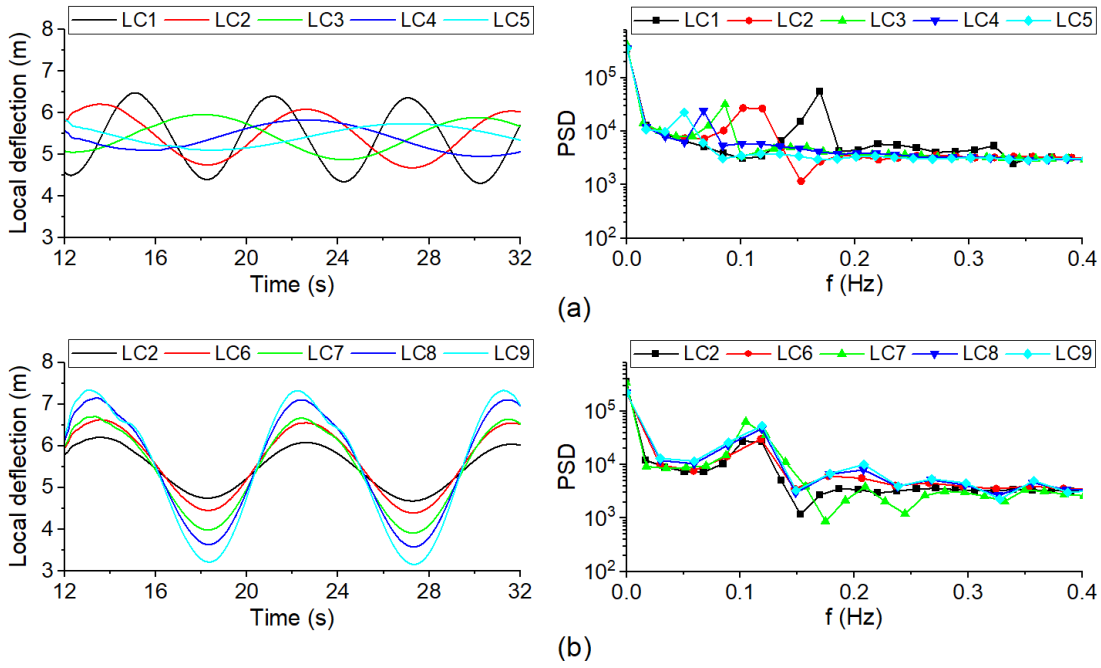

Figure 6-8. FFT analysis for the blade flapwise deflections for (a). G1 and (b). G2 load cases.

The above analysis suggests that changes in the platform surge period may excite additional frequency components in the blade dynamics, potentially leading to structural instabilities and a reduction in fatigue durability.

The additional frequency component remains at a nearly fixed level, which appears to be a low frequency and insensitive to the changes of surge amplitudes. Therefore, its marginal contribution to cumulative fatigue damage is expected to be limited. The overall fatigue sensitivity to surge amplitude is dominated by the fundamental component and the resulting stress-range distribution.

6.5.3 Stresses on the composite blade

The impacts of the platform motion to the blade structural stress performance are evaluated in this section. The stress analysis of the composite blade structure is carried out to reveal the stress conditions on multi-level of the blade structure, namely blade envelope, individual blade component (e.g. shear web), and constituents of blade component (e.g. interlaminar composites).

Firstly, the Von Mises stresses on the composite blade suction surface is presented for LC1, LC3 and LC9, as shown in Figure 6-9 (a), (b) and (c). For each load case, the stresses on the blade from nine moments within one surge period were obtained.

As depicted in Figure 6-9 (a) and (c), the stress contours of LC1 and LC9 indicate that at the 4/8T and the nearby region, the overall stress of the blade exhibits a greater amplitude compared to other moments.

This is because this point in time corresponds to the max. flapwise deflection of the blade, resulting in the maximum principal strain in the flapwise direction. While for LC3 in Figure 6-9 (b), the overall Von Mises stress magnitude on the blade outer surface exhibits less pronounced differences across all time instances.

This reduced variation is likely due to the milder surge motion of LC3 compared with LC1 and LC9, resulting in more subdued fluctuations in the Von Mises stress on the blade.

Noting that in LC9, unlike the other two load cases, the global max. Von Mises stress is observed at 3/8T, occurring at the trailing edge of the blade at a span of r/R = 0.708.

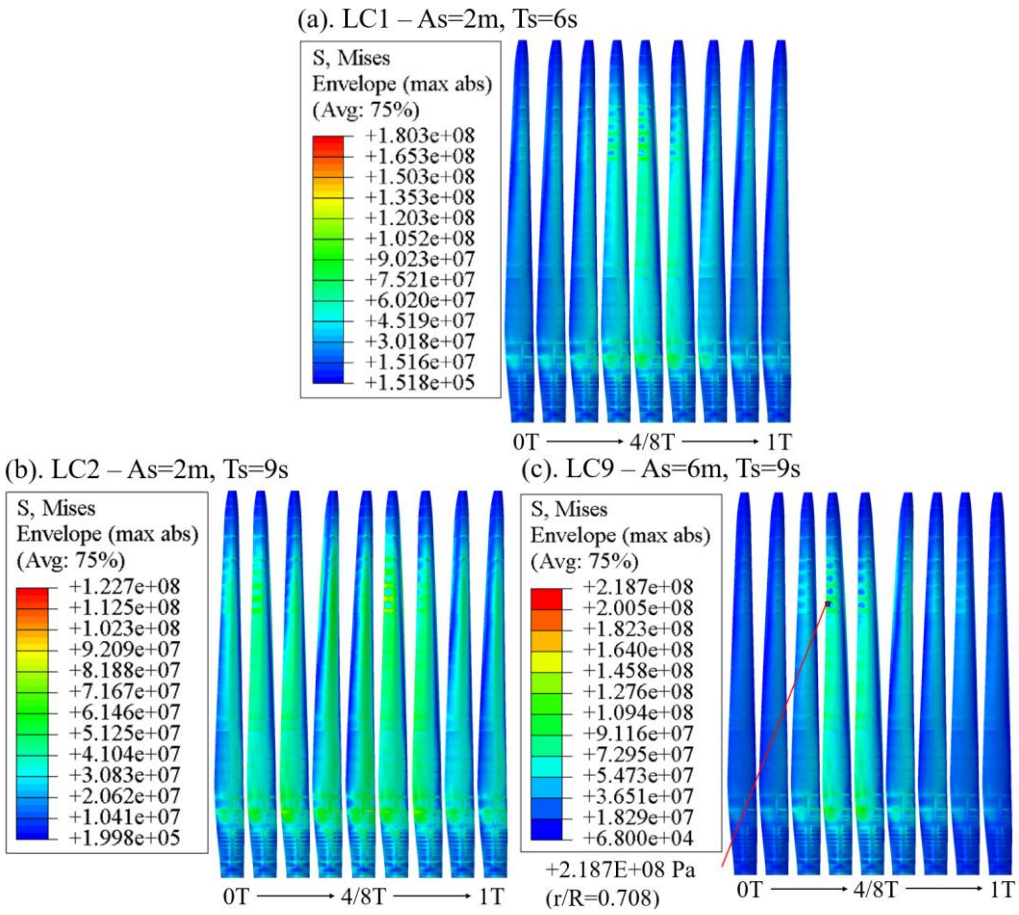

Figure 6-9. Von Mises stress distributions on the blade outer surface, for (a). LC1, (b). LC2 and (c). LC9.

In Figure 6-10, the principal axial and shear stain components at 3/8T in the near-by areas (r/R=[0.68, 0.83]) of the stress concentration location indicates that the blade is experiencing a local buckling. For instance, a significant compression in local 1-direction is observed, denoted by the negative strain (in blue) as shown in the SE1 contour. The '1-direction' and '2-direction' are defined as local directions relative to the shell element length (align with the length of blade span) and width (perpendicular to the length of blade span), respectively (ABAQUS, 2009).

The explanation to such local stress concentration is that the blade deflection is amplified due to the platform motion induced loads, causing larger strains in the further span of the blade, where the stiffnesses are usually lower due to a smaller thickness of the blade shell structure comparing to that in the lower span area (e.g. the blade root).

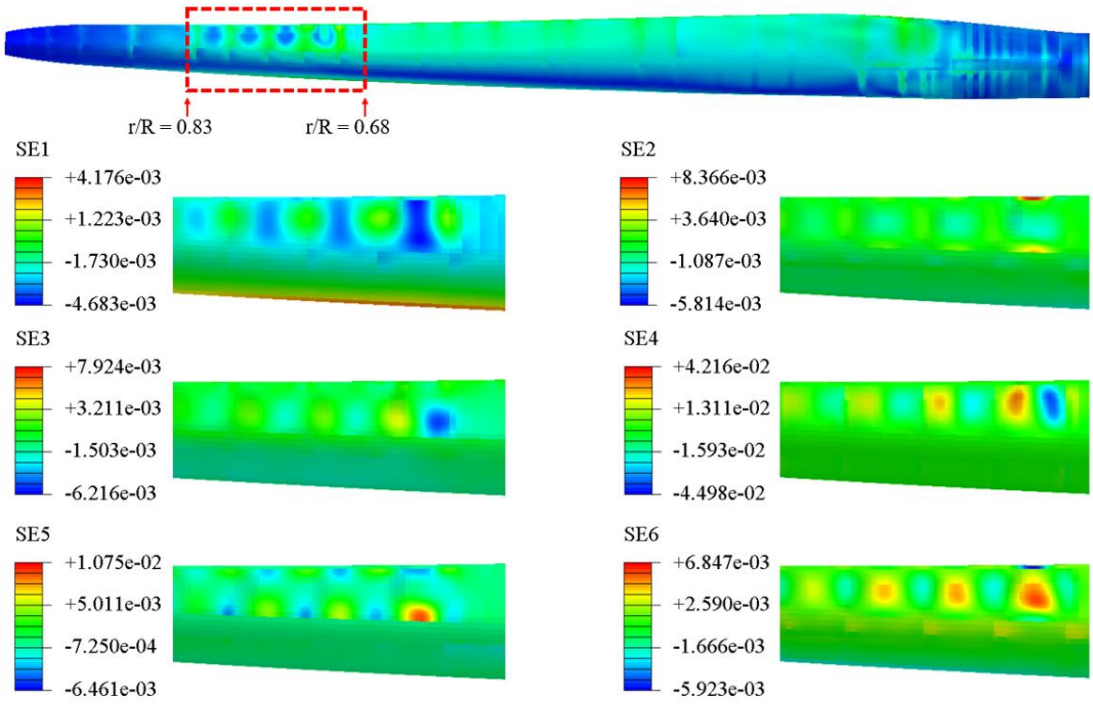

Figure 6-10. Section strain contours on the blade span r/R = [0.68, 0.83]. Six components are: SE1 – direct membrane strain in 1-direction; SE2 – direct membrane strain in 2-direction; SE3 – shear membrane strain in 1-2 plane; SE4 – transverse shear strain in 1-direction; SE5 – transverse shear strain in 2-direction; SE6 – strain in element thickness direction (ABAQUS, 2009).

Another observation from the stress contours is that stress concentration often occurs on the shear web during one surge period. The shear web sub-structure is primarily designed for withstanding the shear forces and reinforcing the bending and torsional stiffness by bounding to the spar caps using mechanical connections or adhesive materials , thereby forming a hollow box-beam structure along the blade spanwise (Haselbach & Berring, 2024). Therefore, it is essential to inspect the stress distributions on the shear web, particularly for stress evaluations on regions close to the bounding areas with the spar caps.

The location of the shear webs is demonstrated in Figure 6-11. An example of stress distributions on the shear web 1 is for LC9 presented in Figure 6-12. As observed from the contours, the location of instantaneous local stress concentration shifts within one surge motion period, jumping from the left edge of the shear web (at 0T and 1T

moments) to the right edge (at intermediate moments). This shift primarily occurs on shear web 1. The maximum Von Mises stress concentration is observed at the 4/8T moment, with a magnitude of 1.551E+08 Pa.

This reveals that the location and magnitude of the stress concentration is time dependent, and the maximum Von Mises stress mainly occurs on the edges of the shear webs. Such quantitative data is essential for determining the strength of the connections between the shear web and spar caps, based on which the engineers may optimise the joining schemes and materials.

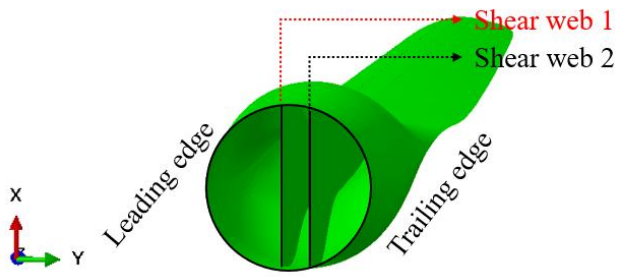

Figure 6-11. Schematic diagram of the shear webs on the blade.

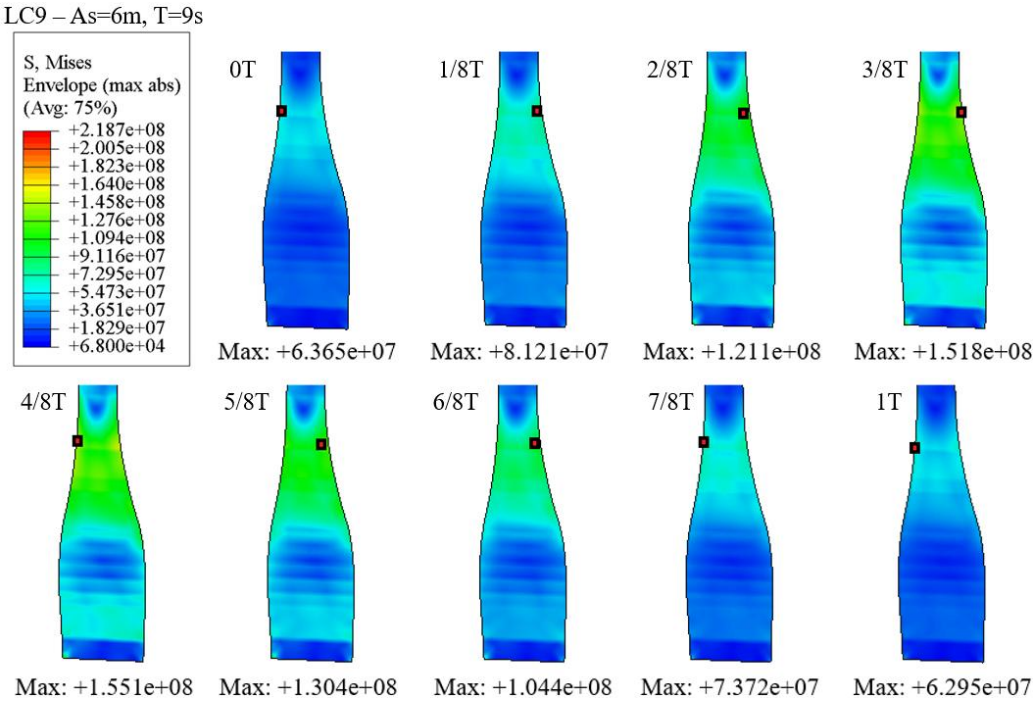

Figure 6-12. Von Mises stress distributions on the shear web 1 for nine moments in a complete surge period of LC9.

Furthermore, the instantaneous in-ply stress distributions on the shear web 1 are resolved, corresponding to the moment when the blade reaches to the maximum flapwise deflection for all load cases. A schematic diagram of the shear web sandwich structure is shown in Figure 6-13. The shear web is composed of the unidirectional glass fibre Seartex laminates on the outer skins (in orange), with FOAM filling the cores (in blue).

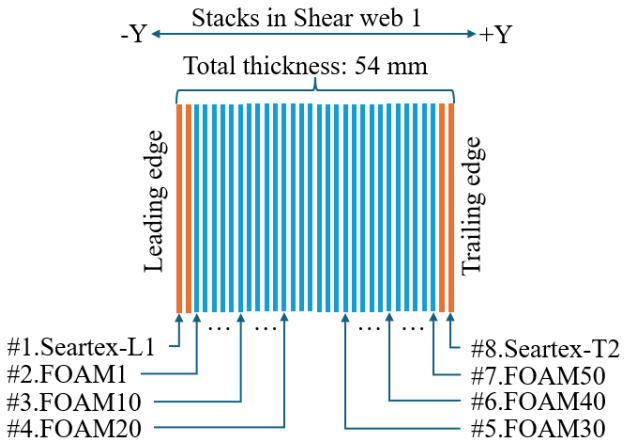

Figure 6-13. Schematic diagram of the shear web sandwich structure.

Worth being noted that, in this study, a ply-to-ply modelling strategy is adopted for the shear web sandwich structure for the convenience of stress distribution demonstrations across each ply.

Such modelling approach does not accurately reflect the manufacturing reality for the shear webs, where the interior FOAM stacks usually form a monolithic structure, rather than a ply-to-ply structure.

Therefore, a numerical validation using both modelling strategies has been conducted which confirms that the predicted max. Von Mises stress shows almost identical distribution across the shear web sandwich structures, as shown in Figure 6-14.

In the monolithic model, a sufficient number of integration points on the thickness direction are defined to provide enough resolutions for stress integration.

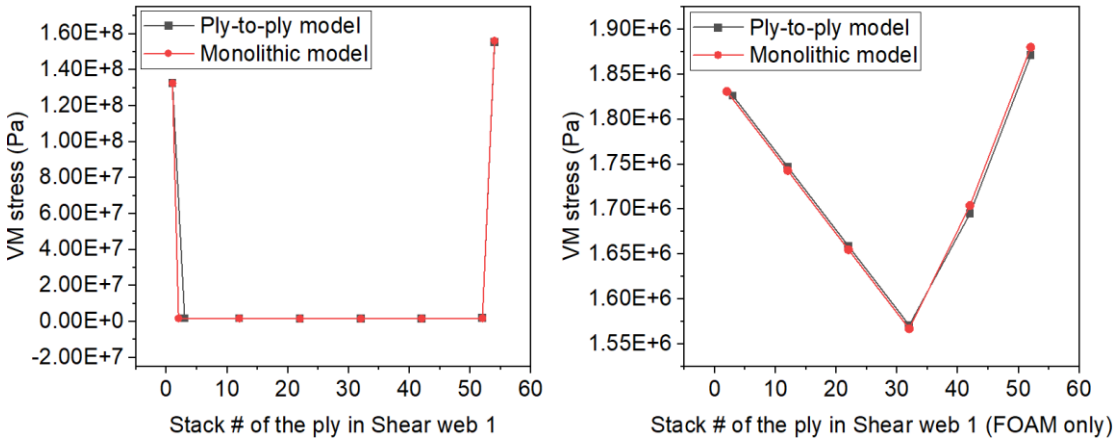

Figure 6-14. Numerical validation for stress predictions across shear web 1 plies using ply-to-ply and monolithic models, LC9 is applied.

Table 6-3 lists the selected plies used to demonstrate stress distributions across shear web 1. As shown in Figure 6-15 shows that the in-ply stress concentrations have a non-consecutive distribution, especially between the adjacent plies of Seartex-L1 and FOAM1. Due to the significant stiffness drop from the composite laminate skin (reinforced glass fibre) to the FOAM core, there is a large reduction in maximum Von Mises stress. The stress magnitudes differ significantly between the Seartex and FOAM plies, with max. Von Mises stresses of 1.325E+08 Pa and 1.826E+06 Pa, respectively, a difference of two orders of magnitude.

Table 6-3. Selections of plies (in shear web 1) for Von Mises stress distribution demonstration.

Name of ply	Thickness of each ply	Stack # of the ply
#1.Seartex-L1	1 mm	1
#2.FOAM1	1 mm	3
#3.FOAM10	1 mm	12
#4.FOAM20	1 mm	22
#5.FOAM30	1 mm	32
#6.FOAM40	1 mm	42
#7.FOAM50	1 mm	52
#8.Seartex-T2	1 mm	54

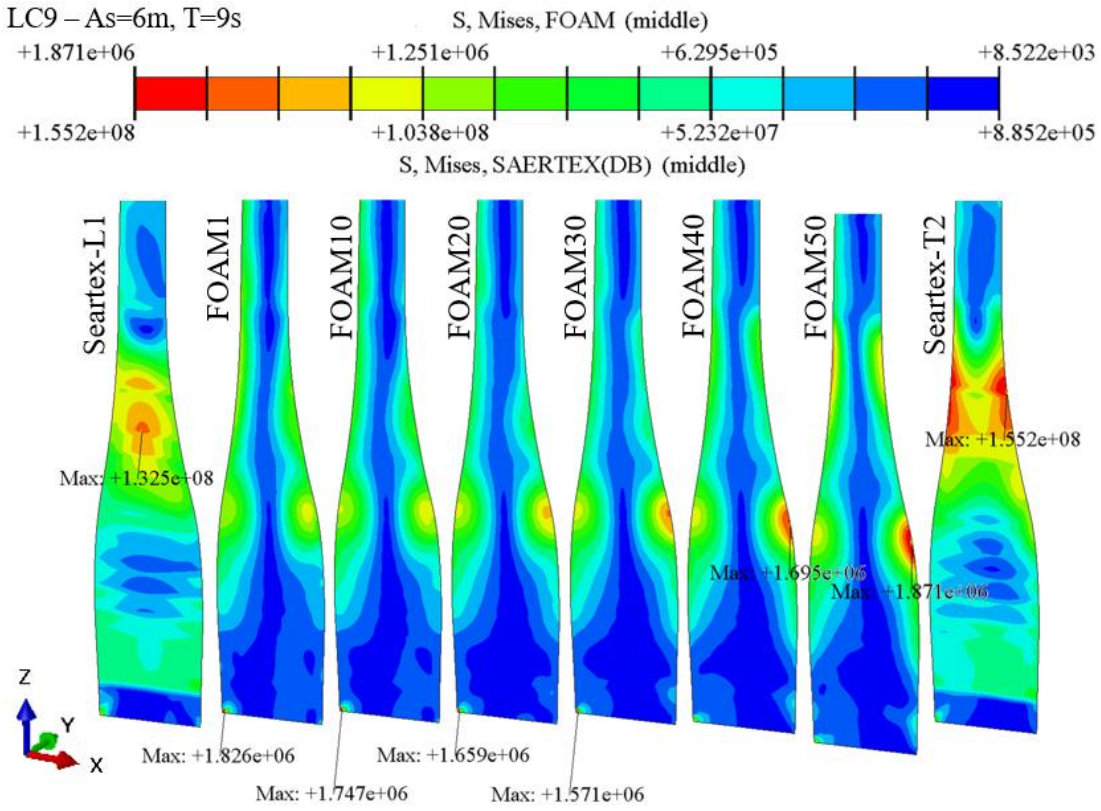

Figure 6-15. Von Mises stress distributions of selected plies on shear web 1, at max. flapwise blade deflection under the LC9.

Additionally, the shifts in location are observed of the max. Von Mises stress across the FOAM plies, from the root of the shear web (on -X direction) to the transitional area of the shear web (on +X direction).

The Von Mises stress distributions for FOAM plies in the shear web 1 under all load cases are firstly displayed in Figure 6-16. The max. Von Mises stress depicted here is an equivalent metric while it cannot explain such shifts phenomena comprehensively.

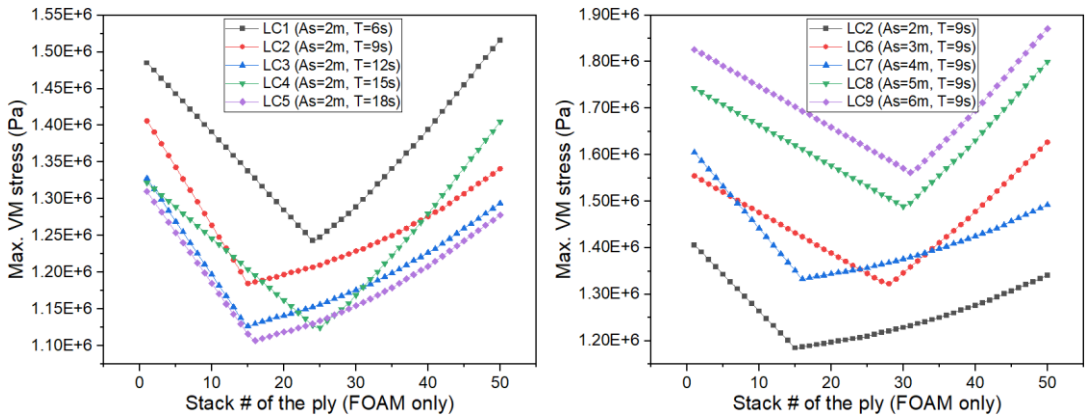

Figure 6-16. Max. Von Mises stress across the FOAM plies for all load cases.

To explain it thoroughly, we selected the stress results of LC9 (As=6m, T=9s), where the direct (S11 and S22) and shear (S12) stress components are quantified and depicted in Figure 6-17.

The variations in each stress components max. magnitude across the FOAM plies exhibit a clear bi-linear characteristic (as the max. Von Mises stress in Figure 6-15).

The locations for each max. stress component in blade spanwise direction are indicated in red, denoting the abrupt changes (i.e. the shifts) of the local max. stress occurrence locations across the FOAM plies.

It is seen that the shifts in blade spanwise of the local max. stress usually occur at the inflection points of the bi-linear stress curves for each stress components. This suggests that the max. stress occurrence locations and the evolution trend of the stress for each stress component are not changing continuously, but performs a sudden ‘jump’ which is a typical nonlinear behaviour.

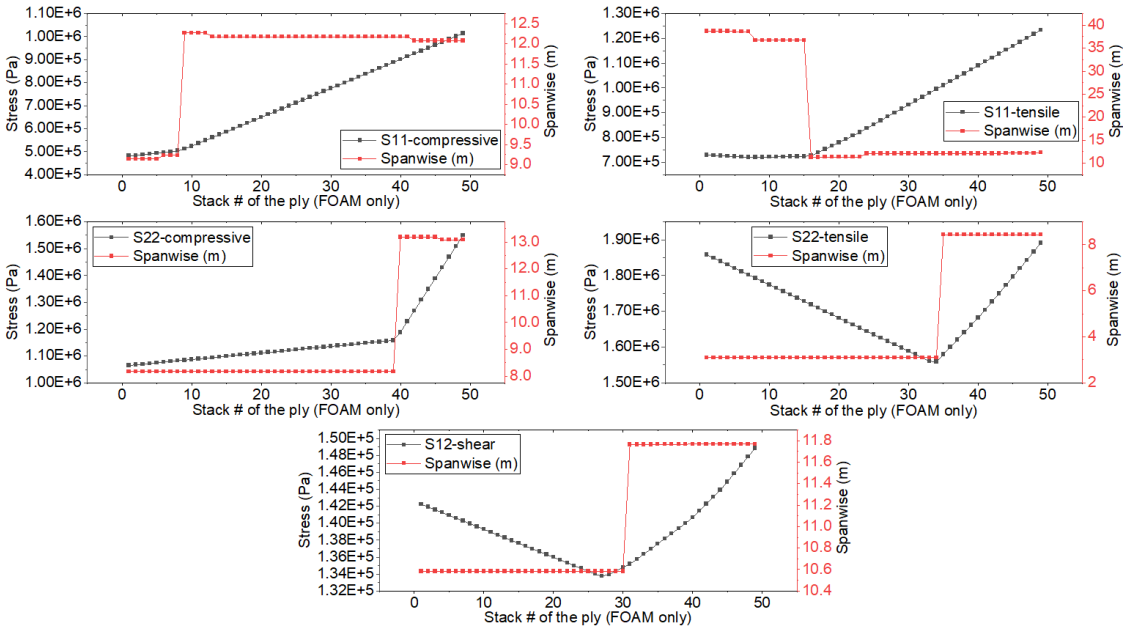

Figure 6-17. Max. direct and shear stress components of FOAM plies on Shear web 1, with correspondence occurrence location on blade spanwise direction. At max. flapwise blade deflection under the LC9.

From the results, all stress components exhibit bi-linear trend across the FOAM core thickness direction, reflecting the characteristics of the stress transfer in the plies of Shear webs when experiencing the shear loading. Besides, this is also consistent with the design purpose of the blade shear web as it withstands torsional loads, which typically can cause a linear variation in stress in structure (here, the FOAM plies).

6.6 Relations between blade stresses and surge motions

From the previous analysis, it is recognised that the max. local Von Mises stress concentration often occurs on the shear webs. In this section, we presented the correlations between the blade Max. Von Mises stress and the surge periods and amplitudes. Here, the resolved Von Mises stress is a global maximum stress, reflecting the largest stress that the blade could potentially experience under each load case.

To provide quantitative evaluation of the amplification of the stress under surge load cases, the blade max. Von Mises stress resolved under the bottom-fixed condition (no platform motion) is retrieved from our previous study (Deng et al., 2024), denoted as

σ_{max_0} for comparison, where σ_{max_0} is 1.035E+08 Pa corresponding to the moment at the infinite.

From Figure 6-18 (a) below, a significant increase by +74.11% of the max. Von Mises stress is observed for the surge period T = 6 s, compared to the σ_{max_0}. While during the surge period T ∈ [9, 12] s, the max. Von Mises stress variations against the σ_{max_0} are less than 20 %. It is clear that the max. Von Mises stress on the shear web is much more prone to a small period (higher frequency) of surge motion. Even though the situation of T = 6 s is not a common load case scenario, this finding still quantifies the potential stress consequences under an 'extreme' load case, showing the capability of the adopted FSI analysis framework.

Similarly, the σ_{max_0} acquired from the previous study is used to give a clear comparison of the variation of the max. Von Mises stress that the blade experiences under the load cases among different surge amplitudes. As can be seen from Figure 6-18 (b), a linear evolution of the max. Von Mises stress across different surge amplitude load cases is observed.

A linear fit is implemented as depicted in red dash line, the correlation coefficient (R^2) of the fitted curve is 0.9822, indicating a strong linear relationship between surge amplitude and the maximum Von Mises stress. This linear relationship allows researchers to easily quantify the impact of variations in surge amplitude on the blade's maximum Von Mises stress. For instance, within the given range of surge amplitudes, an increase in surge amplitude by 1 meter can result in an approximate increase of 5.3E+07 Pa in the maximum Von Mises stress.

Although in LC9, a 6-meter surge amplitude is an uncommon case for FOWT operating conditions, this linear relationship can be effectively captured by our presented FSI framework. This assists designers in quickly determining whether the blade strength can withstand the certain surge amplitudes for new FOWT designs, thereby ensuring the safety and reliability of the blade under various surge conditions.

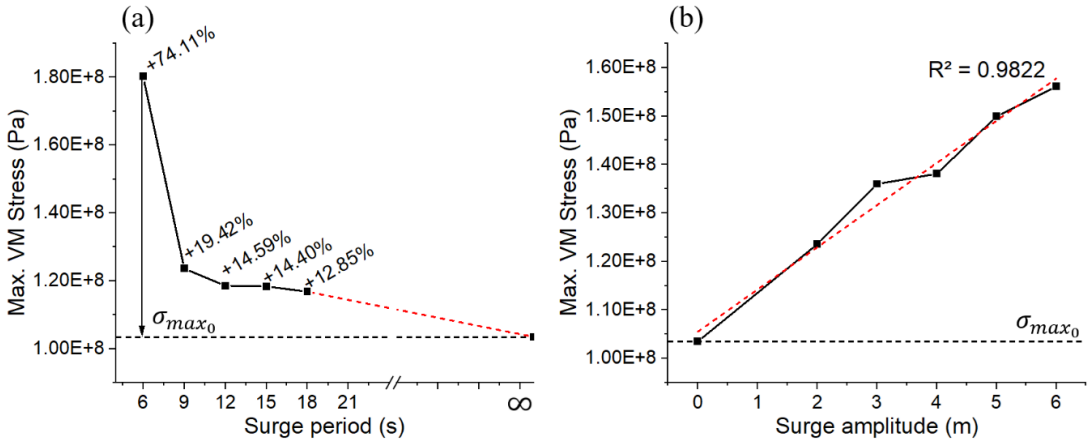

Figure 6-18. Evolution of the (a). max. Von Mises stress vs. different surge periods, (a). max. Von Mises stress vs. different surge amplitudes.

6.7 Concluding Remarks

This study comprehensively investigated the aeroelastic performance of composite wind turbine blades under various surge motions, replicating the platform motions on a NREL 5MW FOWT. The main findings are presented in terms of blade aerodynamic, aeroelastic behaviours and structural stress performances.

The aerodynamic thrust and power from nine load cases are examined, where the variations are quantified by the modified standard deviation $\tilde{\sigma}$. As the surge period increases from 6 s to 18 s for LC1 – LC5, the percentage of the thrust deviation decreases from 22.76% to 7.73%.

While for LC2 – LC9, where the surge amplitude increases from 2 m to 6 m, the $\tilde{\sigma}$ of the thrust increases from 15.36% to 46.22%. The distributions of aerodynamic thrust also support this finding by depicting the thrust force distributions along the blade for each load case. Additionally, a flow disturbance is observed near the blade root and transitional area where r/R = [0.04, 0.16].

An aerodynamic thrust delay with respect to the relative velocity on the FOWT is observed. Due to the interactions between the flexible blade and surrounded wind flow field, the occurrence of the max. thrust, and the largest relative velocity are not exactly synchronised with each other. Especially for the severer load cases, such asymmetry

performance becomes more prominent. This explains partially for the aeroelastic instabilities of an FOWT.

In the FFT analysis for the flapwise deflections in G1 results, the second-order frequencies with non-negligible amplitudes are observed. This suggests that a shorter surge period can introduce additional higher-order frequency excitation to the blade, which is undesired for the blade fatigue durability. This is an extensive topic that can be further investigated in the future.

Due to the intensive interactions between the fluid and structure fields, the blade aerodynamics are strongly influenced by the prescribed surge motion load cases. Generally, the correlation between surge period and amplitude with the blade max. Von Mises stress is opposite.

A linear corelation is found between the max. Von Mises stress and surge amplitude. This can be useful for blade designing purposes as it provides a function with good fit for preliminary determinations of the largest Von Mises stress that a blade may experience under a given surge amplitude. Even though such corelation can be case specific, it still reveals the qualitative relations between the presented variables.

Identifications of stress status on blade component level revealed that the shear webs near the blade root and transitional areas are critical that are prone to local stress concentrations.

This especially necessitates inspections for the blade structural integrity under severe load cases. Besides, the in-ply Von Mises stress distributions on the Shear web 1 comprehensively demonstrated the non-consecutive stress evolution characteristics, with significant drop in stress magnitudes between the plies with different material properties and the noticeable location shifts of max. stress in plies of the FOAM core.

The concluded insights gained from this study contribute to a further understanding of the aeroelastic behaviours of composite wind turbine blades and provide a foundation of effective analysing tools for validating and developing more durable and reliable FOWT systems.

Chapter 7 Blade Structural Optimizations Using Hybrid Active-Sampling Surrogate-Assist NSGA-II Approach

7.1 Overview

With the blade aeroelastics being investigated in previous studies, in this Chapter, a multi-objective structural optimization for the NREL 5MW FOWT composite blade is conducted, aiming to reduce the total weight of the blade while maintaining the peak stress below the allowable stress level of the material under a severe FOWT surge load condition. The focused structural variables are specified in section

To comprehensively consider the anisotropic composite properties and nonlinear structural performance during the optimization process, 59 design variables are considered and thus formulates a high-dimensional optimization problem.

This work proposed a novel hybrid active-sampling surrogate-assisted multi-objective optimization framework. It combines the advantages of conventional high-fidelity code and the rapid-response neural network model, for effectively handling the challenges in multi-objective optimization for high-dimensional systems.

7.2 Problem Description

Existing structural optimization studies have been focusing on, e.g. placement configurations (Pirrera et al., 2012; Barnes & Morozov, 2016), composite material selections (Stegmann & Lund, 2005), the composite laminate thickness (Bottasso et al., 2014; Vianna Neto et al., 2018; Hermansen & Lund, 2024), and interlaminar fibre orientation arrangements (Grujicic et al., 2010; Nomura et al., 2019; Eckrich et al., 2024).

To demonstrate the effectiveness of the proposed workflow, we specifically focused on the design variables of the blade Shear webs and the Spar cap regions. There are two reasons for such selection. First, the weight in the Shear webs and Spar cap account for approximately 40-45 % of the total weight of the blade. Second, these components serve as the primary load-bearing elements, significantly influencing the blade's ability

to support its own weight, counteract flapwise bending moments, and resist torsion-induced shear loads. Consequently, their optimization is critical for ensuring both the ultimate and fatigue performance of FOWT blades (Nijssen & Brøndsted, 2023).

The unidirectional carbon laminates are deployed in the Spar cap region, ranging from 1.5 m to 61.5 m on the blade span. The Shear webs start at the blade span of 1.367 m from the blade root and ends at the blade tip on spanwise of 61.5 m.

The numbering of the Shear webs is defined in Figure 7-1 (a), i.e. Shear web 1 – close to the leading edge, Shear web 2 – close to the trailing edge. The local fibre orientations of the ply stacking are depicted in Figure 7-1 (b) by 1-longditudinal direction, 2-width direction and 3-normal direction with respect to the local shell element. As can be seen from Figure 7-1 (c), the Shear web is composed of two glass fibre reinforced fabrics (Saertex) with a monolithic foam core filling in-between (Resor, 2013), forming a typical sandwich structure as depicted in Figure 7-1 (c). The numbering of Saertex plies is also depicted, which is defined as from the bottom to the top on 3-direction of the local coordinate system.

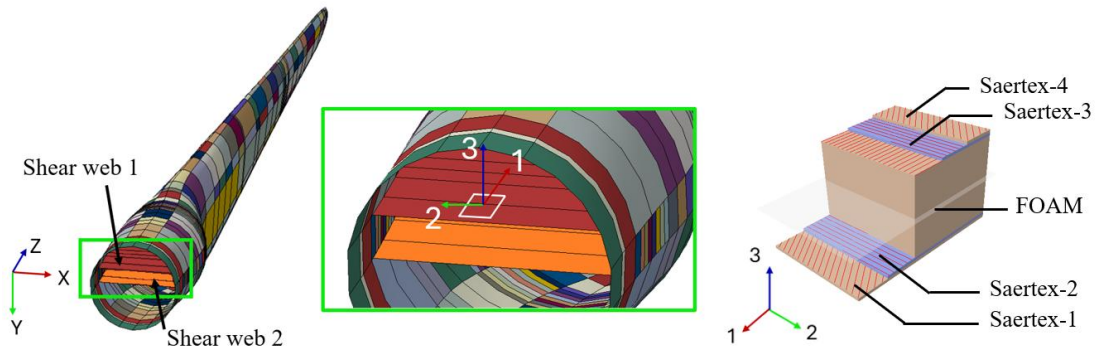

Figure 7-1. Schematic diagram of (a) numbering of Shear webs from global view, (b) local coordinate definition for fibre orientations and (c) ply stacking layup of the sandwich structure.

In next Section, the formulation of the optimization will be given, explaining the optimization objectives and the design variables to be optimized.

The thickness of two fibre reinforced laminates on Spar cap and Shear web, and the fibre orientation of the glass-reinforced laminate on Shear web are the chosen design variables.

7.2.1 Formulation of optimization problem

The optimization objectives are the blade total mass $M(\boldsymbol{x})$ and the max. Von Mises stress $\sigma_{max}(\boldsymbol{x})$ under the given load case LC1. For clarity, the candidate design variables are listed below in Table 7-1.

Table 7-1. Selected variables in structural optimization.

Variable types	Number of variables	Locations
Thickness (Carbon UD)	50	Spar caps
Thickness (Saertex)	4	Shear webs
Thickness (FOAM)	1	Shear webs
Fibre orientation (Saertex)	4	Shear webs
Note: Total number of variables is 59		

The enclosed formulation of the optimization problem with variable limits and objective constraints is defined as:

$$
\begin{gathered}
Minimizing: \\
min\ y = f(\boldsymbol{x}) = [M(\boldsymbol{x}), \sigma_{max}(\boldsymbol{x})] \\
\boldsymbol{x} = [t_{sc1}, \dots, t_{sc50}, t_{sw1}, \dots, t_{sw5}, \theta_{11}, \theta_{12}, \theta_{13}, \theta_{14}, \theta_{21}, \theta_{22}, \theta_{23}, \theta_{24}] \\
\boldsymbol{t}_i^L < \boldsymbol{t}_i < \boldsymbol{t}_i^U, \delta = 1 \pm 0.3 \\
0° < \theta_{11}, \theta_{14}, \theta_{21}, \theta_{24} < 90° \\
-90° < \theta_{12}, \theta_{13}, \theta_{22}, \theta_{23} < 0° \\
\theta_{11} = \theta_{21}, \theta_{12} = \theta_{22}, \theta_{13} = \theta_{23}, \theta_{14} = \theta_{24} \\
s.t. \\
M(\boldsymbol{x}) \leq M_{max} \\
\sigma_{max}(\boldsymbol{x}) \leq \sigma_0
\end{gathered}
$$

where $\boldsymbol{x}$ is the design variable vector and f defines the mapping function between the variable vector $\boldsymbol{x}$ and objectives of $M(\boldsymbol{x})$ and $\sigma_{max}(\boldsymbol{x})$, which are coupled by the weighting factors.

In the scope of this study, the dimension of $\boldsymbol{x}$ is 59. δ is the bounding range for limiting the upper ($\boldsymbol{t}_i^U = 1.3\boldsymbol{t}_i$) and lower ($\boldsymbol{t}_i^L = 0.7\boldsymbol{t}_i$) values for thickness variables. The fibre orientations are bounded in a range of (0, 90) and (-90, 0) degrees for the mirroring Saertex plies with respect to the FOAM core.

For simplicity, the fibre orientations in the same numbering on two Shear web structures are maintained as equal, i.e. $\theta_{11} = \theta_{21}, \theta_{12} = \theta_{22}, \theta_{13} = \theta_{23}, \theta_{14} = \theta_{24}$. The subscript, for example, θ_{21} stands for the fibre orientation of the Saertex-1 ply on the Shear web 2. To constrain the optimization solutions, two physical constraints are defined, i.e. the maximum weight of the blade M_{max}, and the allowable principal stress σ_0. Both constraints are given in the report on the NREL 5MW wind turbine definition, conducted by Sandia Nation Laboratory (Resor, 2013).

7.2.2 Load Case Selection

The term 'load case' in this study can refer to two definitions of boundary conditions implemented on different levels of entities.

The first one, as being discussed in this section, is the loading (motion) specifications to the FOWT platform, resembling the floating platform motions under regular wave conditions.

The second one refers to the aerodynamic force distributions on the blade, which will be used as a boundary condition for the multi-objective structural optimizations of the composite blade.

In this optimization study, the maximum Von Mises stress response of the blade under the severe platform motion condition and aeroelastic loads is one of the focused objectives, we selected a relatively extreme platform surge motion load case, LC1 (Deng et al., 2025), as the benchmark scenario for initializing the optimization. By subjecting the blade design to this extreme load condition, we aimed to ensure that the optimized structure maintains adequate strength while minimizing mass.

The definition of LC1 is given by defining the distance function $H(t)$ that the FOWT platform travels, given as:

$$H(t) = 2\sin\left(\frac{2\pi}{6} \cdot t\right) \tag{7.1}$$

As for the rotor, the rated operation condition of a NREL 5MW reference wind turbine is used to define the boundary and initial aerodynamic conditions, where the incoming freestream velocity $U_0 = 11.4\ m/s$, and the rotational speed $\Omega_0 = 12.1\ RPM$.

Under the given incoming flow, the Reynolds number in the present LC1 is roughly $Re = 1.1\text{E+}07$, thus leads to a highly turbulent problem accompany with intensive flow interactions. The evolution of the instantaneous rotor aerodynamic thrust and the blade tip deflection in reflection to the LC1 load conditions are depicted in Figure 7-2.

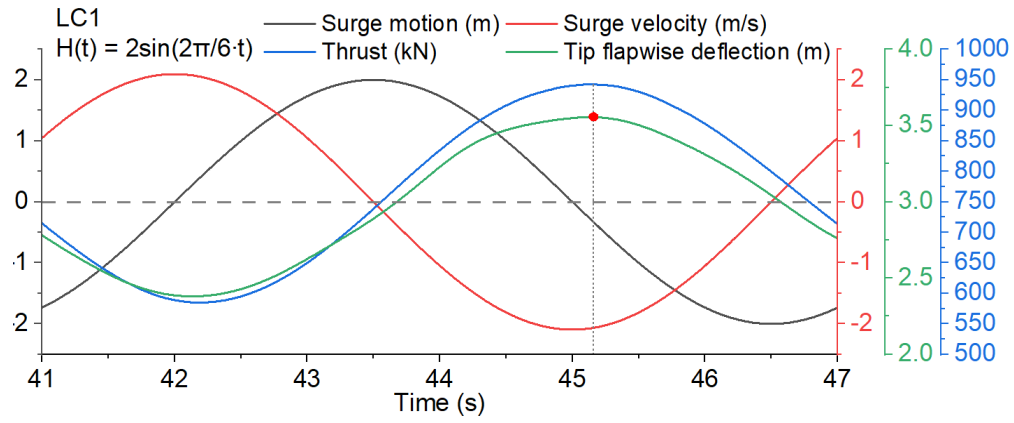

Figure 7-2. Blade aeroelastics evolution under LC1 (Deng et al., 2025).

The most critical moment during the surge motion cycle, occurred at the maximum tip deformation of the blade, is selected for the blade optimization. This ensures that the structural safety margin is sufficiently approached in the blade design, which is a common practice in engineering design.

Meanwhile, due to the time and resource limitations, the way of using the most critical loading simplifies the optimization process by focusing on the critical state of the blade under extreme conditions. This allows a quick demonstration of feasibility and effectiveness of the proposed optimization workflow.

7.3 Results and Analysis – ANN Approximating and Optimised Pareto Solutions

The optimization results with the implementation of the active sampling strategy are discussed and analysed in this section, including the approximating performance of the

ANN surrogate model, the objective responses of the optimized Pareto design candidates, and finalised with a thorough aeroelastic investigation for the Pareto blade designs using the FSI framework.

The specifications for the execution of active sampling process are listed below in Table 7-2. The determination of the active sampling specifications is problem-dependent. The listed specifications have shown a well balance in terms of numerical accuracy and efficiency in the convergence of ANN regression.

Table 7-2. Specifications of active sampling in optimization.

Items	Values	Notes
max_iter	50	Total number of active sampling iteration
k_sample	150	Number of designs for corrections in each active sampling iteration
n_mc	50	Number of MC-dropout in each feedforward for each to-be-corrected design

7.3.1 Evaluation of ANN Performance

The ANN training processes during the active-sampling iterations are firstly evaluated. It is monitored by tracking the evolutions of the training and validation losses throughout the training epochs, as illustrated in Figure 7-3.

An effective learning performance is achieved at the beginning of the training, reflected by the rapid decrease in both training and validation losses. As the number of epochs increases, the loss reduction gradually slows down, where the convergence of losses suggests that ANN model is approaching an optimal representation of the underlying input–output relationships.

The validation loss closely follows the training loss throughout the training process, suggesting good generalization without evident overfitting. Comparing with the 1st active-sampling iteration (blue curves), a significant drop in overall loss at the 50th iteration of active-sampling (green curves) is observed, indicating that the improved data distribution and re-training of ANN have effectively enhanced the model approximation capability to the nonlinear objectives.

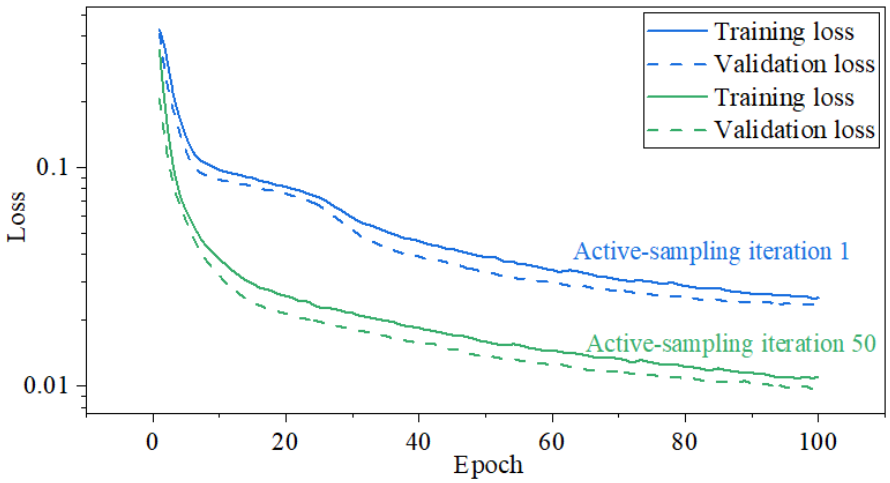

Figure 7-3. Training and validation losses history for ANN training process at the 1st and the 50th iteration of active-sampling.

Then, the coefficient of determination R^2 is evaluated for the ANN, reflecting the fitness of the ANN surrogate model to the training samples. The R^2 is defined as follows, where $\bar{y}_i$ and $\hat{y}_i$ denote the averaged and the predicted value of the objectives, respectively, and y_i is the true value of the objective:

$$R^2 = 1 - \frac{\sum_{i=1}^{n}(y_i - \hat{y}_i)^2}{\sum_{i=1}^{n}(y_i - \bar{y}_i)^2} \tag{7.2}$$

The evolutions of R^2 throughout the active sampling NSGA-II optimization process are depicted in Figure 7-4, showing the ANN improvements with the continuing corrections to the high-σ candidates.

Observing that the R^2 of the blade mass stays around 1.00 throughout the optimization process, while the R^2 of the blade max. Von Mises stress indicates a significant improvement from 0.909 to 0.962, while such increment progressively slowing down from the iterations of 30 to 50, suggesting a model convergence of ANN performance is being approached. This suggested that the approximation of max. Von Mises stress is less accurate due to the stress objective performs with higher nonlinearity. Thus, the uncertainty evaluation for max. Von Mises stress will be focused.

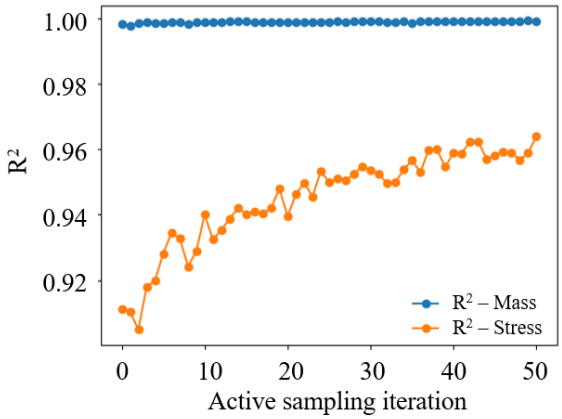

Figure 7-4. R^2 evolutions for blade mass and max. Von Mises stress predictions of the ANN model.

Figure 7-5 compares the ANN performance of approximating the objectives against the FEA validated results at the iteration 1 and 50 during active sampling. It is observed that the ANN is well predicting the mass of the blade for all training samples.

In the comparisons of predicted max. Von Mises stress response at iteration 1, as shown in Figure 7-5 (a), the ANN is failed to capture the responses in the low-stress region where we found there are missing samples in the bottom-left corner regions. While after 50-times of active sampling process, in Figure 7-5 (b), the training samples are effective filled to the low stress region where the NSGA-II Pareto front tends to propagate, improving the ANN approximation performance for more accurate predictions of stress responses of the blade.

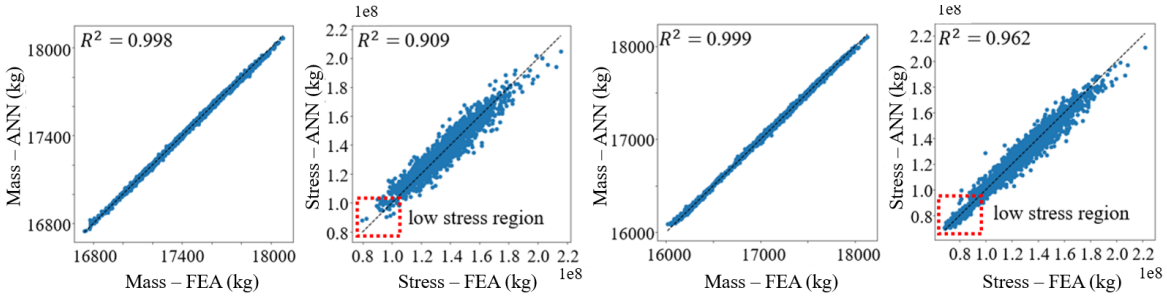

(a). Iteration 1 (b). Iteration 50

Figure 7-5. Approximation performances of ANN at (a) the 1st iteration, and (b) the 50th iteration of optimization process with active sampling.

Figure 7-6 depicts the improvement history of ANN approximation accuracy to the stress objective, by monitoring the maximum uncertainty of stress in Figure 7-6 (a). It

can be seen that the stress prediction uncertainty rapidly decreases from the 1st to 20th active sampling iterations, where such trend gradually slows down during the 30th to 50th iterations that aligning with the trend of the R^2 to the stress objective. The averaged uncertainty of stress drops to 6.74%, reflecting the confidence of approximation of the ANN is increased as the active sampling iteration continues to the final step.

The isotonic regression calibration in Figure 7-6 (b) reflects the averaged relative error between the prediction and the real value of the objective. After the calibrations of uncertainty candidates using FEA cross-validations, the relationship between the uncertainty of stress and the real error of stress evolutes in a stair-wise form, showing the decrease of averaged real stress error during the active sampling process. At the 1st calibration, the uncertainty of stress ranges between 25.60% to 51.95% across all predicted designs, where the calibrated averaged error of stress prediction is 19.16%, showing a low confidence and low accuracy of the surrogate model in objective predictions. As the active sampling continues, at the 50th calibration, the uncertainty of stress significantly drops to a range between 5.81% to 6.44%, with the corresponding averaged prediction error of stress decreasing to 0.78%.

This reflects that the approximation accuracy of the ANN is being improved continuously during the active sampling iteration. The active sampling keeps filtering out the candidates for the FEA corrections, where these candidates exhibit the highest predictive uncertainty of stress by the ANN.

The averaged uncertainty of stress prediction is effectively calibrated by the isotonic regression fitting, converging to a very low percentage around 0.78% between the predicted and the real stress responses on average. This justifies the approach of selecting high-error candidates in each active sampling loop for FEA correction

improves the approximating performance of the ANN model during the NSGA-II optimization.

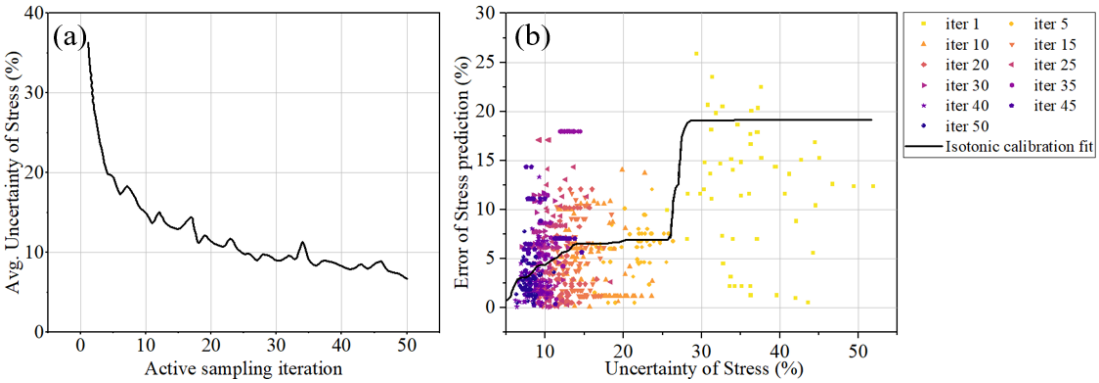

Figure 7-6. (a). Uncertainty and (b). Calibration history for the stress objective during active sampling process.

7.3.2 Pareto front solutions

The Pareto front solutions obtained from 50 iterations in the active sampling process are depicted in Figure 7-7. The yielded Pareto solution (candidate) point clouds from all iterations largely overlap with one another. It can be seen that the mass outliers at iteration 1 (exceeded the mass constraint 17740 kg) were eliminated at the final iteration, i.e. the 50th iteration, showing that the NSGA-II progressively improved the Pareto candidates towards the lighter-weight and lower-stress solution space.

Worth noting that the improvement of Pareto front rapidly diminishes at the early iterations of active sampling process (iterations 1- 10), the solutions become more concentrated comparing to the initial solutions which exhibited a sparser distribution. Start from iteration 20, however, the improvement of the Pareto fronts solutions becomes comparatively insignificant.

The slightly scattered solutions occurred at iteration 40, observing one outlier solution that exceeds the mass constraint. This can be attributed to the exploration mechanism of NSGA-II. Specifically, a number of infeasible or less-optimal solutions are intentionally maintained by the algorithms in order to preserve population diversity and avoid premature convergence. These outliers are subsequently eliminated in the

later iterations, such that by iteration 50 the Pareto front converges smoothly towards the feasible and optimal solution space.

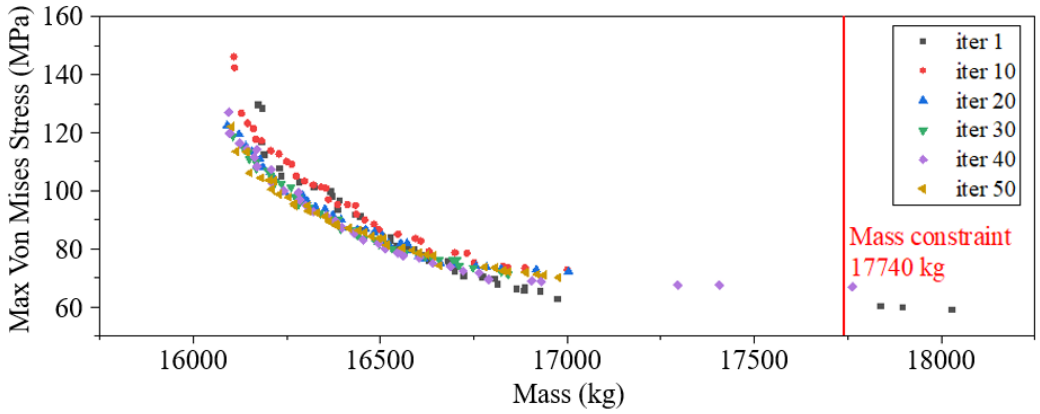

Figure 7-7. Pareto front solutions for each active sampling iteration.

To further examine the accuracy of the optimization with active sampling, as listed in Table 7-3, a thorough cross-validation for all 46 Pareto design candidates using FEA is finalised, with quantifications of the relative error of the objectives between the NSGA-II predicted and FEA responses.

Table 7-3. Predictive error of stress (compared with FEA Cross-validations) for all Pareto candidates at the final active sampling iteration.

Pareto designs 1-12, Errors			**Pareto designs 13-24, Errors**			**Pareto designs 25-36, Errors**			**Pareto designs 37-46, Errors**		
No	*M* (‰)	σ_{max} (%)	*No*	*M* (‰)	σ_{max} (%)	*No*	*M* (‰)	σ_{max} (%)	*No*	*M* (‰)	σ_{max} (%)
1	-0.002	0.3579	*13*	0.000	0.6418	*25*	0.000	1.9789	*37*	-0.001	0.6908
2	-0.001	3.1531	*14*	0.002	3.8960	*26*	0.000	1.7344	*38*	0.003	8.4858
3	-0.002	3.8812	*15*	0.001	1.7044	*27*	-0.002	5.7057	*39*	-0.002	1.4418
4	-0.001	0.5201	*16*	-0.001	1.3576	*28*	0.002	2.9991	*40*	0.002	2.5673
5	0.002	0.8429	*17*	0.002	2.4995	*29*	0.002	1.1418	*41*	-0.003	0.8529
6	-0.001	0.1800	*18*	-0.001	2.4100	*30*	0.003	3.1126	*42*	0.001	4.1811
7	0.002	1.4241	*19*	0.001	1.1669	*31*	0.003	9.0483	*43*	-0.002	3.6553
8	-0.002	1.2012	*20*	-0.002	3.8734	*32*	0.003	7.4170	*44*	-0.002	0.6320
9	-0.002	4.0271	*21*	-0.002	1.5960	*33*	-0.003	8.0212	*45*	-0.001	8.6116
10	-0.002	0.3176	*22*	-0.001	0.9826	*34*	0.002	1.4298	*46*	-0.003	1.2022
11	-0.002	0.1653	*23*	-0.001	3.0416	*35*	0.001	1.5355			
12	-0.001	2.7389	*24*	0.000	1.1075	*36*	0.003	3.5275			

It is observed that the predicted optimized mass objective showed great agreement with the FEA results. For the stress objective, the maximum relative error is 9.05% for the Pareto candidate No. 31, whilst the predictive error of stress for other optimized solutions shown a lower error.

To understand the complexity of the optimization problem, the objective response surfaces for blade mass and max. Von Mises stress with respect to the selected design variables are illustrated in Figure 7-8.

For clarity, the selected representative design variables are: the thicknesses of the first two Carbon (UD) laminates in the Spar cap region (t_{sc1} and t_{sc2}, named as 'Thickness 1' and 'Thickness 2') and two fibre orientation angles of the Saertex laminates in the Shear web (θ_{11} and θ_{12}, named as 'Fibre orientation 1' and 'Fibre orientation 2'). The depicted response surfaces can be regarded as slices of the global response under the 59-dimensional design space.

From Figure 7-8 (a) and (d), the nonlinearities of the objective responses are significant with respect to the varying thicknesses, showing a prominent multi-modal response. Figure 7-8 (c) and (f) further illustrate this behaviour, reflecting the combined nonlinear influences of thicknesses and fibre orientations.

Interestingly, the variations of two fibre orientations (θ_{11} and θ_{12}) have contrasting effects on mass and stress as illustrated in Figure 7-8 (b) and (e). From Figure 7-8 (b), in the case of the small mass and large stress, the Fibre orientation 1 and 2 are deployed close to a +45/-65 degree configuration. While in the case of the large mass and low stress, the configuration of fibre orientation shifts to +38/-90 degree.

The results indicate that when the fibre orientations are deployed closer to a double-bias configuration, the transfer of shear stress and the bending loads in the Shear web structures would be more effective, so that improving the shear stiffness of the Shear web and reduces peak stress. Thereby, the thinner laminates can be employed for weight reduction without compromising structural stiffness.

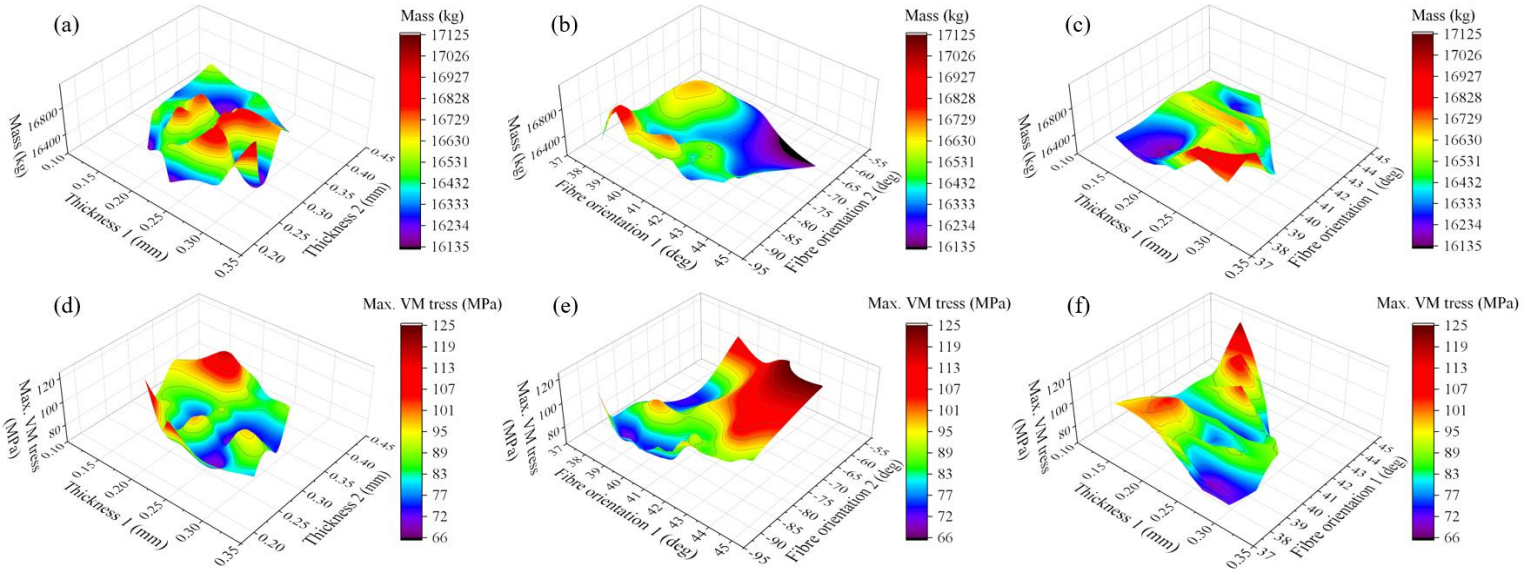

Figure 7-8. Objective response surfaces, numbered with blade (a). mass vs. thicknesses, (b). mass vs. fibre orientations, (c). mass vs. thickness and fibre orientation, (d) max. Von Mises stress vs. thicknesses, (e). max. Von Mises stress vs. fibre orientations, (f). max. Von Mises stress vs. thickness and fibre orientation. Adopting Carbon (UD) laminate thicknesses, and Saertex fibre orientations for plot visualizations.

The analysis through objective response surfaces offers a potential to exploit the interplay between fibre orientation and thickness to identify the optimal trade-offs, where it has seen the stress responses can be significantly adjusted at negligible mass penalty by tunning the fibre orientations under given loadings.

The caveats, however, are that such tailored layups could be case dependent when a fixed loading specification is applied. It may also introduce additional manufacturing complexity and cost, which must be considered when implementing these strategies in practice.

7.3.3 Optimized blade stiffnesses and modal frequencies

Three Pareto design candidates No. 1, No. 23 and No. 46 are selected as examples for the analyses, accounting for the situations of the minimum, middle and maximum blade mass designs, respectively. The objective responses for each optimized blade design are listed below in Table 7-4.

Table 7-4. Comparisons of objective responses of three Parato candidates and the original blade designs.

Pareto candidates	Mass (kg)	Max. Von Mises Stress (MPa)
No. 1 (P1)	16136.96 (-7.37%)	125.013 (+24.11%)
No. 23 (P2)	16448.78 (-5.59%)	84.430 (-16.18%)
No. 46 (P3)	17121.95 (-1.72%)	74.927 (-25.61%)
Original design	17421.80	100.728

The stiffnesses of three selected candidates are depicted in Figure 7-9. It can be seen that the flapwise stiffness (flp_stff), edgewise stiffness (edg_stff), and torsional stiffness (tor_stff) at the blade root regions are enhanced (r/R < 0.2) compared to the original blade. The extensional stiffness (axl_stff) of all three optimized blade designs significantly increased comparing to the original blade.

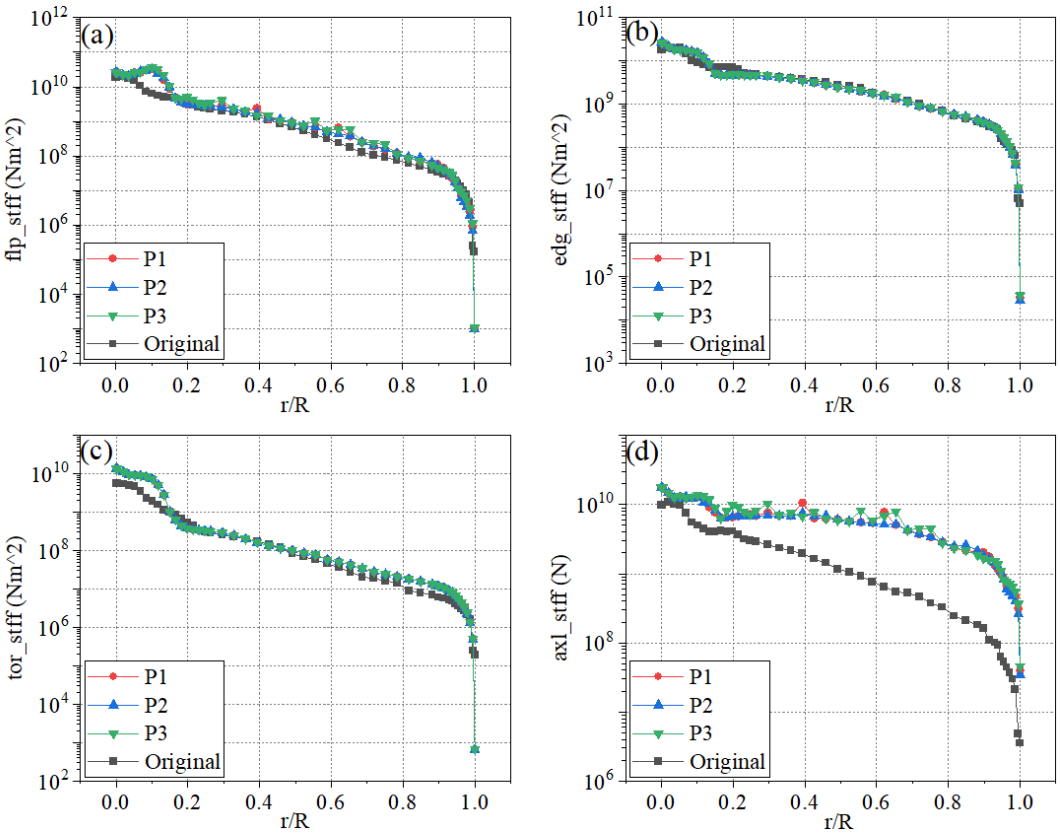

Figure 7-9. Comparisons of (a) flp_stff, (b) edg_stff, (c) tor_stff and (d) axl_stff of the original blade and three optimized blade designs.

Noted that the stiffnesses among three Pareto designs perform an almost identical distribution along the blade spanwise, which is anticipated that such similarity may lead to a little deviation in aerodynamic performances of three Pareto blade designs.

Another evaluation for the blade modal frequencies is finalised. As shown in Figure 7-10, all three optimized blades exhibit nearly identical from the 1st to 6th orders of model frequencies, with small deviations comparing to the original blade design results, especially for the first four modes of the 1st flapwise, edgewise and the 2nd flapwise, edgewise modes. For the 3rd flapwise and the 1st torsional modes, although a slightly larger deviation is observed, the optimized blade results still vary by less than 0.1 Hz, which indicates an insignificant changing of the model properties in optimized blade designs.

This justifies that the optimization process can improve the blade global stiffness distributions while maintaining the modal frequencies within a tight margin of the original blade design, avoiding the adverse influence in the performance of blade resonance resistances.

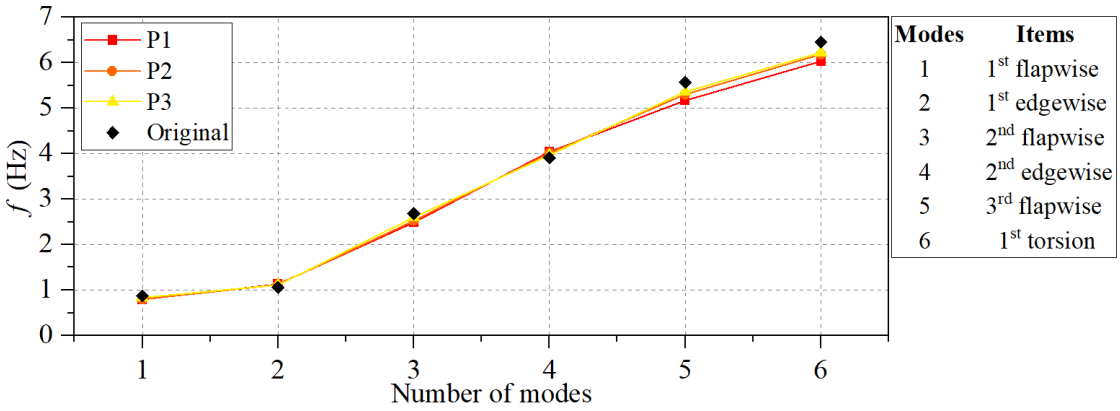

Figure 7-10. Six modes of blade modal frequencies for P1, P2 and P3. With comparisons against the original blade by Resor (2013).

7.4 Results and Analysis – Aeroelastic Analyses for Pareto Candidates

In this section, three Parato candidates as previously listed in Table 7-4 are analysed to evaluate their corresponding aerodynamic performances under different designs.

Full two-way FSI investigations for each Pareto design are finalised, solving for their aeroelastic responses under the platform surge load case of LC1.

It is important to note that the FSI-derived Von Mises stress results of the three Pareto blade designs are expected to differ from those listed in Table 7-4. This discrepancy arises because the aerodynamic loads used during the optimization were calculated based on the stiffness properties of the original blade design.

In contrast, the subsequent aeroelastic analysis incorporates the updated structural parameters, which altered the blade mass and stiffness characteristics, therefore, leading to different stress responses.

7.4.1 Thrust and power

Figure 7-11 shows the thrust and power histories of the P1, P2, and P3 blade designs within one complete surge motion cycle. It is observed that the thrust and power of three Pareto designs are almost identical. This is because of the stiffnesses of three Pareto blade designs are not varied significantly as previously discussed for Figure 7-9. Besides, the thrust and power of three Pareto blade designs slightly outperformed the original blade, especially in the front-half cycle of the surge motion.

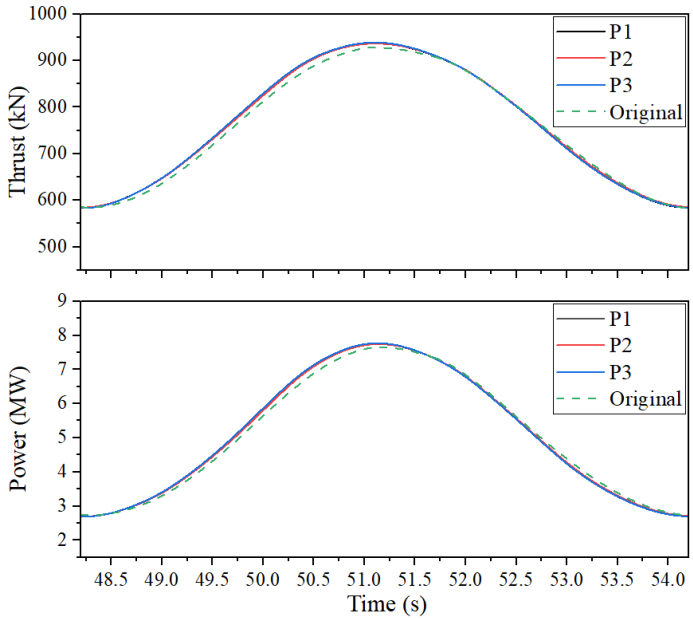

Figure 7-11. Thrust and power history of the optimized Pareto and original blade in one complete surge motion cycle, under the LC1.

A further comparison of aerodynamic thrust distributions among three blade designs and the original blade is given. Considering the instantaneous thrust on the blade when the max. thrust is achieved during the platform surge period, as shown in Figure 7-12, the distributions of thrust for three optimized designs are almost identical.

At the blade span of $r/R = 0.86$, the sectional max. thrust of the optimized blade designs of P1 case is 9050.08 N/m, which slightly outperforms the original blade sectional max. thrust of 8762.31 N/m by approximately 3.28 %.

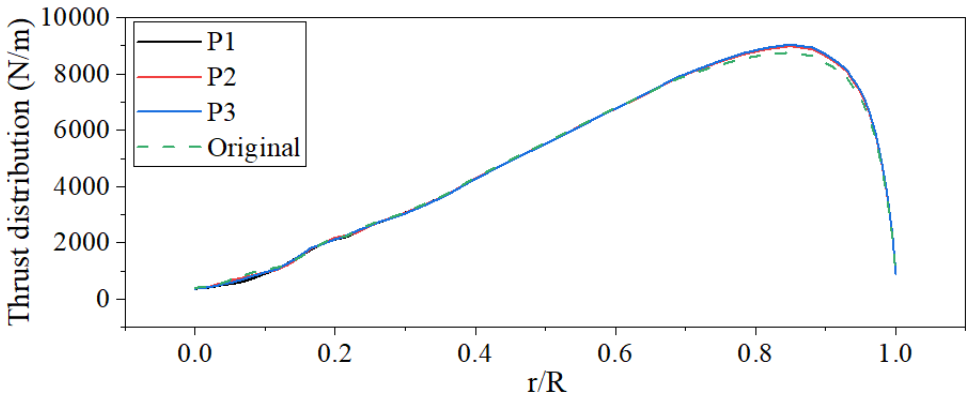

Figure 7-12. Comparisons of instantaneous thrust distributions along the blade for optimized and original designs, at occurrence of the max. thrust.

Figure 7-13 (a), (b) and (c) compares the distributions of pressure coefficient C_P on three cross-sections locations on blade spanwise where $r/R = 0.3$, 0.6 and 0.9, respectively. $x/chord$ denotes the normalized chord distance for each local cross section.

It can be seen that the C_P for each cross section on all designs perform a very close distribution, merely on the blade transitional region where $r/R = 0.3$, an insignificant difference in C_p is seen on the suction surface of the blade where the $x/chord$ ranges between 0.6 and 0.8.

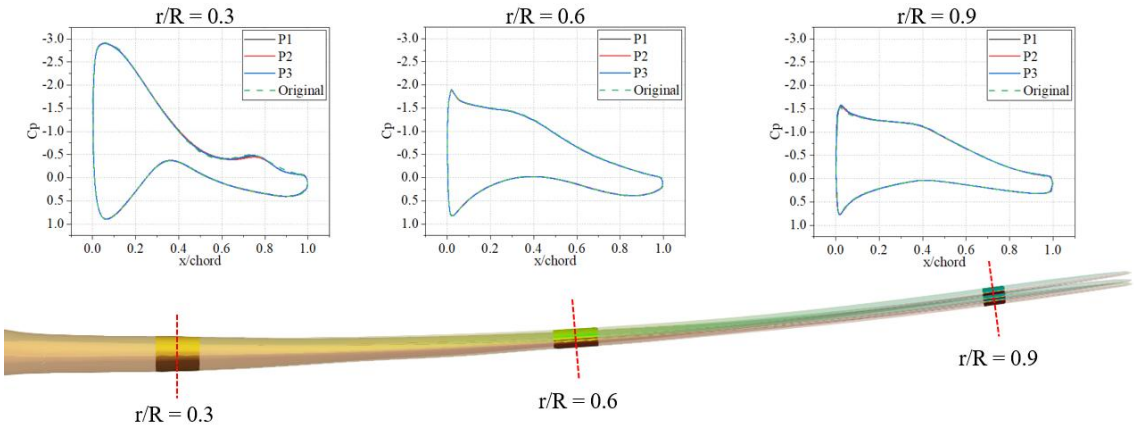

Figure 7-13. Cross-sectional field quantity distributions of C_p, with indications of the deformed blade for each Pareto design. Selecting cross-section location $r/R = 0.3$, 0.6 and 0.9 on the blade spanwise direction.

Such similarity in blade deformations among three Pareto designs are further depicted in Figure 7-14. The deformations of the Pareto blades on flapwise directions are similarly performed with slight variations, however, a prominent smaller deformation is observed comparing to that of the original blade.

This indicates that the optimized blades become stiffer comparing to the original blade design, aligning the previous analysis results for the blade stiffness distributions as presented in Figure 7-9.

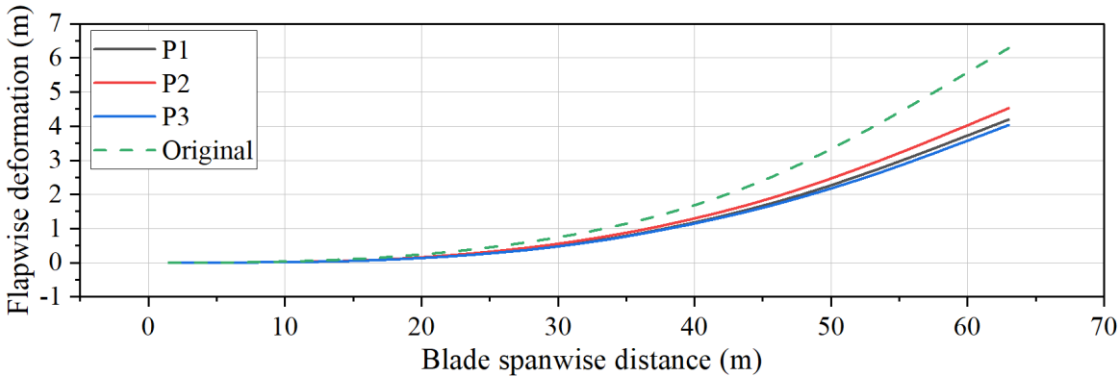

Figure 7-14. Flapwise deformations of the Pareto and the original blade designs.

From above analysis, it is found that the aerodynamic performance of the optimized blades including thrust and power are slightly increased. The pressure distributions are not significantly interfered. However, due to the increase of the blade stiffnesses, the

optimized blades flapwise deformations are significantly decreased, making three Pareto designs feasible that not violating the blade tip-tower clearance constraint.

7.4.2 Stresses on blade shells and Spar caps

In this section, the equilibrium stress and strain fields on different blade structural hierarchy of three Pareto blade designs are presented.

To measure the stress conditions on the blade, the Von Mises yielding criteria (Bertram & Glüge, 2015) is used for stress quantification at first, followed with investigations on their stress components. The definition of Von Mises stress is given as:

$$\sigma_{Von\ Mises} = \sqrt{\frac{(\sigma_{11}-\sigma_{22})^2 + (\sigma_{22}-\sigma_{33})^2 + (\sigma_{33}-\sigma_{11})^2 + 6(\tau_{12}^2 + \tau_{23}^2 + \tau_{31}^2)}{2}} \quad (7.3)$$

σ_{11}, σ_{22} and σ_{33} denotes the normal stress components and the τ_{12}, τ_{23} and τ_{31} stand for the shear stress components with respect to the analysis plane, i.e. here, is the local plane for each S4R element.

The subscript 1 represents the direction in local coordinate aligning with the global blade spanwise direction, similarly, subscript 2 is the local direction perpendicular to 1-direction, and subscript 3 is the surface normal direction of 1-2 plane.

The enveloped Von Mises stresses on the suction and pressure surfaces of three blade designs are firstly depicted in Figure 7-15.

From the contours, it can be seen that the Von Mises stresses on blade suction surface (SS) and pressure surface (PS) for each design are similarly distributed, while a non-consecutive stress transition in the Spar cap regions for the design P1 and P3 is observed. For the design P2, in contrast, such transition in stress is smoother.

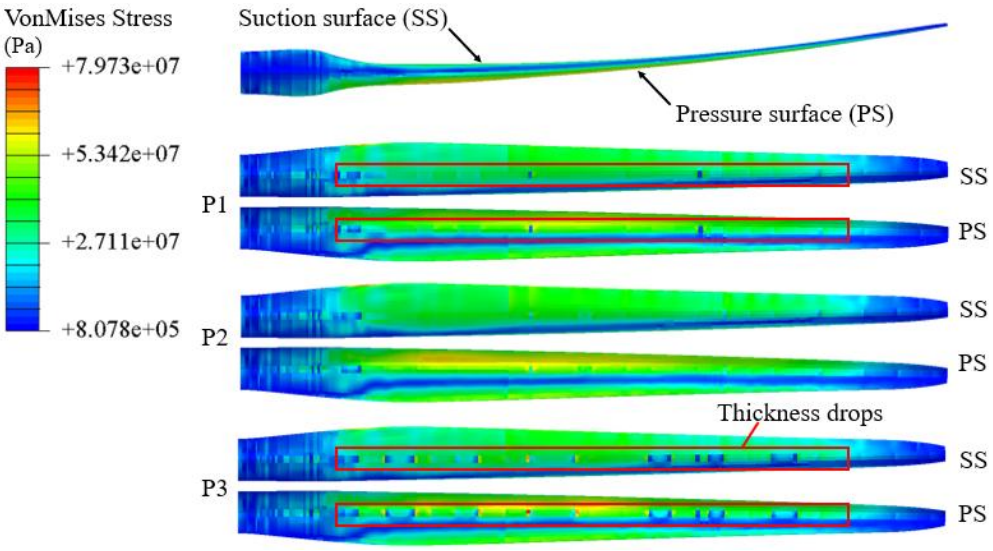

Figure 7-15. Von Mises Stress distributions on blade shells.

The explanation to such difference in stress distributions is the thickness variations of Carbon(UD) laminate in the Spar cap, as depicted in Figure 7-16. A 'sudden-drop' of thickness is observed, particularly from the blade span [10.17, 58.54] m (r/R = [0.165, 0.952]), where the thickness variation of P1 and P3 designs is much significant comparing with P2 design.

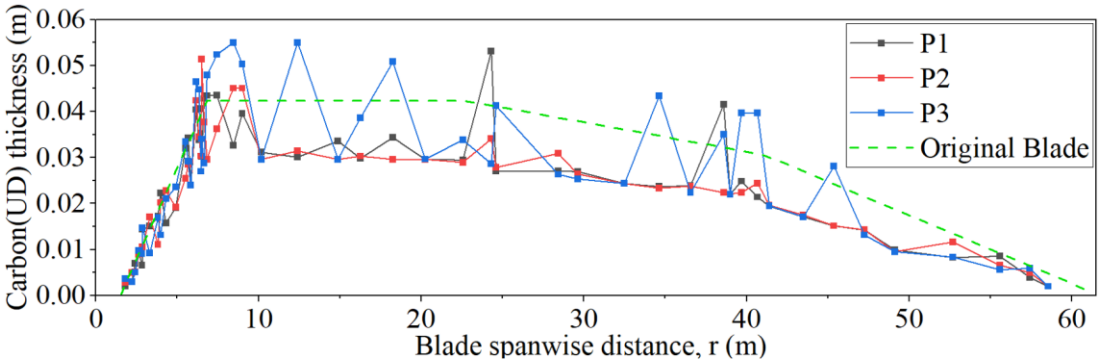

Figure 7-16. Thickness variations of Carbon(UD) along the blade spanwise of three Pareto and original blade designs.

Such 'sudden-drop' in local thickness distributions are completely the results of the NSGA-II optimization, where the thickness variables are individually defined without smoothing constraints being applied for adjacent pairs of local thicknesses.

Additionally, NSGA-II optimization process has the tendency in pushing the thicknesses to their lower bounds, thus achieving a reduction in weight, merely such results are driven mechanically in a numerical approach.

Given the above analysis for the Von Mises stress distribution on the blade shells, the P2 design is potentially a desired solution among the selected Pareto candidates.

The issue of the unsmooth thickness distribution on the Spar cap regions of P1 and P3 blade is that the blades are more likely to be suffered from local stress concentrations.

Also, the hierarchical stress transfer in the Spar cap – Shear web structures can be negatively affected due to the sudden changing thickness, leading to an ineffective load transmission from the blade shells to the blade internal structures, which are discussed subsequently in Section 7.4.3.

7.4.3 Stresses on blade Shear webs

The sandwich-structured Shear webs are subjected to the largest bending loads of the blade and exhibit the maximum Von Mises stress on the blade. Therefore, it is necessary to analyse how the unsmooth thickness variations in Spar cap and the change in Saertex fibre orientations can influence the stress responses on the Shear web structures.

The influence of the Spar cap thickness to the stresses on the Shear web is firstly illustrated in Figure 7-17 (a), showing the stress transmissions in the blade spanwise (BS) regions denoted as BS1 (the blade transitional area, r/R = [0.127, 0.190]), BS2 (r/R = [0.212, 0,424]) and BS3 (r/R = [0.587, 0,787]).

For example, in BS2, a smooth and continuous Von Mises stress transfer path is formed in the case of P2, indicating effective load transmission from the blade shells to the Shear webs.

In contrast, for P1 and P3, the Von Mises stress magnitudes at the connecting interface (between the Spar cap and Shear webs) exhibit an unsmooth distribution compared to that of P2, suggesting an ineffective stress transfer in these cases. For instance, in BS3, the stress transmission on P1 and P3 blades are hindered due to the thickness drops in

their corresponding Spar cap regions. Moreover, the narrower local Shear web width in BS3 further deteriorates the stress transmission, particularly in the P3 blade, where a band-like stress distribution emerges, reflecting a pronounced local stress imbalance.

In BS1 region, the local stress concentration mainly occurred at the connecting interfaces. The stress component distributions in BS1, i.e. the direct stress in local 1-direction, 2-direction and the in-plane stress are shown in Figure 7-17 (b), (c) and (d), respectively, illustrating the contributions to the Von Mises stress of each stress component.

A decreasing trend in both the overall Von Mises stress and local stress components is observed in the BS1 region from P1 to P3 blade designs, despite the fact that the aerodynamic loading conditions remain nearly identical among the three Pareto-optimal blades, as have been discussed in Section 7.4.1.

This counterintuitive trend can be attributed to the increase in structural stiffness from P1 to P3 associated with the gradual increased blade weights.

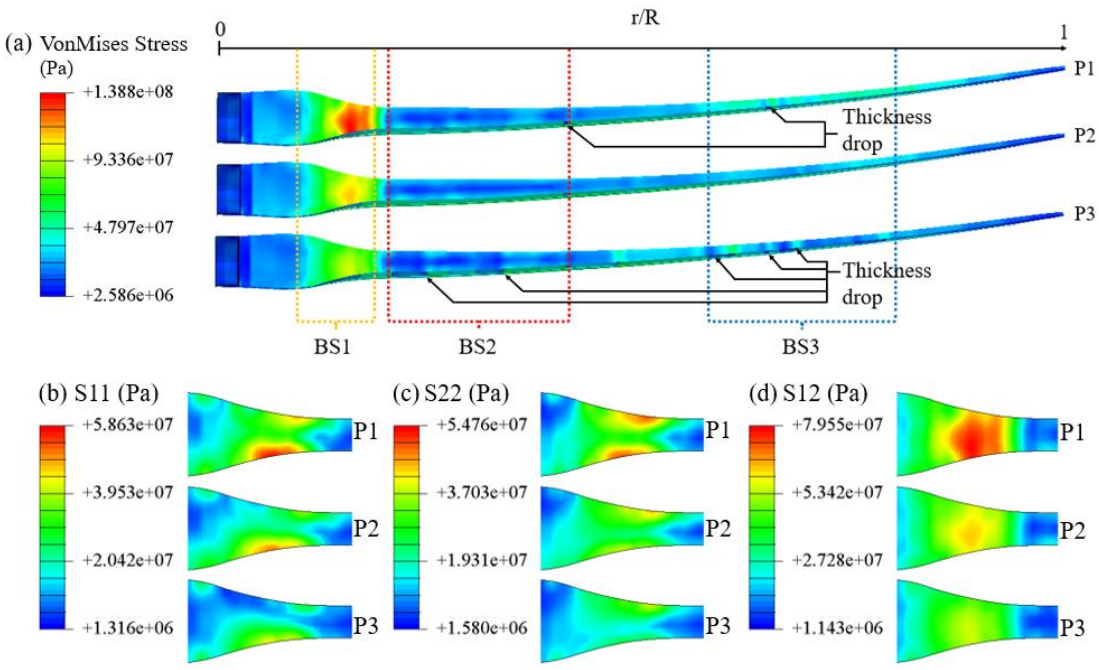

Figure 7-17. (a). Von Mises stress on Shear webs. For the BS1 region, (b) stress component on 1-direction, S11, (c) stress component on 2-direction, S22 and (d) in-plane shear stress S12 distributions on the Shear web 2.

An inspection on thickness variations of Shear web is conducted in the following. Figure 7-18 illustrates the variations of ply thickness with respect to their baseline thickness of each Saertex and FOAM plies in three Pareto blade designs, where the non-dimensional thickness $\bar{t}$ for Saertex plies ($\bar{t}_S$) and FOAM ($\bar{t}_F$) are calculated as:

$$\bar{t}_S = \frac{t_S - t_{S,base}}{t_{S,base}} \tag{7.4}$$

$$\bar{t}_F = \frac{t_F - t_{F,base}}{t_{F,base}} \tag{7.5}$$

In the P1 design, it is observed that the Saertex plies are relatively thin with a slight offset of thickness for Saertex-3, which can be the reason of the largest peak Von Mises stress exhibits on Saertex-3 ply as depicted in Figure 7-19.

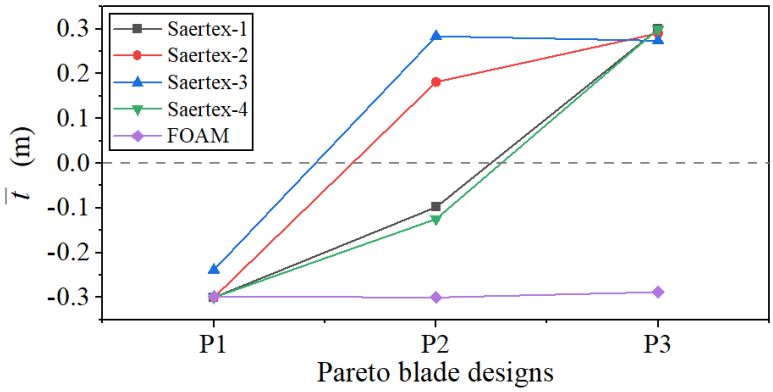

Figure 7-18. Dimensionless thickness variations for each ply in the Shear web.

For P2 design, the Saertex plies are generally thicker while performed an asymmetry distribution, especially for Saertex-2 and Saertex-3. The P3 blade shows an increased thickness with higher uniformity across all four Saertex layers, achieving a more balanced and symmetric laminate configuration.

The thickness variations across three Pareto blade designs can also explain the gradual mitigations of stress concentrations in P2 and P3 designs. Additionally, the FOAM core thicknesses for three Pareto blade designs are nearly identical at a small value, which indicates that the increase of blade mass is mainly due to the thicker plies of

Saertex in the Shear web structures. The stress responses for each Pareto blade design calculated by the FSI framework are listed below in Table 7-5.

Table 7-5. Comparisons of stress responses of three Parato candidates and the original blade designs.

Pareto candidates	**Max. Von Mises Stress (MPa)**
No. 1 (P1)	138.751 (+37.75%)
No. 23 (P2)	112.546 (+11.73%)
No. 46 (P3)	100.233 (-0.49%)
Original design	100.728

Differ from the predicted stresses from the optimization as previously shown in Table 7-4, the stress responses of each Pareto design are larger due to the increased stiffnesses, while the aerodynamic loads are not varied significantly.

Then, we further investigate the influence of fibre orientation to the reduction of stress on Shear web. Since the stress distribution exhibit on the Shear web 1 is slightly lower compared with that on Shear web 2 while the overall distributions are similar, for convenience, the in-ply stress distributions on Shear web 2 are analysed, as shown in Figure 7-19.

The in-ply Von Mises stress distributions in Shear web 2 reveal significant differences across the three Pareto blade designs, depicting four glass fibre reinforced laminates with optimized fibre orientations on Saertex and the monolithic FOAM core.

On the Shear web 2 in P1 blade design, high localised stress concentrations are observed particularly in Saertex-3, reaching a peak Von Mises stress of 1.388×10^{8} Pa. While in the cases of P2 and P3, the stresses are more symmetrically distributed on Saertex-2 and Saertex-3 plies with respect to the FOAM core layers, with an observation of a gradual reduction in peak Von Mises stresses.

This improvement in balanced stress distribution in P2 and P3 designs is attributed to the symmetrically distributed fibre orientations. For example, in P3, the fibre orientations of Saertex-2 and Saertex-3 in P3 are $\theta_{22} = -89.99^{\circ}$ and $\theta_{23} = -88.47^{\circ}$,

respectively, and similarly, the fibre orientations of Saertex-1 and Saertex-4 are $\theta_{21} = 38.89^{\circ}$ and $\theta_{24} = 37.66^{\circ}$, exhibiting a symmetrical distribution with respect to the FOAM core layer, which acts as a compliant interface that mitigates abrupt stress transmissions between adjacent plies in Shear webs.

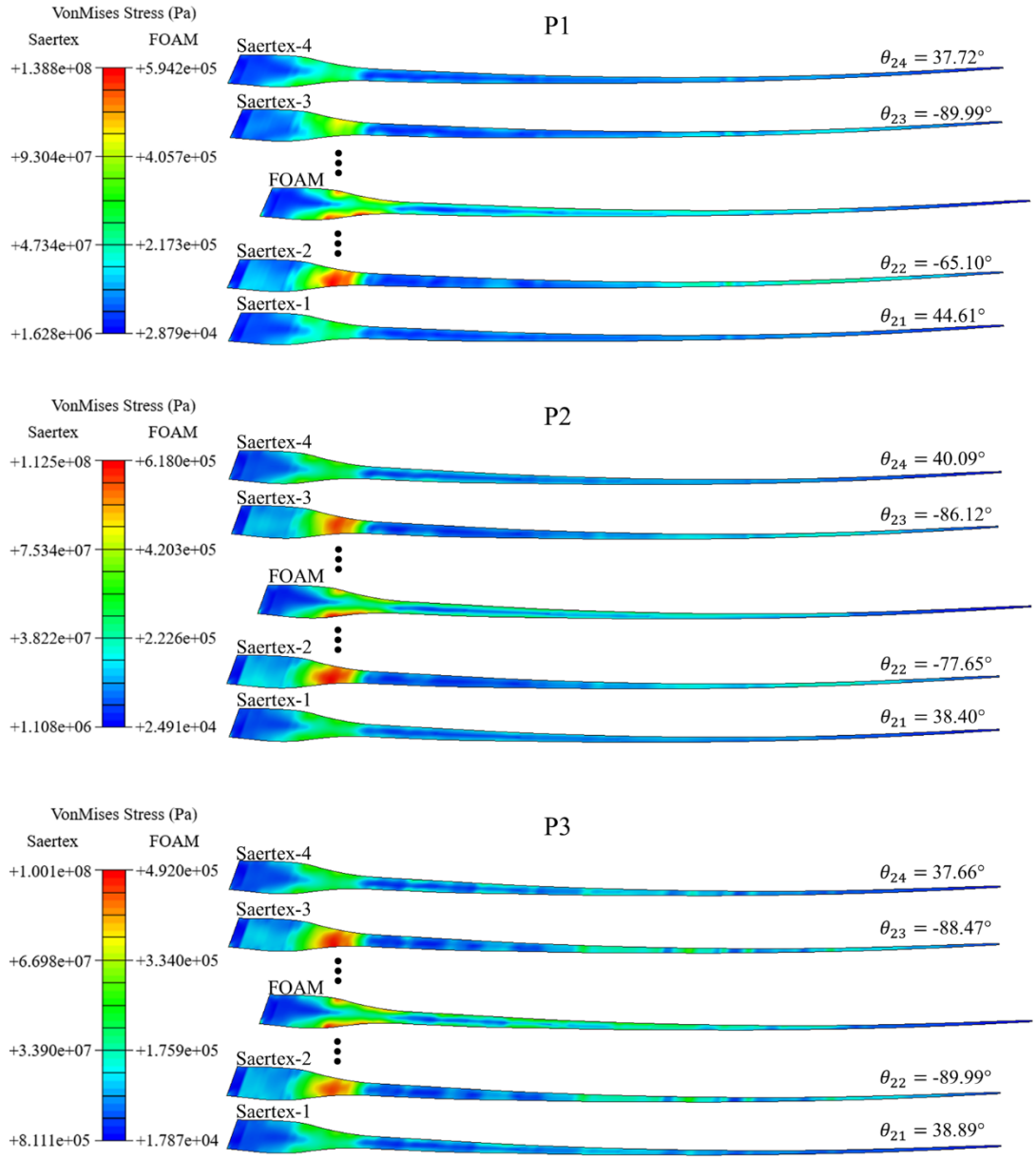

Figure 7-19. In-ply Von Mises stress distributions on Shear web 2 for P1, P2 and P3 blade designs.

In contrast, the P1 blade design exhibits a more pronounced asymmetry in the distributions of fibre orientations ($\theta_{22} = -65.10^{\circ}$ and $\theta_{23} = -89.99^{\circ}$), which may compromise the Shear web load transferring performance and the uniformity of the distributions across the Shear web structure under resisted shear and bending loads.

The symmetrical distribution of fibre orientation is commonly seen in the existing blade design (resembles the double-biased laminate arrangement), which is considered to be a more effective configuration in load transferring across the Shear web structures.

The above results suggest that the reduction in overall and local stresses in the BS1 region is not solely driven by blade weight increase (due to the increase in thickness), but also closely linked to the improved Saertex fibre orientations.

7.5 Concluding Remarks

In this study, we proposed a hybrid active-sampling surrogate-assist multi-objective optimization workflow for the composite wind turbine blade structural performance optimizations. The NSGA-II algorithm is applied for efficient search of global optimal solutions in a typical high-dimensional non-convex problem. To avoid frequent call of conventional codes for calculating the objective responses, an ANN surrogate model is trained for rapid predictions of objectives.

Considering the degradation of generalizability of the ANN model, a self-adapting strategy is implemented to improve the approximating accuracy of the ANN model in the sparse solution space, i.e. the active-sampling approach. The performances of the proposed optimization workflow have been thoroughly evaluated by quantifying the objective prediction accuracy, mainly focusing on the max. Von Mises stress response due to its highly nonlinear response to the varying input design variables.

By conducting a 50-times active-sampling iteration in the optimization process, the ANN approximating performance (quantified by R^2) for the stress objective significantly improved from 0.91 to 0.96. Such improvement is also reflected by evaluating the predicting uncertainty and the calibrated relative error of the stress

objective, where both metrics show great improvement that justifies the effectiveness of the proposed workflow in accurate prediction of the optimized designs.

Then, three Pareto designs of blade with prominent weight reductions and different resultant max. Von Mises stresses are analysed, with comparisons of the equivalent stiffness distributions along the blade spanwise direction, and the modal frequencies among three designs. It has been observed that the overall stiffness and modal frequency properties of the selected optimized blades are performed similarly, with slight deviations to the original blade design.

Further aerodynamic investigations for three optimized blades are conducted. The results show that the wind turbine thrust, power, blade thrust distributions and the pressure coefficients are not exhibiting significant difference comparing to the original blade, while the deformations of the Pareto blades are significantly reduced. This may partially explain the slight increase in thrust and power of the optimized blade designs as the projections of the effective rotor surfaces are slightly increased in P1, P2 and P3 blades, thereby receiving more energy from the incoming freestream.

Meanwhile, the detailed investigations of the stress distributions on multi-hierarchy composite structures are conducted. It is observed that the nonuniform thickness variations on the Spar cap regions (carbon fibre reinforced laminate) would significantly influence the load transfer to the Shear web structures. The in-ply stress magnitudes on the Shear webs are sensitive to the fibre orientations of the Saertex plies. The fibre orientations that are symmetrically deployed on the FOAM core should be identical or closely matched in angle value, so that the abrupt stress transmission can be mitigated.

From the analysis, the P2 design performs as the optimal design under the present load case due to the smooth thickness distributions comparing the other two Pareto designs. For the max. Von Mises stresses, the stress response of P2 is 11.73 % larger than that of the benchmark original blade design. For the blade mass, the P2 design weights at a middle magnitude of 16448.78 kg, which has reached a 5.59 % of weight reduction comparing to the original blade.

In the future work, the essential improvements of the optimization workflow will be conducted, particularly for the composite structure optimizations considering the aero or hydrodynamic loads. The constraints to the design variables and the objective functions will be modified to better adapt the physical characteristics of the system that is being optimized, for example, to apply smoothness constraint to the thickness distribution.

This work provides an efficient and practical reference for the high-dimensional optimization problem of composite wind turbine blades and hold significant value for engineering applications, meanwhile, demonstrating the generality of the workflow and its capabilities in considering actual nonlinear factors during the optimizations which embedded on FSI coupling techniques.

Chapter 8 Conclusions and Future Work

This study consists of three consecutive stages in order to achieve the thorough aeroelastic investigations of the composite blade on a FOWT, and conduct reliable optimization for the composite blade structures to improve the strength-weight performance. A FSI analysis framework that integrates the fully-resolved FEA model is established based on the previously developed two-way CFD-MBD FSI approach by Liu (2019). Main conclusions of each work from Chapter 5 – 7 are given in Section 8.1. Then, recommendations and potential topics for further improvements of current work are provided in Section 8.2.

8.1 Conclusions

8.1.1 A General FSI Framework for Effective Composite Blade Aeroelastic Analysis

This work serves as the foundation for the aeroelastic investigations of the NREL 5MW composite blade structures by showcasing the feasibility of the proposed FSI framework on a bottom-fix configurated turbine, analysed for both the IEC DLC 6.1 and the rated operation condition. To achieve the research objective 1 and 2 as described in Section 1.2, in this study:

1. The aeroelastic performance of the composite structure is effectively considered using the proposed FSI framework, where the transient aerodynamic loads on the composite blades are predicted in CFD using OpenFOAM, with elastic structural response being solved in Multibody dynamics code, MBDyn. Then, the blade kinematics represented by the displacement field is explicitly interpolated to the composite blade model in FEA for detailed stress analysis.

2. The nonlinear aeroelastic response of NREL 5MW composite blade on a bottom-fixed turbine under the IEC DLC 6.1 condition is validated with literature results. A 5.9 % difference in the peak Von Mises stress magnitude from the present work and Miao's work (2019) is seen, with a variance of 7.7 % in the occurrence location of peak Von Mises stress.

3. The critical blade regions experiencing peak stress are identified, mainly locate in the blade transitional area on the localised blade Spar cap and the Shear web structures where r/R = [0.11, 0.21]. A local high stress region near the blade tip in r/R = [0.69, 0.86] is also observed, marking a stress amplification due to the larger imposed aerodynamic thrust loads and the lower stiffness in thinner composite shell structures.

4. This work offered a powerful alternative for the composite structure aeroelastic studies using high-fidelity two-way FSI approach due to its outperformance in computational affordability. The 3D composite stiffness properties are effectively considered by the 6 by 6 diagonal stiffness matrix using the 1D viscoelastic beam elements in MBDyn, ensuring the consistency of structural dynamics between the actual 3D composite structure in FEA and the one solved by the MBDyn code. The scalability of the presented FSI framework is promising and there is no numerical or physical restrictions to the usage of this FSI framework, whilst the most suitable practice of this approach should be focusing on the aero or hydroelastic problems for composite structures.

8.1.2 Investigations of FOWT Platform Motions Impacts to the Composite Blade Stress Behaviours

In the second study, by adopting the proposed FSI analysis framework, we further investigated the aeroelastic responses of the NREL 5MW composite blade on a FOWT. The incoming flow of rated operation condition is adopted. The platform motion is considered where a sinusoidal function is used for describing the excited motion pattern under a regular wave condition. As an essential supplementary work that meets the research objective 1 and 2, in the second study:

1. The correlations between the max. Von Mises stress and the FOWT platform surge motion parameters (i.e. surge amplitude and period) are identified. A sub-exponential decay is seen for the max. stress response with increasing surge period, indicating that in the scope of given load cases, the structural loadings become less sensitive to the low frequency platform motions.

2. For the max. stress response versus surge amplitude, a strong linear correlation is observed, which suggests that the peak stress magnitude is predominantly governed by the magnitude of surge-induced displacements, especially under the large surge period (low frequence) conditions.

3. The instantaneous aerodynamic thrust and power of the FOWT rotor exhibit significantly amplified history during platform surge motions, showing a sensitivity to the change of surge amplitude and period. Nevertheless, the time-averaged thrust remains around 750 kN and the average power output stabilizes around 5 MW, suggesting that the overall aerodynamic performance is not substantially affected by the changes in surge motion parameters.

4. The stress investigations on blade multi-hierarchy component level are conducted. A non-consecutive in-ply Von Mises stress evolution is observed across the Shear web sandwich structure, showing the significant stress magnitude drops and peak stress location shifts between the plies of different composite layers.

8.1.3 Blade Structural Optimizations Using Hybrid Active-Sampling Surrogate-Assist NSGA-II Approach

The third study conducts a multi-objective structural optimization with consideration of realistic aeroelastic predictions of the composite blade on the NREL 5MW FOWT. Given the previous FSI analysis framework has been established, in this study, we can focus on the multi-objective optimization problem for load mitigation (reduction of peak stresses) and weight reduction of a composite blade. The research objective 3, 4 and 5 are met in this study:

1. The NSGA-II is adopted as the ‘search engine’ of the optimization, which has a proven effectiveness in exploring global optimal solution for large-scale parameter system. To accelerate the predictions of objective response, an Artificial Neural Network surrogate model that approximates the time-consuming FEA model is trained and being used during the NSGA-II optimization process.

2. During the study, we observed an out-of-distribution issue of the ANN model in such multi-iteration optimization process, which is a common issue that would happen when optimizing for a high-dimension system. To resolve this issue, an active sampling approach is proposed that has been evaluated to be effective for improving the ANN approximation accuracy during the optimization process.

3. In the scope of this study, 46 Pareto front solutions of blade design are generated. Three Pareto blade designs accounting for the minimum, middle and maximum weight blade designs from the Pareto front solutions are selected for the aeroelastic investigations. Comparing to the original blade, the weight reduction of the Pareto optimized blades is achieved, ranging from 1.72 % to 7.37 %, which is equivalent to around 300 to 1300 kg saving of mass.

4. Due to the increase in stiffnesses of the Pareto blades, the aerodynamic performances of the Pareto blade designs are slightly increased comparing to the original blade design since the projected area to the incoming flow becomes slightly larger.

5. Comparing to the original blade, the peak Von Mises stresses of the selected Pareto blades ranges between -0.49% (100.233 MPa) and +37.75% (138.751 MPa), which are not violating the allowable stress criteria of the material as suggested in the SNL report.

6. By investigating the stress distributions on the local component level and laminate in-ply level, it is observed that a smooth distribution of thickness on the blade Spar cap (mainly for the Carbon UD) is essential for the uniform stress transfer from the blade shell to the internal loading component Shear webs.

8.2 Recommendations for Future Work

This research aims to develop an effective FSI analysis framework that takes the composite material properties into account, then, integrate it with the multi-objective structural optimization that supported with advance machine-learning based surrogate

model, so that the optimizations can be based on realistic load conditions that a composite blade would encounter in a real-world scenario.

However, limitations and shortcomings in this work are also noted, which shall be improved in the future work:

1. All CFD simulations in this study have excluded the effects of the hub, nacelle and tower. Although this can significantly simplify the preparation of the wind turbine geometry and mesh generations for CFD, the potential effect of such treatment remains unclear. For instance, the flow interactions and the aerodynamic load distribution near the blade roots are not realistically reflected in the present CFD models. The tower shadow effect is not considered which might be an important reason of blade fatigues, especially when the platform motion is coupled. As analysed previously, the current 'simplified' rotor CFD model that only focuses the blades may perform similarly to the 'full' wind turbine CFD model in terms of time-averaged aerodynamic performance, while the instantaneous aerodynamics and structural performance would be quite different. Therefore, in future works, a more accurate modelling of the wind turbine is needed to reflect the geometrical details for the considerations of the flow interactions among the wind turbine entities.

2. The FOWT platform surge motions are defined by a sinusoidal function, using the linearly arranged surge amplitudes and periods for the FSI analysis. In the cases when the actual sophisticated sea state and its influence on the blade aeroelastics are of interest, such simplified definition may be inapplicable. However, in the scope of present study, we focus on investigating the relationships between platform motion conditions and blade's aeroelastic performance. Thus, the present work can be a good foundation for the future improvements of, for instance, blade aeroelastic investigations under the realistic irregular sea state condition, where the six-DOF platform motions shall be resolved considering the free-surface interactions in the CFD model.

3. The artificially increased structural damping defined for all FSI analysis is mainly for ensuring the robustness of the numerical simulation, while it may

has suppressed the nonlinearity that a blade would perform under a real-world condition.

4. Due to the limited time and computational resources, the eddy viscous turbulence model is used for predicting the turbulent flow in all CFD simulations. This restricts the scope of the study by limiting the accuracy of turbulence-induced flows and their interactions with the blade surface, particularly in highly unsteady or separated flow regions.

5. Only a limit number of code-to-code comparisons were conducted for the CFD and FEA numerical predictions. The comparisons against the experiment data are only achievable when a model-scale wind turbine is being analysed, while for a full-scale wind turbine, the code-to-code comparisons is often conducted due to the lack of open data for full-scale wind turbines.

6. In this study, the Von Mises criteria is an inappropriate choice for presenting the stress response on orthotropic composite structures, although it appears to be a convenient approach for preliminary comparisons and showing the trend of stress response among different composite blade designs. In the future work, other options such as the maximum stress, Tsai-Wu and Hashin criteria should be applied for further inspections of stress conditions on composite structures, quantifying the stress on the fibre reinforced laminate composites.

7. The structure optimization of the composite blade only discussed on the improvements of structural stiffness when minimising the mass but did not analyse how the structural stability is influenced when exposed under the same extreme load case of LC1. Although, the optimised blade's modal frequencies from the 1^{st} to 6^{th} order are quantified with small deviations from the original blade design, in the future work, the aeroelastic stability of the blade designs should be further investigated by conducting two-way FSI and implement Fast Fourier Transform (FFT) analysis based on their aeroelastic responses in time domain.

References

ABAQUS. (2009). *ABAQUS Analysis User's Manual (v6.6)*.

Akiba, T., Sano, S., Yanase, T., Ohta, T., & Koyama, M. (2019). Optuna: A next-generation hyperparameter optimization framework.

Albanesi, A., Roman, N., Bre, F., & Fachinotti, V. (2018). A metamodel-based optimization approach to reduce the weight of composite laminated wind turbine blades. *Composite Structures*, *194*, 345-356.

Albanesi, A. E., Peralta, I., Bre, F., Storti, B. A., & Fachinotti, V. D. (2020). An optimization method based on the evolutionary and topology approaches to reduce the mass of composite wind turbine blades. *Structural and Multidisciplinary Optimization*, *62*(2), 619-643.

Albazzan, M. A., Harik, R., Tatting, B. F., & Gürdal, Z. (2019). Efficient design optimization of nonconventional laminated composites using lamination parameters: A state of the art. *Composite Structures*, *209*, 362-374.

Allaire, G., & Delgado, G. (2016). Stacking sequence and shape optimization of laminated composite plates via a level-set method. *Journal of the Mechanics and Physics of Solids*, *97*, 168-196.

Ashwill, T. D. (2010). *Sweep-twist adaptive rotor blade: final project report*.

Barnes, R. H., & Morozov, E. V. (2016). Structural optimisation of composite wind turbine blade structures with variations of internal geometry configuration. *Composite Structures*, *152*, 158-167.

Bauchau, O. A., & Nemani, N. (2021). Modeling viscoelastic behavior in flexible multibody systems. *Multibody System Dynamics*, *51*(2), 159-194.

Bazilevs, Y., Hsu, M.-C., Kiendl, J., Wüchner, R., & Bletzinger, K.-U. (2011). 3D simulation of wind turbine rotors at full scale. Part II: Fluid-structure interaction modeling with composite blades. *International Journal for Numerical Methods in Fluids*, *65*, 236-253.

Berg, J. C., & Resor, B. R. (2012). *Numerical manufacturing and design tool (NuMAD v2. 0) for wind turbine blades: user's guide*.

Bertram, A., & Glüge, R. (2015). *Solid Mechanics: Theory, Modeling, and Problems*.

Bhosekar, A., & Ierapetritou, M. (2018). Advances in surrogate based modeling, feasibility analysis, and optimization: A review. *Computers & Chemical Engineering*, *108*, 250-267.

Bir, G., & Migliore, P. (2004). *Preliminary structural design of composite blades for two-and three-blade rotors*.

Bir, G. S. (2001). Computerized Method for Preliminary Structural Design of Composite Wind Turbine Blades. *Journal of Solar Energy Engineering*, *123*(4), 372-381.

Blasques, J. P. A. A. (2011). Optimal design of laminated composite beams.

Bonnie, J., & Jason, J. (2016). *FAST v8 documentation*. https://www.nrel.gov/docs/libraries/wind-docs/readme_fast8-pdf.pdf?sfvrsn=4f3e4e51_1

Bottasso, C. L., Campagnolo, F., Croce, A., Dilli, S., Gualdoni, F., & Nielsen, M. B. (2014). Structural optimization of wind turbine rotor blades by multilevel sectional/multibody/3D-FEM analysis. *Multibody System Dynamics*, *32*(1), 87-116.

Camarena, E., Anderson, E., Paquette, J., Bortolotti, P., Feil, R., & Johnson, N. (2021). Land-based wind turbines with flexible rail transportable blades–Part II: 3D FEM design optimization of the rotor blades. *Wind Energy Science Discussions*, *2021*, 1-28.

Camarena, E., Anderson, E., Paquette, J., Bortolotti, P., Feil, R., & Johnson, N. (2022). Land-based wind turbines with flexible rail-transportable blades – Part 2: 3D finite element design optimization of the rotor blades. *Wind Energ. Sci.*, *7*(1), 19-35.

Cao, Z., Zhang, Y., Wang, X., & Liu, C. (2025). Optimisation of large-Scale composite blade layup using coupled finite element method and machine learning. *Composite Structures*, *364*, 119150.

Celik, I. B., Ghia, U., Roache, P. J., & Freitas, C. J. (2008). Procedure for estimation and reporting of uncertainty due to discretization in CFD applications. *Journal of fluids Engineering-Transactions of the ASME*, *130*(7).

Cesnik, C. E. S., & Hodges, D. H. (1997). VABS: a new concept for composite rotor blade cross‐sectional modeling. *Journal of the American helicopter society*, *42*(1), 27-38.

Chandar, D., & Gopalan, H. (2016). *Comparative Analysis of the Arbitrary Mesh Interface(AMI) and Overset Methods for Dynamic Body Motions in OpenFOAM*.

Chemengich, S. J., Kassab, S. Z., & Lotfy, E. R. (2022). Effect of the variations of the gap flow guides geometry on the savonius wind turbine performance: 2D and 3D studies. *Journal of Wind Engineering and Industrial Aerodynamics*, *222*, 104920.

Chen, H., Yu, W., & Capellaro, M. (2010). A critical assessment of computer tools for calculating composite wind turbine blade properties. *Wind Energy*, *13*(6), 497-516.

Chen, J., Wang, Q., Shen, W. Z., Pang, X., Li, S., & Guo, X. (2013). Structural optimization study of composite wind turbine blade. *Materials & Design (1980-2015)*, *46*, 247-255.

Cheng, P., Huang, Y., & Wan, D. (2019). A numerical model for fully coupled aero-hydrodynamic analysis of floating offshore wind turbine. *Ocean Engineering*, *173*, 183-196.

Chitteth Ramachandran, R., Desmond, C., Judge, F., Serraris, J. J., & Murphy, J. (2022). Floating wind turbines: marine operations challenges and opportunities. *Wind Energ. Sci.*, *7*(2), 903-924.

Couto, L. d. L., Moreira, N. E., Saito, J. Y. d. O., Hallak, P. H., & Lemonge, A. C. C. (2023). Multi-Objective Structural Optimization of a Composite Wind Turbine Blade Considering Natural Frequencies of Vibration and Global Stability. *Energies*.

Cruz, A. S., Caldas, L. R., Mendes, V. M., Mendes, J. C., & Bastos, L. E. G. (2024). Multi-objective optimization based on surrogate models for sustainable building design: A systematic literature review. *Building and Environment*, *266*, 112147.

Danovaro, R., Bianchelli, S., Brambilla, P., Brussa, G., Corinaldesi, C., Del Borghi, A., Dell'Anno, A., Fraschetti, S., Greco, S., Grosso, M., Nepote, E., Rigamonti, L., & Boero, F. (2024). Making eco-sustainable floating offshore wind farms:

Siting, mitigations, and compensations. *Renewable and Sustainable Energy Reviews*, *197*, 114386.

de Almeida, I. T., Lapa, G. V. P., Gay Neto, A., & de Almeida, S. F. M. (2025). Design and extreme structural analysis of wind turbine blades: Beam and shell model comparison and discussion for a 10-MW reference turbine. *Engineering Structures*, *334*, 120155.

De Vaal, J. B., Hansen, M. L., & Moan, T. (2014). Effect of wind turbine surge motion on rotor thrust and induced velocity. *Wind Energy*, *17*(1), 105-121.

Deb, K., Pratap, A., Agarwal, S., & Meyarivan, T. (2002). A fast and elitist multiobjective genetic algorithm: NSGA-II. *IEEE Transactions on Evolutionary Computation*, *6*(2), 182-197.

Deng, Z., Xiao, Q., Huang, Y., Yang, L., & Liu, Y. (2024). A general FSI framework for an effective stress analysis on composite wind turbine blades. *Ocean Engineering*, *291*, 116412.

Deng, Z., Xiao, Q., Yang, L., Liu, Y., & Wang, E. (2025). Aeroelastic investigations of composite blade on floating offshore wind Turbine: Insights into stress responses on multi-hierarchy blade structures. *Ocean Engineering*, *330*, 121305.

Dewan, A., Tomar, S. S., Bishnoi, A. K., & Singh, T. P. (2023). Computational fluid dynamics and turbulence modelling in various blades of Savonius turbines for wind and hydro energy: Progress and perspectives. *Ocean Engineering*, *283*, 115168.

Dose, B., Rahimi, H., Herráez, I., Stoevesandt, B., & Peinke, J. (2018). Fluid-structure coupled computations of the NREL 5 MW wind turbine by means of CFD. *Renewable Energy*, *129*, 591-605.

Eckrich, M., Arrabiyeh, P. A., Dlugaj, A. M., & May, D. (2024). An anisotropic topology optimization procedure for continuous fiber reinforced polymer structures with biaxial fiber layout for improved intersection point design. *Composite Structures*, *337*, 118064.

Esteban, M. D., Diez, J. J., López, J. S., & Negro, V. (2011). Why offshore wind energy? *Renewable Energy*, *36*(2), 444-450.

Fagan, E. M., De La Torre, O., Leen, S. B., & Goggins, J. (2018). Validation of the multi-objective structural optimisation of a composite wind turbine blade. *Composite Structures*, *204*, 567-577.

Ferreira, C., Yu, W., Sala, A., & Viré, A. (2022). Dynamic inflow model for a floating horizontal axis wind turbine in surge motion. *Wind Energ. Sci.*, *7*(2), 469-485.

Finnegan, W., Jiang, Y., Dumergue, N., Davies, P., & Goggins, J. (2021). Investigation and Validation of Numerical Models for Composite Wind Turbine Blades. *Journal of Marine Science and Engineering*, *9*(5), 525.

Ghiasi, H., Pasini, D., & Lessard, L. (2009). Optimum stacking sequence design of composite materials Part I: Constant stiffness design. *Composite Structures*, *90*(1), 1-11.

Ghiringhelli, G. L., Masarati, P., & Mantegazza, P. (2000). Multibody implementation of finite volume C beams. *AIAA journal*, *38*(1), 131-138.

Golzari, A., Haghighat Sefat, M., & Jamshidi, S. (2015). Development of an adaptive surrogate model for production optimization. *Journal of Petroleum Science and Engineering*, *133*, 677-688.

Greco, L., Testa, C., & Bianchini, A. (2023). Chapter 23 - Multifidelity simulation tools for modern wind turbines. In T. M. Letcher (Ed.), *Wind Energy Engineering (Second Edition)* (pp. 333-348). Academic Press. https://doi.org/https://doi.org/10.1016/B978-0-323-99353-1.00013-X

Grujicic, M., Arakere, G., Pandurangan, B., Sellappan, V., Vallejo, A., & Ozen, M. (2010). Multidisciplinary Design Optimization for Glass-Fiber Epoxy-Matrix Composite 5 MW Horizontal-Axis Wind-Turbine Blades. *Journal of Materials Engineering and Performance*, *19*(8), 1116-1127.

Gunwant, D., & Bisht, N. (2024). Multiscale Modelling of Polymer Composites. In S. K. Sethi, H. S. Gupta, & A. Verma (Eds.), *Polymer Composites: From Computational to Experimental Aspects* (pp. 55-81). Springer Nature Singapore. https://doi.org/10.1007/978-981-97-0888-8_3

Guo, F., Song, B., Mao, Z., & Tian, W. (2020). Experimental and numerical validation of the influence on Savonius turbine caused by rear deflector. *Energy*, *196*, 117132.

Guo, Y., Mahadevan, S., Matsumoto, S., Taba, S., & Watanabe, D. (2023). Investigation of Surrogate Modeling Options with High-Dimensional Input and Output. *AIAA journal*, *61*(3), 1334-1348.

Haddad, H. Z., Mohamed, M. H., Shabana, Y. M., & Elsayed, K. (2023). Optimization of Savonius wind turbine with additional blades by surrogate model using artificial neural networks. *Energy*, *270*, 126952.

Haselbach, P. U., & Berring, P. (2024). Spar Cap/Shear Web Debonding Under Fatigue Loading Studied On The DTU 12.6m Wind Turbine Blade. *Procedia Structural Integrity*, *57*, 169-178.

Hendrycks, D., & Gimpel, K. (2016). Gaussian error linear units (gelus). *arXiv preprint arXiv:1606.08415*.

Hermansen, S. M., & Lund, E. (2024). Multi-material and thickness optimization of a wind turbine blade root section. *Structural and Multidisciplinary Optimization*, *67*(7), 107.

Herrema, A. J., Kiendl, J., & Hsu, M. C. (2019). A framework for isogeometric‐analysis‐based optimization of wind turbine blade structures. *Wind Energy*, *22*(2), 153-170.

Hodges, D. H., & Dowell, E. H. (1974). *Nonlinear equations of motion for the elastic bending and torsion of twisted nonuniform rotor blades*.

[Record #465 is using a reference type undefined in this output style.]

Jasak, H. (1996). Error analysis and estimation in the Finite Volume method with applications to fluid flows.

Jasak, H., Jemcov, A., & Tukovic, Z. (2007). OpenFOAM: A C++ library for complex physics simulations.

Jasak, H., & Tukovic, Z. (2006). Automatic mesh motion for the unstructured Finite Volume Method. *Transactions of FAMENA*, *30*, 1-20.

Jiang, Z. (2021). Installation of offshore wind turbines: A technical review. *Renewable and Sustainable Energy Reviews*, *139*, 110576.

Jin, L., Chen, Y., Tang, X., Zhang, J., & Wang, Z. (2023). A numerical study on damage characteristics in composite tapered laminates under cyclic loading with different stress ratios. *Composite Structures*, *311*, 116777.

Jonkman, J., Butterfield, S., Musial, W., & Scott, G. (2009). *Definition of a 5-MW reference wind turbine for offshore system development*.

Kalmikov, A. (2017). Wind Power Fundamentals. In (pp. 17-24). https://doi.org/10.1016/B978-0-12-809451-8.00002-3

Kapusuzoglu, B., Mahadevan, S., Matsumoto, S., Miyagi, Y., & Watanabe, D. (2022). Adaptive surrogate modeling for high-dimensional spatio-temporal output. *Structural and Multidisciplinary Optimization*, *65*(10), 300.

Kassapoglou, C. (2013). *Design and analysis of composite structures: with applications to aerospace structures*. John Wiley & Sons.

Keprate, A., Bagalkot, N., Siddiqui, M. S., & Sen, S. (2023). Reliability analysis of 15MW horizontal axis wind turbine rotor blades using fluid-structure interaction simulation and adaptive kriging model. *Ocean Engineering*, *288*, 116138.

Kim, S.-H., Bang, H.-J., Shin, H.-K., & Jang, M.-S. (2014). Composite Structural Analysis of Flat-Back Shaped Blade for Multi-MW Class Wind Turbine. *Applied Composite Materials*, *21*(3), 525-539.

Kusuma, Y. F., Fuadi, A. P., Hakim, B. A., Sasmito, C., Nugroho, A. C. P. T., Khoirudin, M. H., Priatno, D. H., Tjolleng, A., Wiranto, I. B., Al Fikri, I. R., Muttaqie, T., & Prabowo, A. R. (2024). Navigating challenges on the path to net zero emissions: A comprehensive review of wind turbine technology for implementation in Indonesia. *Results in Engineering*, *22*, 102008.

Lago, L. I., Ponta, F. L., & Otero, A. D. (2013). Analysis of alternative adaptive geometrical configurations for the NREL-5 MW wind turbine blade. *Renewable Energy*, *59*, 13-22.

Laird, D., Montoya, F., & Malcolm, D. (2005, 2005). Finite element modeling of wind turbine blades.

Lanzafame, R., & Messina, M. (2012). BEM theory: How to take into account the radial flow inside of a 1-D numerical code. *Renewable Energy*, *39*(1), 440-446.

Ledoux, J., Riffo, S., & Salomon, J. (2021). Analysis of the blade element momentum theory. *SIAM Journal on Applied Mathematics*, *81*(6), 2596-2621.

Lee, C.-H. (2018). Rough boundary treatment method for the shear-stress transport k - ω model. *Engineering Applications of Computational Fluid Mechanics*, *12*(1), 261-269.

Lee, D., Kang, Y.-e., Kim, D.-H., & Yee, K. (2022, 2022). Improved Surrogate-based Design Optimization of Composite Rotor Blades.

Lee, H., & Lee, D.-J. (2019). Effects of platform motions on aerodynamic performance and unsteady wake evolution of a floating offshore wind turbine. *Renewable Energy*, *143*, 9-23.

Lee, S.-L., & Shin, S. J. (2022). Structural design optimization of a wind turbine blade using the genetic algorithm. *Engineering Optimization*, *54*(12), 2053-2070.

Li, H., & Bachynski, E. E. (2021). Experimental and numerical investigation of nonlinear diffraction wave loads on a semi-submersible wind turbine. *Renewable Energy*, *171*, 709-727.

Li, T., Zhang, Y., Yang, Q., Zhou, X., Zhang, Z., & Wang, T. (2025). Unsteady aerodynamic characteristics of a floating offshore wind turbine in propeller state. *Renewable Energy*, *246*, 122861.

Lienard, C., Boisard, R., & Daudin, C. (2020). Aerodynamic behavior of a floating offshore wind turbine. *AIAA journal*, *58*(9), 3835-3847.

Liu, X., Qin, J., Zhao, K., Featherston, C. A., Kennedy, D., Jing, Y., & Yang, G. (2023). Design optimization of laminated composite structures using artificial neural network and genetic algorithm. *Composite Structures*, *305*, 116500.

Liu, Y. (2018). A CFD study of fluid-structure interaction problems for floating offshore wind turbines.

Liu, Y., Xiao, Q., Incecik, A., & Peyrard, C. (2019). Aeroelastic Analysis of a Floating Offshore Wind Turbine in Platform-induced Surge Motion using a Fully Coupled CFD-MBD Method. *Wind Energy*, *22*(1), 1-20.

Liu, Y., Xiao, Q., Incecik, A., Peyrard, C., & Wan, D. (2017). Establishing a fully coupled CFD analysis tool for floating offshore wind turbines. *Renewable Energy*, *112*, 280-301.

Liu, Z., Liang, J., He, Z., Liu, X., Liu, H., & Shao, Z. (2024). A developed fatigue analysis approach for composite wind turbine blade adhesive joints using finite-element submodeling technique. *Engineering Failure Analysis*, *164*, 108701.

Lobitz, D. W., Veers, P. S., Eisler, G. R., Laino, D. J., Migliore, P. G., & Bir, G. (2001). The use of twist-coupled blades to enhance the performance of horizontal axis wind turbines.

Loshchilov, I., & Hutter, F. (2017). Decoupled weight decay regularization. *arXiv preprint arXiv:1711.05101*.

Luo, L., Zhang, B., Zhang, G., Li, X., Fang, X., Li, W., & Zhang, Z. (2021). Rapid prediction and inverse design of distortion behaviors of composite materials using artificial neural networks. *Polymers for Advanced Technologies*, *32*(3), 1049-1060.

Luo, W., Liu, W., Chen, S., Zou, Q., & Song, X. (2024). Development and Application of an FSI Model for Floating VAWT by Coupling CFD and FEA. *Journal of Marine Science and Engineering*, *12*(4), 683.

Mark, H., & Feng, Z. (2023). *GLOBAL WIND REPORT 2023*. https://gwec.net/globalwindreport2023/

Martulli, L. M., Diani, M., Sabetta, G., Bontumasi, S., Colledani, M., & Bernasconi, A. (2025). Critical review of current wind turbine blades' design and materials and their influence on the end-of-life management of wind turbines. *Engineering Structures*, *327*, 119625.

Masarati, P., Morandini, M., & Mantegazza, P. (2014). An Efficient Formulation for General-Purpose Multibody/Multiphysics Analysis. *Journal of Computational and Nonlinear Dynamics*, *9*, 041001.

Meng, H., Jin, D., Li, L., & Liu, Y. (2022). Analytical and numerical study on centrifugal stiffening effect for large rotating wind turbine blade based on NREL 5 MW and WindPACT 1.5 MW models. *Renewable Energy*, *183*, 321-329.

Menter, F. R. (2009). Review of the shear-stress transport turbulence model experience from an industrial perspective. *International Journal of Computational Fluid Dynamics*, *23*(4), 305-316.

Menter, F. R., Kuntz, M., & Langtry, R. (2003). Ten years of industrial experience with the SST turbulence model. *Turbulence, heat and mass transfer*, *4*(1), 625-632.

Miao, W., Li, C., Wang, Y., Xiang, B., Liu, Q., & Deng, Y. (2019). Study of adaptive blades in extreme environment using fluid–Structure interaction method. *Journal of Fluids and Structures*, *91*, 102734.

Micallef, D., & Rezaeiha, A. (2021). Floating offshore wind turbine aerodynamics: Trends and future challenges. *Renewable and Sustainable Energy Reviews*, *152*, 111696.
Micallef, D., & Sant, T. (2015). Loading effects on floating offshore horizontal axis wind turbines in surge motion. *Renewable Energy*, *83*, 737-748.
Mishnaevsky Jr, L., Brøndsted, P., Nijssen, R., Lekou, D. J., & Philippidis, T. P. (2012). Materials of large wind turbine blades: recent results in testing and modeling. *Wind Energy*, *15*(1), 83-97.
Moriarty, P. J., & Hansen, A. C. (2005). *AeroDyn theory manual*.
Moukalled, F., Mangani, L., & Darwish, M. (2015). The finite volume method. In *The finite volume method in computational fluid dynamics: An advanced introduction with OpenFOAM® and Matlab* (pp. 103-135). Springer.
Muyan, C., & Coker, D. (2020). Finite element simulations for investigating the strength characteristics of a 5 m composite wind turbine blade. *Wind Energ. Sci.*, *5*(4), 1339-1358.
Navadeh, N., Goroshko, I., Zhuk, Y., Etminan Moghadam, F., & Soleiman Fallah, A. (2021). Finite element analysis of wind turbine blade vibrations. *Vibration*, *4*(2), 310-322.
Nijssen, R. P. L., & Brøndsted, P. (2023). 7 - Fatigue as a design driver for composite wind turbine blades. In P. Brøndsted, R. Nijssen, & S. Goutianos (Eds.), *Advances in Wind Turbine Blade Design and Materials (Second Edition)* (pp. 217-248). Woodhead Publishing. https://doi.org/https://doi.org/10.1016/B978-0-08-103007-3.00006-9
Nomura, T., Kawamoto, A., Kondoh, T., Dede, E. M., Lee, J., Song, Y., & Kikuchi, N. (2019). Inverse design of structure and fiber orientation by means of topology optimization with tensor field variables. *Composites Part B: Engineering*, *176*, 107187.
Omidi, M., & Baumann, T. (2025). Integrated numerical simulation of reactive bubble columns: A coupled approach with openFOAM and PhreeqC. *Chemical Engineering Journal*, *518*, 163301.
Ortolani, A., Persico, G., Drofelnik, J., Jackson, A., & Campobasso, M. S. (2020, 2020). High-fidelity calculation of floating offshore wind turbines under pitching motion.
Papi, F., Jonkman, J., Robertson, A., & Bianchini, A. (2023). Going beyond BEM with BEM: an insight into dynamic inflow effects on floating wind turbines. *Wind Energy Science Discussions*, *2023*, 1-29.
Peeters, M., Santo, G., Degroote, J., & Van Paepegem, W. (2018a). Comparison of Shell and Solid Finite Element Models for the Static Certification Tests of a 43 m Wind Turbine Blade. *Energies*, *11*(6).
Peeters, M., Santo, G., Degroote, J., & Van Paepegem, W. (2018b). High-fidelity finite element models of composite wind turbine blades with shell and solid elements. *Composite Structures*, *200*, 521-531.
Pirrera, A., Capuzzi, M., Buckney, N., & Weaver, P. (2012, 2012). Optimization of wind turbine blade spars.
Reid, A., Rossi, R., Cottini, C., & Benassi, A. (2025). CFD simulation of a Rushton turbine stirred-tank using open-source software with critical evaluation of MRF-based rotation modeling. *Meccanica*, *60*(6), 1613-1637.

Resor, B. R. (2013). *Definition of a 5MW/61.5m wind turbine blade reference model*. https://www.osti.gov/servlets/purl/1095962

Resor, B. R., Maniaci, D. C., Berg, J. C., & Richards, P. W. (2014). *Effects of increasing tip velocity on wind turbine rotor design*. https://www.osti.gov/biblio/1177045

https://www.osti.gov/servlets/purl/1177045

Rezaei, F., Contestabile, P., Vicinanza, D., & Azzellino, A. (2023). Towards understanding environmental and cumulative impacts of floating wind farms: Lessons learned from the fixed-bottom offshore wind farms. *Ocean & Coastal Management*, *243*, 106772.

Riziotis, V. A., Voutsinas, S. G., Politis, E. S., Chaviaropoulos, P. K., Hansen, A. M., Madsen, H. A., & Rasmussen, F. (2008). Identification of structural non-linearities due to large deflections on a 5MW wind turbine blade. Proceedings of the EWEC,

Rostami, H., Fallah Najafabadi, M., & domiri ganji, D. (2021). Analysis of Timoshenko beam with Koch snowflake cross-section and variable properties in different boundary conditions using finite element method. *Advances in Mechanical Engineering*, *13*, 168781402110609.

Roth-Johnson, P., Wirz, R. E., & Lin, E. (2014). Structural design of spars for 100-m biplane wind turbine blades. *Renewable Energy*, *71*, 133-155.

Sayed, M., Klein, L., Lutz, T., & Krämer, E. (2019). The impact of the aerodynamic model fidelity on the aeroelastic response of a multi-megawatt wind turbine. *Renewable Energy*, *140*, 304-318.

Scott, S., Greaves, P., Macquart, T., & Pirrera, A. (2022, 2022). Comparison of blade optimisation strategies for the IEA 15MW reference turbine.

Scott, S., Greaves, P., Weaver, P. M., Pirrera, A., & Macquart, T. (2020). Efficient structural optimisation of a 20 MW wind turbine blade. *Journal of Physics: Conference Series*, *1618*(4), 042025.

Sebastian, P.-B., Francesco, P., Joseph, S., David, M., Alessandro, B., & Oliver, C. P. (2019). Is the blade element momentum theory overestimating wind turbine loads?—a comparison with a lifting line free vortex wake method. *Wind Energy Sci*, *5*, 721-743.

Serhat, G. (2021). Concurrent Lamination and Tapering Optimization of Cantilever Composite Plates under Shear. *Materials*, *14*(9), 2285.

Serhat, G., & Basdogan, I. (2019). Multi-objective optimization of composite plates using lamination parameters. *Materials & Design*, *180*, 107904.

Sharifi, A., & Nobari, M. R. H. (2013). Prediction of optimum section pitch angle distribution along wind turbine blades. *Energy Conversion and Management*, *67*, 342-350.

Simeon, B. (2006). On Lagrange multipliers in flexible multibody dynamics. *Computer Methods in Applied Mechanics and Engineering*, *195*(50), 6993-7005.

SIMULIA. (2014). *ABAQUS Theory Manual*

Stegmann, J., & Lund, E. (2005). Discrete material optimization of general composite shell structures. *International Journal for Numerical Methods in Engineering*, *62*(14), 2009-2027.

Sun, Q., Li, G., Duan, L., & He, Z. (2023). The coupling of tower-shadow effect and surge motion intensifies aerodynamic load variability in downwind floating offshore wind turbines. *Energy*, *282*, 128788.

Tang, S., Sweetman, B., & Gao, J. (2021). Nonlinear effects and dynamic coupling of floating offshore wind turbines using geometrically-exact blades and momentum-based methods. *Ocean Engineering*, *229*, 108866.

Tarfaoui, M., Shah, O. R., & Nachtane, M. (2019). Design and Optimization of Composite Offshore Wind Turbine Blades. *Journal of Energy Resources Technology*, *141*(5).

Tavares, R. P., Bouwman, V., & Van Paepegem, W. (2022). Finite element analysis of wind turbine blades subjected to torsional loads: Shell vs solid elements. *Composite Structures*, *280*, 114905.

Thapa, M., & Missoum, S. (2022). Surrogate-based stochastic optimization of horizontal-axis wind turbine composite blades. *Structural and Multidisciplinary Optimization*, *65*(2), 41.

Tran, T. T., & Kim, D.-H. (2016a). A CFD study into the influence of unsteady aerodynamic interference on wind turbine surge motion. *Renewable Energy*, *90*, 204-228.

Tran, T. T., & Kim, D.-H. (2016b). Fully coupled aero-hydrodynamic analysis of a semi-submersible FOWT using a dynamic fluid body interaction approach. *Renewable Energy*, *92*, 244-261.

Tran, T. T., & Kim, D. H. (2018). A CFD study of coupled aerodynamic‐hydrodynamic loads on a semisubmersible floating offshore wind turbine. *Wind Energy*, *21*(1), 70-85.

Verma, A. S., Vedvik, N. P., Haselbach, P. U., Gao, Z., & Jiang, Z. (2019). Comparison of numerical modelling techniques for impact investigation on a wind turbine blade. *Composite Structures*, *209*, 856-878.

Vianna Neto, J. X., Guerra Junior, E. J., Moreno, S. R., Hultmann Ayala, H. V., Mariani, V. C., & Coelho, L. d. S. (2018). Wind turbine blade geometry design based on multi-objective optimization using metaheuristics. *Energy*, *162*, 645-658.

Wang, L., Kolios, A., Nishino, T., Delafin, P.-L., & Bird, T. (2016). Structural optimisation of vertical-axis wind turbine composite blades based on finite element analysis and genetic algorithm. *Composite Structures*, *153*, 123-138.

Wang, L., Liu, X., & Kolios, A. (2016). State of the art in the aeroelasticity of wind turbine blades: Aeroelastic modelling. *Renewable and Sustainable Energy Reviews*, *64*, 195-210.

Wang, L., Liu, X., Renevier, N., Stables, M., & Hall, G. M. (2014). Nonlinear aeroelastic modelling for wind turbine blades based on blade element momentum theory and geometrically exact beam theory. *Energy*, *76*, 487-501.

Wang, L., Quant, R., & Kolios, A. (2016). Fluid structure interaction modelling of horizontal-axis wind turbine blades based on CFD and FEA. *Journal of Wind Engineering and Industrial Aerodynamics*, *158*, 11-25.

Wang, Z., Suiker, A. S. J., Hofmeyer, H., van Hooff, T., & Blocken, B. (2020). Coupled aerostructural shape and topology optimization of horizontal-axis wind turbine rotor blades. *Energy Conversion and Management*, *212*, 112621.

Wen, B., Tian, X., Dong, X., Peng, Z., & Zhang, W. (2017). Influences of surge motion on the power and thrust characteristics of an offshore floating wind turbine. *Energy*, *141*, 2054-2068.

Wiegard, B., König, M., Lund, J., Radtke, L., Netzband, S., Abdel-Maksoud, M., & Düster, A. (2021). Fluid-structure interaction and stress analysis of a floating wind turbine. *Marine Structures*, *78*, 102970.

Williams, R., & Zhao, F. (2023). Global Offshore Wind Report 2023.
Wu, J., Ma, Y., Wang, Z., & Yu, Z. (2022). Structurally coupled characteristics of rotor blade using new rigid-flexible dynamic model based on geometrically exact formulation. *Chinese Journal of Aeronautics*, *35*(6), 186-197.
Wu, X., Feng, K., & Li, Q. a. (2024). A Numerical Method for the Dynamics Analysis of Blade Fracture Faults in Wind Turbines Using Geometrically Exact Beam Theory and Its Validation. *Energies*, *17*(4).
Xu, Y., Wang, F., Liang, D., Lv, G., & Chen, C. (2024). A comprehensive review of waste wind turbine blades in China: Current status and resource utilization. *Journal of Environmental Chemical Engineering*, *12*(3), 113077.
Yang, J., Peng, C., Xiao, J., Zeng, J., Xing, S., Jin, J., & Deng, H. (2013). Structural investigation of composite wind turbine blade considering structural collapse in full-scale static tests. *Composite Structures*, *97*, 15-29.
Yang, L., Liao, K., Ma, Q., Ma, G., & Sun, H. (2023). Investigation of wake characteristics of floating offshore wind turbine with control strategy using actuator curve embedding method. *Renewable Energy*, *218*, 119255.
Yu, D. O., & Kwon, O. J. (2014). Predicting wind turbine blade loads and aeroelastic response using a coupled CFD–CSD method. *Renewable Energy*, *70*, 184-196.
Yu, W., Hodges, D. H., Volovoi, V., & Cesnik, C. E. S. (2002). On Timoshenko-like modeling of initially curved and twisted composite beams. *International Journal of Solids and Structures*, *39*(19), 5101-5121.
Yu, W., Volovoi, V. V., Hodges, D. H., & Hong, X. (2002). Validation of the variational asymptotic beam sectional analysis. *AIAA journal*, *40*(10), 2105-2112.
Yu, Z., Hu, Z., Zheng, X., Ma, Q., & Hao, H. (2020). Aeroelastic Performance Analysis of Wind Turbine in the Wake with a New Elastic Actuator Line Model. *Water*, *12*(5), 1233.
Zhang, Y., Song, Y., Shen, C., & Chen, N.-Z. (2023). Aerodynamic and structural analysis for blades of a 15MW floating offshore wind turbine. *Ocean Engineering*, *287*, 115785.
Zheng, T., Chen, N.-Z., & Yuan, L. (2023). Structural strength assessment for thin-walled blade root joint of floating offshore wind turbine (FOWT). *Thin-Walled Structures*, *191*, 111057.
Zhou, L., Shen, X., Chen, J., Yin, F., & Du, Z. (2022). Effects of the Surge Motion on the Performance of Floating Wind Turbine Considering Blade Structural Flexibility. ASME Turbo Expo 2022: Turbomachinery Technical Conference and Exposition,
Zhou, Y., Xiao, Q., Liu, Y., Incecik, A., Peyrard, C., Wan, D., Pan, G., & Li, S. (2022). Exploring inflow wind condition on floating offshore wind turbine aerodynamic characterisation and platform motion prediction using blade resolved CFD simulation. *Renewable Energy*, *182*, 1060-1079.
Zhu, G., Zhang, Y., Niu, X., Duan, C., Wang, Z., & Zhao, X. (2025). Novel multiscale modeling strategy for hybrid fiber reinforced composites. *International Journal of Mechanical Sciences*, *287*, 109997.
Zuo, Z. H., & Xie, Y. M. (2014). Maximizing the effective stiffness of laminate composite materials. *Computational Materials Science*, *83*, 57-63.